Thèse
de doctorat
de l'UTT

Juan XIN

From Synthesis to Assembly: Study of a Silicon based Metasurface Fabrication

Champ disciplinaire :
Sciences pour l'Ingénieur

2025TROY0020

Année 2025

utt
UNIVERSITÉ DE TECHNOLOGIE
TROYES

THESE

pour l'obtention du grade de

DOCTEUR
de l'UNIVERSITE DE TECHNOLOGIE DE TROYES

en SCIENCES POUR L'INGENIEUR

Spécialité : MATERIAUX, MECANIQUE, OPTIQUE ET NANOTECHNOLOGIE

présentée et soutenue par

Juan XIN

le 22 mai 2025

From Synthesis to Assembly: Study of a Silicon based Metasurface Fabrication

JURY

Mme Agnès MAÎTRE	PROFESSEURE DES UNIVERSITES	Présidente
Mme Glenna DRISKO	DIRECTRICE DE RECHERCHE	Rapporteure
Mme Laurence RESSIER	PROFESSEURE DES UNIVERSITES	Rapporteure
M. Julien PROUST	ENSEIGNANT CHERCHEUR	Examinateur
M. Tao XU	ASSOCIATE PROFESSOR	Examinateur
M. Jérôme PLAIN	PROFESSEUR DES UNIVERSITES	Directeur de thèse

ACKNOWLEDGEMENTS

The successful development of doctoral projects is closely tied to financial support. First of all, I would like to thank Prof. Xiaowei Sun (Southern University of Science and Technology) for his financial support at the beginning of my PhD. At the same time, I also would like to thank CSC for its overseas high-level projects and Prof. Jerome PLAIN for his partial financial support. Without the help of these funds, I would not be able to successfully complete my doctoral project.

I would like to express my deepest gratitude again to Prof. Xiaowei Sun of Southern University of Science and Technology for the invaluable opportunity to pursue my doctorate at UTT. Without his recommendation, I would not have been introduced to UTT, nor would I have had the privilege of working with my supervisor, Prof. Jérôme PLAIN.

I was incredibly fortunate to receive guidance from Prof. Jerome PLAIN during my doctoral studies. When I first arrived in France, it was Professor Jerome who helped me quickly adapt to the learning environment. Under his guidance, I soon delved into my field of study. Each discussion on research progress left me inspired and full of hope for scientific discovery. One of the most impactful things he told me was, 'You are not a baby student; you need to have your own mind to develop and control your subject. This advice was crucial throughout my doctoral journey. Professor Jerome also provided numerous opportunities to attend academic conferences, which helped me stay updated on cutting-edge trends and allowed me to interact with fellow researchers. These experiences have been immensely beneficial to my growth. Whenever I faced difficulties in my studies or personal life, Professor Jerome consistently offered encouragement and support. I am also thankful to Prof. Julien PROUST, my second supervisor at UTT. He often worked with my supervisor Jerome to guide the progress of my doctoral project and gave me a lot of valuable thinking

and guidance. He would help me build light paths, teach me to test spectra, and help me solve many problems encountered in experiments.

Once again, I would like to deeply thank my two supervisors Jerome and Julien for their patience in accepting my mistakes and for their continuous guidance, which made my study experience at L2n both pleasant and fruitful.

I am also grateful to Prof. Christophe Couteau, the department head of our L2n laboratory. He always arranges a lot of academic seminars regularly, so that we have more opportunities for academic exchanges. At the same time, we will also arrange Christmas celebrations, welcome activities, King cake tasting activities, etc., so that our laboratory is very loving and dynamic. Special thanks to Prof. Renaud Bachelot, who encouraged me to join Nanophot School. On this platform, I have more opportunities to participate in academic seminars and conferences related to the academic field, which is a great inspiration for my doctoral project. I think joining Nanophot was the right decision! I am also grateful to Regis, Jeremie, Serguei and Anna for their help in the progress of my experiment! I also would like to thank Ms. Pascale Denis, Ms. Patricia Caillot and Ms. Sandrine Boyon for their administrative assistance.

A special note of thanks to my colleague Theo, it’s too lucky we have same supervisor. I always turn to Theo for help whenever I have difficulties in the lab. He is so kind that he is always patient to help me. Once my key was locked in the office and I was in a hurry. But when Theo found out, he quickly helped me solve the problem, just like a superman! I would like to thank Ke Li, my partner who went to France with me to study for a PhD. During the one and a half years that Ke Li has been in UTT, she has been very helpful to me both in study and life. I am also grateful to Margaux, Mingyu Chen, Kuan_Ting Wu, Borui Li, Hongshi Chen, Qingmeng Li, Wei Tao, Yuqing Zhao, Fusheng Du, Nawres, Basma, Yanli Chen, Xiao Liu, Hui Chen, Yusen Li, Baoxing Wang, Kunzhang Guo for their support and companionship during my PhD journey.

Finally, I want to express my deep gratitude to my family for their support. They are my sustenance and my spiritual pillar. It is their company that makes me feel down-to-earth and gives me the strength to face any difficulties. A heartfelt thank you to my boyfriend for taking care of me throughout my PhD studies.

De la synthèse à l'assemblage : Étude de la fabrication d'une métasurface à base de silicium

Résumé:

Cette étude explore la synthèse, l'assemblage et l'application des nanoparticules de silicium (Si NPs) dans les dispositifs nanophotoniques, en mettant l'accent sur leur rôle dans la fabrication de métasurfaces diélectriques hautement efficaces. Deux méthodes de broyage mécanique — la méthode du mixeur de cuisine et la méthode du broyage à billes — ont été utilisées pour préparer les Si NPs, chacune présentant des avantages distincts en termes de morphologie des particules, de dispersibilité et de compatibilité avec l'assemblage. La méthode du mixeur de cuisine a offert une approche économique et respectueuse de l'environnement, produisant des Si NPs uniformément dispersées dans de l'eau déionisée, ce qui a facilité leur assemblage précis par microfluidique. En revanche, la méthode du broyage à billes a permis un meilleur contrôle morphologique, mais a conduit à la dispersion des nanoparticules dans de l'éthanol anhydre, posant des défis liés à la volatilité du solvant et à l'agrégation des particules.

Pour réaliser un assemblage précis des Si NPs sur des substrats nano-structurés, la technologie microfluidique SmartForce a été employée, exploitant les forces capillaires et les dynamiques d'évaporation contrôlée. Les résultats expérimentaux ont démontré que les Si NPs préparées par la méthode du mixeur de cuisine présentaient une efficacité d'assemblage et une intégrité structurelle supérieures, ce qui en fait le choix privilégié pour la fabrication de métasurfaces nano-structurées. De plus, cette étude a examiné l'impact de la géométrie du substrat, de la modification de surface (traitement APTES) et du contrôle dynamique des fluides sur le positionnement des nanoparticules, révélant que l'optimisation des paramètres d'assemblage améliore considérablement la précision et la reproductibilité de la fabrication des métasurfaces.

Au-delà de leur application dans les métasurfaces optiques, l'étude a également exploré le potentiel des Si NPs dans les circuits photoniques intégrés, la biosensibilité et l'informatique quantique, notamment lorsqu'elles sont associées à des matériaux bidimensionnels comme le graphène et le MoS_2. De plus, l'intégration des Si NPs avec des pérovskites et des nanocomposites hybrides a été examinée, mettant en évidence leur potentiel pour les dispositifs optoélectroniques avancés et la conversion d'énergie solaire à haute efficacité.

Dans l'ensemble, cette recherche établit une approche évolutive, économique et de haute précision pour la synthèse et l'assemblage des Si NPs, fournissant ainsi une base solide pour les applications nanophotoniques et optoélectroniques de nouvelle génération. Ces résultats ouvrent la voie à de futures avancées dans les domaines de la communication optique, des technologies de détection et des dispositifs métasurfaces multifonctionnels.

Mots clés : [Nanosilicium]**,** [Lithographie par faisceau d'électrons], [Métasurfaces], [Chimie des surfaces], [Autoassemblage], [Microfluidique]

From synthesis to assembly: Study of a Silicon based metasurface fabrication

Abstract

This study explores the synthesis, assembly, and application of silicon nanoparticles (Si NPs) in nanophotonic devices, focusing on their role in fabricating high-efficiency all-dielectric metasurfaces. Two mechanical grinding methods—the kitchen blender method and the ball milling method—were employed to prepare Si NPs, each exhibiting distinct advantages in particle morphology, dispersibility, and assembly compatibility. The kitchen blender method provided a cost-effective and environmentally friendly approach, yielding uniformly dispersed Si NPs in deionized water, which facilitated precise microfluidic-assisted assembly. In contrast, the ball milling method enabled better morphological control but resulted in nanoparticles dispersed in anhydrous ethanol, posing challenges due to solvent volatility and particle aggregation.

To achieve precise assembly of Si NPs onto nano-patterned substrates, SmartForce microfluidic technology was employed, leveraging capillary forces and controlled evaporation dynamics. Experimental results demonstrated that Si NPs prepared via the kitchen blender method exhibited higher assembly efficiency and structural integrity, making them the preferred choice for constructing nano-patterned metasurfaces. Moreover, this study investigated the impact of substrate geometry, surface modification (APTES treatment), and dynamic fluidic control on nanoparticle positioning, revealing that tunable assembly parameters significantly enhance the precision and reproducibility of metasurface fabrication.

Beyond their application in metasurface-based optics, the study further explored the potential of Si NPs in integrated photonic circuits, biosensing, and quantum

computing, particularly when combined with 2D materials such as graphene and MoS_2. Additionally, the integration of Si NPs with perovskites and hybrid nanocomposites was examined, highlighting their potential for advanced optoelectronic devices and high-efficiency solar energy conversion.

Overall, this research establishes a scalable, cost-effective, and high-precision approach for Si NP synthesis and assembly, providing a solid foundation for next-generation nanophotonic and optoelectronic applications. The findings pave the way for future advancements in optical communication, sensing technologies, and multifunctional metasurface devices.

Keywords: [Nanosilicon]**,** [Lithography, Electron beam], [Metasurfaces], [Surface Chemistry], [Self-assembly (Chemistry)], [Microfluidics]

Laboratoire Lumière, nanomatériaux et nanotechnologies – L2n, Université de Technologie de Troyes & CNRS UMR 7076, 12 rue Marie Curie, CS 42060, 10004 Troyes Cedex, France

Context of the PhD

This PhD research focuses on the synthesis, assembly, and application of silicon nanoparticles (Si NPs) in all-dielectric metasurfaces, integrating nanomaterials science, microfluidic-assisted assembly, and optical engineering to develop scalable, high-precision fabrication methods for nanophotonic devices.

Scientific Background and Motivation:

Metasurfaces, composed of subwavelength nanostructures, enable miniaturization, enhanced optical control, and multifunctionality for applications in optical communication, biosensing, imaging, and quantum technologies. Si NPs, with their high refractive index, low optical loss, and CMOS compatibility, are ideal for metasurfaces. However, achieving precise, large-scale assembly remains a challenge, addressed in this research through novel Si NP synthesis and assembly techniques.

Research Objectives and Methodology:

This study explores two mechanical synthesis methods—kitchen blender and ball milling—to optimize Si NP morphology, dispersibility, and assembly compatibility. The kitchen blender method provides a cost-effective, environmentally friendly approach with well-dispersed Si NPs in deionized water, facilitating microfluidic-assisted capillary force assembly. The ball milling method offers better morphology control but faces solvent volatility issues, limiting its application in nanopatterned assembly.

Using SmartForce microfluidic technology, the study optimizes solvent evaporation, airflow, and surface functionalization (APTES treatment) to enhance particle adhesion and stability. This enables precise Si NP assembly on nano-patterned silicon and ITO glass substrates, including complex structures like the Einstein image array, demonstrating high-resolution metasurface fabrication potential.

Technological and Industrial Relevance:

This research advances scalable, precise nanoparticle-based metasurface fabrication, with applications in photonic circuits, optical sensors, high-resolution imaging, and quantum photonics. Integrating Si NPs with 2D materials (graphene, MoS_2) and perovskites unlocks new opportunities for hybrid optoelectronic devices and biosensors with ultra-sensitive molecular detection capabilities.

Future Directions:

This study presents a scalable and low-cost method for fabricating silicon nanoparticle (Si NP)-based metasurfaces using a bottom-up, microfluidic-assisted approach. To improve Si NP quality, future research should explore ultrasound-assisted grinding and chemical surface modification for better dispersion and uniformity. For more precise assembly, techniques like electric, magnetic, and optical trapping can help build 3D nanostructures. These advances will support the use of Si NP-based metasurfaces in photonic chips, optical modulators, and high-speed data systems. Combining Si NPs with 2D materials or perovskites could also improve performance, offering new possibilities for optoelectronic applications.

A brief description of the different chapters is presented below:

- **Chapter 1:** Introduction to Si NPs and Their Application Background.

This chapter presents Si NPs as key materials for all-dielectric metasurfaces, emphasizing their cost-effective synthesis, unique properties, and applications in optics and nanotechnology. It highlights the kitchen blender method as an efficient and scalable fabrication approach.

- **Chapter 2:** Fundamentals of Metasurfaces and Assembly Techniques.

This chapter highlights the advantages of all-dielectric metasurfaces, comparing top-down fabrication with bottom-up microfluidic assembly, emphasizing efficiency, scalability, and sustainability.

- **Chapter 3:** Si NPs Preparation and Experimental Design.

This chapter compares kitchen blender and ball milling methods for Si NP preparation

and explores microfluidic-assisted assembly for precise nanostructure fabrication.

- **Chapter 4:** Microfluidic Assembly of Si NPs on Silicon Substrates.

This chapter presents a microfluidic approach for assembling Si NPs on silicon substrates, using the kitchen blender method for synthesis and silanization for adhesion, achieving stable nanopatterns with the SmartForce device.

- **Chapter 5:** Ball Milling Method and Assembly on ITO Glass Substrates.

This chapter examines the ball milling method for Si NP synthesis, highlighting ethanol's volatility issues and proposing alternative solvents to enhance assembly stability.

- **Chapter 6:** Si NPs Assembly on Complex Nano-Patterned Substrates.

This chapter explores Si NP assembly on complex nano-patterned substrates using the kitchen blender method and microfluidic technology, achieving high precision, efficiency, and stability.

- **Chapter 7:** Conclusion and Prospect.

This chapter summarizes key findings, challenges, and contributions while proposing future research on Si NP synthesis, hybrid materials, and advanced assembly techniques.

- **Chapter 8:** French Summary.

General table of contents

Chapter 1: Introduction to Si NPs and Their Application Background 2
1.1 Silicon as a Material for metasurfaces 2
1.2 Preparation Methods and Application Background of Si NPs 4
1.2.1 Preparation Methods of Silicon Nanoparticles 4
1.2.2 Performance of Silicon Nanoparticles in Specific Applications 12
1.3 Prospects and Future Research Directions 15
1.3.1 Optimization of Fabrication Techniques 15
1.3.2 Exploration of Novel Assembly Techniques 16
1.3.3 Multifunctional Integration 16
1.3.4 Green Manufacturing and Sustainability 17
1.4 Conclusion 17
Chapter 2: Fundamentals of Metasurfaces and Assembly Techniques 19
2.1 Background on Metasurface Fabrication 19
2.1.1 Concept of Metasurfaces 19
2.1.2 The Significance of Metasurfaces in Modern Technology 21
2.1.3 Recent Advances in Metasurfaces 24
2.1.4 Applications of Metasurfaces 27
2.1.5 Top-Down Metasurface Fabrication Methods and Limitation Analysis 30
2.2 Development of Microfluidic Technology 36
2.2.1 Principles of Microfluidic Technology in Nanostructure Assembly 37
2.2.2 Research Status and Advantages of Microfluidic Technology 39
2.3 Significance of This Study 44
2.3.1 Exploration of Efficient and Low-Cost Silicon Nanoparticle Preparation Methods 44
2.3.2 Innovative Application of Nanoparticle Assembly Techniques 44
2.3.3 Critical Role of Silanization Reactions in Assembly Stability 45
2.3.4 Innovation and Expansion of Silicon-Based Metasurface Fabrication 45
2.3.5 Promoting Low-Cost Nanomanufacturing Technologies 46
2.3.6 Academic and Industrial Impact 46
2.4 Conclusion 47
Chapter 3: Si NPs Preparation and Experimental Design 49
3.1 Material preparation method 49
3.1.1 Si nanoparticles Preparation by Kitchen blender 49
3.1.2 Si nanoparticles Preparation by ball mill 50
3.2 Experimental design of capillary force assisted Si nanoparticle assembly 50
3.2.1 Preparation of Nanopatterned Substrates 51
3.2.2 The process of Silanization Reaction 52
3.2.3 The process of Si nanoparticles Assembly 53
3.2.4 Lift-off process 54
3.3 Characterization tools and data analysis methods 55

3.3.1 SEM (Scanning Electron Microscopy) 55
3.3.2 AFM (Atomic Force Microscopy) 56
3.3.3 Dark-field Microscope 57
3.3.4 Dynamic Light Scattering 58
3.3.5 Extinction spectrum 59
3.3.6 Finite-Difference Time-Domain (FDTD) 60
3.4 Conclusions 62
Chapter 4: Microfluidic Assembly of Si NPs on Silicon Substrates 64
4.1 Introduction 64
4.2 Experimental section 66
4.3 Results and Discussion 68
4.3.1 Characterization Analysis of Si Nanoparticles 68
4.3.2 Preparation and Analysis of Nanopatterned Substrate 70
4.3.3 Theoretical Analysis of the Silanization Reaction 72
4.3.4 The Assembly Process and Result Analysis of Si Nanoparticles 73
4.4 Auxiliary Analysis of the Reference Experiment 78
4.5 FDTD Lumerical Simulations Results 81
4.6 Conclusions 84
Chapter 5: Ball Milling Method and Assembly on ITO Glass Substrates 86
5.1 Introduction 86
5.2 Experimental section 88
5.3 Results and Discussion on preparation of Si NPs by ball mill 91
5.3.1 Motivation for using a ball mill to prepare Si nanoparticles 91
5.3.2 Fundamental Research on the Preparation of Si NPs via Ball Milling (Using Inox Balls as Grinding Media) 94
5.3.3 Fundamental Research on the Preparation of Si NPs via Ball Milling (Using ZrO2 Balls as Grinding Media) 97
5.3.4 Fundamental Research on the Preparation of Si NPs via Ball Milling (Using ZrO2 Grinding Balls to get Si Nanocubes) 100
5.4 Si NP Dispersion and Assembly in ETOH and DI Water 103
5.5 Conclusion 109
Chapter 6: Si NPs Assembly on Complex Nano-Patterned Substrates 111
6.1 Introduction 111
6.2 Experimental section 111
6.3 Results and Discussion 112
6.3.1 Reasons for Choosing Kitchen Blender-Prepared Si NPs for Assembling Complex Metasurface Structures 112
6.3.2 Assembly of Complex Patterned Substrate: Einstein Pattern 114
6.4 Conclusion 124
Chapter 7: Conclusion and Prospect 126
7.1 Research Conclusion 126
7.1.1 Comparison of Si NP Preparation Methods 126
7.1.2 Assembly Performance of Si NPs on Nano-Patterned Substrates 127
7.1.3 Application of Si NPs on Complex Nano-Patterned Substrates 127

7.2 Future Prospects 128
7.2.1 Further Optimization of Si NP Preparation Methods 128
7.2.2 Development of High-Precision Nano-Assembly Techniques 129
7.2.3 Expanding the Application of Si NPs in Optoelectronic Devices 129
7.2.4 Development of Novel Nanocomposite Materials 130
7.3 Research Summary 130
References 132
Chapter 8: French Summary 151
8.1 Introduction aux nanoparticules de silicium (Si NPs) et aux métasurfaces : principes, fabrication et assemblage 151
8.2 Fundamentals of Metasurfaces and Assembly Techniques 151
8.3 Préparation des nanoparticules de silicium (Si NPs) et conception expérimentale 152
8.3.1 Méthodes de préparation des matériaux 153
8.3.2 Experimental design of capillary force assisted Si nanoparticle assembly 154
8.3.3 Characterization tools and data analysis methods 156
8.3.4 Conclusions 157
8.4 Assemblage microfluidique des nanoparticules de silicium 157
8.4.1 Introduction 158
8.4.2 Partie expérimentale 158
8.4.3 Résultats et discussion 159
8.4.4 Analyse auxiliaire des expériences de référence 166
8.4.5 Résultats de simulation FDTD avec Lumerical 168
8.4.6 Conclusions 170
8.5 Méthode de broyage à billes et assemblage sur substrats en verre ITO 171
8.5.1 Introduction 171
8.5.2 Méthodologie expérimentale 171
8.5.3 Résultats et discussion 173
8.5.4 Dispersion et assemblage des nanoparticules 180
8.5.5 Conclusion 184
8.6 Assemblage de nanoparticules de Si sur des substrats nano-structurés complexes 184
8.6.1 Introduction 184
8.6.2 Méthodologie expérimentale 185
8.6.3 Results and Discussion 185
8.6.4 Conclusion 191

Chapter 1

Introduction to Si NPs and Their Application Background

This chapter explores the unique advantages of silicon nanoparticles (Si NPs) as key materials for all-dielectric metasurfaces and their potential for future development. Silicon, with its high refractive index, low optical loss, and compatibility with existing semiconductor processes, holds a central position in metasurface technology**[1-2]**. The uniform size and excellent optical properties of Si NPs make them uniquely valuable in metasurface fabrication, significantly enhancing the functional performance and application scope of metasurfaces**[3-4]**. By compares several Si NP preparation methods—mechanical milling, chemical precipitation, sol-gel, and laser ablation—highlighting their differences in cost, efficiency, and control. These insights help guide future optimization and large-scale production. Si NPs are not only effective in traditional optics, biosensing, and communication, but also show strong potential in aerospace and environmental monitoring due to their thermal and mechanical stability. Looking forward, their role in metasurface fabrication will grow, enabling precise assembly, complex nanostructures, and multifunctional integration. These strengths support ongoing innovation in metasurface and optoelectronic technologies.

Chapter 1: Introduction to Si NPs and Their Application Background

1.1 Silicon as a Material for metasurfaces

Silicon (Si) possesses unparalleled advantages in the fields of nanophotonics and electronic devices**[5]**. Firstly, the unique optical properties of silicon, including a high refractive index and low optical loss, enable more efficient light manipulation in the design of all-dielectric metasurfaces. Secondly, silicon is an abundant, cost-effective, and easily processed material, offering significant economic advantages for large-scale manufacturing compared to metals or rare materials**[6]**. Additionally, silicon's chemical stability and biocompatibility make it ideal for environmentally friendly manufacturing and biomedical applications**[7]**. Moreover, silicon nanoparticles prepared via mechanical milling techniques, such as the kitchen blender method or ball milling, exhibit excellent size uniformity and dispersion stability. These particles are also highly compatible with microfluidic technologies, providing an ideal foundation for the assembly of complex nanostructures. Therefore, the selection of silicon for subsequent metasurface assembly not only meets the demands for superior optical performance but also ensures technological support for green manufacturing and efficient assembly. These features will be discussed in greater detail in the following chapters.

Silicon is highly valued for its exceptional optical properties, which include a high refractive index and low optical loss in the near-infrared (NIR) range. These characteristics are crucial for many optical and photonic applications**[8]**. The high refractive index of silicon, approximately 3.5 at 1550 nm, allows for strong light confinement and precise manipulation, enabling the development of compact and efficient optical components such as lenses, waveguides, and modulators. Furthermore, silicon's low optical loss in the NIR range, particularly around the

telecommunications wavelengths of 1310 nm and 1550 nm, ensures minimal signal attenuation, making it ideal for high-speed optical communication systems. These properties enable silicon metasurfaces to manipulate light with high efficiency and precision, facilitating advanced functionalities in a wide range of photonic applications**[9]**. In addition, High-index dielectric materials for the visible range and their corresponding aspect ratios was shown in **Figure 1.1**. Aspect ratio is defined as the ratio of a structure's thickness and its critical feature size. The aspect ratio of the material is closely related to the properties of the corresponding metasurface structure.

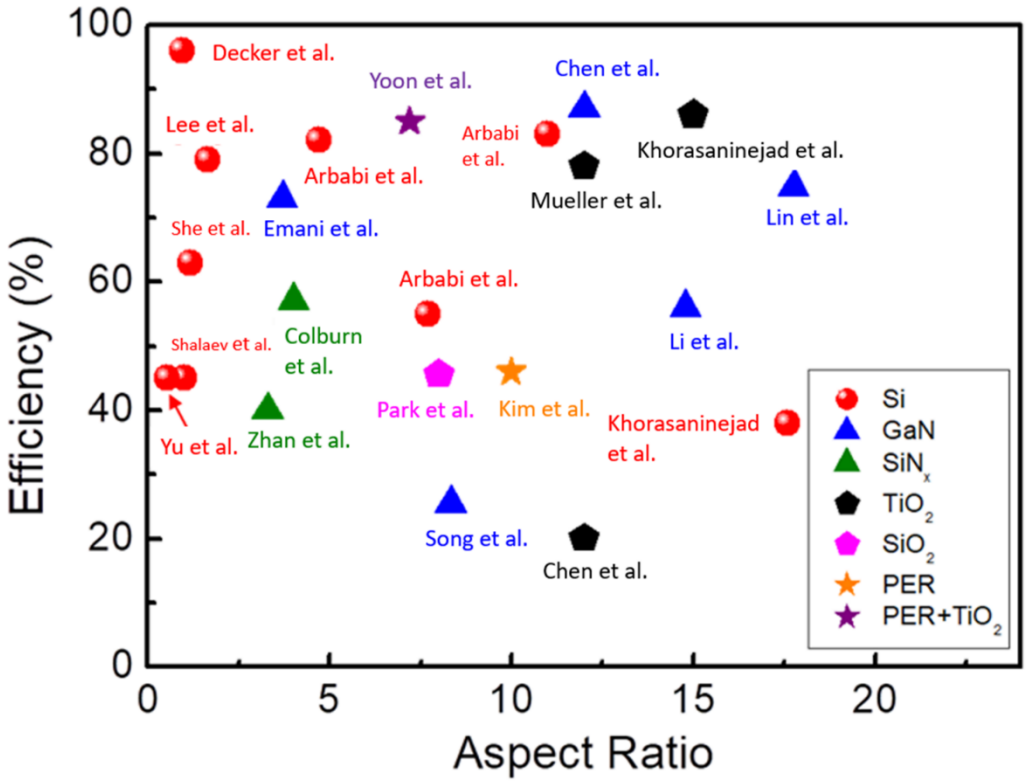


Figure 1.1: Aspect ratio versus efficiency of metasurfaces based on different materials**[10]**.

Silicon's effectiveness in the near-infrared spectrum makes it particularly suitable for applications in telecommunications, such as fiber optics**[11]**, infrared imaging**[12]**, and sensing technologies**[13-14]**. In telecommunications, silicon metasurfaces can be integrated into optical fibers and photonic circuits to enhance data transmission

efficiency and signal integrity. For infrared imaging, silicon-based devices offer high sensitivity and resolution, improving the performance of cameras and sensors used in medical diagnostics, security, and environmental monitoring. The compatibility of silicon with infrared wavelengths extends its utility across various fields, driving innovation and improving the capabilities of modern technology.

Silicon is well-suited for metasurfaces due to its excellent thermal and optical stability**[15-16]**. It can endure high temperatures and changing environments, making it ideal for high-power and industrial applications. Its compatibility with infrared light also supports the development of efficient optical devices. As the demand for advanced photonic systems increases, silicon metasurfaces are gaining importance. They integrate easily with existing semiconductor technologies and enable compact, high-performance photonic circuits. This helps improve data transmission, processing, and secure communication in next-generation optical and quantum devices.

1.2 Preparation Methods and Application Background of Si NPs

The preparation and application of silicon nanoparticles (Si NPs) are key to advancing all-dielectric metasurface technology. Producing size-uniform, well-dispersed Si NPs efficiently is essential for building complex nanostructures. Common methods include mechanical grinding, chemical precipitation, and laser ablation, each with different advantages in cost and efficiency. Si NPs have wide applications in nanophotonics, biosensing, communications, and environmental monitoring. By improving preparation methods and combining them with microfluidic assembly, their performance can be further enhanced. This section introduces the main preparation techniques and explores the application potential of Si NPs in modern technologies.

1.2.1 Preparation Methods of Silicon Nanoparticles

The preparation methods of silicon nanoparticles (Si NPs) directly influence their size, morphology, and dispersion properties, thereby determining their performance in

metasurface assembly. Current preparation techniques mainly include mechanical grinding, chemical synthesis, and laser ablation, each exhibiting different levels of uniformity, production cost, and scalability. By comparing and optimizing these methods, the most suitable preparation process can be selected based on specific requirements, laying a solid foundation for the efficient assembly and functional application of metasurfaces. The following discussion will delve into these preparation methods, analyzing their advantages, limitations, and applicability.**[17]**

(1) Top-down Method

◆ **Mechanical grinding** is a common and efficient method for preparing nanoparticles, utilizing external mechanical force to break down bulk materials into nanoscale particles. This technique is cost-effective, simple to operate, and suitable for large-scale production, making it particularly advantageous for preparing silicon nanoparticles (Si NPs). The following introduces two main mechanical grinding methods — kitchen blender method and ball milling — and provides a detailed comparison of their features.

***kitchen blender method*：** The kitchen blender method is an innovative and cost-effective technique for preparing silicon nanoparticles (Si NPs), utilizing a standard kitchen blender to perform high-intensity mechanical grinding of silicon blocks. As shown in **Figure 1.2**, the specific procedure is as follows: high-purity silicon blocks (99.9999%) are mixed with deionized water (DI water) and placed in the blender container. Intermittent high-speed blending is used to gradually reduce the particle size. During the process, the blender operates for 3 minutes and then pauses for 2 minutes to prevent overheating. As a household appliance, the kitchen blender is significantly cheaper than specialized laboratory grinding equipment, making it ideal for budget-constrained experimental research.

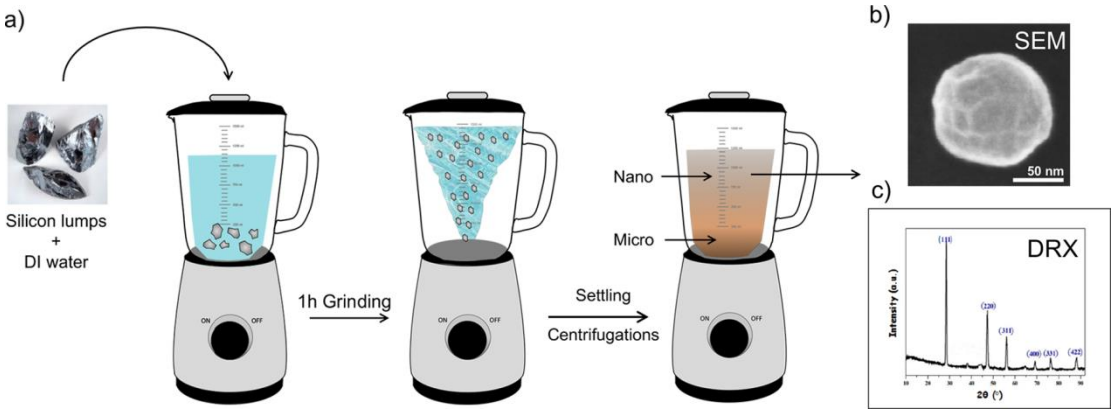


Figure 1.2: (a) Schematic representation of the process (grinding, clarification) used to prepare colloidal silicon nanoparticles. (b) High-magnification SEM image of a typical crystalline Si nanoparticle deposited onto a silicon substrate. (c) XRD pattern of Si nanoparticles powder where the indices show Si phase**[18]**.

This method is simple to operate and does not require complex experimental conditions. Particle preparation can be optimized by adjusting the blending time and speed. After grinding, the particles can be centrifuged and resuspended to obtain silicon nanoparticles with a uniform size distribution, typically in the range of 50–300 nm. The Si NPs exhibit excellent dispersibility in DI water, making the aqueous dispersion suitable for capillary-force-driven assembly in microfluidic technologies. However, a potential drawback of this method is the irregular morphology of some particles, including sharp-edged fragments, which might limit its applicability in specific use cases.

Ball milling method **[19]:** Ball milling is a high-energy grinding method that uses balls (steel or ceramic) to break down materials into nanoparticles. In this process, silicon blocks are mixed with anhydrous ethanol and milled, with particle size controlled by adjusting the speed, time, and ball size. This method is efficient and allows for precise control of particle size. However, it has some drawbacks. The resulting silicon nanoparticles can usually only be dispersed in anhydrous ethanol, which has high volatility. This can lead to uneven particle distribution during

assembly and may damage sensitive substrates. Ethanol is also not compatible with some microfluidic devices, limiting its use in assembling complex nanostructures.

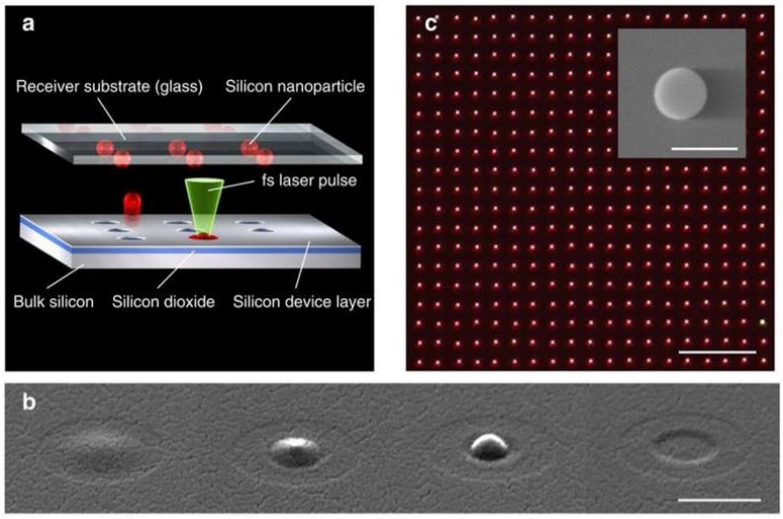


Figure 1.3: Laser-printing process of Si nanoparticles.[20] (a) Femtosecond lasers transfer silicon nanoparticles from a silicon wafer to glass. (b) SEM images show that higher laser energy ejects more particles, leaving holes in the silicon. (c) Dark-field and SEM images display a uniform array of ~160 nm silicon nanoparticles.

◆ **Laser printing：** Femtosecond laser printing is a precise method for fabricating silicon nanoparticles (Si NPs) by using high-energy laser pulses to ablate a silicon-on-insulator (SOI) substrate and transfer the particles onto a glass receiver. As shown in **Figure 1.3(a)**, laser pulses eject Si NPs from the silicon layer to the receiving substrate. **Figure 1.3(b)** displays SEM images of the substrate before and after ejection, showing increased laser energy leading to visible holes. **Figure 1.3(c)** shows a regular array of Si NPs (~160 nm) under dark-field and SEM imaging. This method provides high precision and uniform particle shape, making it suitable for fabricating nanostructures. However, it also has limitations: low production speed due to point-by-point processing, high equipment costs, and sensitivity to laser parameters. Additionally, the process often requires vacuum or inert environments and consumes significant energy. While ideal for high-quality, small-scale production, femtosecond laser printing remains less practical for large-scale industrial applications.

(2) Bottom-up method

◆ **Pyrolysis of silane:** The pyrolysis of silane (SiH_4) is a laser-assisted gas-phase method for producing high-purity silicon nanoparticles (Si NPs). As shown in **Figure 1.4**, the system includes a quartz tube, a laser inlet, and gas nozzles for silane and nitrogen. Silane gas flows through the tube in an inert nitrogen atmosphere, while a high-energy laser heats the reaction zone, causing the silane to break down into silicon atoms that form nanoparticles. These are then cooled and collected.

This method allows good control over particle size and purity. However, it has several drawbacks: silane is expensive and hazardous, requiring strict safety measures; the equipment is complex and costly; and the process consumes a lot of energy. Particle aggregation can still occur, and scaling up for industrial use is difficult. While effective for research, this technique is less practical for large-scale production.

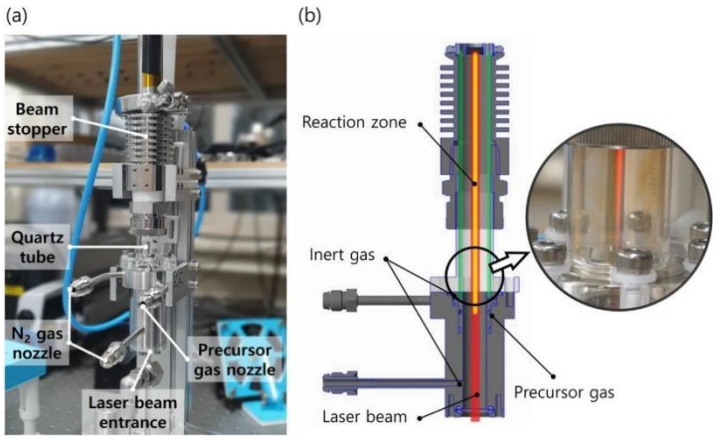


Figure 1.4: (a) A picture and (b) a schematic of the coaxial reactor.**[21]**

◆ **Reduction of silicon tetrachloride**: This method involves producing silicon nanoparticles (Si NPs) by reducing silicon tetrachloride ($SiCl_4$) using metallic reducing agents such as magnesium powder or aluminum powder at high temperatures, resulting in high-purity elemental silicon. The principle of the reaction is that the silicon atoms in silicon tetrachloride are reduced to elemental silicon by the metallic reducing agent, with by-products such as magnesium chloride or aluminum

chloride being generated. For example, the reaction of $SiCl_4$ with magnesium is expressed as:

$SiCl_4 + 2Mg \rightarrow Si + 2MgCl_2$.

As shown in **Figure 1.5**, silicon nanoparticles (Si NPs) can be made by reducing silicon tetrachloride with a metal like magnesium or aluminum at high temperatures (500–800 °C) in an inert gas atmosphere to prevent oxidation. After the reaction, by-products such as $MgCl_2$ are removed with acid or water, and the Si NPs are collected by centrifugation or filtration, then washed and dried. This method produces high-purity, well-dispersed Si NPs with controllable size. However, the use of expensive materials and the handling of chemical by-products make the process costly and complex, limiting its large-scale application.

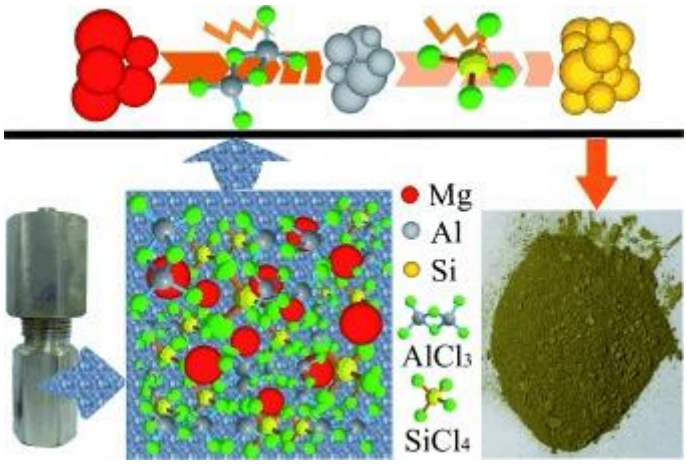


Figure 1.5: Si nanoparticles are produced by reducing $SiCl_4$ with Mg in molten $AlCl_3$ at 200 ℃. $AlCl_3$ acts as both solvent and reactant. The resulting Si NPs are highly crystalline and ideal for lithium-ion batteries.**[22]**

(3) Reduction of silica particles

◆ **Carbonthermal reduction:** The CO_2 laser-assisted carbothermal reduction is a fast method to produce silicon (Si) from silicon dioxide (SiO_2). As shown in **Figure 1.6**, a high-power CO_2 laser heats a SiO_2–carbon black mixture in a nitrogen atmosphere, causing rapid chemical reactions that form silicon. The process is quick

and precise, producing Si in just a few seconds. While effective for small-scale production, the method requires careful control of laser settings and is not ideal for large areas. Still, it offers a promising way to quickly make silicon nanoparticles.

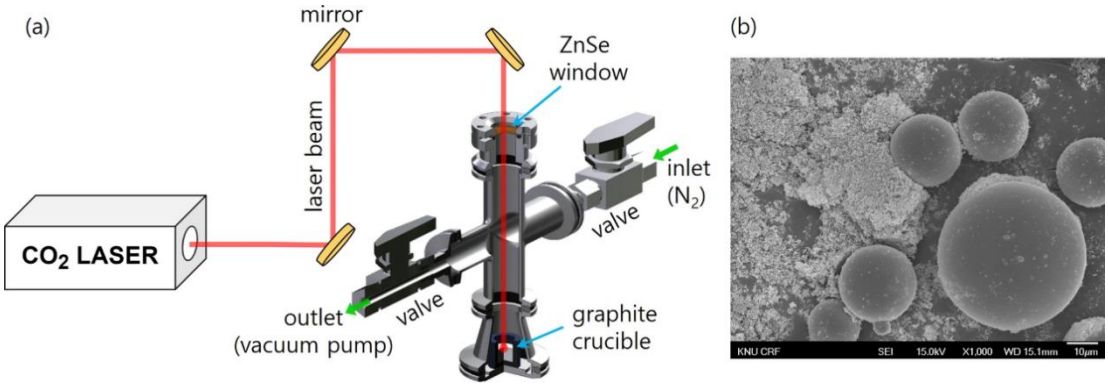


Figure 1.6: (a) A schematic of the experimental setup and (b) a SEM image of the pristine mixture.**[23]**

◆ **Magnesiothermic reduction:** The magnesiothermic reduction method is an efficient approach for producing silicon nanoparticles (Si NPs) by reducing silicon dioxide (SiO_2) with magnesium gas at high temperatures. As shown in **Figure 1.7**, the fundamental chemical reaction is as follows:

SiO_2 (s) + 2Mg (g) → Si (s) + 2MgO (s)

The magnesiothermic reduction method uses mesoporous SiO_2 structures to efficiently produce high-purity silicon nanoparticles (Si NPs). As shown in **Figure 1.7**, SiO_2 is first formed into vertically aligned mesoporous films on graphene oxide using precursors like TEOS and surfactants under alkaline conditions. These films are mixed with magnesium powder and heated to 650°C in an argon-hydrogen atmosphere. Magnesium gas enters the mesopores and reacts with SiO_2, forming Si and MgO. The thin walls (~1.5 nm) and porous design help ensure complete conversion. After the reaction, acid washing removes MgO and by-products, yielding uniform, well-dispersed Si NPs (~10 nm). This method offers good purity and control at relatively low temperatures, making it promising for batteries, sensors, and

optoelectronics. However, challenges include possible residue, acid-induced damage, and scalability issues.

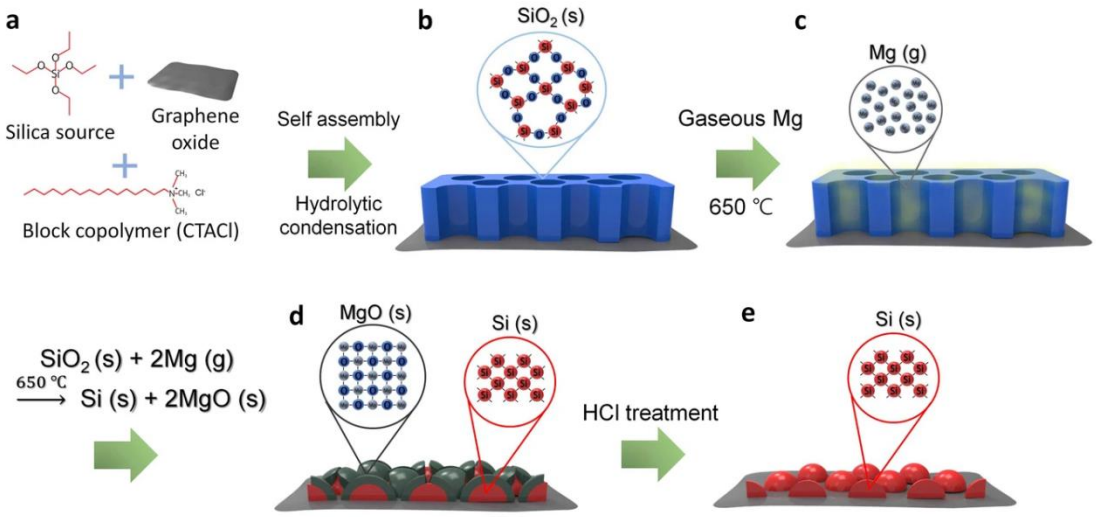


Figure 1.7: Schematic diagram of the fabrication process. (a) Mixing of silica source, block copolymer and graphene oxides (b) Synthesis of vertically oriented mesoporous silica channels on two-dimensional substrates. (c) Infiltration of gaseous magnesium into mesoporous silica. (d) Formation of magnesium oxide and silicon nanoparticles. (e) The formation of completely reduced silicon nanoparticles after removal of magnesium oxide by treatment with hydrochloric.**[24]**

In summary, each method for preparing silicon nanoparticles (Si NPs) has its strengths and limitations. Mechanical grinding (kitchen blender and ball milling) is low-cost, simple, and scalable, though it may produce irregular particle shapes. Laser printing offers high precision but suffers from low efficiency and high cost. Chemical precipitation and silane pyrolysis yield high-purity, uniform particles but involve complex and costly processes. Carbothermal and magnesiothermic reductions use inexpensive materials but require high temperatures and can lead to incomplete reactions. For microfluidic assembly, the kitchen blender method is particularly suitable. It produces well-dispersed Si NPs in deionized water, ideal for capillary-driven assembly, and is also affordable and easy to operate. Overall, this method best

meets the study's goals of cost-efficiency, process compatibility, and effective nanoparticle assembly on complex substrates.

Table 1. Advantages and challenges of silicon nanoparticle fabrication method

Preparation of Si nanoparticle		Advantages	Challenges
Top-down Method	Mechanical grinding	Relativiely simple fabrication process	Reduced sphericity of the resulting silicon nanoparticles
	Laser printing	Spherical silicon nanoparticles positioned at desired location	Production volume limitation
Bottom-up method	Pyrolysis of silane	Mass production	Difculty in controlling the nanoparticle size
	Reduction of silicon tetrachloride	Mass production with low cost	Difculty in controlling the nanoparticle size and generation of by-products
Reduction of silica particles	Carbonthermal reduction	Reduction of relatively inexpensive silica for silicon nanoparticle production	Reaction at temperatures above 2000 °C
	Magnesiothermic reduction	Reduction of relatively inexpensive silica for silicon nanoparticle production at temperatures around 650 °C	Incomplete reduction resulting in the formation of unreacted silica or magnesium silicide

1.2.2 Performance of Silicon Nanoparticles in Specific Applications

Silicon nanoparticles (Si NPs), due to their unique optical, physical, and chemical properties, are widely utilized in various cutting-edge fields, including nano-optical devices, biosensing, quantum technologies, environmental monitoring, and aerospace technology. The following provides a detailed discussion of their specific application areas along with relevant examples.

Silicon nanoparticles (Si NPs), with their high refractive index and low optical loss, demonstrate powerful capabilities in efficient light manipulation, making them widely applicable in fields such as optical lenses**[25]**, waveguides**[26]**, and modulators**[27].** Silicon nanoparticles (Si NPs) are useful in optical devices because they can control light well. In lenses, they help create ultra-thin designs that improve image quality in smartphones. In waveguides, they guide light efficiently, reducing loss in optical

circuits. Si NPs are also used in high-speed modulators, such as those needed for 5G. These applications show that Si NPs are valuable for making advanced, compact, and efficient optical devices.

Silicon nanoparticles (Si NPs), with their controllable size, high refractive index, and excellent chemical stability, demonstrate immense application potential in the fields of biosensing and high-resolution imaging. **Figure 1.8** shows the applications of silicon nanoparticles (Si NPs) in biosensing and high-resolution imaging. In biosensing (**Figure 1.8a**), different silicon nanostructures—like nanoparticles and nanowires—are used to detect biomolecules quickly and accurately, helping with real-time monitoring and early disease diagnosis. In imaging (**Figure 1.8b**), functionalized Si NPs with fluorescent and radioactive tags allow dual-mode imaging, clearly showing organs like kidneys in mice. This highlights their value for precise and multifunctional imaging.

In summary, Si NPs have strong potential in medical sensing and imaging. In the future, they may be integrated into advanced microscopes for real-time 3D observation and better biomedical applications.

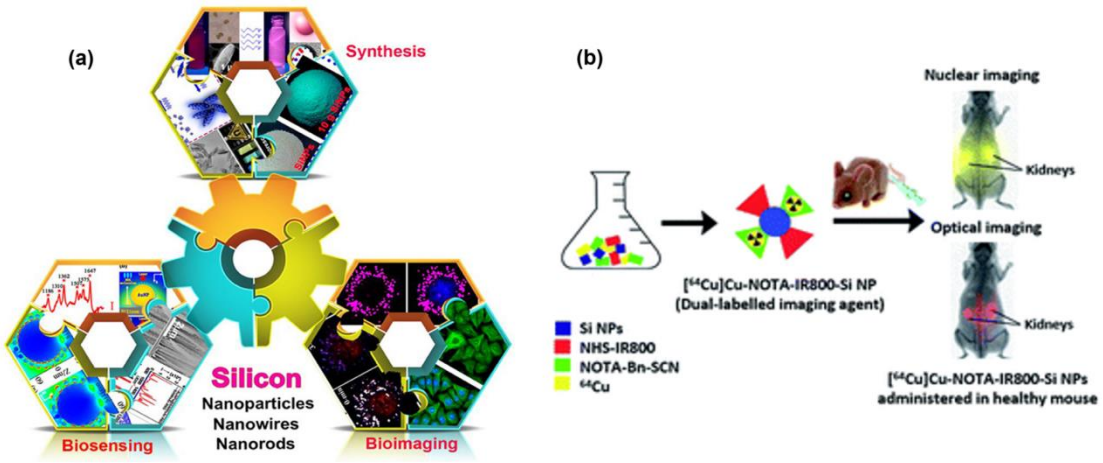


Figure 1.8: (a) Fabrication of silicon nanomaterial-based platform for biochemical applications**[28]**. (b) Ultrasmall silicon nanoparticles as a promising platform for multimodal imaging**[29]**.

Silicon nanoparticles (Si NPs) can be used in optical manipulation and printing. As shown in **Figure 1.9**, a combined method using hole-mask colloidal lithography (HCL) and laser-induced transfer (LIT) produces uniform, spherical Si NPs with good optical properties. These particles can be used for controlling light, optical trapping, and laser printing onto different substrates. The method is efficient and precise, making it useful for creating high-quality Si NPs. These can be applied in nano-optics, such as metasurfaces, sensors, spectroscopy, and color printing.

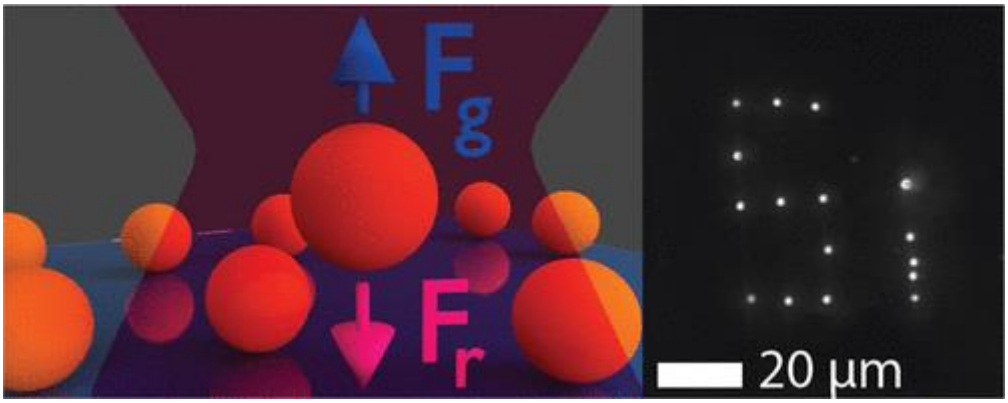


Figure 1.9: Fabrication of Monodisperse Colloids of Resonant Spherical Silicon Nanoparticles: Applications in Optical Trapping and Printing.**[30]**

Silicon nanoparticles (SiNPs) can be used as biological probes. As shown in **Figure 1.10**, a simple one-step hydrothermal method was used to prepare green fluorescent, water-soluble SiNPs for detecting flavonoids like rutin. These SiNPs have strong fluorescence, good stability, and resist photobleaching. The study shows that rutin can quench the fluorescence of SiNPs through the inner filter effect, allowing for sensitive and selective detection. This method has been successfully applied to measure rutin in tablets and herbal samples. Though promising, it faces limitations such as interference from similar compounds and the need to improve fluorescence at longer wavelengths.

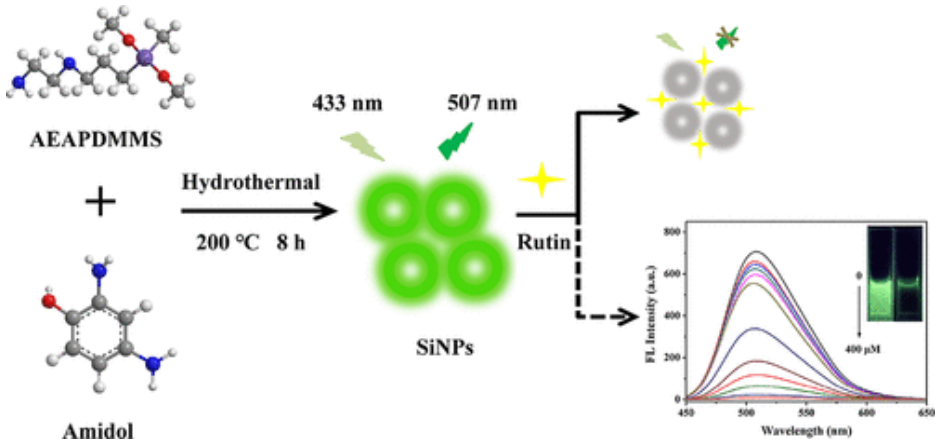


Figure 1.10: Water Soluble Silicon Nanoparticles as a Fluorescent Probe for Highly Sensitive Detection of Rutin.**[31]**

In summary, the multifunctional applications of Si NPs in optics, sensing, imaging, and biological fields not only drive technological innovation in these areas but also provide a critical experimental foundation and theoretical guidance for the development of more efficient and flexible functional materials and devices in the future. These studies highlight that Si NPs are an integral component of next-generation optical and functional material technologies, possessing immense potential for future advancements.

1.3 Prospects and Future Research Directions

Silicon nanoparticles (Si NPs), as essential components of high-performance optical and functional materials, hold tremendous potential for advancements in preparation and application technologies. Future research will focus on optimizing fabrication techniques, exploring novel assembly methods, developing multifunctional integration, and advancing green manufacturing and sustainability practices.

1.3.1 Optimization of Fabrication Techniques

Mechanical grinding methods like kitchen blenders and ball milling are widely used to produce silicon nanoparticles (Si NPs) because they are simple, efficient, and low-

cost. However, issues like uneven particle size, limited dispersion stability, and difficulty in large-scale production still exist. Future improvements aim to develop better equipment, such as combining ultrasonic energy with grinding to improve uniformity, and using smart systems to monitor and control grinding conditions. New materials like nano-ceramic balls and eco-friendly dispersants can boost efficiency and reduce environmental impact. For industrial-scale production, continuous flow systems and 3D-printed grinding tools can help achieve high output with consistent quality. In summary, improving equipment, materials, and production methods will make Si NP preparation more efficient and suitable for broader applications.

1.3.2 Exploration of Novel Assembly Techniques

Silicon nanoparticle (Si NP) assembly is key to building advanced metasurfaces. Future research will aim to make this process more precise, flexible, and functional. One promising direction is combining bottom-up techniques like microfluidics with top-down methods such as lithography. This can create more complex and accurate structures. Another focus is developing tunable assembly methods using external fields (electric, magnetic, or optical) to control particle placement. This allows metasurfaces to adapt in real time for changing needs. Combining Si NPs with materials like liquid metals may also lead to flexible and reconfigurable devices. Finally, integrating features across different size scales—from nano to millimeter—can enable metasurfaces with multiple functions for use in sensing, imaging, or smart devices. In short, improving Si NP assembly will help create more advanced, versatile, and high-performance metasurfaces for future technologies.

1.3.3 Multifunctional Integration

Silicon nanoparticles (Si NPs) have unique optical, electrical, and chemical properties that make them suitable for integration with other functional materials. This multifunctional integration could expand their use in advanced optoelectronics, biomedicine, and smart systems. For example, combining Si NPs with conductive materials (like metals or polymers) can enhance devices such as solar cells and

thermoelectric systems by improving light absorption and charge transport. Integrating Si NPs with biomolecules (like proteins or DNA) can lead to sensitive biosensors and targeted drug delivery, useful in diagnostics and precision medicine. In addition, artificial intelligence (AI) can help optimize the design and assembly of Si NPs, enabling adaptive optical systems that respond to environmental changes. Overall, combining Si NPs with conductive, biological, and AI technologies opens new opportunities for smart and multifunctional applications.

1.3.4 Green Manufacturing and Sustainability

To meet global sustainability goals, the production of silicon nanoparticles (Si NPs) must focus on eco-friendly and efficient methods. First, using water-based or low-toxicity solvents instead of harmful chemicals can reduce pollution. Improving grinding equipment and lowering energy use also help cut carbon emissions. Second, designing recyclable or biodegradable Si NPs can reduce waste, especially for single-use devices like medical sensors or environmental monitors. Finally, using clean energy (like solar or wind) in production and evaluating the full life cycle of materials ensures the process stays environmentally friendly. In short, greener production methods make Si NP technology both high-performing and sustainable.

1.4 Conclusion

This chapter highlights the value of silicon nanoparticles (Si NPs) in all-dielectric metasurfaces, thanks to their high refractive index, low optical loss, and semiconductor compatibility. The kitchen blender method offers a low-cost, efficient, and eco-friendly way to produce Si NPs at scale. With strong potential in nanophotonics, biosensing, and aerospace, Si NPs enable advanced light control and are biocompatible and flexible. Future work will focus on improving synthesis, developing multifunctional and tunable systems, and advancing green, smart technologies.

Chapter 2

Fundamentals of Metasurfaces and Assembly Techniques

All-dielectric metasurfaces enable precise light control with high efficiency and low loss, making them valuable in optics, electronics, and sensing. Silicon nanoparticles (Si NPs), with their high refractive index and CMOS compatibility, are ideal for building these structures. While top-down fabrication methods offer high precision, they are costly and hard to scale. In contrast, bottom-up assembly using microfluidic techniques is low-cost, flexible, and well-suited for large-area or complex metasurfaces. It uses capillary forces and solvent evaporation to guide nanoparticle assembly. In this study, Si NPs are assembled using microfluidics to create scalable, efficient metasurfaces. This method supports the transition from lab-scale research to practical, industrial applications.

Chapter 2: Fundamentals of Metasurfaces and Assembly Techniques

2.1 Background on Metasurface Fabrication

2.1.1 Concept of Metasurfaces

Metasurfaces are two-dimensional equivalents of metamaterials, distinguished by their structure and unique optical properties. They consist of an array of subwavelength-spaced elements, commonly referred to as "meta-atoms." These meta-atoms are meticulously engineered to manipulate electromagnetic waves in ways that surpass the capabilities of natural materials **[32]**. The design of metasurfaces involves arranging these meta-atoms in precise patterns, where each element can have different shapes, sizes, and compositions **[33]**. This structural arrangement allows metasurfaces to achieve a wide array of optical functions, making them highly versatile and powerful tools in modern optics **[34]**.

The core functionality of metasurfaces lies in their unparalleled ability to control the phase, amplitude, and polarization of incident light locally **[35]**. This control is achieved by carefully designing the geometry, orientation, and material composition of each meta-atom **[36]**. By manipulating these parameters, metasurfaces can produce a variety of desired optical effects across a wide range of wavelengths **[37]**. For instance, altering the phase of incoming light at specific points enables the creation of flat lenses, or metalenses, which can focus light without the bulk of traditional lenses **[38]**. Adjusting the amplitude can lead to the development of optical filters and beam shaping devices that can direct and mold light beams with high precision **[39]**. Furthermore, controlling the polarization state of light allows metasurfaces to convert linear polarized light to circular polarized light, or vice versa, and to design devices that manage different polarization states efficiently **[40]**. The theory and phenomena

required to control the optical properties of the metasurfaces (such as absorption, transmission, reflection, phase delay, resonant frequency, bandwidth, nonlinear coefficient, and chirality) are illustrated in **Figure 2.1**.

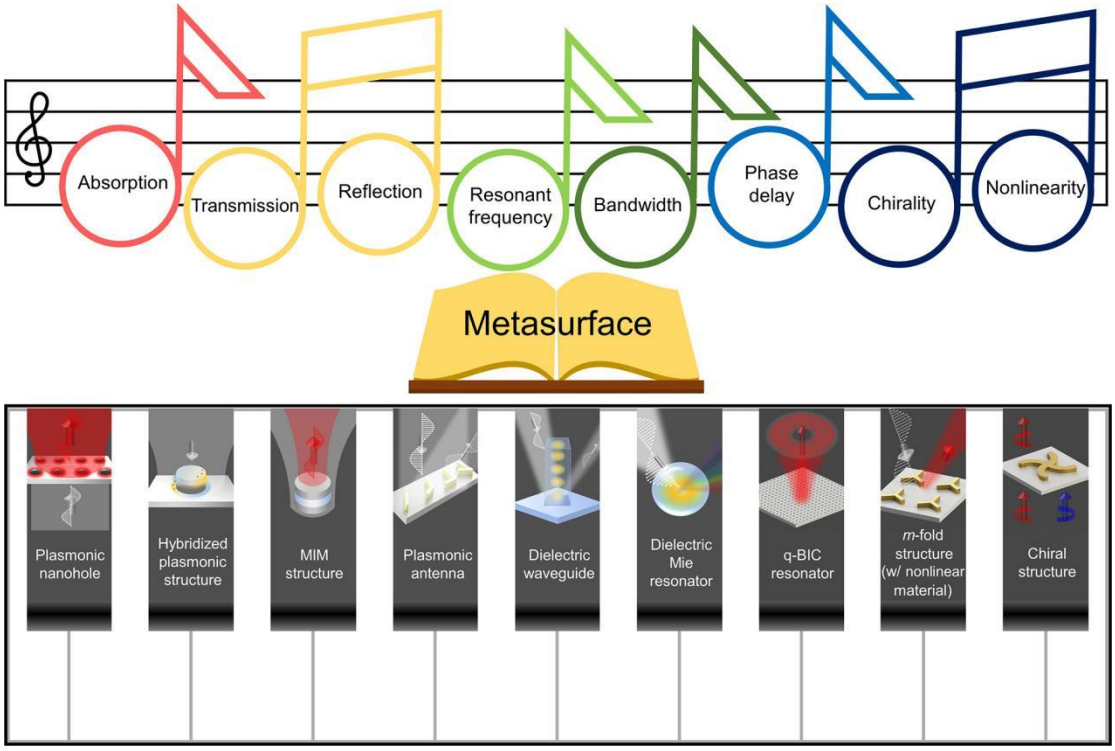


Figure 2.1: Diagram of the fundamentals of metasurfaces devices and optical properties.**[41]**

The ability to engineer such precise control over light-matter interactions makes metasurfaces invaluable in numerous applications. They are used in imaging systems to enhance resolution and clarity **[42]**, in communication systems to improve data transmission efficiency **[43]**, and in sensing technologies to increase sensitivity and specificity **[44]**. By harnessing the principles of metasurfaces, scientists and engineers can develop advanced optical devices that are not only more compact and efficient but also capable of achieving performance levels previously thought impossible with conventional materials.

2.1.2 The Significance of Metasurfaces in Modern Technology

Metasurfaces represent a significant advancement in optical technology by providing a compact and flat alternative to traditional bulky optical components**[45]**. This miniaturization is particularly advantageous in applications where size, weight, and integration are critical**[46]**. For instance, in consumer electronics, metasurfaces can be integrated into devices like smartphones and wearables, leading to thinner and lighter products without compromising optical performance**[47]**. Portable medical devices also benefit from the reduced footprint and enhanced functionality of metasurfaces, enabling advanced diagnostic and therapeutic tools that are easier to handle and more efficient**[48]**. Additionally, space technologies gain from the compact nature of metasurfaces, as reducing the size and weight of optical systems is crucial for space missions where every gram counts**[49]**. This miniaturization facilitates more sophisticated instrumentation on spacecraft and satellites, enhancing their capabilities without increasing launch costs.

Metasurfaces offer unprecedented control over light, allowing for the creation of highly efficient optical components with superior performance**[50]**. This includes high-resolution lenses**[51]**, beam shaping devices**[52]**, and ultra-thin holograms**[53-54]** that outperform their conventional counterparts. The design flexibility of metasurfaces allows for customization to specific applications, enabling tailored solutions that address unique technological challenges. This versatility makes metasurfaces applicable across a diverse range of fields, from telecommunications to bio-sensing. Some applications of metasurface structures are shown in **Figure 2.2**.

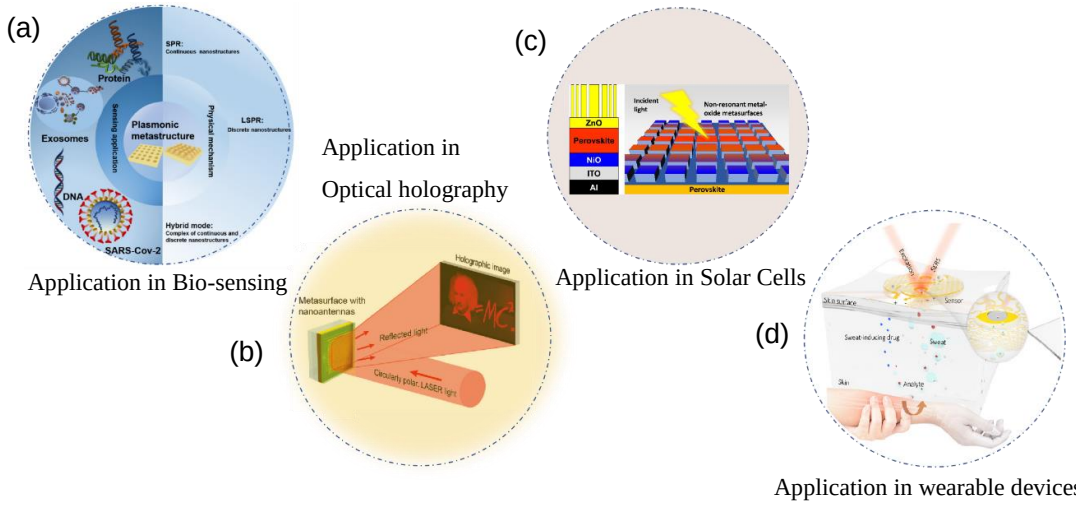


Figure 2.2: Application of metasurface structures. (a)The typical sensing structure of plasmonic metasurfaces application in bio-sensing**[48]**. (b). Illustration of the reflective nanorod-based CGH under a circularly polarized incident beam application in optical holography**[54]**. (c) Non-resonant metal-oxide metasurfaces for efficient perovskite solar cells**[55]**. (d).Plasmonic metamaterial–integrated wearable SERS sensing device**[47]**.

All-dielectric metasurfaces exhibit significantly lower optical losses compared to their plasmonic counterparts. This is because they avoid the inherent resistive losses associated with metals, leading to higher efficiency in transmitting and manipulating light. As a result, they are particularly advantageous for applications requiring minimal energy dissipation and maximum efficiency**[43]**. Due to their low-loss nature, all-dielectric metasurfaces can achieve high efficiency in controlling the phase, amplitude, and polarization of light. This high efficiency makes them ideal for applications demanding precise and efficient light manipulation, such as advanced imaging systems and optical communication devices**[56]**. All-dielectric materials support broadband operation, meaning they can effectively manipulate light over a wide range of wavelengths. This versatility is beneficial for applications across different spectral regions, including visible, infrared, and beyond. This property enhances their utility in various fields, from telecommunications to medical imaging**[57]**.

All-dielectric metasurfaces can be fabricated with high-resolution lithographic techniques, allowing for the creation of intricate and precise nanostructures. This precision enhances their performance and enables the realization of complex optical functionalities that are difficult to achieve with other materials**[37]**. Dielectric materials generally have high thermal stability, meaning that all-dielectric metasurfaces can withstand higher temperatures without degradation. This makes them suitable for applications in harsh environments or high-power laser systems where thermal management is crucial**[58]**. All-dielectric metasurfaces are compatible with standard CMOS (Complementary Metal-Oxide-Semiconductor) fabrication processes. This compatibility facilitates their integration with existing semiconductor technologies, paving the way for advanced photonic and optoelectronic devices. This integration is key to the development of next-generation optical components**[56]**.

Dielectric materials typically exhibit minimal absorption of light, contributing to the high transmission efficiency of all-dielectric metasurfaces. This is particularly important for applications where maintaining the intensity of transmitted light is critical, such as in optical sensors and communication systems**[59]**. Many all-dielectric metasurfaces can be designed to be polarization-independent, meaning their optical response is the same regardless of the polarization state of the incident light. This feature simplifies the design process and broadens the range of potential applications, making them highly versatile**[37]**. The fabrication processes used for all-dielectric metasurfaces are scalable, enabling mass production. This scalability is essential for commercial applications and widespread adoption in various industries, ensuring that these advanced optical devices can be produced cost-effectively and in large quantities**[60].** Dielectric materials can exhibit strong nonlinear optical effects, which can be harnessed in all-dielectric metasurfaces to create devices for applications such as frequency conversion, optical switching, and modulation. These nonlinear effects are crucial for developing advanced photonic devices with enhanced functionalities**[61]**. The schematic diagram illustrates typical fabrication techniques for all-dielectric metasurfaces as shown in **Figure 2.3**.

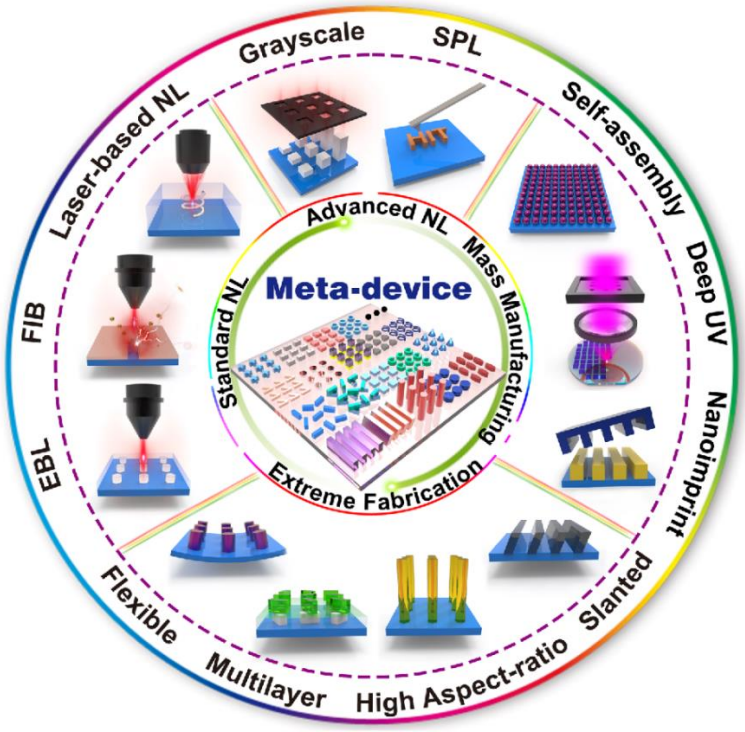


Figure 2.3: The diagram summarizes four main fabrication approaches for all-dielectric metasurfaces: standard lithography (e.g., EBL, FIB, laser techniques), advanced lithography (e.g., grayscale and scanning probe lithography), mass production methods (e.g., self-assembly, DUV lithography, nanoimprint), and specialized techniques for high-aspect-ratio, slanted, flexible, and multilayer structures.**[16]**

In summary, all-dielectric metasurfaces offer a compact and efficient design, enhanced performance, and unmatched versatility and customizability. These attributes make them a pivotal technology in modern applications, driving innovation and enabling new functionalities in consumer electronics, medical devices, space technology, telecommunications, bio-sensing, and beyond.

2.1.3 Recent Advances in Metasurfaces

Metasurfaces are at the forefront of revolutionizing the field of optics and photonics by enabling functionalities that were previously difficult or impossible to achieve with traditional materials**[50, 62]**. One of the most notable advancements is the creation of

flat lenses, or metalenses, which can focus light without the aberrations typically associated with conventional lenses. These metalenses are not only ultra-thin and lightweight but also capable of delivering high-resolution imaging with minimal distortion**[63-64]**. Recent advances in metalenses are shown in **Figure 2.4**. Additionally, metasurfaces have paved the way for the development of compact beam steerers**[65]**, which can direct light with high precision and flexibility, essential for applications in LIDAR systems, free-space optical communications, and holography. Moreover, metasurfaces have significantly improved polarization control, resulting in highly efficient polarization converters that can manipulate light polarization states for enhanced imaging, sensing, and communication technologies**[66]**.

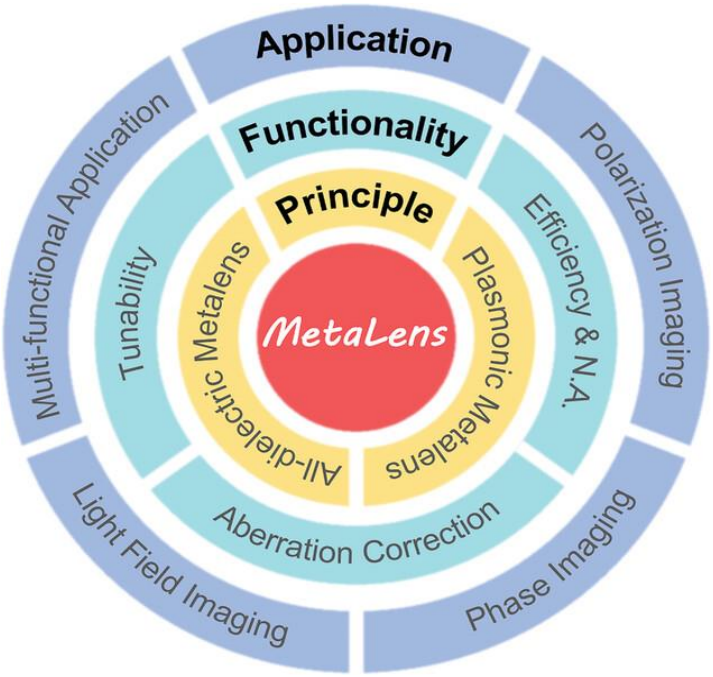


Figure 2.4: Schematic showing the recent progress in meta-lenses.**[67]**

The integration of silicon-based metasurfaces with existing semiconductor processes represents a major advancement. Compatible with the silicon photonics platform, these metasurfaces enable the efficient development of high-performance photonic circuits. This compatibility supports optical computing and high-speed data communication by allowing metasurfaces to be integrated into photonic chips. It also

reduces cost and boosts precision, promoting the commercialization of advanced photonic technologies and enabling multifunctional chips that combine electronic and photonic functions.

Emerging research in dynamic and tunable metasurfaces represents another leap forward in optical technology**[68]**. Working principle of the electrically tunable optical metasurface for polarization conversion as shown in **Figure 2.5.** These metasurfaces can alter their properties in response to external stimuli such as electrical, thermal, or optical signals. This tunability enables the development of adaptive optics systems that can dynamically adjust their focus, beam direction, and other optical characteristics in real-time. Such capabilities are critical for applications in smart sensing systems, where the ability to adapt to changing environmental conditions can significantly enhance detection accuracy and reliability. Dynamic metasurfaces also hold promise for reconfigurable photonic devices, which can switch between different operational modes or functionalities on demand, providing unprecedented flexibility and control in optical system design. This adaptability is essential for next-generation technologies in areas such as augmented reality, adaptive lenses, and responsive optical filters.

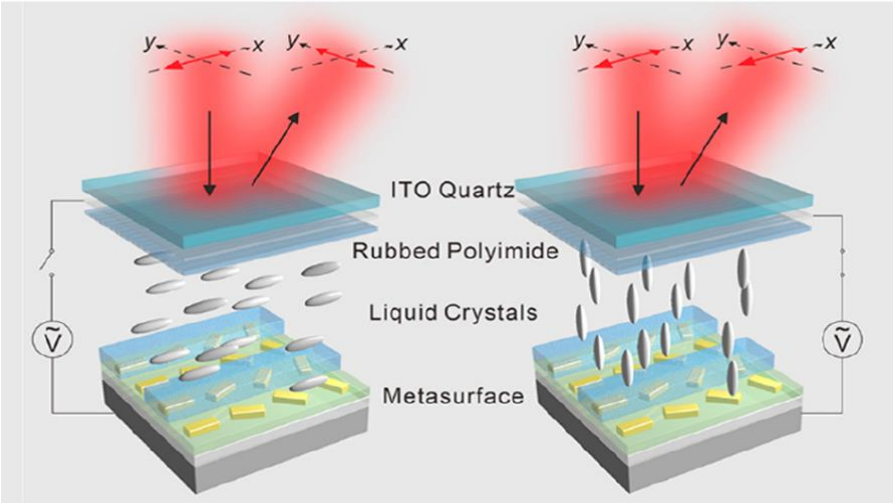


Figure 2.5: Working principle of the electrically tunable optical metasurface for polarization conversion**[68]**.

In summary, metasurfaces are driving technological advancements by transforming optics and photonics, integrating seamlessly with silicon photonics, and enabling dynamic and tunable optical components. These innovations are not only enhancing existing technologies but also paving the way for new applications and functionalities in various fields, from high-speed communications and optical computing to advanced imaging and adaptive sensing systems.

2.1.4 Applications of Metasurfaces

Metasurfaces are poised to transform optical communication by improving efficiency and signal quality. Through nanoscale light control, they enable advanced modulation schemes that boost network speed and capacity—especially important for 5G and future networks. Metasurfaces also help reduce signal loss and improve key components like modulators and detectors, making data transmission faster and more reliable across global networks.

Metasurfaces are being explored for their potential to significantly advance medical imaging and diagnostics. The plasmonic metasurfaces for medical diagnosis applications**[48]**. Their ability to control light with high precision leads to higher resolution and greater sensitivity in imaging systems. This translates to more accurate and detailed images, which are vital for effective diagnostics. Metasurfaces can be integrated into various imaging modalities, such as optical coherence tomography (OCT) and endoscopic imaging, making these tools less invasive and more efficient. Enhanced imaging capabilities can improve early detection and diagnosis of diseases, leading to better patient outcomes. Furthermore, the compact size and versatility of metasurfaces enable the development of portable and wearable diagnostic devices, which can provide real-time health monitoring and facilitate remote healthcare.

Figure 2.6 highlights the use of metasurfaces in bioimaging and biosensing. They enable high-resolution imaging methods (e.g., OCT, fluorescent and super-resolution imaging) and improve detection of biomolecules like DNA, proteins, and cancer

markers. The figure also points to future developments, such as adaptive imaging, wearable sensors, and bioinspired designs, showing strong potential for advanced biomedical applications. The incorporation of metasurfaces into consumer electronics has the potential to dramatically enhance device performance and functionality**[69]**. In smartphones, cameras, and wearable devices, metasurfaces can lead to significant improvements in optics, such as better focusing, higher resolution imaging, and advanced light control. These enhancements result in clearer pictures, more immersive augmented reality experiences, and superior overall device performance. Additionally, metasurfaces contribute to the reduction of device form factors, making electronics thinner, lighter, and more aesthetically pleasing without compromising functionality. This miniaturization opens up new design possibilities and drives innovation in the consumer electronics market, offering users enhanced experiences and more sophisticated technology.

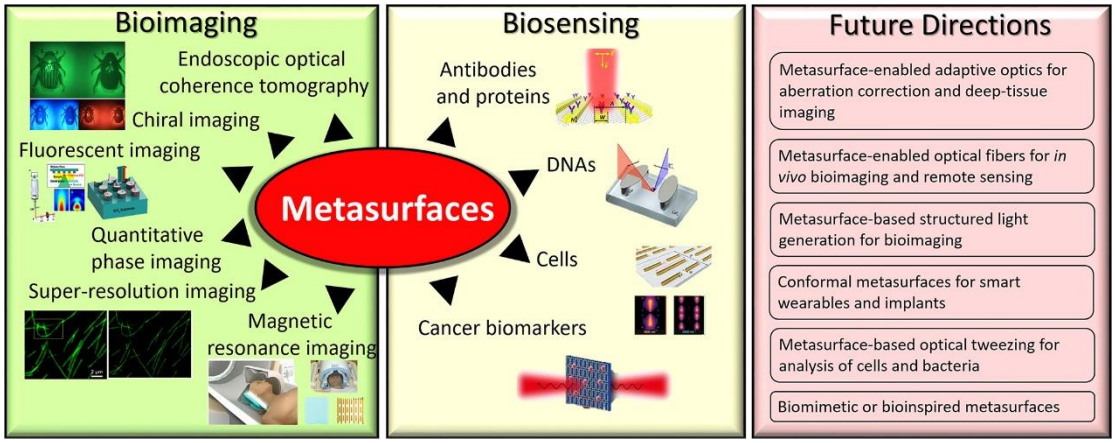


Figure 2.6: Overview of metasurfaces for bioimaging and biosensing applications and future directions. **[70]**

Metasurfaces, when combined with diffractive optical elements, photonic crystals, and microcavities, enhance light-matter interaction and show strong potential in optical sensing technologies. As shown in **Figure 2.7**, various micro/nanostructures—such as integrated waveguides and metasurfaces — enable advanced sensing functions. Metasurfaces allow sensitive detection of medium concentration changes,

composition analysis, and molecular chirality. They also support precise particle manipulation and enhance detection through nonlinear optical effects. These capabilities make metasurfaces key components in developing next-generation, high-performance optical sensors.

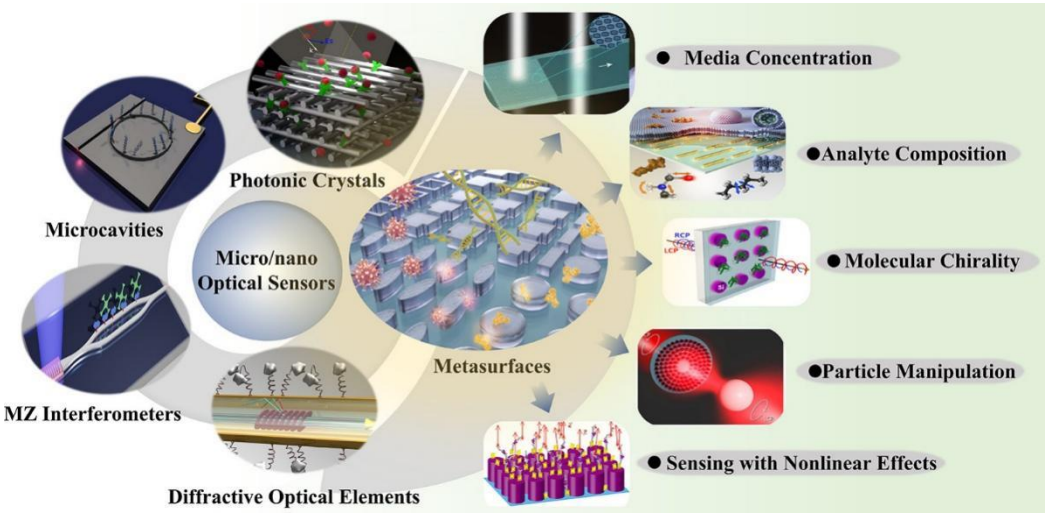


Figure 2.7: An overview of optical sensors with different micro/nanostructures, including diffractive optical elements, integrated waveguides, microcavities, photonic crystals, and metasurfaces.**[71]**

Metasurfaces are driving significant advancements across various fields, from enhancing data transmission in optical communication systems and advancing medical imaging and diagnostics to improving the performance and functionality of consumer electronics. Their ability to manipulate light with unprecedented precision enables a wide range of applications, making them a pivotal technology for the future. As research and development in metasurfaces continue to progress, their impact on modern technology will likely expand, leading to further innovations and improved capabilities in multiple industries.

2.1.5 Top-Down Metasurface Fabrication Methods and Limitation Analysis

Top-down metasurface fabrication methods, such as electron beam lithography (EBL), focused ion beam (FIB) etching, and nanoimprint lithography (NIL), have played a critical role in achieving precise fabrication of nanoscale metasurface structures**[72]**. Top-down fabrication methods can precisely control the shape and layout of meta-atoms, helping create high-performance metasurfaces. However, they have limitations—methods like EBL and FIB are slow and expensive, while NIL can have uniformity issues over large areas. These techniques also require complex equipment and strict conditions, making large-scale production difficult. To overcome these challenges, new approaches are needed. Bottom-up methods, such as microfluidic-assisted assembly, offer a simpler and more scalable solution for metasurface fabrication and will be discussed in the following sections.

(1) Electron Beam Lithography

Electron Beam Lithography (EBL) is a technique that uses a high-energy electron beam to directly write nanoscale patterns onto a photoresist**[73]**. It is one of the most commonly used methods for nanoscale patterning. The working principle involves the precise scanning of the photoresist surface with an electron beam, inducing chemical reactions that create high-resolution patterns consistent with the design. Subsequently, the patterns are developed and etched onto the substrate material. As shown in **Figure 2.8**, the fabrication process of GaN achromatic meta-lenses working in the visible spectrum is demonstrated. Nanopatterns are defined using EBL technology, followed by metal deposition and lift-off. Subsequently, hard mask etching is performed, and the final GaN nanostructures are achieved through inductively coupled plasma reactive ion etching (ICP-RIE) and buffered oxide etching (BOE).

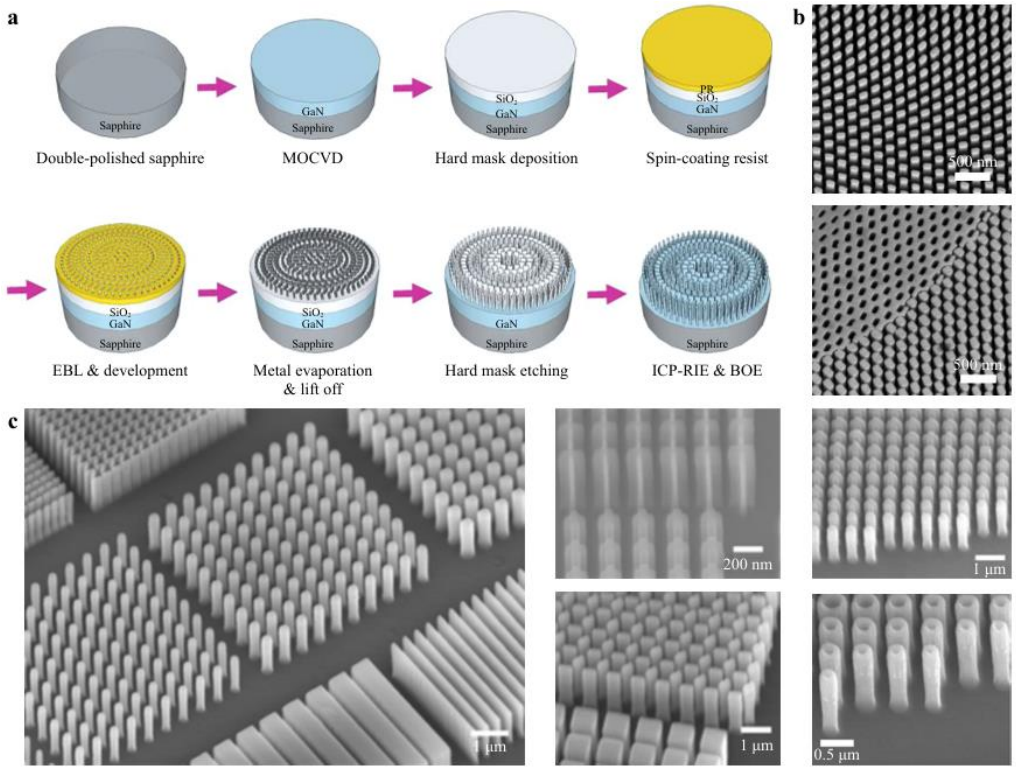


Figure 2.8: Electron-beam lithography. a The process flow for the fabrication of GaN achromatic meta-lens working in the visible. b The corresponding SEM images of GaN nanopillars (top) and the inverse nanostructures (bottom)**[74]**. c The tilted view SEM images of the TiO_2 nanostructures, including circular pillars, crosses, and rectangle pillars**[75]**.

Electron Beam Lithography (EBL) offers extremely high resolution, with patterning precision below 10 nm, making it ideal for creating complex and precise nanostructures in research settings. However, its relatively low efficiency, high cost, and limited processing area may pose challenges for large-scale production. Despite these drawbacks, EBL remains a key tool for prototyping metallic and dielectric metasurfaces and plays an important role in nanophotonics research.

(2) Focused Ion Beam Etching (FIB)

Focused Ion Beam (FIB) etching is a technique that uses a high-energy ion beam to locally bombard the surface of a material, precisely removing material to form the desired nanostructures**[76]**. Its working principle involves scanning the sample surface

with a focused ion beam, using physical bombardment to remove material and create high-precision three-dimensional nanostructures.

Tseng et al. experimentally realized a 3D chiral metasurface by FIB adopting gallium ions**[77]**, as shown in **Figure 2.9a, 2.9b**. **Figure. 2.9c** depicts the SEM images of an $LiNbO_3$ metasurface, which boosts the second harmonic in the visible region**[78]**. The $LiNbO_3$ thin film is milled directly by FIB. The side walls of $LiNbO_3$ nanopillars have an angle of 83.6°. FIB is suitable for freeform surface patterning. Gorkunov et al. show a chiral metasurface on crystal silicon film fabricated by digitally controlled FIB**[79]**, as given in **Figure. 2.9d**. SEM images show that the meta-atoms have smooth 3D shapes with four-fold symmetry, rather than flat patterns. Focused Ion Beam (FIB) does not require photoresist and allows direct etching, simplifying the process. It can create complex 3D structures and works well on non-flat surfaces. However, FIB is not suitable for large-scale production due to high cost and low speed. It also faces challenges like limited aspect ratio, ion contamination, long milling times, and possible damage to samples.

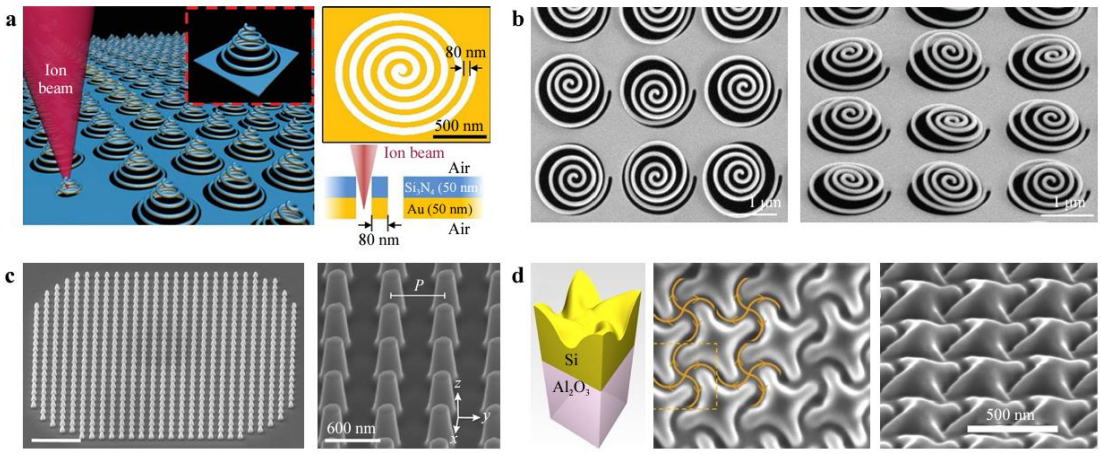


Figure 2.9: Focused ion beam lithography. (a) Schematic of Archimedean spiral metasurface fabrication process by FIB. (b) The corresponding top (left panel) and tilted (right panel) SEM images of the fabricated metasurface. (c) SEM images of $LiNbO_3$ metasurface for second harmonic enhancement. (d) Schematic configuration of the metasurface unit cell and the corresponding SEM images.

(3) Nanoimprint Lithography (NIL)

Nanoimprint Lithography (NIL) is an efficient technique that creates nanoscale patterns by physically imprinting a mold onto the surface of a photoresist**[10, 80-81]**. This process uses a pre-made mold with nanoscale features, which is pressed into a photoresist under heat or pressure. After curing and removing the mold, the pattern is transferred to the substrate.

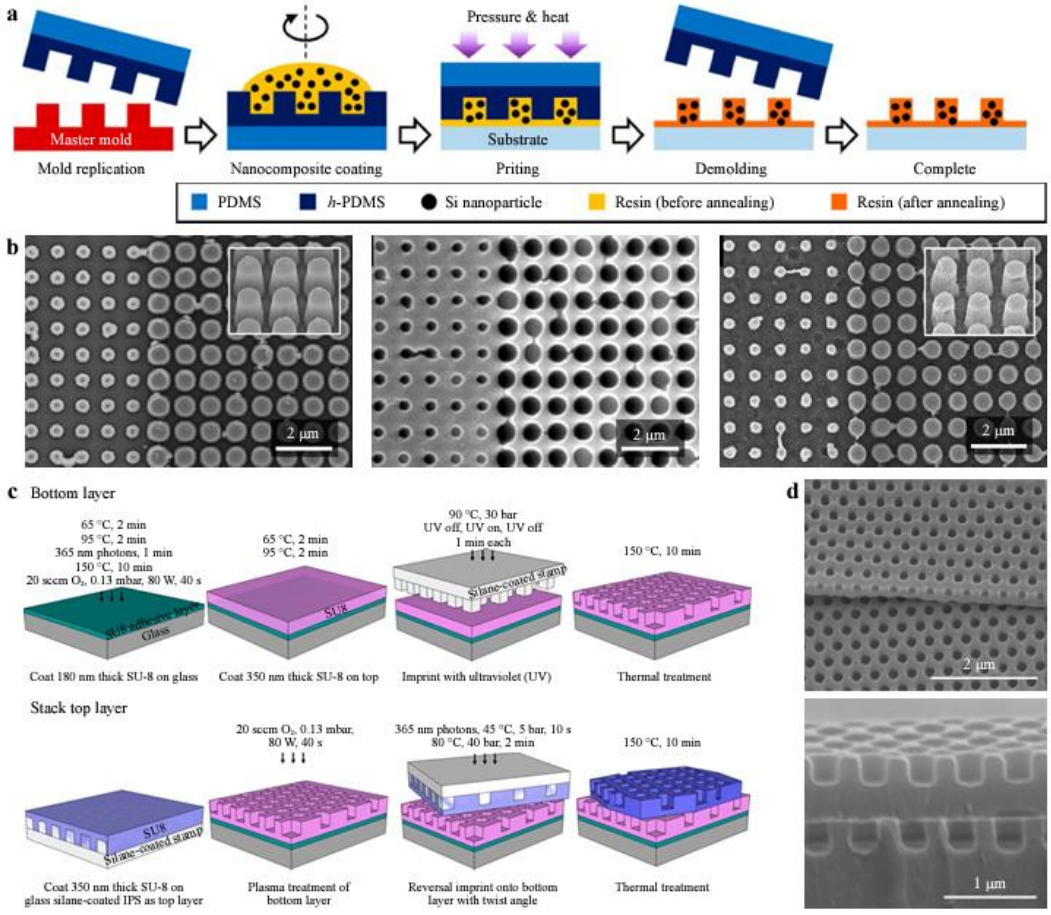


Figure 2.10: Nanoimprint lithography. a. The process flow for one-step NIL on meta-lens fabrication. b. The SEM images of master mold (left), soft mold (middle), and fabricated meta-lens (right)**[82]**. c. The NIL fabrication process for bilayer chiral meta-device. d. The corresponding top and cross SEM images of bilayer meta-device**[83]**.

Nanoimprint lithography (NIL) offers high resolution (below 20 nm), fast large-area production, and low cost due to reusable molds. Figure 2.10 shows how NIL is used to make nanostructured metasurfaces. Ongoing research in NIL is important for scaling up metasurface production. However, NIL depends on high-precision mold fabrication and has limited design flexibility, making it less ideal for applications needing frequent pattern changes.

(4) Laser Ablation

Laser ablation is a precise and high-purity nanomaterial fabrication technique**[84]**. While it offers significant advantages in terms of environmental adaptability and material purity, its limitations hinder its scalability for industrial applications.

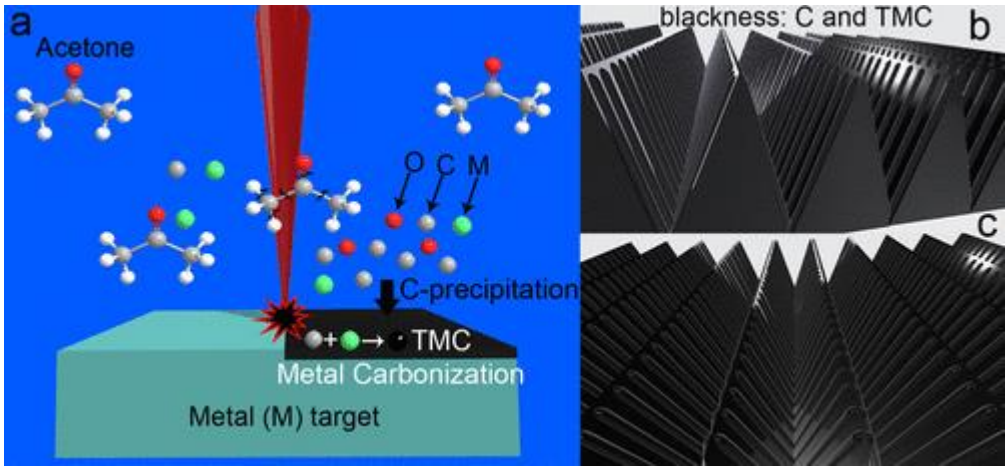


Figure 2.11: (a) Scheme of the FLAMOS technique, which enables simultaneous metal carbonization/C-precipitation and nanostructuring (the black region indicates the ablated region). (b and c) Schematic side and top views of the FLAMOS-induced hybrid micro/nanostructures observed, respectively. Note that C and TMC are gray and black in part a, respectively.**[85]**

As shown in **Figure 2.11**, laser ablation can be used to fabricate metasurfaces by irradiating a metal target with a focused laser beam, sometimes in the presence of a reactive gas such as oxygen or acetone, depending on the desired surface

modification. This forms cone-shaped nanostructures with strong light absorption. The method allows precise control of shape and materials, useful for optical coatings and absorbers. However, it has low efficiency, high cost, and requires complex equipment. The particle sizes can vary, needing extra steps to sort them. Strict control of laser settings and environment is also needed. While promising, this technique is limited by its low yield and high expense for large-scale use.

(5) Deep Ultraviolet Lithography (DUV)

Deep Ultraviolet Lithography (DUV) is a pattern transfer technique based on deep ultraviolet light with wavelengths of 193 nm or shorter. It uses photomasks to replicate patterns onto photoresist and employs etching processes to precisely transfer these patterns onto substrate materials.

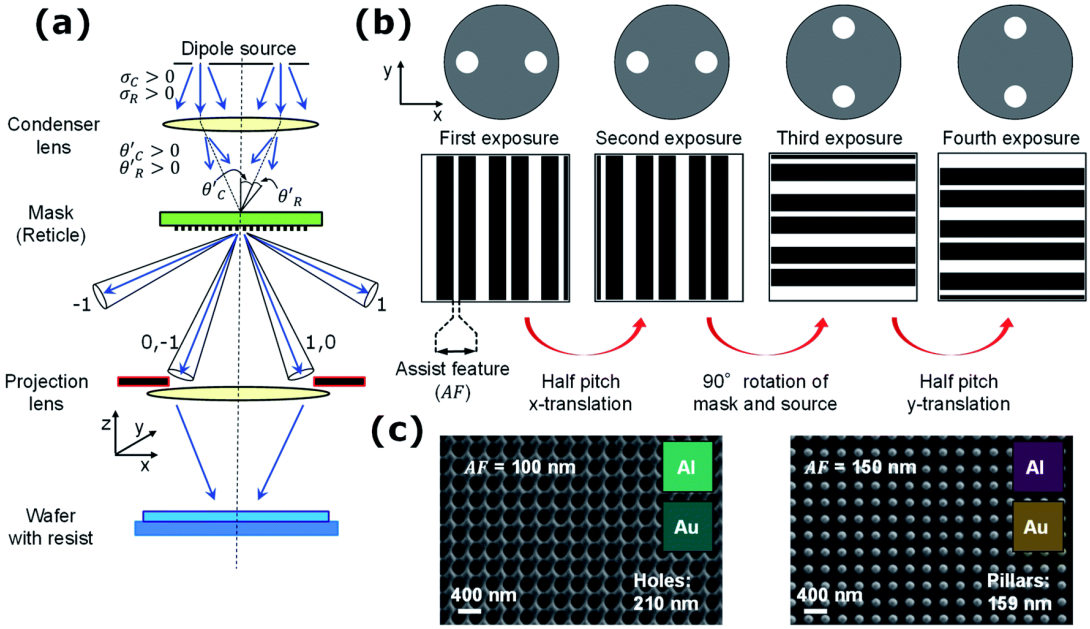


Figure 2.12: (a) Schematic of the beam trace through the DUV stepper tool. (b) A source stopper plate fitted with two off-axis symmetrical apertures constitutes the dipole illumination source with σ_C = 0.6 and σ_R = 0.2. (c) Two examples of scanning electron microscope (SEM) images of developed resist patterns that have undergone the dipole illumination and double/cross exposure with varied AF widths.**[86]**

DUV lithography uses precise light exposure through a mask to create nanoscale patterns on a photoresist-coated wafer, as shown in **Figure 2.12**. This method achieves high resolution and uniformity, making it suitable for metasurface fabrication. Although DUV is efficient and widely used, it has major limitations. The equipment is very expensive, and the resolution is limited by the light's wavelength. Like other top-down methods, it is hard to scale up for large or complex metasurfaces due to high cost and limited flexibility. To address these limitations, bottom-up fabrication methods have gradually become a focal point of research**[87]**.

2.2 Development of Microfluidic Technology

Top-down methods can make precise metasurfaces but are costly, slow, and hard to scale**[88]**. They also have limited flexibility. Bottom-up methods**[89-90]**, like microfluidic assembly, offer a simpler and cheaper alternative. Microfluidic technology uses fluid channels to guide nanoparticles into patterns. It allows better control, saves materials, and doesn't need expensive equipment, making it ideal for large-scale and flexible fabrication. These attributes give microfluidic technology a unique advantage in the large-scale production of metasurfaces**[91-93]**.

Microfluidic technology shows great promise for metasurface fabrication due to its efficiency, low cost, and flexibility. By controlling fluid flow, evaporation, and capillary forces, it allows precise nanoparticle assembly without complex or expensive equipment. Adjustable parameters like flow rate, solvent type, and temperature make it suitable for various designs, especially for large-area or multifunctional metasurfaces. Overall, microfluidics offers a practical and scalable alternative to top-down methods, paving the way for more accessible and efficient metasurface production.

As demand grows for low-cost, high-efficiency manufacturing, microfluidic technology offers new solutions for metasurface fabrication. By combining microfluidics with advanced materials, researchers can assemble complex

nanostructures more precisely and affordably. This promotes the use of metasurfaces in optics, electronics, and biomedicine. The next sections will discuss the principles, benefits, and future applications of microfluidic technology in this field.

2.2.1 Principles of Microfluidic Technology in Nanostructure Assembly

The working principles of microfluidic technology in nanoparticle assembly are based on precise control of fluid dynamics, solvent evaporation effects, and capillary forces, leveraging multiple mechanisms to achieve high-precision self-assembly of nanoparticles**[94-95]**. As shown in **Figure 2.13**, this microfluidic setup enables capillarity-assisted nanoparticle assembly. It includes an optical microscope, a patterned substrate slide, a temperature-controlled holder, a slide height adjuster, a motorized translator, and an XY positioning stage. The microscope monitors the deposition in real time, while the temperature control stabilizes evaporation. The slide height and position can be finely adjusted to ensure uniform assembly. Capillary forces guide the nanoparticles into place, and the slide's speed and temperature influence the outcome. This system enables efficient, precise assembly, ideal for structured nanoparticle patterning.

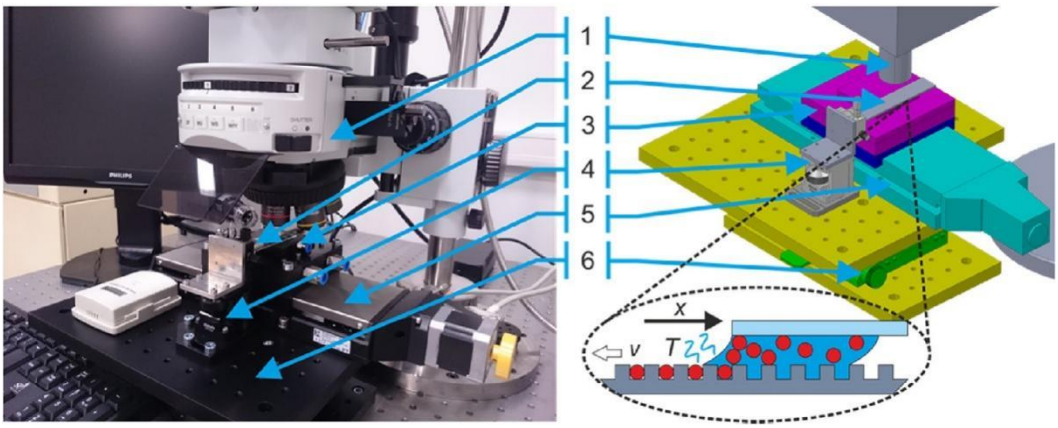


Figure 2.13: Photograph and schematic of a capillary force-assisted particle assembly system: 1) Optical microscope; 2) Glass slide; 3) Temperature-controlled sample holder; 4) Height adjuster; 5) Motorized translator; 6) XY stage. The inset shows particles depositing as the stage moves at speed v and solution temperature T, along the x-axis.**[96]**

Capillarity-assisted assembly uses capillary forces and liquid evaporation to guide nanoparticles into precise positions. By adjusting temperature, speed, and solution concentration, the process ensures uniform and efficient particle deposition, making it a reliable method for microfluidic and nanoscale fabrication. The working principle of capillarity-assisted nanoparticle assembly is further illustrated in **Figure 2.14**. The microfluidic setup operates based on the deposition of particles within traps. Panel (A) shows a fluorescence microscopy image, providing a top-down view of a droplet of colloidal suspension moving from right to left on a PDMS template. The brighter region represents the particle accumulation zone, indicating the gradual deposition of particles along with the droplet's movement. Panel (B) depicts the schematic of particle assembly in rectangular traps, along with an enlarged view of a single trap.

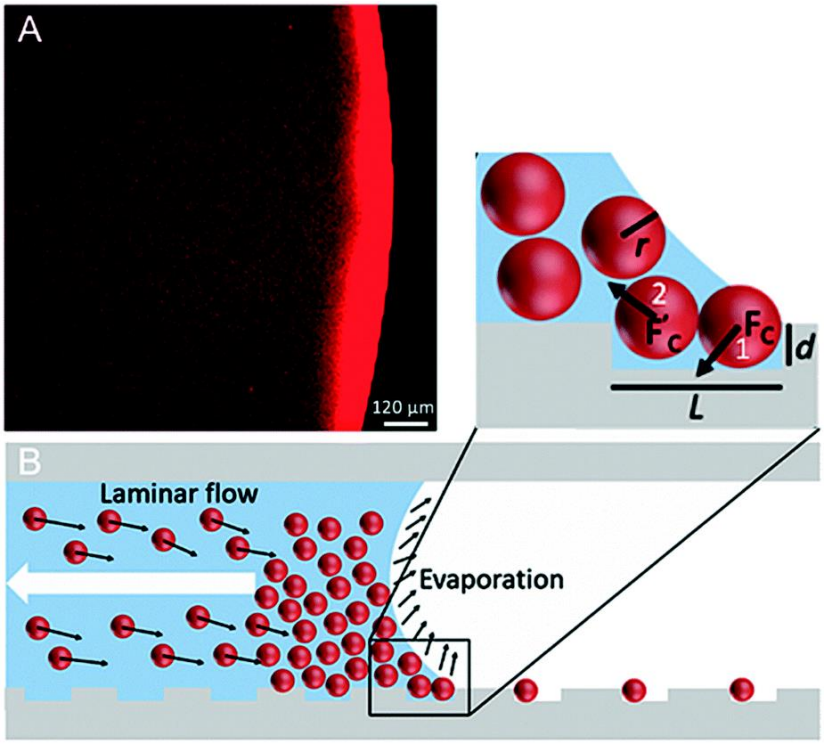


Figure 2.14: Working principle of particle deposition in a trap: (A). A droplet moves on a PDMS template from right to left, and particles gather in the bright region. (B). The front particle is pushed into a rectangular trap by capillary force (FC) as the liquid moves. This force also pushes the rear particle upward, so only the front particle stays in the trap.**[97]**

The trap depth (d) is on the same scale as the particle radius (r). The droplet's interface (meniscus) exerts a capillary force (FC) perpendicular to the meniscus on the leading particle (Particle 1), pushing it toward the end of the trap (left side in the schematic) and stabilizing it within the trap. Simultaneously, part of the capillary force is transmitted to the rear particle (Particle 2), generating an upward force (F'C) that pushes Particle 2 out of the trap. As a result, only Particle 1 is accurately deposited within the trap. This working principle relies on the interplay of liquid evaporation and capillary forces, enabling precise deposition of particles at predetermined geometric positions. This trap-based assembly method offers high precision and controllability, making it particularly suitable for nanoparticle assembly and patterning in microfluidic technologies.

In summary, microfluidic technology integrates solvent evaporation dynamics, capillary forces, and directed fluid manipulation, coupled with advanced temperature control and positioning systems, to achieve high-precision and high-efficiency nanoparticle assembly. This principle offers an innovative method for fabricating complex nanostructures and serves as a critical tool in metasurface manufacturing.

2.2.2 Research Status and Advantages of Microfluidic Technology

In recent years, microfluidic technology has made significant progress in the assembly of nanostructures**[96, 98]**. As a bottom-up manufacturing method, microfluidic technology has gradually become a core tool for efficiently assembling complex nanostructures, showing strong potential in both theoretical research and practical applications. Currently, research on microfluidic technology mainly concentrates on three aspects: optimization of fluid control mechanisms, enhancement of nanoparticle assembly precision, and development of multifunctional structures**[99]**.

Compared to traditional top-down fabrication methods, microfluidic technology demonstrates significant advantages, particularly in terms of cost efficiency, scalability, flexibility, and environmental sustainability**[100]**. First, microfluidic

technology is a highly efficient and cost-effective assembly method**[95]**. Unlike traditional techniques that rely on expensive large-scale electron beam lithography (EBL) or deep ultraviolet (DUV) lithography equipment, microfluidic technology significantly reduces manufacturing costs**[101]**. It is worth noting that microfluidic technology does not entirely eliminate the need for a lithographie step (EBL, NIL…) but rather integrates it as a tool for creating assembly templates. This approach minimizes the risk of sample collapse, especially when assembling high-aspect-ratio nanostructures, ensuring stable nanoparticle distribution. Moreover, by combining microfluidic assembly with nanoimprint lithography, the method effectively reduces the number of lithography steps, further cutting costs and improving production efficiency.

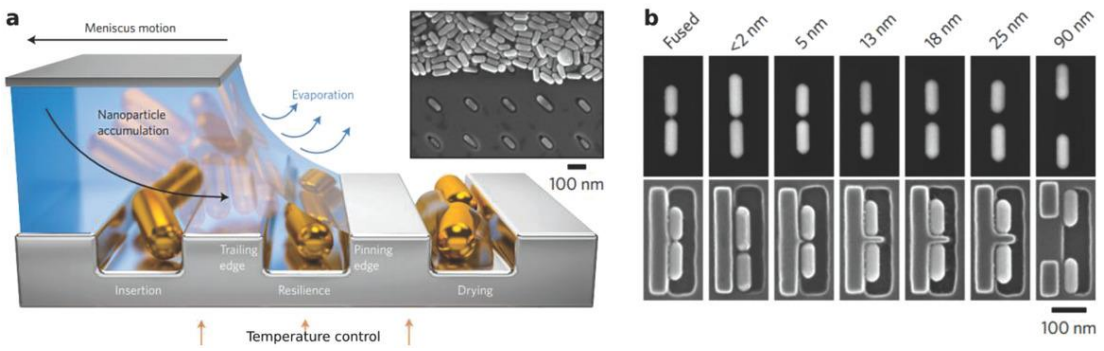


Figure 2.15: Capillarity-assisted particle assembly (CAPA): (a). A colloidal solution is pulled over a patterned surface. As it evaporates, nanoparticles gather and fill the template, forming dense nanorod arrays. (Inset: nanorods and dried meniscus highlight the high concentration area.) (b). Electron beam lithography enables precise fabrication of nanoparticle dimers. Adapted with permission.**[102-103]** Copyright 2016, Springer Nature.

Second, microfluidic technology supports scalable fabrication of metasurfaces by using parallel channels to assemble nanoparticles over large areas with high uniformity. This makes it suitable for both lab research and industrial production. When combined with nanoimprint methods, it improves efficiency and consistency in making complex structures. As shown in **Figure 2.15**, panel (a) illustrates capillarity-

assisted assembly, where nanorods fill a patterned surface as the solvent evaporates. The inset shows dense particle accumulation after drying. Panel (b) shows dimer structures with different gap sizes created using electron beam lithography. This approach enables precise and scalable fabrication of nanostructures for advanced devices.

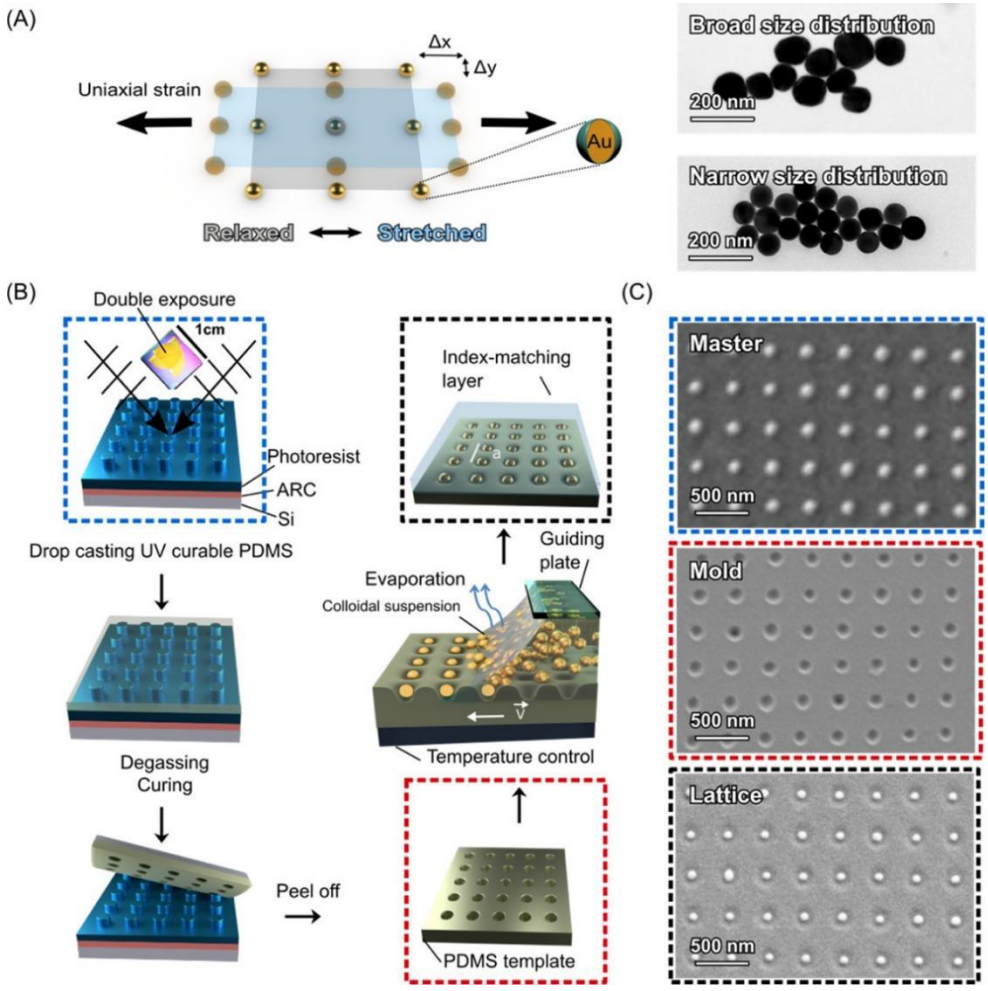


Figure 2.16: Soft lithography for nanoparticle assembly: (A). A stretchable 2D plasmonic lattice under strain, with TEM images showing particles of different size uniformity. (B). The lattice is made using laser lithography, soft molding, and self-assembly. ARC is an anti-reflective coating. (C). SEM images show the nanopillar mold, nanohole array, and final uniform 2D lattice.**[104]**

Microfluidic technology is highly flexible, allowing precise control over nanoparticle assembly by adjusting suspension composition, concentration, and flow. This enables

the fabrication of multifunctional metasurfaces with diverse optical or biosensing properties in a single process. It also supports real-time adjustments, expanding its use in complex applications. As shown in **Figure 2.16**, capillarity-assisted particle assembly offers an efficient and scalable method to create functional nanophotonic devices. Panel (A) shows a stretchable 2D plasmonic lattice that changes structure under strain, tuning its optical properties. Panel (B) outlines the fabrication steps: creating a nanopillar template using laser-induced lithography, transferring the structure to soft PDMS, and assembling nanoparticles through solvent evaporation. Panel (C) presents SEM images showing each stage of the process. This combined method enables accurate and reliable construction of 2D plasmonic lattices.

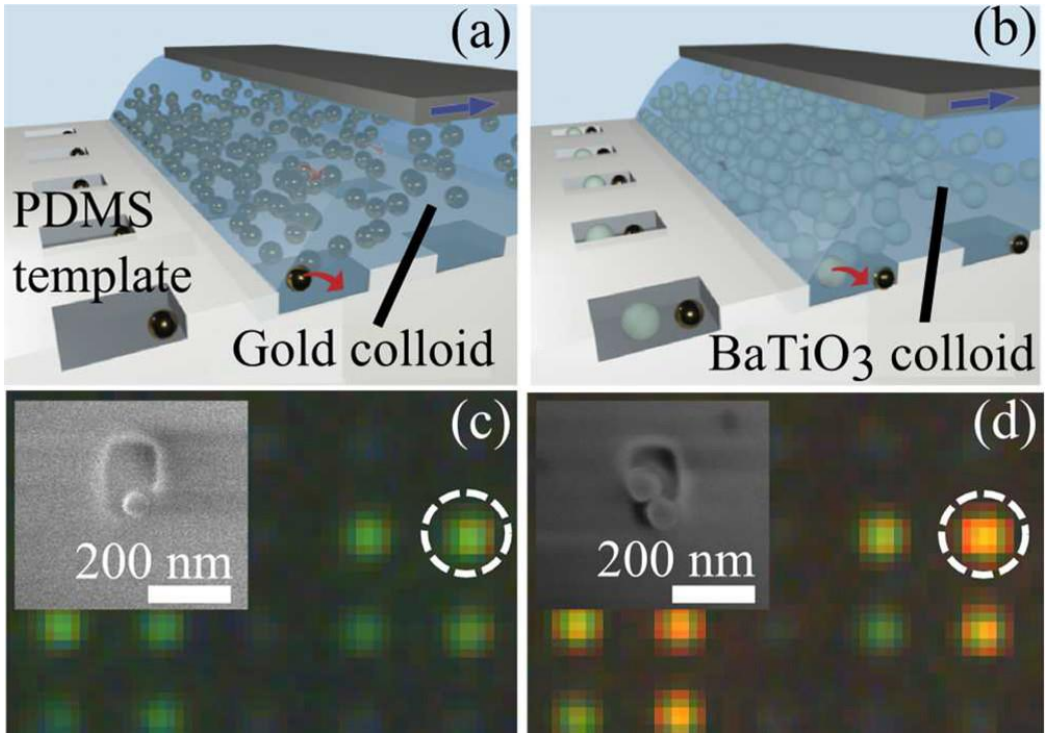


Figure 2.17: (a, b) Schematic of step-by-step capillarity-assisted assembly of nanodimers. (c) Dark-field image shows a single gold nanoparticle; (d) Adding a $BaTiO_3$ nanoparticle at the same spot increases brightness. Insets: SEM images confirm the presence of single and paired nanoparticles.**[105]**

Capillarity-assisted particle assembly is a precise and efficient self-assembly technique based on surface tension and capillary forces, ideal for building

nanostructures with tailored optical properties. As shown in **Figure 2.17**, this method enables the step-by-step assembly of gold and $BaTiO_3$ nanoparticles within a PDMS template. Panels (a) and (b) show how gold colloids first fill the grooves, followed by $BaTiO_3$, forming nanoparticle dimers. Panels (c) and (d) provide dark-field images comparing the optical intensity of a single gold nanoparticle and its dimer with $BaTiO_3$. SEM insets confirm the structural details. The enhanced optical response of the dimers demonstrates the potential of this method for fabricating advanced nanophotonic structures.

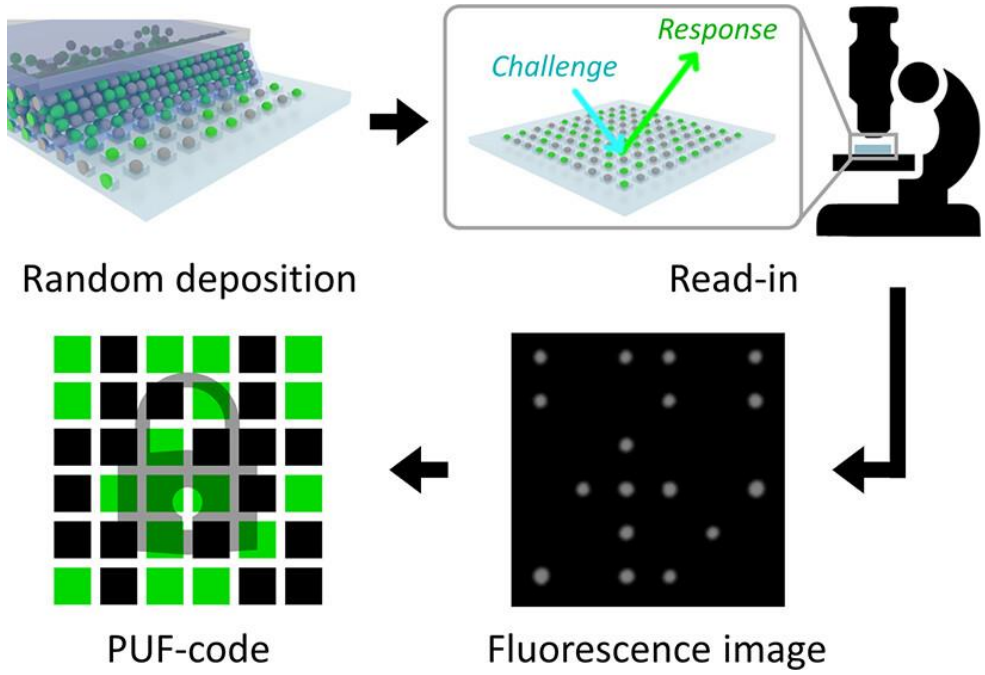


Figure 2.18: Pixelated Physical Unclonable Functions through Capillarity-Assisted Particle Assembly.**[106]**

Capillarity-assisted particle assembly can be used in information security and anti-counterfeiting by creating unique nanoparticle patterns, as shown in **Figure 2.18**. These patterns are read through microscopy and converted into optical codes (PUFs), which are highly unique and hard to replicate, making them useful for secure identification and encryption. Microfluidic technology is also environmentally friendly. It operates under mild conditions, uses less solvent, and avoids high-energy equipment, reducing waste and energy use. When combined with template or

nanoimprint methods, it further lowers material and process costs. Overall, microfluidics offers a low-cost, scalable, flexible, and green approach for metasurface fabrication, supporting future development in advanced optical technologies.

2.3 Significance of This Study

This study focuses on the fabrication and assembly of silicon-based metasurfaces, with an emphasis on the complete process from the preparation of silicon nanoparticles (Si NPs) to their high-precision assembly on complex patterned substrates. The research systematically analyzes and optimizes the key fabrication and assembly processes.

2.3.1 Exploration of Efficient and Low-Cost Silicon Nanoparticle Preparation Methods

This study demonstrates that the kitchen blender method offers a simple, cost-effective, and efficient approach for producing Si NPs with uniform size and stable dispersion in deionized water—ideal for microfluidic assembly and scalable for industrial use. Additionally, by optimizing ball-milling parameters and using anhydrous ethanol, the study achieved Si NPs (~90 nm) and Si nanocubes (~190 nm), expanding the method's potential for shape control. However, ball milling has drawbacks, such as FeSi contamination from steel balls. While zirconia balls improve purity and size consistency, ethanol's volatility causes particle aggregation and substrate damage during assembly.

2.3.2 Innovative Application of Nanoparticle Assembly Techniques

The study demonstrated that microfluidic technology, leveraging capillary forces, enables precise assembly of Si NPs on regular and complex patterned substrates. This method overcomes the high cost and low efficiency of traditional assembly techniques while achieving high particle packing density and uniformity within nanoscale structures. By assembling Si NPs on complex Einstein-patterned substrates, the study

validated the high compatibility and applicability of microfluidic techniques with Si NPs prepared using the kitchen blender method. This experiment highlights the potential for precise positioning of particles in intricate nanoscale patterns, offering a reference for assembling complex functional nanomaterials in the future.

2.3.3 Critical Role of Silanization Reactions in Assembly Stability

Silanization reactions play a crucial role in enhancing the chemical bonding between Si NPs and substrates, thereby improving the mechanical stability and uniformity of the assembly. During the assembly process, silanization agents (e.g., 3-aminopropyltriethoxysilane, APTES) undergo hydrolysis to form silanol groups (Si–OH), which react with hydroxyl groups (-OH) on the substrate or particle surfaces, forming strong siloxane bonds (Si–O–Si). This chemical bonding enhances the adhesion between particles and substrates, preventing particle detachment caused by mechanical impacts or solvent effects during the removal of PMMA templates or subsequent acetone cleaning. Additionally, the uniform monolayer formed by silanization on the substrate surface enhances particle distribution uniformity, minimizing slippage and aggregation. This ensures precise filling of patterned cavities. Experiments showed that silanized substrates maintained a near 100% packing density, even in complex patterns (e.g., curves and boundaries of the Einstein pattern). This

technique's reliability and efficiency not only suit the current experimental requirements but also provide a foundation for future large-scale manufacturing and applications.

2.3.4 Innovation and Expansion of Silicon-Based Metasurface Fabrication

This study showcases the entire fabrication process of silicon-based metasurfaces, from Si NP preparation to complex pattern assembly, optimizing material preparation and assembly techniques to advance silicon-based optical devices and functional

surfaces. With their superior optical properties of high refractive index and low loss, silicon-based metasurfaces hold significant potential in optical sensing, nanoantennas, high-resolution imaging, and quantum optics. The successful assembly of complex Einstein patterns demonstrated the adaptability and high-precision assembly capabilities of Si NPs in intricate, customized optical structures, expanding the application scenarios of silicon-based metasurfaces. This research provides technical support for developing high-performance sensors, information storage, and anti-counterfeiting technologies, bridging functional material research with practical applications.

2.3.5 Promoting Low-Cost Nanomanufacturing Technologies

The silicon-based metasurface fabrication route proposed in this study stands out for its simplicity and cost-effectiveness, laying the foundation for the widespread adoption of low-cost nanomanufacturing technologies. By using kitchen blenders and ball-milling methods to prepare Si NPs, the study significantly reduced equipment costs and operational complexity, providing an efficient and reliable alternative for resource-limited laboratories and industrial settings. Additionally, the introduction of microfluidic technology enhanced assembly precision and automation, reducing reliance on complex lithography equipment. This low-cost and highly adaptable process meets the functional requirements of high-performance metasurfaces while scaling up for industrial manufacturing. Particularly in small and medium-sized research institutions and emerging industries, this simplified process has significant promotional value, lowering the barriers to innovation and enabling the industrial application of nanomanufacturing technologies across diverse fields.

2.3.6 Academic and Industrial Impact

This research presents a complete innovation chain from Si NP preparation to substrate design and assembly, promoting progress in nanophotonics, electronics, and functional materials. Academically, it provides solid theoretical and experimental support, enhancing the understanding of silicon-based metasurface optics and

assembly on complex patterns, and advancing precise nanoparticle positioning techniques. Industrially, the low-cost, efficient nanomanufacturing processes developed here overcome traditional lithography limitations, making them suitable for large-scale, cost-sensitive applications. The successful assembly of the complex Einstein pattern shows the method's potential for creating customized materials, with broad value in research and industry.

2.4 Conclusion

This chapter introduced the development of metasurface fabrication and emphasized the advantages of microfluidic technology. All-dielectric metasurfaces have broad applications in optics, communication, and medicine, but traditional top-down methods are limited by high cost and complexity. Microfluidic technology, as a bottom-up approach, offers efficient, low-cost, and scalable solutions. By controlling solvent evaporation and capillary forces, it enables precise assembly of nanoparticles, especially on complex and large-area patterns. Combined with electron beam lithography, it improves manufacturing precision while reducing cost and process steps. Moreover, its mild operating conditions and low environmental impact make microfluidic technology well-suited for green and sustainable production. Overall, it provides a practical and promising method for large-scale metasurface fabrication and advanced nanodevice applications.

Chapter 3

Si NPs Preparation and Experimental Design

This chapter discusses the preparation, experimental design, and characterization of silicon nanoparticles (Si NPs) and their assembly into nanopatterned structures. Two methods were used: the kitchen blender method, which is cost-effective and suitable for microfluidic assembly, and ball milling, which allows precise control over particle size and morphology. Electron beam lithography (EBL) created high-precision substrates, followed by silanization with APTES to enhance particle adhesion. Microfluidic technology and capillary force-assisted assembly were used to deposit Si NPs into grooves, with the PMMA template removed post-assembly for analysis. Characterization using SEM, AFM, dark-field microscopy, extinction spectroscopy, and FDTD simulations confirmed the success of the processes and provided insights into the structural and optical properties of the Si NP assemblies. The integration of these methods successfully created stable Si NP nanopatterns, providing a foundation for future applications in nanophotonics, optical sensing, and multifunctional materials.

Chapter 3: Si NPs Preparation and Experimental Design

3.1 Material preparation method

This study uses two methods to prepare Si nanoparticles: the kitchen blender method and ball milling. The kitchen blender method is simple, low-cost, and suitable for large-scale production. It quickly produces uniform Si nanoparticles, ideal for use with microfluidic technology, improving accuracy and efficiency in assembly. The ball milling method offers precise control over particle size and shape, making it useful for studying how these factors affect assembly. While ethanol can cause some issues during assembly due to its volatility, it is still effective for producing high-purity particles. In summary, the kitchen blender method is efficient and cost-effective for assembly, while ball milling provides more precision and flexibility. Together, they support the preparation and research of Si nanoparticles.

3.1.1 Si nanoparticles Preparation by Kitchen blender

In our study, one of the preparation methods of Si nanoparticles was carried out following the method proposed by Chaabani et al. **[18]**, as shown in **Figure 3.1**. This method involves using a kitchen blender to grind silicon blocks into Si NPs. Silicon lumps with 99.9999% purity from Alfa Aesar and DI water from a Veolia system (18.2 MΩ.cm resistivity) were used. A standard kitchen blender with a 1500 W motor and six steel blades was employed. We added 10g of Si lumps and 300 mL of DI water into the blender and ground them in intervals: 3 minutes of grinding followed by 2 minutes of rest for two hours. After grinding, 85% of the top solution was extracted, stored in a sealed bottle, and left in the refrigerator for three days, allowing larger Si NPs to settle. Finally, centrifugation was used to obtain the desired particle size. The kitchen blender method is convenient, cost-effective, and safe, offering reliable results compared to specialized equipment.

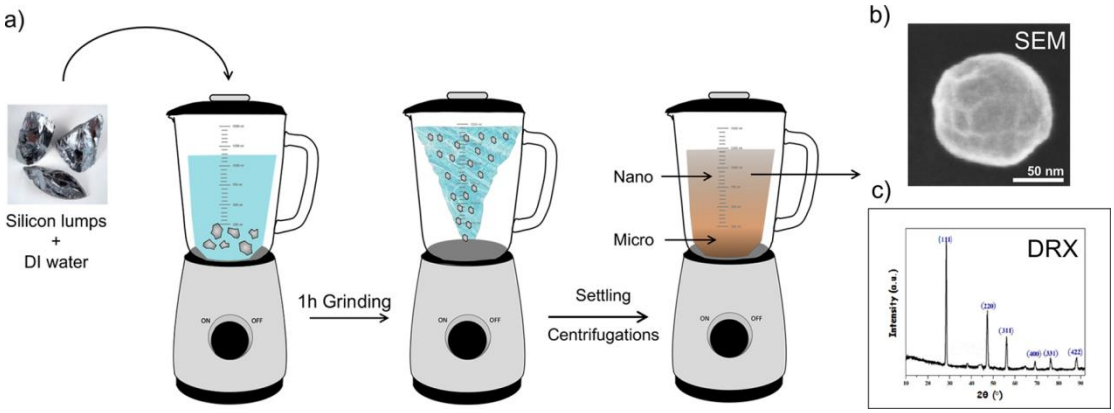


Figure 3.1: (a) Schematic representation of the process (grinding, clarification) used to prepare colloidal silicon nanoparticles. (b) High-magnification SEM image of a typical crystalline Si nanoparticle deposited onto a silicon substrate. (c) XRD pattern of Si nanoparticles powder where the indices show Si phase.**[18]**

3.1.2 Si nanoparticles Preparation by ball mill

In this study, another preparation method for Si nanoparticles was carried out by using a ball mill machine**[107-108]**. This method uses a ball mill to grind silicon powder into Si NPs. We used silicon powder with 99.9999% purity from Alfa Aesar and DI water (18.2 MΩ.cm resistivity) from a Veolia system. We added 1g of Si powder, 30 mL of DI water/ethanol, and 1g of Inox/ZrO_2 balls into the mill, setting the speed to 500 rpm for 4 hours. During grinding, the temperature control device was monitored to ensure safe operation. After grinding, 85% of the top solution was extracted and stored in a sealed bottle. The solution was refrigerated for three days, then left outside for a day to allow larger particles to settle. Finally, we used centrifugation to achieve the desired particle size. The ball milling method is cost-effective and suitable for large-scale production compared to other methods like chemical vapor deposition.

3.2 Experimental design of capillary force assisted Si nanoparticle assembly

This section describes the process for assembling Si nanoparticles (Si NPs) using capillary force-assisted assembly. First, nanopatterned substrates were prepared on n-

type silicon wafers with electron beam lithography (EBL), followed by cleaning, drying, and plasma treatment. A 150 nm PMMA layer was spin-coated, and nanopatterns were created. To improve particle adhesion, the substrates were silanized with aminopropyltriethoxysilane (APTES) in ethanol for 3 hours. This ensured the particles stayed attached during PMMA removal. Si NPs were assembled using microfluidic technology with the Smart Force device. Parameters like evaporation rate and temperature were controlled to deposit particles accurately. After assembly, the PMMA template was removed using acetone, and the particles remained securely attached. The process was validated with SEM and dark-field microscopy, showing precise and stable nanopatterns suitable for applications in optics, electronics, and sensors.

3.2.1 Preparation of Nanopatterned Substrates

Electron beam lithography is used to create very precise patterns, primarily utilized in the semiconductor industry and the production of microprocessors and other microsystems. In this study, we used e-beam lithography to prepare the nanopatterned substrates. A silicon wafer with a 300 nm thick SiO_2 layer was used as substrate. The size of the Si substrate was limited to 1cm x 1cm due to the limitation of working space for assembling instruments. Firstly, the Si substrate was ultrasonically cleaned with neutracon solvent for 5 minutes, followed by two 5-minute ultrasonic cleanings with DI water. After drying on a hot plate, the substrate was treated with a plasma cleaner for 4 minutes. Subsequently, polymethyl methacrylate (PMMA) was spin-coated onto the substrate to achieve a thickness of 150 nm, a process detailed in **Figure 3.2**. Following this, we used e-beam lithography to create nanopatterned substrates for nanohole arrays, which will be elaborated upon later. The flow chart of the e-beam lithography preparation process is presented in **Figure 3.3. (a)**.

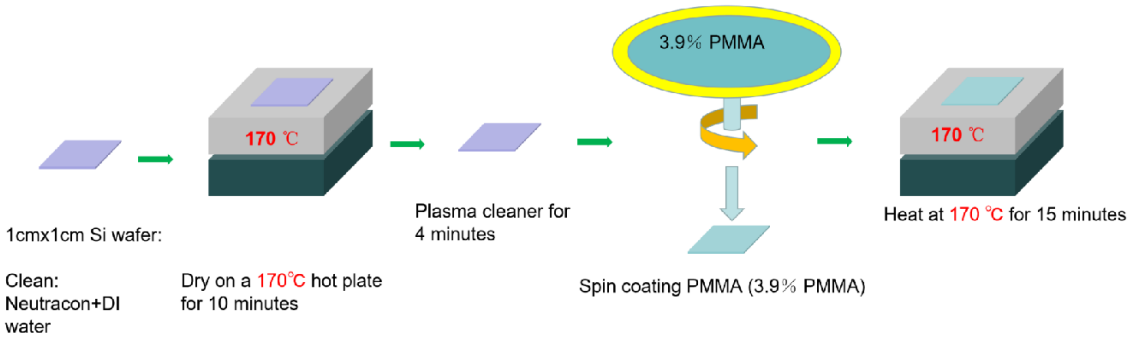


Figure 3.2: Schematic diagram of the spin coating process of PMMA.

3.2.2 The process of Silanization Reaction

Silanization is a versatile technique and can be tailored by changing the type of silane, the substrate, or the reaction conditions to achieve specific surface characteristics. It's widely used in applications ranging from biosensor fabrication to coatings for medical devices and in the stabilization of NPs. In this study, as the PMMA template needs to be removed post-assembly of the Si NPs, a silanization reaction is necessary to chemically bond the Si NPs to the nanopatterned substrate. The silanization reaction involved using 3-Aminopropyltriethoxysilane (APTES) and plasma processing. APTES readily undergoes hydrolysis to release ethanol, resulting in the formation of the corresponding Si-O-Si condensates. The amino group, present in the C-NH_2 bond of the molecule, can react with hydroxyl groups among others**[109]**.

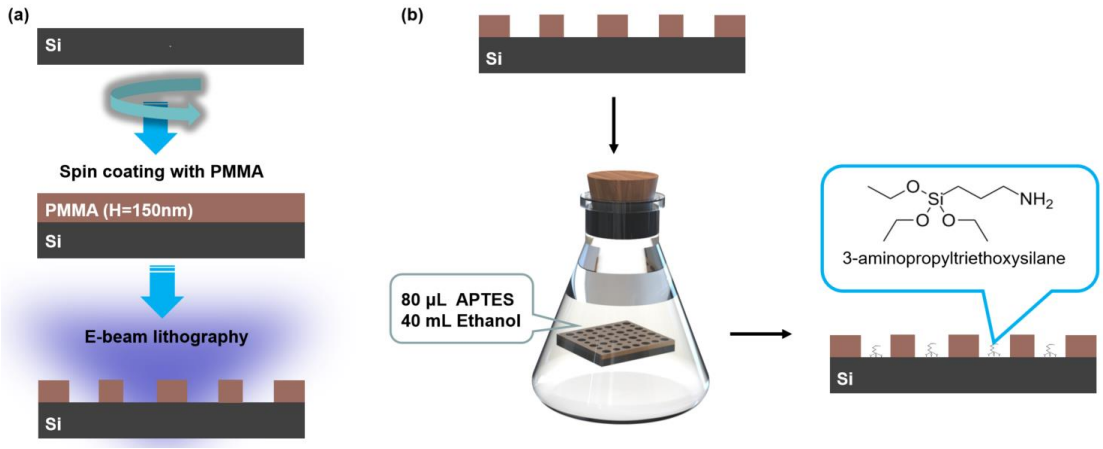


Figure 3.3: (a) Experiment design flow chart of fabricated nanopatterned substrate by e-beam lithography. (b) Diagram of the silanization reaction process.

Here, samples prepared via e-beam lithography were immersed for 3 hours in a closed container with a mixture of APTES and ethanol, to complete the silanization reaction. The diagram of the silanization reaction is shown in Figure 3.3.(b).

3.2.3 The process of Si nanoparticles Assembly

Microfluidic techniques control fluids at a small scale, typically in channels measuring tens to hundreds of micrometers. These methods are widely used in biology, chemistry, and medicine. In this study, microfluidic techniques were employed for metasurface fabrication using capillary-assisted assembly of Si NPs. The Smart Force device, based on microfluidic technology, uses capillary forces from evaporating droplets to deposit nanoparticles into nanopatterned substrates. In the Smart Force device, droplet movement is driven by airflow and temperature control of the sample platform. **Figure 3.4(a)** depicts the experimental setup for controlled convective and capillary assembly of NPs on surfaces. Initially, the Smart Force device was activated, setting the temperature and airflow parameters. Subsequently, the sample was positioned in a sealed microfluidic chamber, and the concentrated Si NP solution was syringed into the assembly area through the microfluidic channel. **Figure 3.4(b)** illustrates the Si NP assembly process, which takes approximately one day. The working principle of capillary force-assisted assembly is based on the effect of capillary forces and solution evaporation. A uniform laminar flow of liquid forms on the substrate surface, and as the solution evaporates, particles are driven by capillary forces to gradually move towards the patterned substrate grooves and deposit. The particles are pushed to the edges of the pattern by the capillary force (Fc) at the meniscus. For larger particles, the residual capillary force is transmitted to adjacent particles, generating an upward force (F'c), thereby achieving precise particle alignment. On the nanopatterned substrate, the geometric parameters of the grooves, such as depth (H) and diameter (D), play a critical role in determining the assembly outcome. Key factors such as solution evaporation rate, substrate temperature, and movement speed significantly affect the uniformity of particle deposition and the

precision of alignment. Ultimately, a 3-hour acetone soak of the assembled sample facilitates the removal of the PMMA template.

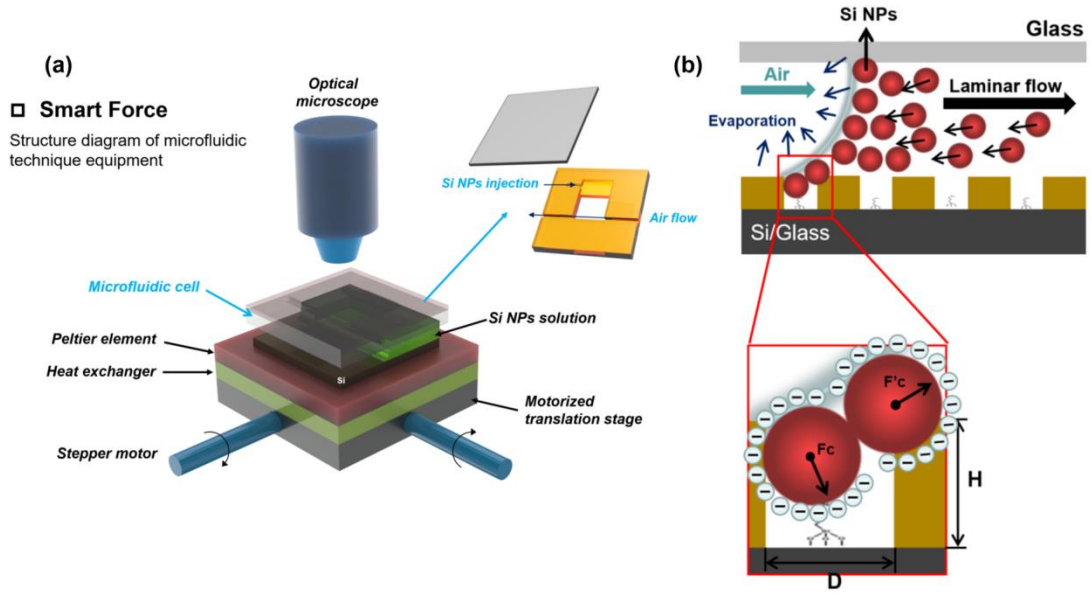


Figure 3.4: (a) The experimental setup, as illustrated, is specifically designed for the controlled convective and capillary assembly of Si NPs on a nanopatterned substrate. In this setup, the temperature of the substrate is regulated by a Peltier element. (b) Diagram of capillary force assisted Si nanoparticle assembly.

3.2.4 Lift-off process

To remove the PMMA matrix after assembling silicon nanoparticles (Si NPs), the samples were soaked in acetone for 3 hours. This dissolved the PMMA, leaving the Si NPs securely attached. The silanization step ensured the particles stayed in place during PMMA removal. SEM and dark-field microscopy confirmed the successful removal, with the Si NPs remaining in the nanopattern. Removing the PMMA template exposes the nanoparticles for further use, improving surface properties and preventing contamination. This step is crucial for enabling the nanoparticles to perform their intended functions in applications like optics, electronics, or biosensing.

3.3 Characterization tools and data analysis methods

This section discusses the characterization tools and data analysis methods used to study the properties and behaviors of silicon nanoparticles (Si NPs) and their assembled structures. Key techniques like Scanning Electron Microscopy (SEM), Atomic Force Microscopy (AFM), and Dark-Field Microscopy (DFM) were employed to examine the physical and structural characteristics. Additionally, Dynamic Light Scattering (DLS) and Extinction Spectroscopy provided insights into particle size distribution and optical properties. Finite-Difference Time-Domain (FDTD) simulations offered a theoretical understanding of light interaction with the nanostructures. These combined methods ensure a comprehensive evaluation of the preparation and assembly processes.

3.3.1 SEM (Scanning Electron Microscopy)

SEM (Scanning Electron Microscopy) analysis was performed using a FEG system (Hitachi SU 8030) to characterize the morphological properties of both the Si NPs and the metasurface nanostructure assembled by Si NPs. For the SEM analysis, we prepared the Si NPs sample by dropping a dispersion of Si colloids onto a clean Si substrate.

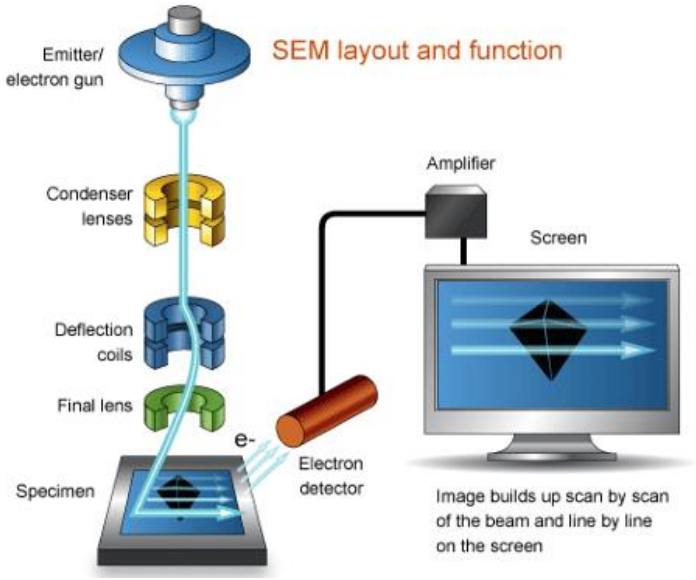


Figure 3.5: Schematic diagram of the SEM layout and main components.**[110]**

The **Figure 3.5** illustrates the basic structure and working principle of a Scanning Electron Microscope (SEM). The electron beam is generated by the emitter (electron gun) and shaped by a series of electromagnetic lenses (condenser and final lenses) and deflection coils. The focused beam scans across the specimen surface in a raster pattern. As the electrons interact with the sample, various signals are emitted and detected by an electron detector. These signals are then amplified and displayed on a screen, forming an image line by line. SEM enables high-resolution imaging of surface topography and composition.

3.3.2 AFM (Atomic Force Microscopy)

Additionally, AFM (Atomic Force Microscopy) analysis was conducted using an Agilent 5100 system in Air analysis mode. We used a silicon AFM tip (Nanosensors, PPP-NCLR-50, force constant: 21−98 N/m, resonance frequency: 146−236 kHz) for characterizing the morphology of the assembled structure by Si NPs.

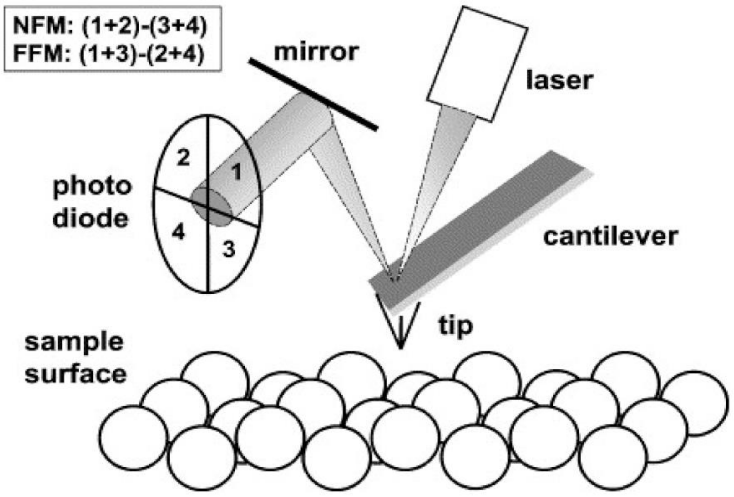


Figure 3.6: Schematic illustration of the working principle of Atomic Force Microscopy (AFM).**[111]**

The Atomic Force Microscope (AFM) is a high-resolution scanning probe microscopy technique used to study the surface morphology and physical properties of samples. The **Figure 3.6** shows the fundamental working mechanism of AFM. A sharp tip mounted on a flexible cantilever scans the sample surface. As the tip interacts with the

surface atoms, it experiences forces that cause the cantilever to deflect. A laser beam is reflected off the back of the cantilever onto a segmented photodiode detector via a mirror. The detector measures the position of the reflected laser beam, providing information about the cantilever's deflection in both normal and lateral directions.

3.3.3 Dark-field Microscope

The dark-field microscope images of the assembled structure were obtained using a dark-field optical microscope (Zeiss Axio Imager Z2). (Supplement the instrument parameters of extinction spectrum measurement).

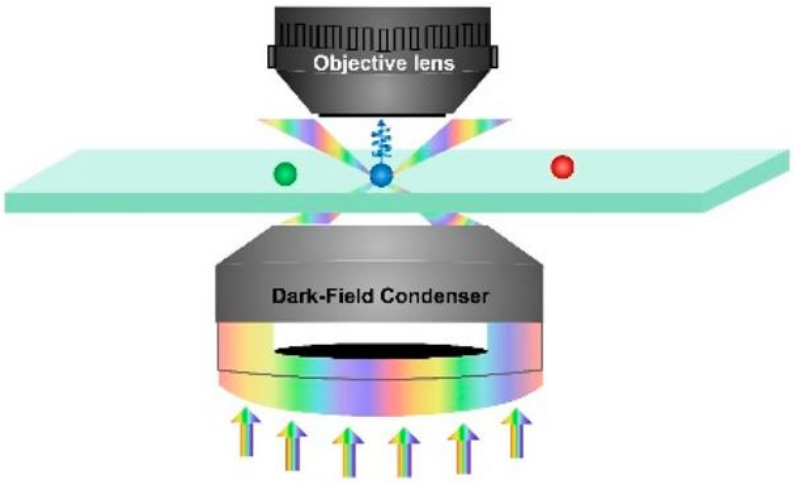


Figure 3.7: (A) Schematic of the typical optical path of the DFM with the dark-field condenser.**[112]**

The working principle of Dark-Field Microscopy (DFM) is based on a specific optical path design that effectively detects scattered light from a sample while blocking direct light. **Figure 3.7** illustrates the optical path of a dark-field microscope, which uses a dark-field condenser and objective lens. The condenser focuses light at an oblique angle onto the sample, forming a hollow light cone. Only scattered or refracted light from the sample enters the objective lens, while direct light is blocked, creating a dark background. This setup allows fine structures like particles or cells that scatter light to appear bright, improving detection sensitivity for subtle features. The microscope is particularly useful for observing small particles, nanostructures, or cells, making it

ideal for live-cell imaging and tracking nanoparticles or biomolecules in real time. Dark-field microscopy is a powerful tool in life sciences, materials science, and nanotechnology.

3.3.4 Dynamic Light Scattering

Dynamic light scattering (DLS) is a very popular technique for the measurement of particle size distributions in colloidal suspensions and emulsions. According instrumentation is widely available, easy to use, and inexpensive in maintenance and facilitates quick analyses. DLS is commonly used to characterize suspensions of isolated nanoparticles or nanoparticle aggregates for various analytical purposes, for instance, to check product specification or to assess dispersing procedures. However, the technique also shows specific application limits, for example, with regard to working range and information content.

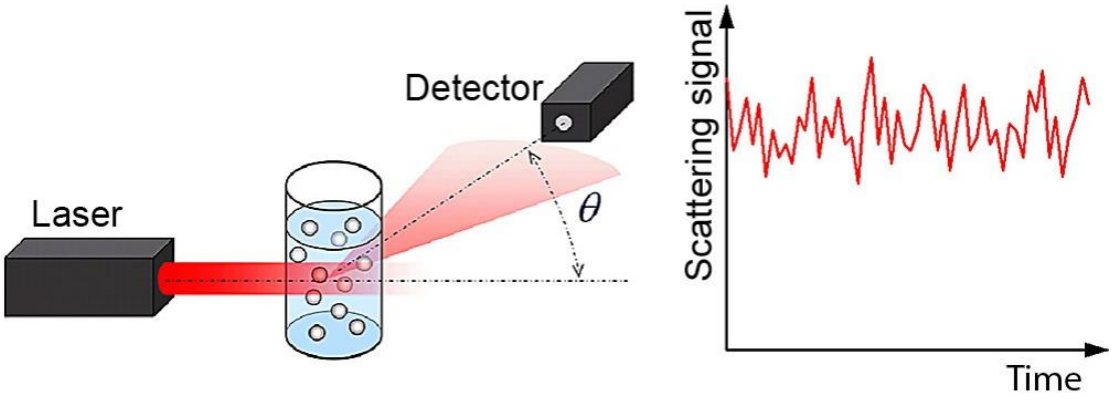


Figure 3.8: Principle of DLS: light scattered by a fine particles illuminated with a laser is measured with high time resolution under a defined angle θ; the fluctuation of the scattering signal reflects the dynamics of microstructural processes such as the particles' Brownian motion.**[113]**

Figure 3.8 illustrates the principle of Dynamic Light Scattering (DLS). A laser beam illuminates a sample containing fine particles, and the scattered light is detected at a specific angle. The fluctuation in the scattered light over time, caused by the particles' Brownian motion, provides information about their size and motion. DLS is widely used to measure particle size distribution and analyze nanomaterials. The technique

detects fluctuations due to the thermal motion of particles, occurring on very small time scales (microseconds or nanoseconds). For instance, DLS can probe the vibrations in par-ticle networks, which offers an opportunity to study phase transitions in colloidal suspensions and to quantify the elastic properties of gels**[114]**.

3.3.5 Extinction spectrum

Extinction spectroscopy is a classical optical technique for characterizing the interaction between light and matter**[115]**. It measures the attenuation of light passing through a material, providing insights into both absorption and scattering phenomena. Absorption involves the conversion of light into other forms of energy, while scattering redirects light due to structural features or particulate matter. This technique is widely applied in the study of localized surface plasmon resonance (LSPR) in nanoparticles and metamaterials, offering valuable information on their optical properties. In micro- and nanostructure analysis, extinction spectroscopy is particularly effective in revealing the arrangement and coupling behavior of nanostructures, such as resonance modes in nanoparticle arrays.

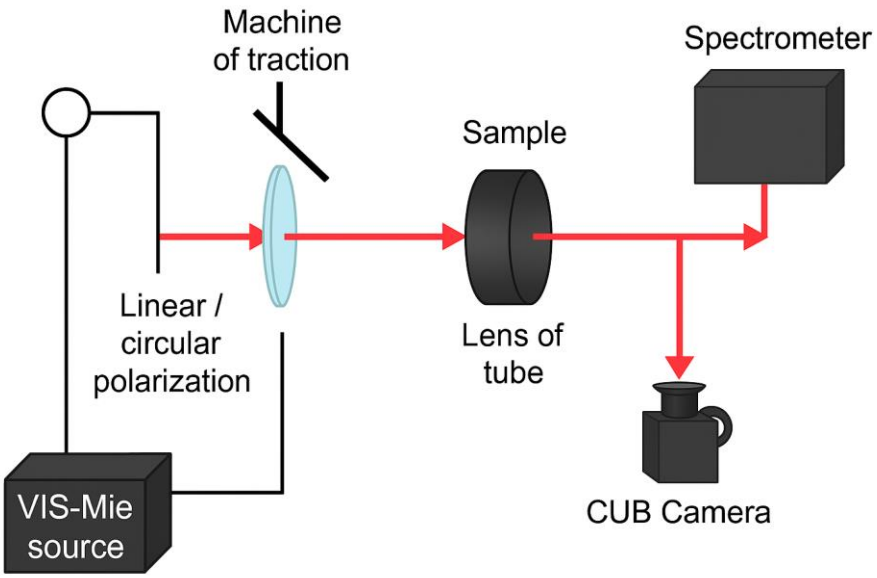


Figure 3.9: Schematic diagram of reflection structures in a spectral system of structures assembled by Si nanoparticles.

Figure 3.9 illustrates a schematic setup designed to investigate the reflection-based spectral response of structures assembled by silicon nanoparticles. A VIS-Mie source emits visible light that passes through a linear or circular polarizer, allowing precise control over the polarization state. The beam is then directed to the sample, which can be subjected to mechanical stress using a traction device during measurement. Reflected light from the sample is collected through a lens system and subsequently split toward a CUB camera and a spectrometer. This configuration enables simultaneous spatial imaging and spectral analysis, allowing detailed characterization of the optical response of the Si NP-based structures.

3.3.6 Finite-Difference Time-Domain (FDTD)

FDTD Lumerical simulations harness the advantages of the Finite-Difference Time-Domain (FDTD) method by integrating sophisticated features and functionalities into the Lumerical software suite**[116-117]**. This platform offers users an intuitive interface coupled with robust tools tailored for modeling intricate optical systems, devices, and materials. Through precise simulation of the electromagnetic behavior of these systems, FDTD Lumerical simulations empower researchers and engineers to achieve profound understanding of the fundamental physics and refine designs for enhanced performance.

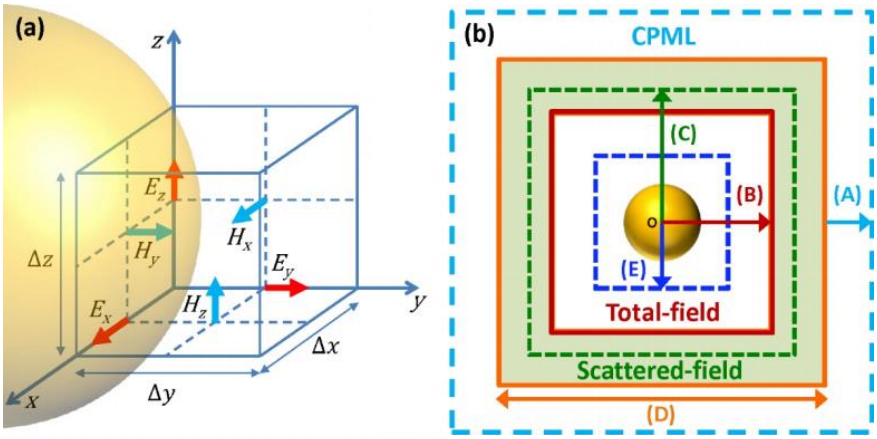


Figure 3.10: (a) Yee FDTD cell and per-component meshing technique illustration (not in scale). (b) FDTD simulation domain setup: (A) CPML thickness, (B) TF/SF position, (C) S_{sca} position, (D) physical box length, and (E) S_{abs} position.**[118]**

The FDTD simulation includes regions for boundary absorption, scattered field detection, and absorption monitoring. It accurately analyzes nanoparticle scattering and its interaction with incident and scattered waves by discretizing electromagnetic fields. **Figure 3.10** shows the FDTD setup, with panel (a) displaying the Yee grid and the arrangement of electromagnetic components. Panel (b) shows the simulation domain, including regions for boundary absorption (CPML), field separation (TF/SF), scattered field detection (Ssca), and absorption detection (Sabs), optimizing the study of nanoparticle scattering.

This study uses various characterization methods to evaluate Si nanoparticles (Si NPs) throughout different stages. Dynamic light scattering (DLS) ensures the size distribution and stability of the Si NPs, while scanning electron microscopy (SEM) and atomic force microscopy (AFM) analyze their morphology and structural features. Dark-field microscopy (DFM) and extinction spectroscopy characterize their optical properties. Finite-difference time-domain (FDTD) simulations provide numerical insights, helping optimize experimental designs. Together, these methods ensure a comprehensive understanding of Si NPs, supporting future research in nanoparticle assembly and optical applications. In conclusion, these methods provide a comprehensive analysis of Si nanoparticle preparation, assembly, and optical properties, ensuring accurate insights for various applications.

3.4 Conclusions

This chapter presents the preparation and assembly of silicon nanoparticles (Si NPs) into nanopatterned structures. Two fabrication methods were used: the kitchen blender method, which is simple and effective for producing uniform Si NPs, and the ball milling method, which offers better control over particle size and shape. Nanopatterned substrates were fabricated using electron beam lithography (EBL), and silanization was applied to improve particle adhesion. Microfluidic techniques and capillary forces enabled precise and uniform assembly of the nanoparticles. The process and results were analyzed using SEM, AFM, dark-field microscopy, extinction spectroscopy, and FDTD simulations. Overall, the study provides an efficient strategy to build well-ordered Si NP structures for nanophotonics and multifunctional applications.

Chapter 4

Microfluidic Assembly of Si NPs on Silicon Substrates

Metasurfaces, composed of sub-wavelength nanostructure arrays, rely on the periodic arrangement of nanostructures to define their functionality. In **Chapter 4**, we refined a previous method by improving the ratio of silicon lumps to deionized water, using a kitchen blender to grind silicon blocks into nanoparticles (Si NPs). We then designed and assembled the metasurface structure by depositing the Si NPs onto a nanopatterned Si substrate using microfluidic techniques. This process uses capillary forces from evaporating droplets in microfluidic channels to deposit Si NPs into microfabricated traps. This method overcomes the limitations of traditional top-down approaches, such as high cost, complexity, and beam damage to sensitive materials. Key factors like Si NP quality, silanization, and precise control of temperature and airflow were found to significantly impact the assembly process. This capillary force-assisted method offers vast potential for applications in materials science, nanotechnology, and various industries.

Chapter 4: Microfluidic Assembly of Si NPs on Silicon Substrates

4.1 Introduction

Metasurfaces are composed of subwavelength nanostructure arrays known as meta-atoms**[116, 119]**. The periodic arrangement of these meta-atoms is crucial in defining the functionality of metasurface devices. The geometry and composition of meta-atoms can be tailored to achieve specific optical properties, like controlled phase delay**[120]**, group delay**[121]**, and targeted transmission/reflection at a particular wavelength**[122]** or over a range of wavelengths**[123]**. These capabilities of metasurfaces facilitate their use in optical cloaking**[124]**, advanced displays**[125]**, high-resolution imaging**[126]**, ultra-thin lenses**[127]**, and anti-counterfeiting devices**[128]**. The metasurface structures are usually composed of plasmonic materials and dielectric materials. However, thermal loss in metal plasmonic materials, such as Au and Ag, hinders the advancement of these nanomaterials in practical applications**[43]**. An alternative is using high-refractive-index dielectric NP, like Si or Ge, for a low-loss, high magnetic field response**[129]**.

Nanotechnology has significantly advanced in recent years, with the preparation and precise spatial arrangement of NP presenting both key opportunities**[130]** and challenges**[131]**. Top-down methods like lithography, laser printing, and etching**[132-133]** for preparing nanostructures are generally costly and less suitable for large-area fabrication. Conversely, bottom-up assembly utilizes unique physicochemical properties**[18, 134]** of NPs to create nanostructures with specific compositions**[135]**, geometries**[136]**, and functionalities**[137-138]**. However, various NP assembly methods have been proposed, including self-assembly**[139]**, pick-and-place**[140]**, directed assembly**[141]**, and so on. Self-assembly techniques use controlled particle interactions to form ordered structures. A major limitation is the strong dependence of

their efficiency on operating conditions**[142]** and the specific properties of the particles, which dictate their interactions with each other and the substrate. This sensitivity often hampers achieving the high yield, reproducibility, and precision essential for various applications, including microelectronics. Pick-and-place methods, like optical tweezers, enable precise particle assembly and complex structure formation. However, achieving this precision comes with a trade-off: it incurs a high cost and results in limited production capacity. Directional assembly, using external forces, efficiently and cost-effectively organizes colloidal nanoparticles into complex structures with high yield and precision.

Capillary-assisted NP assembly, developed recently, is a promising directional assembly technique**[143]**. This method selectively places NP into nanohole arrays on substrates using topographic patterns and surface chemical conditioning**[33, 144]**. Capillary assembly combines the advantages of physical or chemical synthesis of NPs**[18, 134]** with top-down patterning, effectively positioning NPs accurately on large surfaces with diverse topographic features. Organized colloidal NP arrays exhibit collective properties**[145]** beneficial for innovative optical devices**[123, 146]**, sensitive chemical sensors**[147-148]**, and high-density data storage**[149-150]**, with applications in electronics**[151]**, plasmonics**[148, 152]**, and biology**[153]**. Wolf et al**[154]** detailed particle placement control via convection and capillary force assembly. They were the first to demonstrate that controlling the speed and direction of suspended particles could be used to assemble or disassemble them. This was achieved by adjusting the temperature of the colloidal suspension above or below the dew point. Later, Brugger et al further studied nanoscale morphology control in capillary force assembly of NP**[102]**. It was demonstrated that topographic features on solid substrates, including photolithographic funnel traps and auxiliary sidewalls, can definitively guide the capillary assembly of gold nanorods, thereby simultaneously controlling position, orientation, and interparticle distance at the nanoscale. The result presents substrates with up to 100% assembly yield over the centimeter scale. Recently, Eleonora et al elaborated on capillary force-assisted NP sequence assembly

in microfluidic channels**[97]**. It is illustrated that the microfluidic platform can be used to create a variety of patterns and that the microfluidic channel easily allows surface functionalization of captured particles.

In this work, our focus remains on exploring the design of metasurface structures, specifically for facilitating Si NP assembly assisted by capillary forces. Firstly, we adopted the method proposed by Chaâbani et al**[18]**, which involves obtaining Si NPs by physically stripping and grinding Si blocks, using a kitchen blender for this process. By adjusting the ratio of Si blocks to DI water, we produced Si NPs with a more uniform size and regular shape. This allowed us to control the wetting angle of the substrate through a silanization reaction, which also bonded the Si NPs to the surface. Using capillary force-assisted assembly, we arranged the Si NPs into nanohole and Einstein image arrays. The process deposits Si NPs into microfabricated traps, using capillary forces from evaporating droplets in a microfluidic channel. Key factors such as Si NP solution quality, silanization, and controlled temperature and airflow were crucial for the assembly. This technique has potential for creating sensitive sensors with applications in monitoring, security, and diagnostics, as well as electronics and medicine.

4.2 Experimental section

In this experiment, we employed a combination of nanopatterning, chemical modification, and capillary force-assisted assembly techniques to achieve high-precision alignment of Si nanoparticles (Si NPs) on the substrate. **Figure 4.1** illustrates the detailed steps and corresponding mechanisms. First, preparation of the nanopatterned substrate (**Figure 4.1a**). This process involves two steps: spin-coating of PMMA and electron beam lithography (E-beam lithography). Initially, a 150 nm thick layer of PMMA is coated on the silicon-glass substrate to form a lithographic mask. Subsequently, using E-beam lithography, nanohole array patterns are etched onto the PMMA layer. The diameter and arrangement of these holes are precisely controlled, providing a high-precision template for the subsequent nanoparticle

assembly. The accuracy of this process is critical for achieving uniform and efficient filling of the nanoholes with nanoparticles. The second step of the process is the silanization of the substrate (**Figure 4.1b**). To ensure the Si nanoparticles adhere firmly to the substrate, the substrate undergoes silanization treatment. The silanization process is conducted in a sealed container with a solution of 80 µL APTES dissolved in 40 mL ethanol, in which the substrate is immersed to facilitate chemical modification. During the silanization reaction, stable Si-O-Si bonds are formed on the substrate surface, functionalizing it and enhancing the adhesion between the nanoparticles and the substrate. This chemical modification is critical to prevent the nanoparticles from detaching during the subsequent removal of the PMMA template. Finally, the assembly of nanoparticles was achieved through capillary forces (**Figure 4.1c**). During the capillary force-assisted assembly, evaporation of the solution creates a laminar flow at the air-liquid interface, concentrating the suspended Si nanoparticles at the interface.

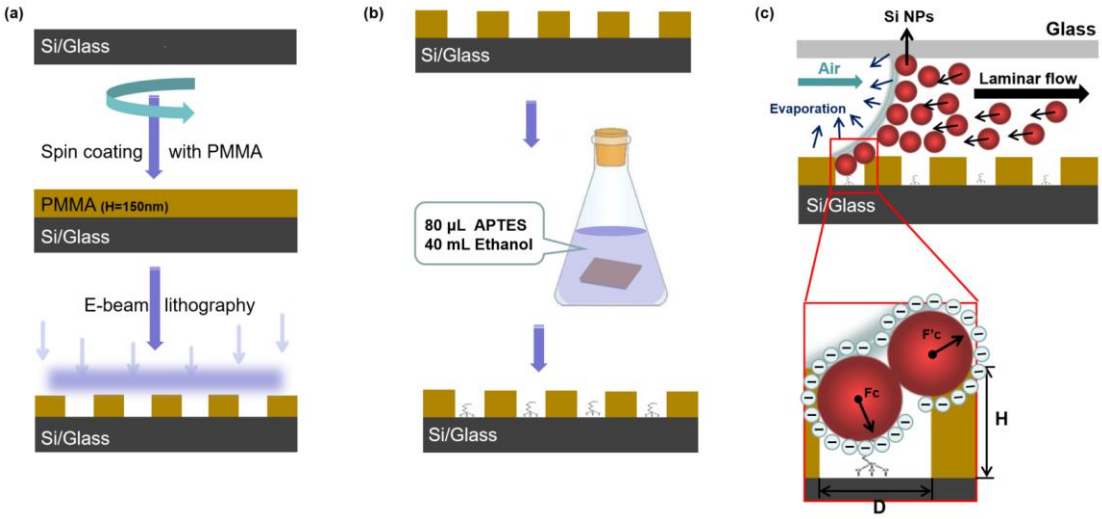


Figure 4.1: (a) Diagram showing the preparation of nanopatterned substrates using PMMA spin coating and E-beam lithography. (b) Silanization with 80 µL APTES in 40 mL ethanol to enhance surface adhesion. (c) Capillary assembly of Si NPs: evaporation drives flow that concentrates particles at the interface, where capillary forces (Fc) guide them into nanoholes. Inset shows how hole depth (*H*) and diameter (*D*) affect assembly precision.

As the interface retreats, capillary forces (Fc) guide the particles into the nanohole arrays on the substrate surface, achieving high-precision alignment. During this process, key parameters of the nanoholes, including hole depth (H) and diameter (D), significantly influence the efficiency of particle capture and alignment quality. Additionally, by adjusting temperature and airflow, the evaporation rate of the solution can be controlled, further optimizing the alignment precision.

In summary, this experiment utilized an integrated multi-step approach to achieve precise assembly of Si nanoparticles while showcasing the potential applications of combining nanopatterning techniques with fluid dynamics in materials science and nanotechnology. This method not only provides robust technical support for studying the optical and electronic properties of nanoparticles but also lays the foundation for subsequent functional applications.

4.3 Results and Discussion

In this section, we present and analyze the experimental results to evaluate the preparation, assembly, and characterization of Si nanoparticles (Si NPs) on nanopatterned substrates. By integrating various fabrication techniques, including the kitchen blender method for nanoparticle synthesis and capillary force-assisted assembly on silanized substrates, we investigate the effectiveness of each step.

4.3.1 Characterization Analysis of Si Nanoparticles

In the assembly experiment involving Si NPs, the quaily of these NPs is a crucial factor in determining the success of the experiment. As referenced earlier, we synthesized Si NPs following the method by Chaâbani et al**[18]**. As shown in **Figure 4.2(a)**, the preparation of silicon nanoparticles (Si NPs) using the kitchen blender method demonstrates a cost-effective and scalable approach for producing uniform nanoparticles with good dispersibility. The process benefits from the simplicity of mechanical grinding and allows for the separation of nano-sized particles through settling and centrifugation. The resulting Si NPs exhibit a stable colloidal suspension,

as evidenced by the zeta potential of -33.5 mV, indicating strong electrostatic repulsion among particles, which prevents aggregation. The SEM image highlights the morphology and size uniformity of the particles, essential for applications requiring consistent optical and electronic properties. The optical images in **Figure 4.2(b)** further illustrate the influence of particle size on light scattering, where distinct color variations arise due to size-dependent scattering effects, particularly relevant for optical sensing and plasmonic applications. The size range of the particles, from 45 nm to 220 nm, offers flexibility in tailoring their properties for specific uses.

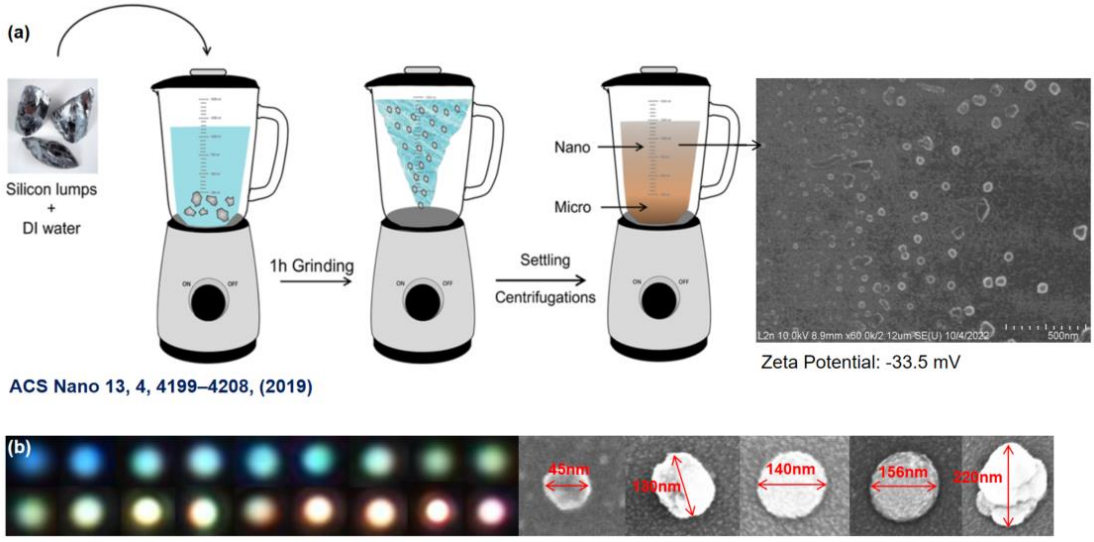


Figure 4.2: (a) Si nanoparticles are prepared by grinding silicon lumps in DI water using a kitchen blender. After settling and centrifugation, stable nanoparticles are obtained (zeta potential: –33.5 mV). SEM shows their shape. (b) Optical and SEM images show uniform Si nanoparticles (45–220 nm). Color differences are due to light scattering by different sizes.

It's worth emphasizing again that we modified the ratio of Si blocks to DI water, as illustrated in **Figure 4.3.** The SEM images illustrate the impact of varying the Si-to-DI water ratios on the morphology and distribution of Si nanoparticles (Si NPs). Among the tested ratios, the mixture of 10 g Si and 300 mL DI water (**Figure 4.3b**) produced the most uniform and well-dispersed nanoparticles, suggesting that this ratio achieves an optimal balance between grinding efficiency and particle stability. The higher ratio

of 20 g Si to 300 mL DI water (**Figure 4.3c**) resulted in increased aggregation and uneven distribution, likely due to insufficient liquid medium for effective particle dispersion. Conversely, the lower ratio of 5 g Si to 300 mL DI water (**Figure 4.3a**) yielded sparse particles, which may limit the scalability of nanoparticle production. On the whole, we achieved Si NPs with optimal size and distribution when the mixture consisted of 10 g Si lumps and 300 mL DI water.

To increase the concentration of the Si NP solution, we used evaporation by heating it on a hot plate. This process effectively concentrates the solution by evaporating the water solvent, without introducing organic solvents, keeping the process environmentally friendly. The optimized ratio and concentration method provide a scalable, reproducible pathway for producing Si NPs, suitable for applications in nanophotonics, sensing, and catalysis, where particle uniformity and concentration are crucial. Future studies could focus on refining these parameters to improve particle size control and dispersion stability.

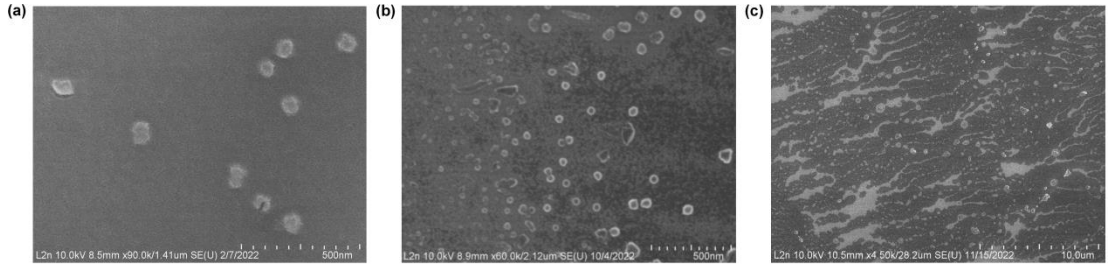


Figure 4.3: The SEM image of Si nanoparticles were prepared by kitchen blender. The preparation ratio of three kinds of raw materials was tried (a) 5g Si and 300mL DI water (b) 10g Si and 300mL DI water (c) 20g Si and 300mL DI water.

4.3.2 Preparation and Analysis of Nanopatterned Substrate

We will experiment to analyze the results of capillary force-assisted NP assembly. This experiment will involve using a kitchen mixer to prepare Si NPs, which will then be combined with a substrate that has undergone top-down patterned treatment. The experiment was initially carried out on nanohole arrays structured on a Si substrate. As shown in **Figure 4.4**, the nanohole arrays structure was designed into two areas

called area 1 and area 2, respectively. Area 1 consists of square sub-zones, each featuring a hole of varying sizes (150 nm, 200 nm, 250 nm, and 300 nm) in each corner, with a periodicity of 600 nm. Area 2 features a nanohole array with each hole measuring 300 nm in diameter and a periodicity of 600 nm. Notably, both types of nanohole array structures are present on the same sample.

In summary, this experiment marks important progress in understanding and improving capillary force-assisted nanoparticle assembly. By adjusting the geometry of nanohole arrays—such as size and spacing—and applying stable chemical bonding methods, the study achieved more precise and reliable nanoparticle placement. This not only enhances control over nanoscale assembly but also supports the development of functional nanostructures for applications in nanophotonics, sensing, and advanced materials.

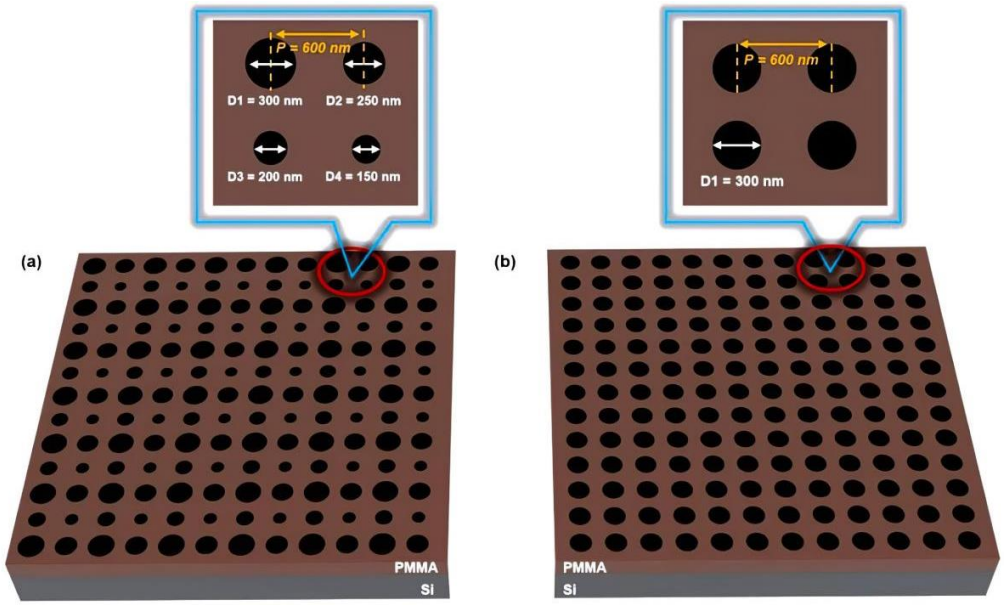
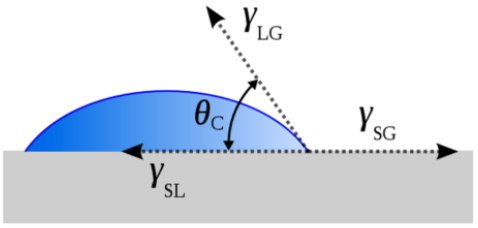
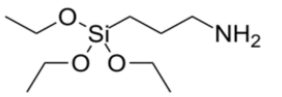


Figure 4.4: Fabrication of the nanopatterned substrate. (a) Area 1 is a nanohole array with four different size squares, with hole diameters of 150 nm, 200 nm, 250 nm, and 300 nm, the period is 600 nm; (b) Area 2 is a nanohole array of the same size, with a diameter of 300 nm, the period is 600 nm.

4.3.3 Theoretical Analysis of the Silanization Reaction

The silanization reaction was conducted in a sealed container with a mixture of 3-aminopropyl triethoxysilane (APTES) and ethanol. To guarantee the success of the subsequent assembly experiment, it was essential to verify the outcome of the silanization reaction. At that point, three samples were prepared, all of them on Si substrates, as illustrated in **Figure 4.5.** Sample 1 was treated with UV irradiation as a reference sample, and samples 2 and 3 were subjected to plasma O_2 and silanization reactions. The efficacy of the silanization reaction was assessed by measuring the contact angle of the three samples. For sample 1 without silanization, the contact angle of the surface was 4.31°. Following the silanization reaction, samples 2 and 3 exhibited contact angles of 62.60° and 62.63°, respectively. This align with the results obtained amino silanes reported in **[155]**. Taking these into account, we considered the silanization process as successful, this is a crucial step for the subsequent assembly experiment.





3-aminopropyltriethoxysilane

	Si+UV Light	Si+UV Light+silanization reaction[soak the sample in a mixture of ethanol(40mL) and APTES(80μL) for 3 hours]	
Sample	1	2	3
Contact angle (θc)	4.31	62.60	62.63
Surface free energy		46.14 mN/m Part dispersive: 31.41 Part polarize: 14.72	46.89 mN/m Part dispersive: 32.76 Part polarize: 14.13

Figure 4.5: The contact angle measurement of Si substrate before and after the Si silanization reaction.

In the broader context of the study, the successful silanization reaction represents a foundational step in ensuring the reliability of the subsequent experiments. By confirming the chemical modification of the substrate, this analysis provides a robust basis for exploring the interactions between the silanized substrate and Si nanoparticles, which will be key to understanding and optimizing the assembly process. Additionally, this method could be extended to other substrates or functionalization chemistries, broadening its applicability in nanomaterial assembly and surface engineering.

4.3.4 The Assembly Process and Result Analysis of Si Nanoparticles

Next, we will deliver into the use of a microfluidic technique device, termed Smart Force, for assembling Si NPs on a nanopatterned Si substrate. As shown in **Figure 4.6 (a)**, during the Si NP assembly process in the Smart Force device, temperature and airflow control plays a pivotal role. It induces convection in the receding liquid due to evaporation, which in turn brings the suspended Si NPs closer to the air-liquid interface.

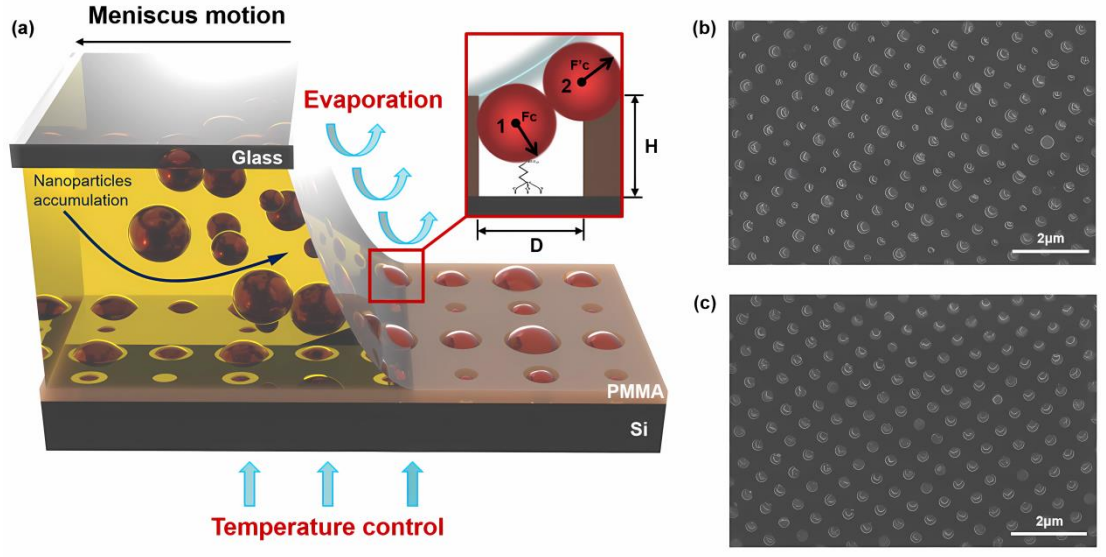


Figure 4.6: NP assembly. (a) Schematic diagram of capillary force assisted Si NP assembly process. SEM micrograph of a randomly selected assembly (b) area 1 and (c) area 2 showing the deposition of single NPs.

This interface area, known as the accumulation zone, is characterized by a high concentration of Si NPs. Starting directly at the air-liquid interface in contact with the template, Si NPs in the accumulation zone are deposited into the nanohole arrays on the substrate. This deposition is predominantly driven by capillary forces. Furthermore, the rate and size of the accumulation zone, formed due to evaporation, can be modulated by adjusting the temperature and airflow in the microfluidic channel. For our experiment, we set the temperature at 35.6℃ and maintained an airflow of 50.2 mL/min. As mentioned previously, we achieved optimal template wetting conditions, characterized by a retreating contact angle close to 62°, by silanizing the surface of the nanopatterned substrate. The assembly process was completed after approximately one day. The above necessary conditions will ensure that we can achieve an excellent assembly result.

As shown in the detailed picture in **Figure 4.6. (a),** the meniscus exerts a capillary force F_C perpendicular to the meniscus itself on nanoparticle 1, thus pushing the Si nanoparticles to enter the nanohole array on the substrate surface while the meniscus moves towards the end of the trap. Meanwhile, part of the F_C force is transferred to nanoparticle 2 behind, causing the upward force F'_C to push nanoparticle 2 out of the trap. Thus, only one particle is deposited in one trap. Based on the completion of this series of assembly processes, we initially characterized our assembly results using SEM. As illustrated in **Figure 4.6. (b) and (c)**, which is an SEM micrograph of a randomly selected assembly area 1 and area 2, we observed the deposition of single NP into the PMMA matrix. We can clearly see the deposition of Si NP in the corresponding nanohole arrays on the substrate, with the filling rate being close to 99%.

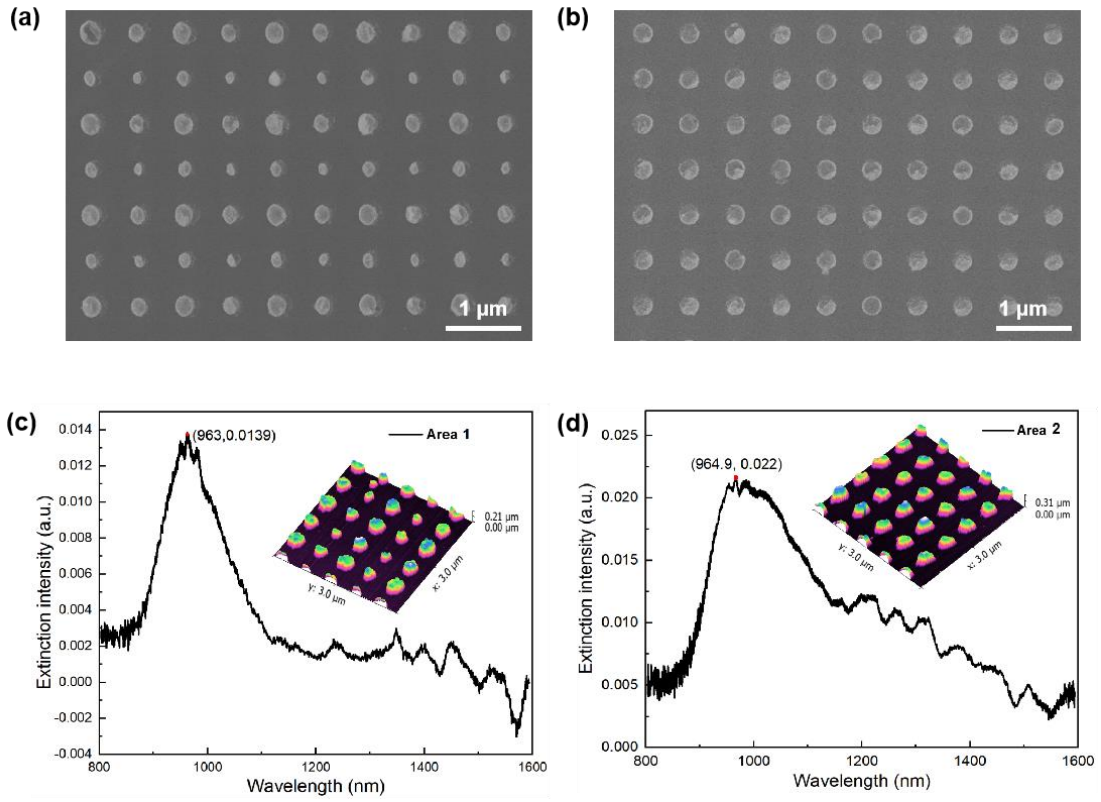


Figure 4.7: SEM micrograph of a randomly selected assembly of (a) area 1 and (b) area 2 showing the deposition of single NPs after remove PMMA. (c) Extinction spectrum of area 1 assembled by SmartForce after removing PMMA. The inset picture is the corresponding AFM image for this area. (d) Extinction spectrum of area 2 assembled by SmartForce after removing PMMA. The inset picture is the corresponding AFM image for this area.

To obtain better optical properties, it was necessary to remove the PMMA matrix arrays while retaining the Si nanoparticles on the substrate. We soaked the sample in acetone for 3 hours to achieve this, the results of this process are displayed in **Figure 4.7 (a) and (b).** The SEM micrographs of randomly selected areas show the single NPs deposited after removed PMMA. The AFM image in **Figure 4.7 (c)** inset confirms the successful assembly in area 1, showcasing the precision of our method. Additionally, the inset of **Figure 4.7 (d)** provides a clear AFM image of the assembled structure in area 2. These images collectively validate the effectiveness and reliability of our assembly method, demonstrating that the Si nanoparticles remain

firmly attached to the substrate even after PMMA removal. Furthermore, initial optical transmission measurements for both areas 1 and 2, as illustrated in **Figures 4.7 (c) and (d)**, reveal optical resonance in the Near-Infrared (NIR) range, indicating the potential applications of our method in optical devices.

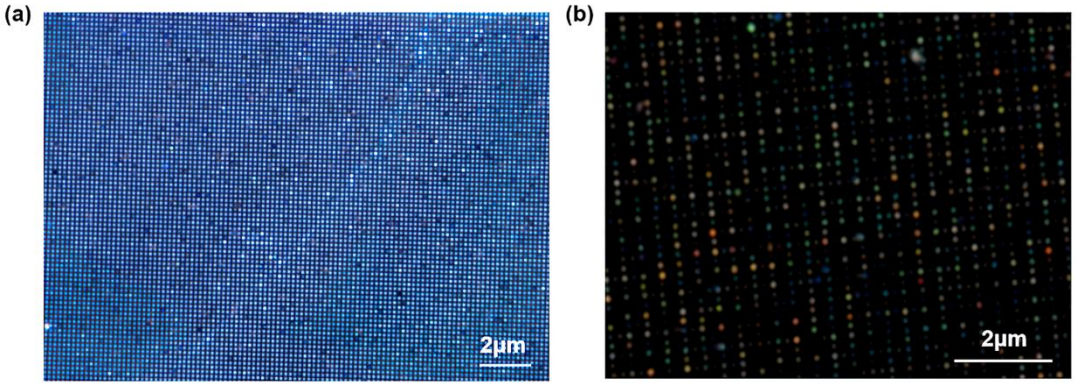


Figure 4.8: Dark-field microscope image of assembly Si nanoparticles in a nanopatterned substrate (a) with PMMA matrix (b) without PMMA matrix.

At the same time, in addition to the SEM analysis, we also examined the assembly results using a dark-field microscope. The structure of the PMMA matrix is shown in **Figure 4.8. (a)**, while **Figure 4.8. (b)** displays the assembly results after the removal of PMMA. These dark-field microscope images provide a different perspective on the assembly results and are complementary to the findings shown in **Figures 4.7 (a) and (b)**. The comparison of these images offers a comprehensive view of the successful attachment of Si nanoparticles to the substrate and the effectiveness of the PMMA removal process. The silanization reaction, as previously discussed, played a pivotal role in ensuring the stability of the Si nanoparticles during the PMMA removal, which is evident in the microscopy results.

To take our analysis a step further, we measured the average size of nanoparticles on the drawing containing 4 types of holes (150 nm, 200 nm, 250 nm, and 300 nm) and the corresponding RGB colors. The results are shown in **Figure 4.9**. **Figure 4.9(a)** shows the area on which we performed the analysis. **Figure 4.9(b)** shows the results for the size of nanoparticles immobilized on each pattern. The average sizes are

151nm ± 20nm, 197nm ± 15nm, 236nm ± 10nm and 288nm ± 14nm, with an overlap close to zero for each nanoparticle size. **Figure 4.9(c)** corresponds to the dark-field microscopy image of the SEM image shown in **Figure 4.9(a)**. In the dark-field image, the nanoparticles in the four different holes exhibit distinct color highlights, which are related to their size and scattering light characteristics. Through optical imaging, the distribution and optical responses of the nanoparticles in the holes can be intuitively observed. Next, we studied the corresponding RGB colors for the four hole sizes. **Figure 4.9(d)** shows the corresponding colors. We see a range of scattered colors from pink to blue as a function of hole size.

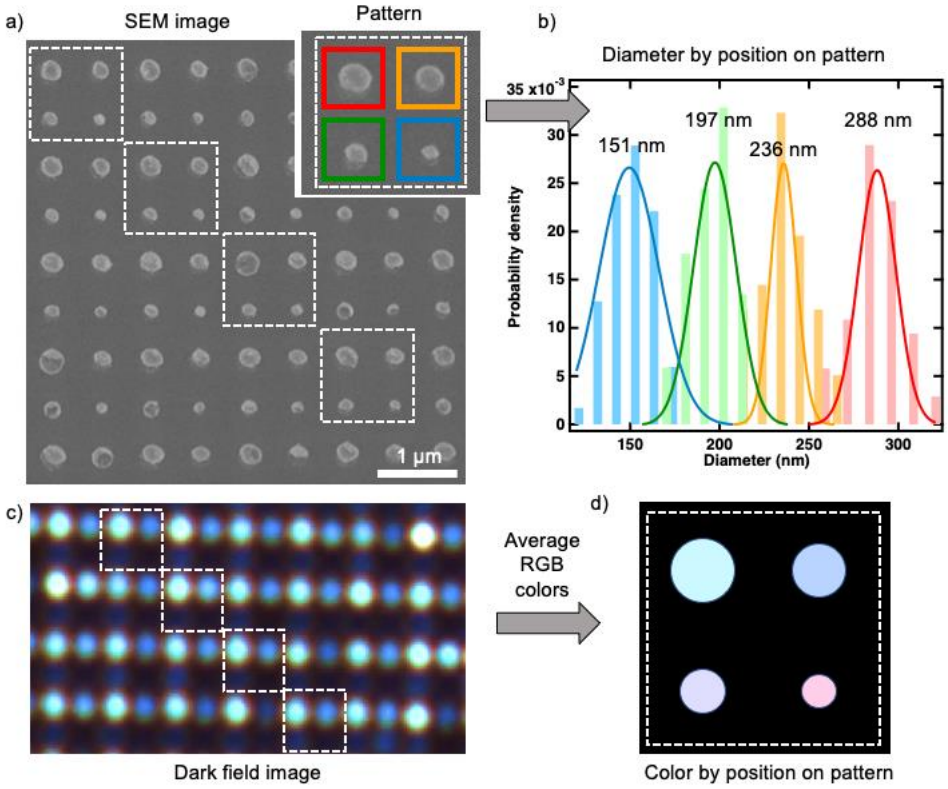


Figure 4.9: (a) Zoom image on SEM image of the pattern made from 4 different sizes of holes. (b) Histograms of the diameter of the Si NPs trapped on the 4 different holes. (c) Corresponding Dark field image of the SEM image presented on (a). (d) Schematic representation of the RGB colors.

This demonstrates the capture efficiency and optical properties of Si nanoparticles in patterned substrates with different hole diameters through a combination of SEM and dark-field microscopy techniques, along with statistical analysis. The SEM images

provide structural and particle size distribution information, while the dark-field images further reveal the optical properties of the nanoparticles. This multidimensional characterization method validates the ability to selectively capture Si nanoparticles by adjusting the hole diameters and highlights the color variation characteristics of nanoparticles of different sizes through optical analysis. It provides a reliable data foundation for subsequent studies on optical applications.

This study systematically developed a comprehensive approach for preparing, assembling, and characterizing silicon nanoparticles (Si NPs) on nanopatterned substrates, demonstrating their structural and optical properties. Using the cost-effective kitchen blender method, Si NPs with a uniform size range (45–220 nm) and high stability (-33.5 mV zeta potential) were produced by optimizing the Si-to-DI water ratio. Nanopatterned substrates were fabricated using electron beam lithography, and silanization treatment with APTES ensured chemical stability for nanoparticle attachment. Through a capillary force-assisted assembly process in a microfluidic device, Si NPs achieved near-perfect filling rates (~99%) in nanohole arrays. SEM and dark-field microscopy confirmed precise deposition and strong retention of Si NPs after PMMA removal, while extinction spectroscopy and dark-field imaging revealed distinct optical resonances in the Near-Infrared (NIR) range, correlating particle size with scattering behavior and RGB color variations. This work provides a scalable, precise, and versatile framework for nanophotonics and optical sensing applications.

4.4 Auxiliary Analysis of the Reference Experiment

In addition to analyzing the successful assembly, we also examined failed assembly samples to better understand the key factors required for successful assembly. **Figures 4.10 (a) and (d)** depict instances where no nanoparticles were present in the nanohole arrays. Notably, as illustrated in **Figures 4.10 (b) and (e)**, a 3-hour soak in acetone resulted in no visible nanoparticles, aligning with the AFM images in **Figures 4.10 (c) and (f)**.

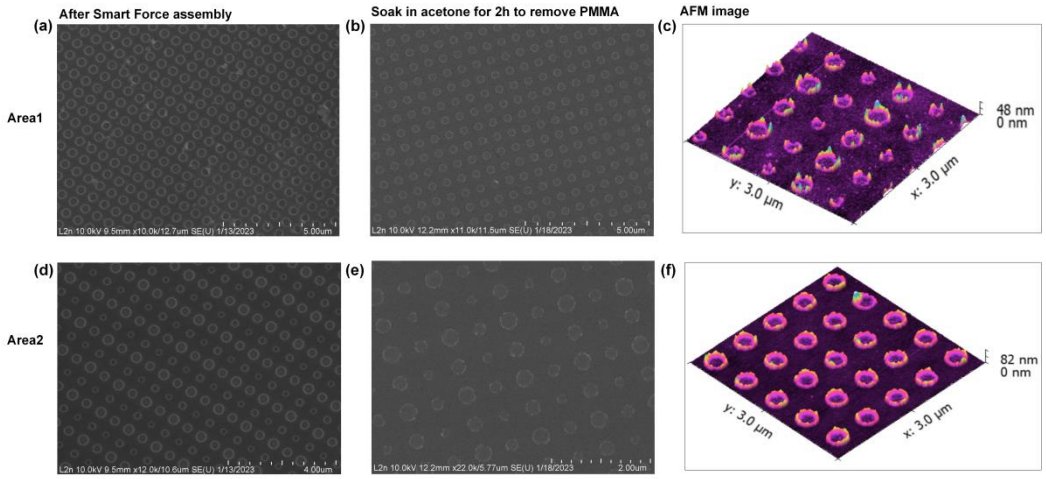


Figure 4.10: SEM and AFM images show Si nanoparticle (NP) assembly in two random areas of reference sample 1. (a, d) show NPs deposited with PMMA; (b, e) show the same areas after PMMA removal. (c, f) are AFM images confirming the NP arrangement in both areas.

These AFM images show only residual PMMA rings on the silicon substrate, with no nanoparticles present. Dark-field microscopy of these samples, shown in **Figures 4.11 (a) and (b)**, also revealed an absence of Si nanoparticles post-PMMA removal, in stark contrast to the successful results in **Figure 4.11 (b)**.

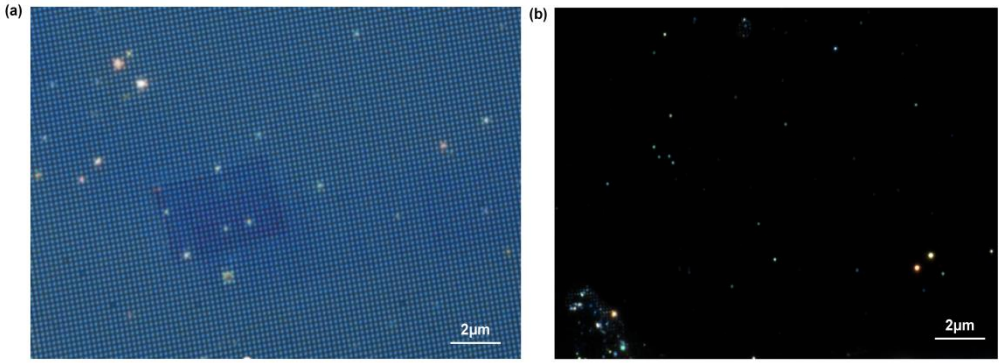


Figure 4.11: Dark field microscope image of reference sample assembly Si nanoparticles in a nanohole arrays (a) with PMMA matrix (b) without PMMA matrix.

In these failed experiments, a low concentration of Si nanoparticle solution without evaporation treatment was used, which hindered the formation of an accumulation zone near the meniscus. Interestingly, in cases where the Si nanoparticle concentration

was too high, excessive particles accumulated on the surface of the nanohole array structures, making characterization challenging.

To mitigate this, the sample was soaked in acetone for 3 hours and then subjected to ultrasonic cleaning. However, as shown in **Figure 4.12,** numerous Si nanoparticles remained on the substrate, underscoring the effectiveness of our silanization reaction in chemically bonding the Si nanoparticles to the substrate. These controlled experiments highlight the crucial role of the Si nanoparticle solution concentration in assembly, demonstrating that both excessively high and low concentrations can be detrimental to successful assembly.

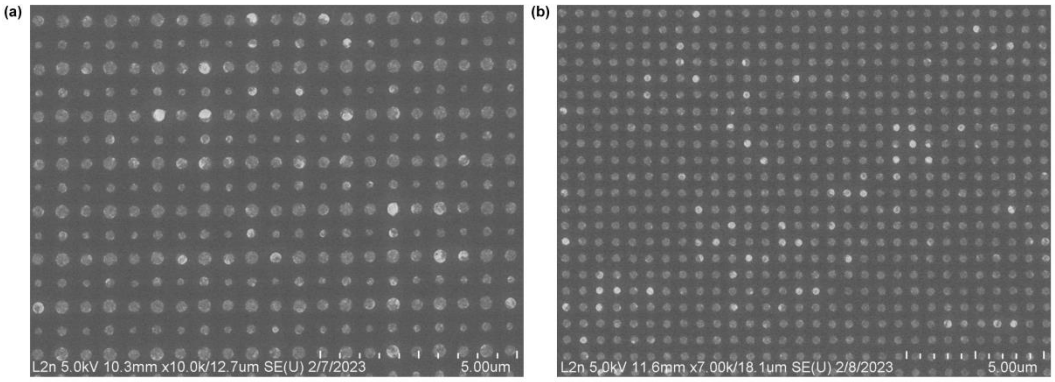


Figure 4.12: The SEM micrograph of a randomly selected assembly (a) area 1 and (b) area 2 of the reference sample 2 which was soking in acetone for 2h and soaked in acetone with treated by ultrasound.

In conclusion, the auxiliary analysis of the reference experiments provided critical insights into the factors influencing the success of Si nanoparticle (Si NP) assembly. The absence of Si NPs in failed samples emphasized the importance of maintaining an optimal nanoparticle solution concentration. Low concentrations hindered the formation of an accumulation zone near the meniscus, while excessively high concentrations led to particle overaccumulation, complicating characterization. The silanization reaction proved effective in ensuring the stable attachment of Si NPs to the substrate, even under challenging conditions, as evidenced by the residual nanoparticles after cleaning treatments. These findings highlight the necessity of

precise control over key parameters such as nanoparticle concentration and substrate preparation to achieve efficient and reliable nanoparticle assembly, further reinforcing the robustness of the proposed methodology for nanofabrication and its potential for optical applications.

4.5 FDTD Lumerical Simulations Results

"FDTD Lumerical simulations" refers to simulations conducted using the Finite-Difference Time-Domain (FDTD) method in Lumerical**[156-157]**. This is a specialized numerical analysis technique used to solve problems related to electromagnetic fields in both time and space, commonly employed for calculating complex scenarios of light-matter interactions. Lumerical is the name of a series of simulation software developed by Lumerical Solutions, Inc. in Canada, which are widely used in the fields of photonics, electronics, and nanotechnology for simulating and analyzing the propagation, scattering, absorption, and emission of light waves in different media.

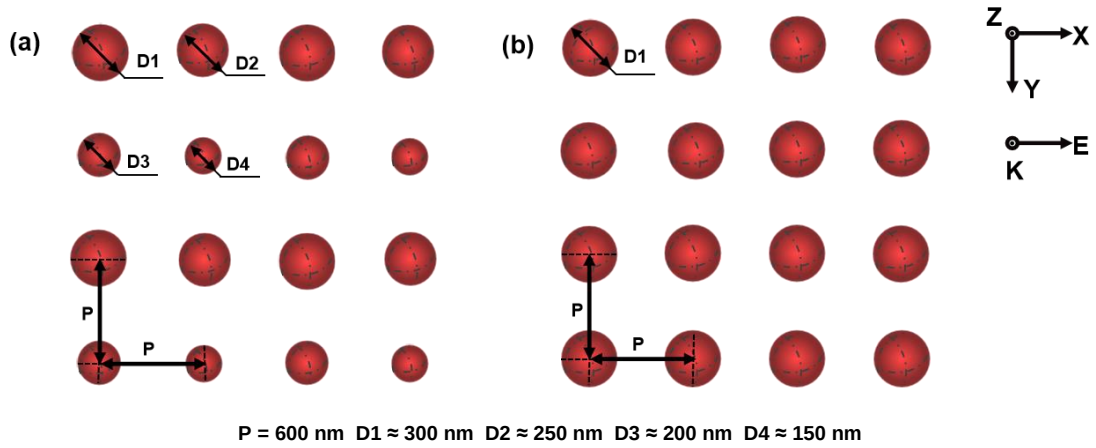


Figure 4.13: Schematic view of the considered metasurface, composed of nanospheres, arranged in a square lattice (Here present two different size designs), and definition of basic parameters. The metasurface is irradiated by FDTD sources and a plane monochromatic light wave at normal incidence.

FDTD (Finite-Difference Time-Domain) Lumerical simulations have been performed to analyse the optical response of our assembled structures. **Figure 4.13** presents the schematic representations of the considered metasurfaces, i.e. area 1 (left) and 2 (right) respectively. The incident electric field E is parallel to x and propagates along z. The pitch of the array is P=600 nm along both directions x and y. The diameter of the hole in area 1, a pixel is defined by four holes with four different diameters D1 = 300 nm, D2 = 250 nm, D3 = 200 nm, and finally D4 = 150 nm. Area 2 is defined to be 300 nm.

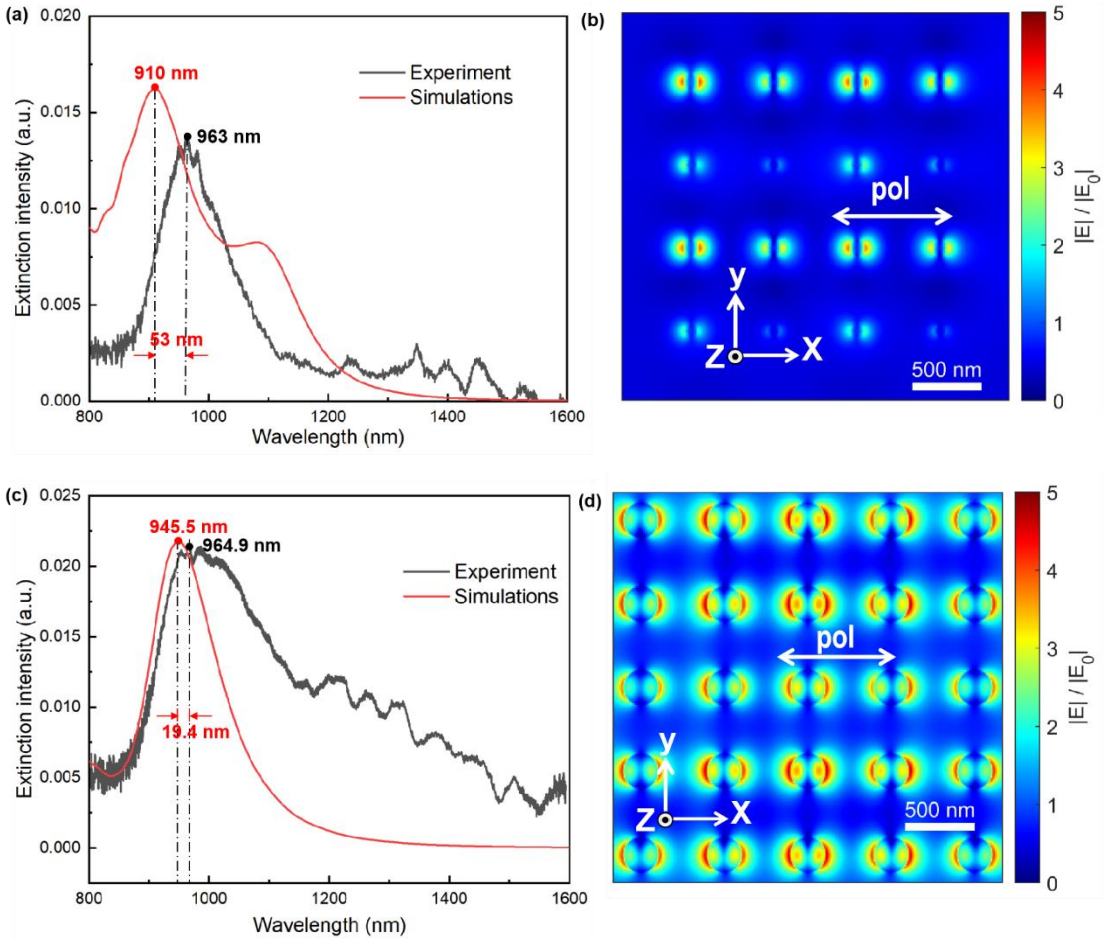


Figure 4.14: (a) Extinction spectra of the metasurface in assembly area 1. (b) Normalized electric field modulus maps for area 1 lattice periods in the bottom direction. λ = 963 nm. (c) Extinction spectra of the metasurface in assembly area 2. (d) Normalized electric field modulus maps for area 2 lattice periods in center cross-section, λ = 964.9 nm.

In our research, we utilized FDTD Lumerical, a commercial software, to analyze the electric and magnetic fields and the extinction spectrum of a system comprising spherical Si nanoparticles. The extinction spectrum was particularly focused on assessing optical resonance in the Near-Infrared (NIR) range, which extends from about 800 nm to 1600 nm. Such resonance is crucial due to its broad applications across sensing and spectroscopy, photonics and optoelectronics, thermal management and imaging, and security and counterfeit detection.

Figure 4.14 (a) presents the extinction spectrum for assembly area 1, where the experimental results are plotted as a black curve, and the corresponding FDTD simulation results are depicted in red. Notably, the simulation result exhibits a slight blue shift relative to the experiment. This shift may be attributed to two primary factors: the incomplete removal of PMMA during the experiment, as suggested by **Figure 4.10**, and the disparity between the simulated perfect spherical Si nanoparticles shape and size and the irregular shapes and size distribution (see **Figure 4.9b**) observed in the experiment. Despite these differences, the experimental and simulation curves are in quite good agreement. The normalized electric field modulus maps in **Figure 4.14 (b)** reveal the dipolar resonance of the Si nanoparticles at an incident wavelength of 963 nm for lattice periods in area 1, demonstrating the ability of the simulations to capture these resonant effects.

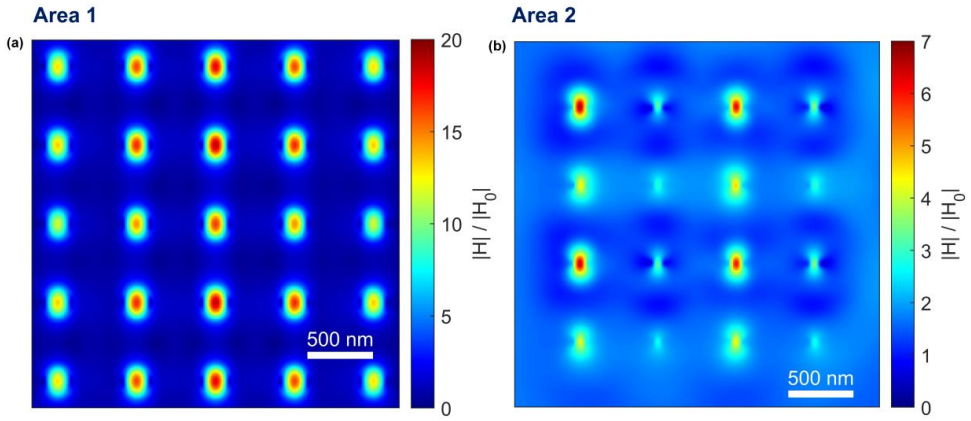


Figure 4.15: Normalized magnetic field modulus maps for (a) area 1 and (b) area 2 lattice periods. The wavelengths of the incident light were 964.9 nm and 963 nm, respectively.

The extinction spectrum for assembly area 2 is shown in **Figure 4.14 (c)**, where the experimental (black curve) and simulation (red curve) results show a consistent difference with those from area 1, reinforcing our understanding of the discrepancies between the simulated and experimental conditions. Furthermore, **Figure 4.14 (d)** exhibits the normalized electric field modulus maps for area 2, also indicating the dipolar resonance within the Si nanoparticles at an incident wavelength of 964.9 nm for lattice periods in area 2. The normalized magnetic field modulus maps for the lattice periods in both areas are documented in **Figure 4.15**.

Overall, the optical measurements of extinction and the field modulus maps corroborate the presence of optical resonance in the NIR range, which has significant potential to advance various technological and scientific fields. The slight discrepancies observed between experimental and simulation results highlight the importance of refining simulation models to closely represent the complex physical geometries encountered in practical scenarios. Our findings thus underscore the critical role of NIR optical resonance and the need for ongoing research and development in this promising area.

4.6 Conclusions

This study successfully used microfluidic techniques to assemble Si nanoparticles into nanohole arrays and complex Einstein patterns on silicon substrates. A kitchen blender was creatively adapted to grind silicon blocks, producing a nanoparticle solution with uniform size and spherical shapes. The concentration of this solution was key to successful assembly. Silanization modified the substrate's wetting angle and bonded the Si nanoparticles to the surface, preventing particle loss during PMMA removal. The Smart Force device, with precise control of temperature and airflow, created a stable accumulation zone for nanoparticle deposition. The assembled structures remained intact for over two months, showing the reliability of the method. This approach allows for accurate nanoparticle positioning and reduced contamination, offering a promising route for advanced silicon surface patterning.

Chapter 5

Ball Milling Method and Assembly on ITO Glass Substrates

As described in **Chapter 4**, we attempted to prepare Si nanoparticles using a kitchen blender and obtained a colloidal Si nanoparticle solution with controllable size. Ultimately, we used microfluidic technology assisted by capillary forces to assemble Si nanoparticles on nanopatterned Si substrates, resulting in a full dielectric Si-based metasurface. However, we found that the method using a kitchen blender was influenced by various factors, such as the sharpness of the blender blades and the power of the blender, which affected the shape and size of the final Si nanoparticles. Therefore, in **Chapter 5,** we used the technique of milling Si powder with a ball mill to obtain a colloidal Si nanoparticle solution. The method of preparing Si nanoparticles with a ball mill is efficient and controllable, and is expected to be widely applied in the field of nanomaterial preparation. In this chapter, we mainly studied the effects of different grinding solvents on the experimental results and explored the possibility of assembling the prepared Si nanoparticle solution on nanopatterned glass substrates.

Chapter 5: Ball Milling Method and Assembly on ITO Glass Substrates

5.1 Introduction

Silicon nanoparticles have become a key component in nanoscience and nanoengineering due to their inherent properties, such as high energy capacity and excellent optical characteristics**[5]**. To date, many manufacturing and characterization techniques have been studied, and a range of applications utilizing them have been developed. Silicon is the second most abundant element on Earth, following oxygen. Its abundant presence and cost-effectiveness make it one of the most accessible inorganic materials. Over the past few decades, the global semiconductor-related industries have experienced rapid growth, highlighting the significant role of silicon. In recent technological advancements, a mainstream application of silicon is in the field of energy storage. Compared to graphite, silicon has a specific capacity over 10 times higher (4200 mAh/g, instead of 372 mAh/g)**[158]**. This makes it a primary candidate for high-capacity battery anode materials. Further research indicates that when the size of silicon particles is below 150 nm, they can alleviate the cracking issues that occur during repeated lithiation and delithiation processes **[159]**. Another major application lies in the optical domain. Silicon nanoparticles with a size range of 100 to 200 nm can be used in applications that exhibit structural colors due to Mie resonance **[160]**. When they are reduced to the order of 1 nm, they appear in the form of photonic materials, particularly quantum dots**[161]**. Interestingly, confinement effects suggest that the smaller these quantum dots are, the stronger their luminescent properties become.

The methods for preparing Si nanoparticles are diverse, encompassing chemistry, physics, and mechanical fields. First, chemical vapor deposition (CVD) and physical vapor deposition (PVD) as two major vapor deposition technologies, form Si nanoparticles under specific conditions through chemical reactions of silicon source

gases and the evaporation or sputtering of silicon materials, respectively**[162]**. The solution method provides two paths: the reaction of metal silicides with acids, or the hydrolysis and acidification of silicates, both of which can effectively generate Si nanoparticles at the nanoscale**[163-164]**. The laser ablation method utilizes laser energy to induce plasma generation on the surface of silicon targets, thus producing Si nanoparticles**[165]**. The thermal decomposition method involves the thermal decomposition of silicon compounds under the protection of an inert gas to produce nanoparticles**[166]**. The electrochemical deposition method causes Si nanoparticles to deposit and grow on the electrode surface under the action of an electric field**[167]**. The hydrothermal synthesis method uses hydrothermal reactions under high temperature and pressure to promote the generation of Si nanoparticles**[168]**. The sol-gel method converts silicon alkoxides into Si nanoparticles through hydrolysis and condensation, followed by heat treatment**[169-170]**. The microwave synthesis method uses the rapid and efficient characteristics of microwave heating to promote the synthesis of Si nanoparticles**[171]**. The flame synthesis method directly burns silicon source materials in a flame to generate nanoparticles**[172]**. Finally, the mechanical grinding method uses physical methods, such as ball milling or stirring, to grind Si powder or SiO_2 powder into nanoscale particle solutions**[173-174]**. These methods each have their own characteristics and are suitable for different preparation needs and application scenarios.

In this chapter, we used the ball mill method to prepare silicon nanoparticles (Si NPs), which is simple, cost-effective, and suitable for large-scale production. Compared to expensive methods like chemical vapor deposition, it offers low equipment and operational costs, high yield, and continuous production. By adjusting parameters such as speed, media, and time, we can control the size and shape of the nanoparticles. In **Chapter 5**, we tested different solvents for preparing Si nanoparticle solutions. Using ZrO2 balls instead of stainless steel avoided impurity contamination. With deionized water and ethanol, we achieved uniform dispersion. Centrifugation allowed

us to separate smaller Si nanoparticles from larger ones. These results provide valuable insights for future nanoparticle assembly research.

5.2 Experimental section

In this experiment, silicon nanoparticles (Si NPs) were prepared using a high-energy ball mill (Emax) with two types of milling balls and solvents, as shown in **Figure 5.1**. Silicon powder, high-purity DI water, and ethanol were used, along with 3 mm stainless steel balls (Inox) and 1 mm zirconia balls (ZrO_2). The ball mill was set to 500 rpm for 4 hours with temperature control to prevent overheating. After milling, the top 85% of the solution was extracted, refrigerated for 3 days, and allowed to settle for 1 day. Centrifugation was used to separate nanoparticles by size, and the solution was concentrated by heating. Finally, SEM and DLS were used to analyze the size distribution and morphology of the nanoparticles. This experiment studied the effect of milling ball types and solvents on Si nanoparticle characteristics, providing valuable data for further research.

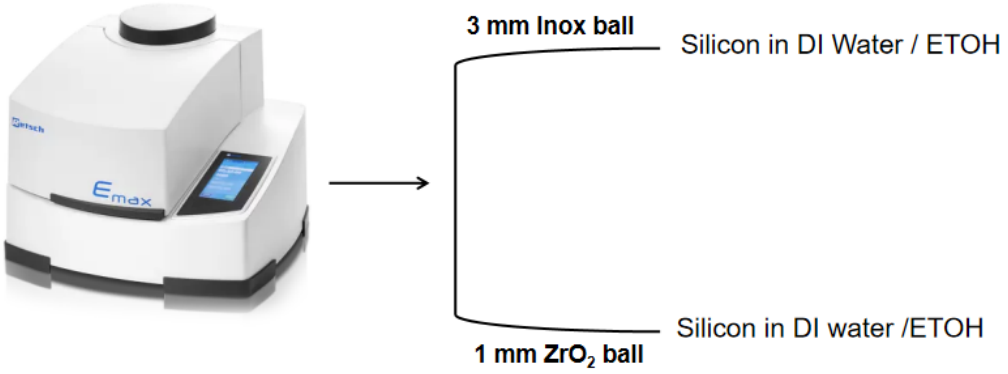


Figure 5.1: Schematic of the ball milling process for making silicon nanoparticles. A high-energy ball mill (Emax) is used with two types of balls: 3 mm stainless steel and 1 mm zirconia. Silicon powder is ground in either deionized water or ethanol. The type and size of the balls affect the size, shape, and dispersion of the resulting nanoparticles.

In this study, we employed EBL to fabricate nanopatterned substrates using ITO glass as the base material. Due to the limitations of the assembly instruments, the ITO glass

substrate size was restricted to 1 cm x 1 cm. The preparation process began with the ultrasonic cleaning of the ITO glass substrate. First, the substrate was cleaned in Decon 90 solvent for 5 minutes, followed by two 5-minute ultrasonic cleanings with DI water. Afterward, the substrate was dried on a hot plate and treated with a plasma cleaner for 4 minutes to remove any residual contaminants and ensure proper surface activation. Next, polymethyl methacrylate (PMMA) was spin-coated onto the cleaned ITO glass to form a uniform layer with a thickness of 150 nm, as illustrated in **Figure 5.2**. The PMMA layer serves as a resist material during the EBL process. Subsequently, the nanopatterned ITO glass substrate was created using EBL to define nanohole arrays. This process ensures the fabrication of high-precision patterns for use in further experiments. The complete EBL preparation workflow is summarized in **Figure 5.3(a)**, highlighting each critical step in the process. This methodology provides a robust platform for exploring nanoscale assembly and optical applications.

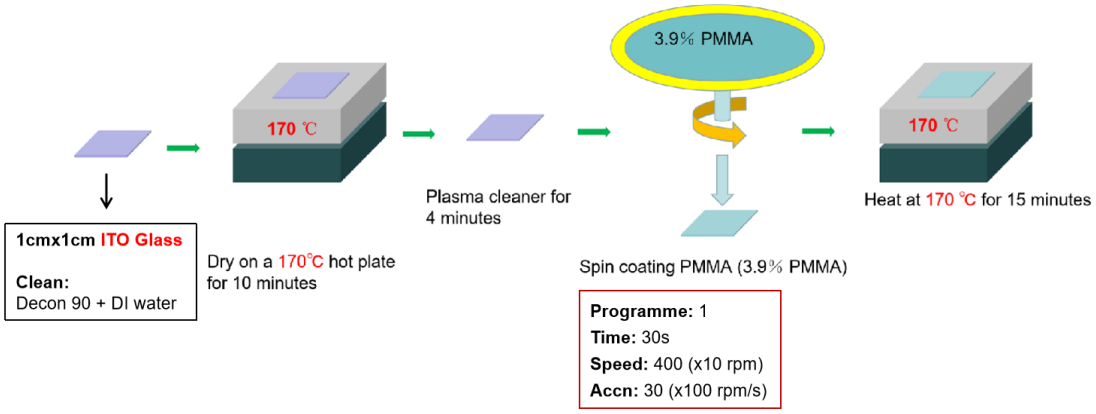


Figure 5.2: Schematic diagram of the spin coating process of PMMA.

Silanization is a versatile surface modification technique widely applied in fields such as biosensor fabrication, medical device coatings, and nanoparticle stabilization. By adjusting the type of silane, substrate material, or reaction conditions, specific surface characteristics can be achieved. In this study, silanization was essential for chemically bonding Si nanoparticles (Si NPs) to the nanopatterned ITO glass substrate, especially since the PMMA template required removal post-assembly. The silanization reaction utilized 3-aminopropyltriethoxysilane (APTES) and involved plasma processing for substrate activation. APTES undergoes hydrolysis to release ethanol, forming silanol

condensates that react with surface hydroxyl groups. The amino group (-NH_2) in APTES further enhances the bonding by interacting with the substrate's functional groups. Samples prepared via electron beam lithography (EBL) were immersed in a closed container with a mixture of APTES (80 µL) and ethanol (40 mL) for 3 hours to ensure complete silanization. This process established robust chemical bonds between the Si NPs and the ITO glass substrate, ensuring stability during subsequent experimental steps. The silanization reaction mechanism is illustrated in **Figure 5.3(b)**, highlighting the formation of silane-surface linkages critical to the success of the assembly process.

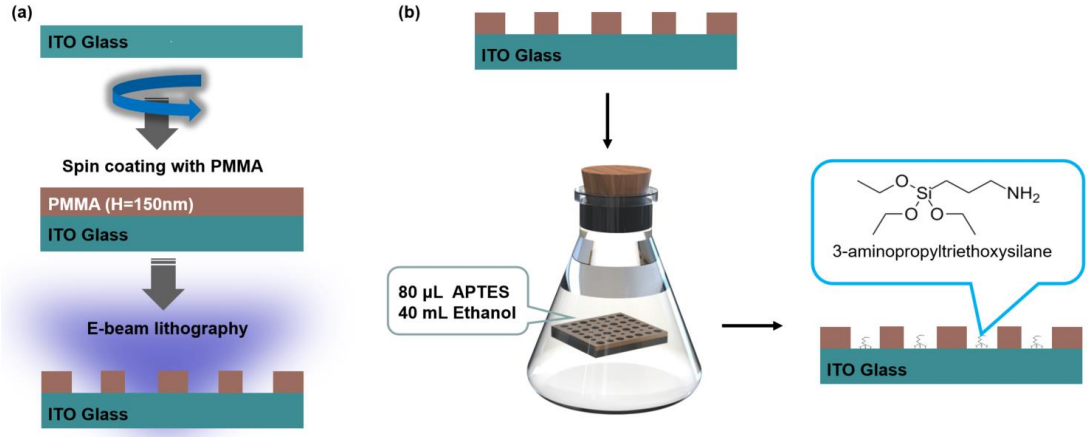


Figure 5.3: (a) Experiment design flow chart of fabricated nanopatterned ITO glass substrate by e-beam lithography. (b) Diagram of the silanization reaction process.

Microfluidic techniques allow precise control of fluids at the microscale and are widely used in biology, chemistry, and medicine. In this study, microfluidic technology was used for capillary-assisted assembly of silicon nanoparticles (Si NPs) to create metasurface structures on nanopatterned ITO glass substrates. The Smart Force device, based on microfluidic principles, controlled droplet movement and capillary forces, ensuring precise deposition of Si NPs. Parameters like temperature and airflow were optimized for uniform assembly. The experimental setup involved activating the Smart Force device, introducing a concentrated Si NP solution into a sealed microfluidic chamber, and ensuring even deposition onto the nanopatterned substrate. The preparation of Si NPs using ball milling and their assembly on ITO

glass substrates with capillary force-assisted techniques will be further detailed in later sections. In summary, the methods used in this study included high-energy ball milling to control Si NP size and morphology, EBL for precise nanohole array fabrication, silanization for strong particle-substrate bonding, and microfluidic techniques for capillary force-assisted assembly. These techniques provided a comprehensive approach to preparing and assembling Si NPs onto nanopatterned substrates.

5.3 Results and Discussion on preparation of Si NPs by ball mill

The preparation of Si nanoparticles (Si NPs) through ball milling has shown significant potential for producing uniform and well-defined nanostructures. In this section, we explore the effects of various parameters, including the choice of grinding balls (stainless steel or ZrO_2), grinding solvents (ethanol or deionized water), and milling conditions such as rotational speed and duration. The aim is to optimize the process for achieving high-quality Si nanoparticles with minimal contamination and aggregation. Through detailed characterization and analysis, we evaluate how these parameters influence the morphology, size distribution, and stability of the prepared nanoparticles.

5.3.1 Motivation for using a ball mill to prepare Si nanoparticles

In the previous chapter, we used a kitchen blender to prepare size-tunable silicon (Si) nanoparticles and successfully assembled them onto nanopatterned silicon substrates using capillary force-assisted microfluidic technology. However, we identified a few challenges during the preparation process. First, the condition of the blender blades is crucial, as high-speed rotation can cause damage to the blades due to silicon's hardness. This damage results in inconsistencies in nanoparticle size and shape, as shown in **Figures 5.4(a) and (b)**. Additionally, Si nanoparticles prepared with this method showed reduced stability over time, with aggregation occurring after several months, leading to poorer dispersion. To improve long-term stability, alternative preparation methods or stabilizing agents may be needed.

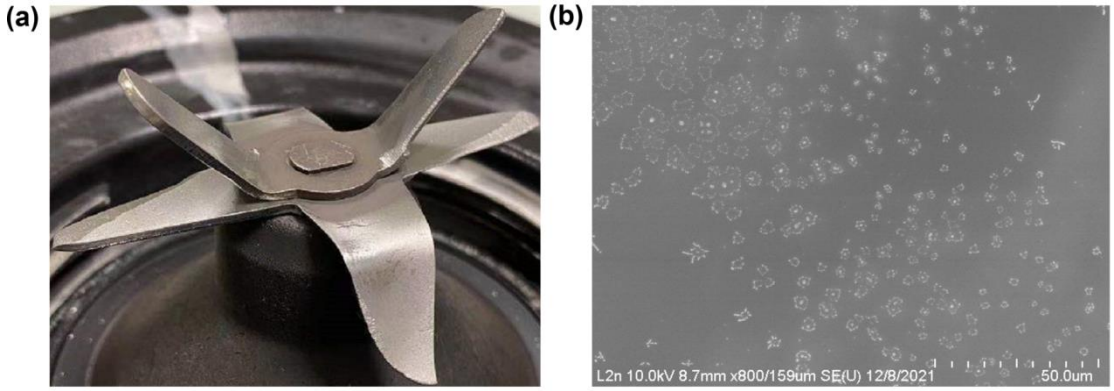


Figure 5.4: (a) Image of blender blades showing damage from grinding silicon blocks. (b) SEM image reveals uneven nanoparticle size and shape caused by blade defects, highlighting the need to maintain blade quality for consistent results.

When the size, shape, and stability of silicon (Si) nanoparticles are compromised, it affects assembly outcomes. **Figure 5.5** shows the process of filling Si nanoparticles into a nanoporous array on an ITO glass substrate using capillary force-assisted microfluidic technology. The nanopores, created with electron beam lithography, had diameters of 150 nm, 200 nm, 250 nm, and 300 nm. The goal was for Si nanoparticles to fill the corresponding pores based on their size. However, due to nanoparticle aggregation from prolonged storage, smaller particles filled the smaller pores, and multiple smaller particles aggregated in the larger pores, as seen in **Figures 5.5(a) and 5.5(b)**. This prevented precise, one-to-one placement of particles in the pores. The results show that nanoparticle quality is crucial for accurate assembly, and fresh solutions should be used to prevent aggregation and ensure better assembly performance.

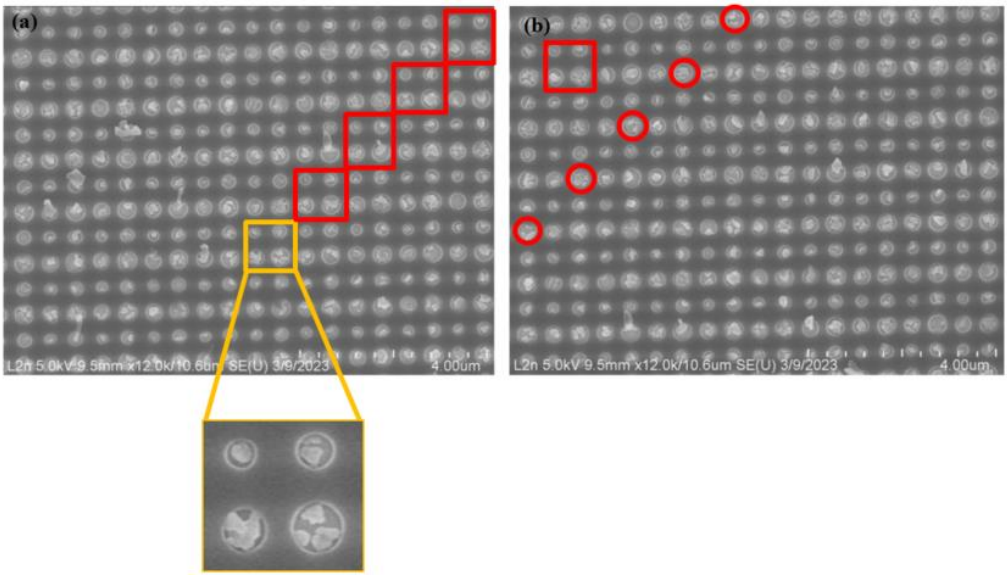


Figure 5.5. (a) SEM image shows Si nanoparticles assembled into a nanoporous array on an ITO glass using capillary microfluidic assembly. The inset displays nanoholes of 150 – 300 nm; smaller pores are mostly filled with single particles. (b) SEM image highlights aggregation of multiple small nanoparticles in larger pores (red circles), deviating from ideal one-to-one filling.

The quality of Si nanoparticle solutions prepared using a kitchen blender is affected by both the blender's blade sharpness and the solution's storage time. High rotational forces and interparticle collisions during grinding can cause irregular particle shapes, which affect their motion under capillary forces, leading to difficulty in entering nanopores during assembly. This mismatch in particle size and capillary forces can result in some particles failing to fit into the nanopores, while smaller particles tend to aggregate in certain pores. The irregular shapes and aggregation of nanoparticles, along with size variability, limit the precision of the kitchen blender method for nanoparticle assembly. To improve the process, we could add post-processing steps like centrifugation to improve particle uniformity and stability. Alternatively, adopting advanced synthesis techniques like laser ablation or ball milling could offer better control over particle size and shape. In conclusion, while the kitchen blender method is simple and cost-effective, its limitations should be addressed for high-precision applications, with further refinements or alternative techniques needed for consistent, high-quality nanoparticle solutions.

5.3.2 Fundamental Research on the Preparation of Si NPs via Ball Milling (Using Inox Balls as Grinding Media)

Studies have demonstrated that ball milling is an effective method for preparing Si nanoparticles with uniform size distribution and regular shapes**[107, 175]**. Unlike the kitchen blender method, ball milling eliminates the issue of blade wear, which can lead to inconsistencies in particle shape. The literature further indicates that the choice of grinding material, type of grinding solvent, rotational speed, and grinding duration significantly influence the size and morphology of the Si nanoparticles produced. To investigate the optimal preparation parameters and conditions, we utilized an Emax ball mill. Two types of grinding solvents were tested: 30 mL of deionized (DI) water and 30 mL of ethanol (ETOH), to observe how solvent type affects the colloidal Si nanoparticle solution. For consistency, 1 g of Si lumps and 3 mm Inox balls were used as grinding materials, with the grinding rate set to 2000 rpm. As illustrated in **Figure 5.6**, 60 stainless steel balls (3 mm in diameter), 1 g of Si powder, and 30 mL of DI water were added to the grinding chamber. The samples were milled at 2000 rpm for varying durations—20, 30, 40, 50, and 60 minutes. As illustrated in **Figure 5.6b**, bubbles were observed in the milling suspensions collected under different grinding conditions. This phenomenon strongly suggests the generation of hydrogen gas during the ball milling process. The most plausible explanation is a redox reaction between freshly fractured silicon surfaces and water molecules in the deionized (DI) water medium. Under the high-energy mechanical impacts and frictional heating generated by the milling process, this reaction is significantly accelerated, leading to the simultaneous formation of a thin oxide layer on the particle surfaces and the release of molecular hydrogen (H_2). After milling, centrifugation was performed to obtain colloidal Si nanoparticle solutions with uniform size distribution, as shown in **Figure 5.6(c)**. SEM analysis of the Si nanoparticle solutions obtained at different grinding durations revealed a thin oxide-like film on the surface of the particles (**Figure 5.6(d)**). Beneath the cracks in this film, uniformly sized, nearly spherical Si nanoparticles were observed. This finding suggests that using DI water as a grinding

solvent resulted in partial oxidation of Si during the milling process. Consequently, DI water is unsuitable as a grinding solvent for ball-milling-based preparation of Si nanoparticles.

The oxide layer on Si nanoparticles is formed due to interactions between Si and DI water during grinding, where heat and energy from high-speed milling accelerate surface oxidation. This may affect the stability and performance of the nanoparticles in later applications. Ethanol, with its lower polarity, may provide a more inert environment, reducing oxidation and preserving particle integrity. Future experiments should explore how ethanol and other solvents impact nanoparticle morphology, size, and stability. Additionally, the properties of grinding materials, such as hardness and wear resistance, should be considered. In conclusion, while the ball-milling method is effective for producing uniform Si nanoparticles, the choice of solvent and milling conditions are crucial for ensuring high-quality results.

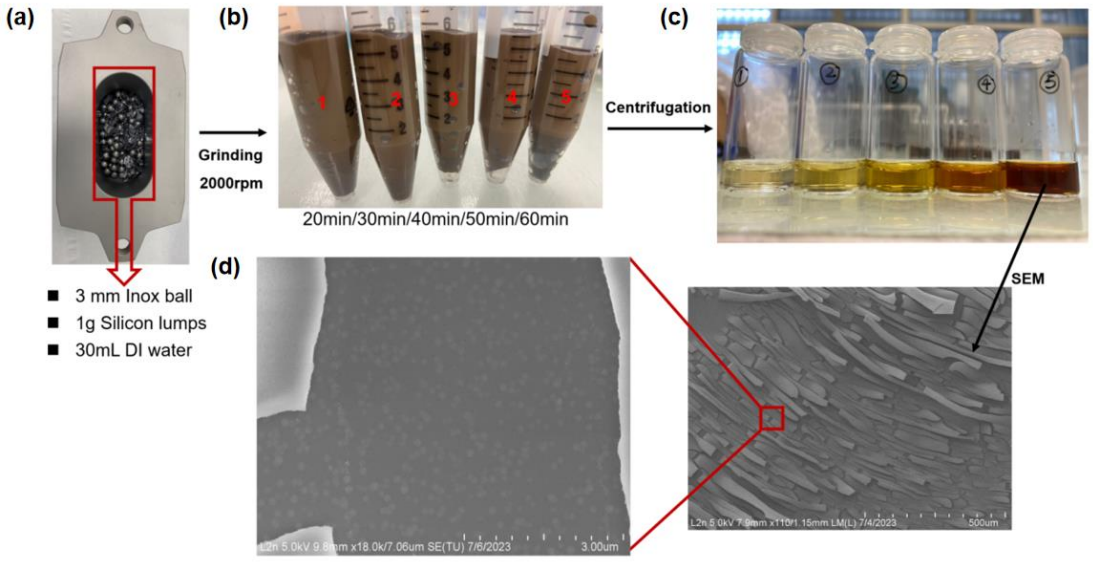


Figure 5.6: (a) Emax ball mill loaded with 60 stainless steel balls (3 mm), 1 g of silicon, and 30 mL DI water. (b) Colloidal solutions after 20–60 minutes of grinding at 2000 rpm show gradual changes. (c) Centrifuged samples reveal different sedimentation levels and clarity. (d) SEM images show uniformly distributed Si nanoparticles; inset reveals a thin oxide layer, indicating partial oxidation during milling.

Figure 5.7 presents the results of an experiment where 60 stainless steel balls (3 mm in diameter), 1 g of Si powder, and 30 mL of anhydrous ethanol (ETOH) were placed into a grinding chamber and milled at 2000 rpm for various durations: 20, 30, 40, 50, and 60 minutes. A significant amount of sediment was observed in the collected grinding solutions, as shown in **Figure 5.7(b)**. Suspecting the sediment to be ferrosilicon, we tested its magnetic properties using a magnet. This hypothesis was confirmed when the sediment was attracted to the magnet, as illustrated in the inset of test tube 5 in **Figure 5.7(b)**. From **Figure 5.7(b)**, it is evident that the volume of ferrosilicon sediment increases with grinding duration, particularly between 20 and 50 minutes. However, beyond 50 minutes, the sediment volume plateaus, with little to no further increase observed between 50 and 60 minutes. This suggests that under the experimental conditions—1 g of Si lumps, 60 stainless steel balls, a grinding rate of 2000 rpm, and 30 mL of ethanol—the grinding process reaches a saturation point after approximately 50 minutes. At this point, the preparation of Si nanoparticles is likely complete. To evaluate the Si nanoparticles produced, SEM analysis was performed on the upper layer of the solution in test tube 5 (**Figure 5.7(b)**). We observed that when anhydrous ethanol was used as the solvent, no bubble formation was detected during the milling process. This suggests that ethanol, due to its lower polarity and reduced reactivity, effectively suppresses such side reactions, thereby preserving the morphology and chemical integrity of the resulting Si nanoparticles. These findings highlight the critical influence of solvent selection on both the chemical stability and quality of ball-milled Si nanoparticle suspensions. The SEM results, shown in **Figure 5.7(c)**, reveal that the Si nanoparticles are nearly spherical, with a size distribution of approximately 150 nm. In a separate experiment, the same setup was used, and the mixture was milled continuously for 60 minutes. Once again, significant sedimentation was observed in the grinding solution, as shown in **Figure 5.7(d)**. SEM analysis of the upper layer of this solution (**Figure 5.7(e)**) indicated that the Si nanoparticles had transitioned to a cubic shape. Despite the extended grinding duration, ferrosilicon sediment continued to form, highlighting a recurring issue with this preparation method.

The ferrosilicon sediment is likely caused by wear on the stainless steel grinding balls and chamber, which introduces iron into the silicon during high-speed milling. This contamination reduces the purity of the Si nanoparticles and limits the method's scalability for high-purity applications. The plateau in ferrosilicon sediment volume after 50 minutes indicates that this is the optimal milling duration. The transition from spherical to cubic nanoparticles at 60 minutes suggests that prolonged milling changes particle morphology.

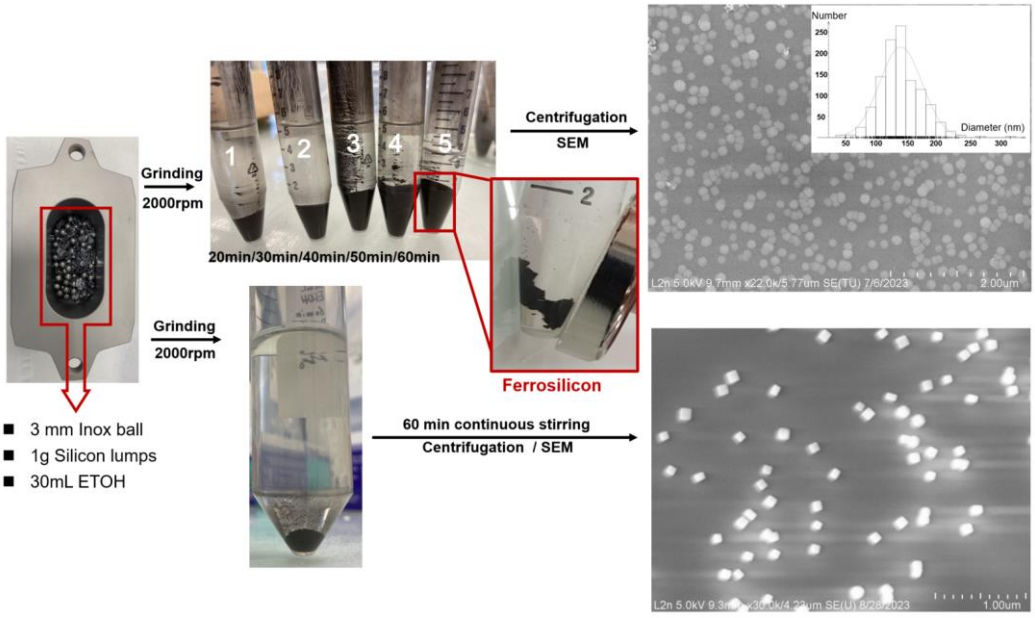


Figure 5.7: (a) Emax ball mill setup using 60 stainless steel balls (3 mm), 1 g Si powder, and 30 mL ethanol at 2000 rpm. (b) Samples after 20 – 60 minutes of grinding show increased sediment, confirmed as ferrosilicon (inset: magnetic test of tube 5). (c) SEM image of nanoparticles from the upper layer of tube 5 reveals nearly spherical Si NPs (~150 nm). (d) Solution after 60 minutes shows heavy sedimentation. (e) SEM image shows particles transitioning to cubic shapes after extended milling.

To reduce ferrosilicon contamination, alternative grinding materials like ZrO_2 or tungsten carbide should be used, and grinding time should be limited to 50 minutes. Additionally, lower rotational speeds, alternative solvents, or purification techniques like magnetic separation could improve nanoparticle quality and purity. Although ethanol helps minimize oxidation, further studies on solvent effects and ferrosilicon formation are needed. In conclusion, while the ball-milling process is effective for

producing Si nanoparticles, improving grinding parameters and using alternative materials are crucial for achieving higher-purity products.

5.3.3 Fundamental Research on the Preparation of Si NPs via Ball Milling (Using ZrO_2 Balls as Grinding Media)

We observed that Si nanoparticles prepared using ethanol (ETOH) as the grinding solvent exhibit more regular shapes compared to those prepared with deionized (DI) water, as illustrated in **Figure 5.7** and **Figure 5.6**, respectively. However, to eliminate the adverse effects of ferrosilicon contamination caused by the use of stainless steel (Inox) balls, which can affect the shape of the Si nanoparticles and complicate the purification of the colloidal solution, we decided to replace the Inox balls with ZrO_2 (zirconium oxide) grinding balls.

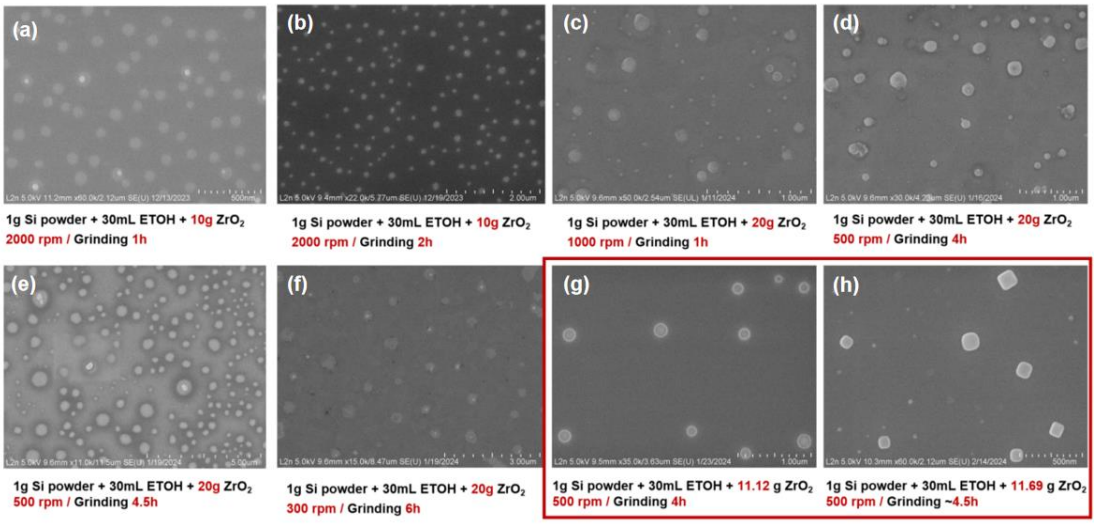


Figure 5.8: SEM images show the effects of different conditions using ZrO_2 balls for Si nanoparticle preparation: (a) Milling at 2000 rpm for 1 hour produces irregular particles; (b) Extending to 2 hours improves particle uniformity; (c) Reducing speed to 1000 rpm results in poor dispersion; (d) Milling at 500 rpm for 4 hours yields larger, more uniform particles; (e) Extending to 4.5 hours causes aggregation; (f) Further lowering to 300 rpm shows little improvement; (g, h) Optimal conditions—500 rpm for 4–4.5 hours—produce uniform cubic Si nanoparticles with narrow size distribution. ZrO_2 balls enable high-quality synthesis while minimizing contamination.

To optimize the experimental parameters for grinding Si powder with ZrO_2 balls, we conducted a series of trials, as shown in **Figure 5.8**. After iterative adjustments, we found that mixing 1 g of Si powder, 30 mL of anhydrous ethanol, and approximately 10 g of ZrO_2 grinding balls in the milling chamber, followed by grinding at a rotational speed of 500 rpm for four hours, produced the desired colloidal solution of Si nanoparticles with uniform size distribution. The results are depicted in **Figure 5.8(g) and 8(h)**, confirming the effectiveness of this optimized process.

In summary, replacing stainless steel grinding balls with ZrO_2 balls allowed us to determine the optimal grinding parameters. To further explore the impact of the grinding solvent, we conducted another experiment using deionized (DI) water as the solvent. Specifically, 1 g of Si powder, 30 mL of DI water, and approximately 10 g of ZrO_2 grinding balls were placed in the grinding chamber and milled at 500 rpm for four hours. As shown in **Figure 5.9**, severe aggregation was observed in the resulting solution. This finding indicates that, regardless of whether stainless steel or ZrO_2 grinding balls are used, DI water is unsuitable as a grinding solvent. The use of DI water leads to significant oxidation and aggregation of the Si nanoparticles, ultimately compromising the quality of the colloidal solution.

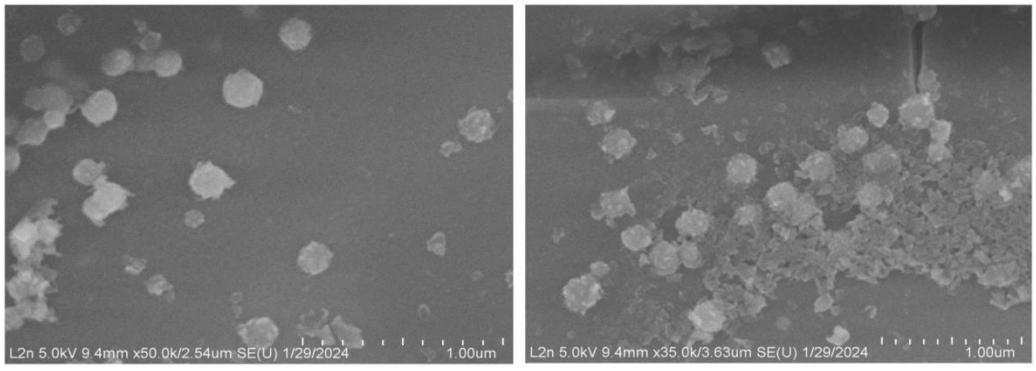


Figure 5.9: SEM images showing aggregation of Si nanoparticles milled with ZrO_2 balls in DI water, indicating poor dispersion due to oxidation.

5.3.4 Fundamental Research on the Preparation of Si NPs via Ball Milling (Using ZrO2 Grinding Balls to get Si Nanocubes)

Using the grinding parameters and reagents we optimized, we successfully prepared Si nanoparticles via ball milling. The preparation steps and workflow are illustrated in **Figure 5.10(a)**. Specifically, we combined 1 g of Si powder, 30 mL of anhydrous ethanol, and 11.4293 g of ZrO_2 grinding balls in the milling chamber and processed the mixture at 500 rpm for four hours. The resulting grinding solution was then collected for subsequent centrifugation. The solution was first centrifuged at a force of 10 kg, and the upper clear liquid was collected and centrifuged again at 3000 rcf for 5 minutes. The resulting supernatant was subjected to ultrasonic dispersion for 10 minutes to ensure uniformity. After the ultrasonic treatment, the Si nanoparticle solution was allowed to settle, and both the upper and lower fractions were analyzed via SEM. The SEM analysis revealed that the upper fraction contained Si nanoparticles with an average diameter of approximately 90 nm, as shown in **Figure 5.10(b)**, while the lower fraction contained cubic Si nanoparticles with an average diameter of approximately 190 nm, as shown in **Figure 5.10(c)**. These findings are consistent with the results obtained in our previous experiments using stainless steel grinding balls in an anhydrous ethanol solvent.

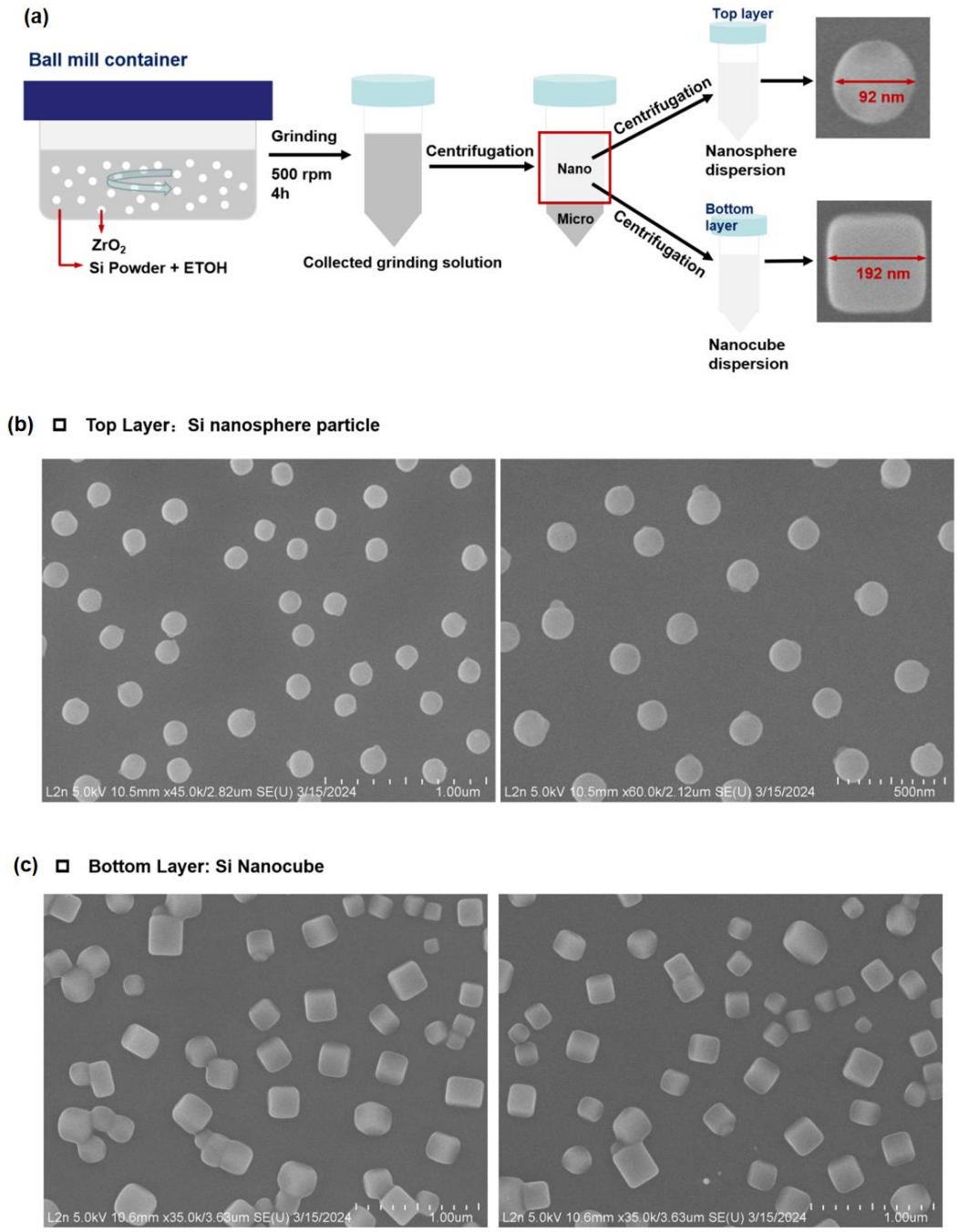


Figure 5.10: (a) Ball milling workflow using ZrO_2 balls and ethanol to prepare Si nanoparticles. (b) SEM image of top layer shows ~92 nm spherical Si nanoparticles. (c) SEM image of bottom layer shows ~192 nm cubic Si nanoparticles. Results confirm morphology control through optimized grinding.

The centrifugation and ultrasonic dispersion steps effectively separated Si nanoparticles into distinct size distributions, with smaller spherical particles in the upper fraction and larger cubic particles in the lower fraction. This demonstrates the

method's ability to control particle size for various applications. Using ZrO_2 grinding balls instead of stainless steel prevented ferrosilicon contamination, ensuring higher purity while maintaining similar particle size and morphology. The spherical and cubic nanoparticle shapes likely result from differences in mechanical stress or particle interactions during grinding.

The consistency of these results across experiments highlights the method's reproducibility. While the process is effective, further optimization of parameters like grinding duration, speed, and centrifugation could improve size distribution and morphology control. In conclusion, ZrO_2 grinding balls produce high-purity Si nanoparticles with well-defined size and morphology, and the developed workflow provides a reliable method for advanced applications. Further optimization could improve precision and scalability.

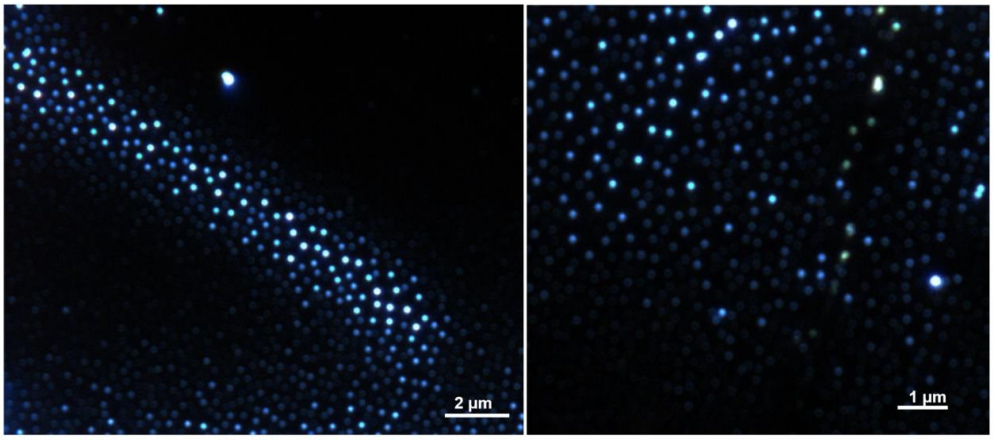


Figure 5.11: Dark-field microscopy images of Si nanoparticles prepared via the ball milling process.

We further characterized the Si nanoparticles using a dark-field microscope, as shown in **Figure 5.11**. The absence of large clusters and the homogeneous scattering contrast confirm that the ball milling and post-treatment protocols (e.g., centrifugation, solvent choice) were effective in producing discrete, well-dispersed Si NPs, suitable for optical characterization and potential device integration.

The dark-field microscopy analysis reinforces the conclusion that ball milling, under the optimized conditions, can reliably produce Si nanoparticles with regular and well-defined shapes. This additional characterization step underscores the quality and potential utility of the prepared nanoparticles in advanced technological applications. Further exploration of the structural uniformity across larger sample sets could provide deeper insights into process scalability and consistency.

Table 2 – Effects of Grinding Ball Type and Solvent on Silicon Nanoparticles

Solvent / Grinding Ball	Deionized Water (DI)	Anhydrous Ethanol (ETOH)
1 mm ZrO_2 ball	✖ Oxidation	✔Well-shaped Si NP
3 mm Inox ball	✖ Oxidation and Ferrosilicon	✖ Ferrosilicon

The results summarized in **Table 2** highlight the critical influence of both grinding ball type and solvent on the outcome of the silicon nanoparticle (Si NP) fabrication process. When 1 mm zirconia (ZrO_2) balls were used in anhydrous ethanol (ETOH), well-shaped Si nanoparticles were successfully obtained, indicating this condition is optimal for preserving particle morphology and preventing contamination. In contrast, the use of 3 mm stainless steel (Inox) balls led to the formation of ferrosilicon byproducts in both DI water and ethanol, due to possible abrasion and alloying effects. Moreover, oxidation was prominent in aqueous environments, particularly with ZrO_2 balls. These findings suggest that using smaller, inert grinding media in anhydrous conditions effectively minimizes unwanted reactions and promotes the formation of high-quality Si NPs.

5.4 Si NP Dispersion and Assembly in ETOH and DI Water

To facilitate the subsequent assembly of the prepared Si nanoparticles, it is essential to investigate the impact of the grinding solvent on the dispersion of Si nanoparticles in the solution. For this purpose, we used 1 g of Si powder, 30 mL of ethanol (ETOH), and 10 g of ZrO_2 grinding balls. The milling process was carried out at a rotational

speed of 500 rpm for approximately 4.5 hours. Afterward, the resulting mixture was subjected to centrifugation at a force of 10 kg for 5 minutes to extract the dispersed nanoparticle solution.

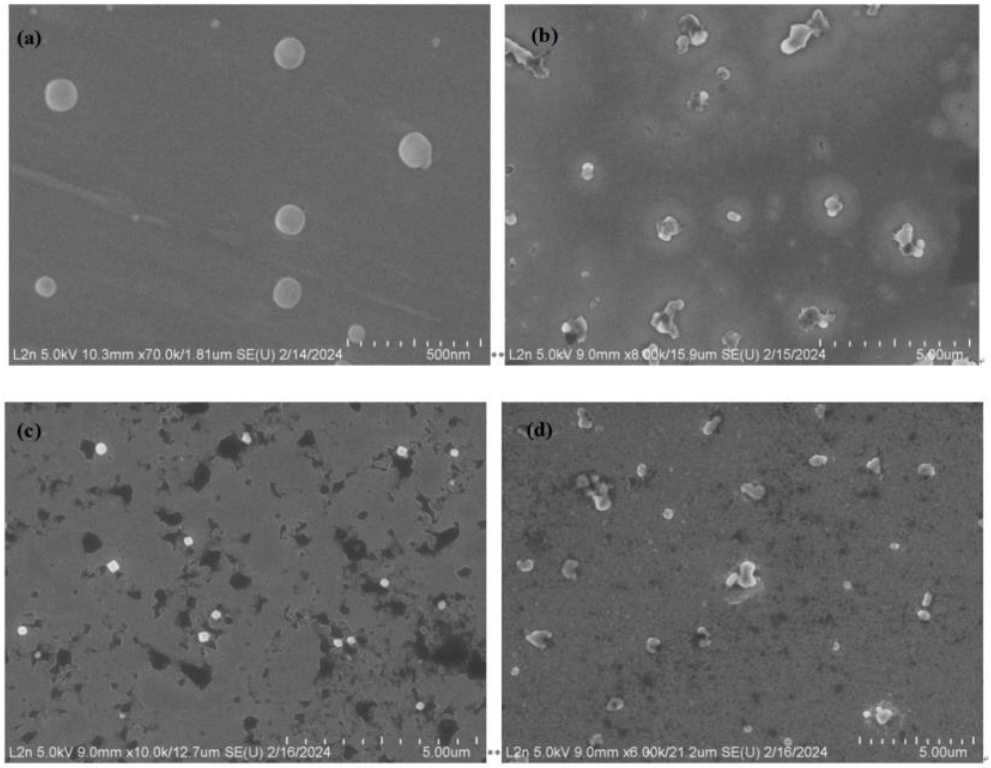


Figure 5.12: SEM images of Si nanoparticles under different solvent conditions: (a) In ethanol, particles are spherical and well-defined. (b) After full ethanol evaporation and DI water replacement, strong aggregation occurs. (c) Partial ethanol evaporation followed by DI water addition improves dispersion. (d) Some aggregation remains in the mixed solvent.

Figure 5.12(a) shows the morphology of Si nanoparticles in their initial solution, as characterized by SEM. The particles exhibit a regular, spherical shape with well-defined edges. Subsequently, the Si nanoparticle solution (using ethanol, ETOH, as the solvent) was placed on a heating platform at 80°C until the solvent completely evaporated. Deionized (DI) water was then added to the residue, and the solution was ultrasonicated to disperse the Si nanoparticles. SEM characterization of the resulting nanoparticles is shown in **Figure 5.12(b)**. Compared to **Figure 5.12(a)**, the particles' shape changed significantly, and aggregation was observed, indicating that complete

evaporation of ETOH and replacement with DI water led to the clustering of Si nanoparticles and a loss of their morphology. This negatively impacts their dispersion. To address this issue, we optimized the solvent evaporation process. Instead of complete evaporation, the Si nanoparticle solution was partially evaporated on the 80°C heating platform, and DI water was added before all the ETOH was removed. SEM characterization of the resulting nanoparticles is presented in **Figure 5.12(c)**. Compared to **Figure 5.12(b)**, the nanoparticles retained a more regular shape and were more evenly distributed, demonstrating that an ETOH/DI water mixture helps preserve the morphology and improves dispersion. However, some degree of aggregation still occurred, as highlighted in **Figure 5.12(d)**, emphasizing the need for precise tuning of the ETOH/DI water ratio to achieve effective separation and stabilization of Si nanoparticles. Next, we attempted to assemble the Si nanoparticle solution into nanopore arrays using capillary force-assisted microfluidic technology. A low-concentration Si nanoparticle solution in ETOH was used for assembly, with parameters set at T = 30.6°C and Q = 50.8 mL/min. After two assembly cycles, we were unable to precisely position the Si nanoparticles within the nanopore arrays, as illustrated in the SEM characterization in **Figure 5.13(a)**.

The transition from ETOH to DI water as the solvent significantly impacts the morphology and dispersion of Si nanoparticles. Complete replacement of ETOH with DI water leads to severe aggregation, disrupting the spherical shape and uniform distribution of the nanoparticles. In contrast, partial evaporation of ETOH and subsequent dilution with DI water preserves particle morphology and improves dispersion. The results demonstrate that ETOH/DI water mixtures offer a more stable environment for Si nanoparticles, minimizing aggregation and retaining shape. However, the presence of residual aggregation suggests that fine-tuning the solvent ratio is critical for achieving optimal dispersion and stability. Despite achieving a relatively well-dispersed Si nanoparticle solution, the inability to precisely position nanoparticles within the nanopore arrays highlights limitations in the assembly

process. Potential reasons could include insufficient particle stability in the solvent, suboptimal assembly parameters, or uneven particle distribution.

This study highlights the critical role of solvent composition in maintaining the morphology and dispersion of Si nanoparticles. While an ETOH/DI water mixture shows promise in addressing aggregation, further optimization is required for consistent results. Additionally, improvements in both solvent and assembly parameters are necessary to achieve precise nanoparticle positioning in nanopore arrays, which is essential for advanced nanofabrication applications.

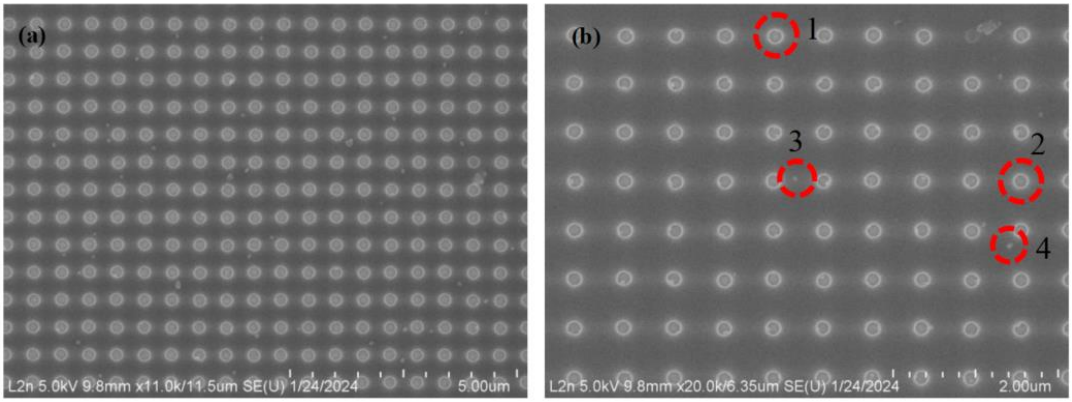


Figure 5.13: SEM images of Si nanoparticle assembly on nanopore arrays: (a) After two assembly cycles, many nanopores remain unfilled. (b) Close-up shows empty pores (Circles 1, 2) and misplaced nanoparticles outside the pores (Circles 3, 4). These issues are likely due to low particle concentration and suboptimal assembly conditions.

We observed that some Si nanoparticles were deposited outside the nanopores, failing to precisely align within the prepared nanopore arrays. A closer examination of the nanopore arrays using SEM, shown in **Figure 5.13(b)**, confirmed that certain nanopores remained unfilled, as indicated by marked regions Circle 1 and Circle 2. Additionally, some Si nanoparticles were deposited on the substrate outside the nanopores, as highlighted in Circle 3 and Circle 4. This suggests that the low concentration of Si nanoparticles in the solution may be a contributing factor. To address this, we increased the number of assembly cycles and adjusted the assembly conditions by reducing the ethanol evaporation rate. This was achieved by turning off

the temperature and airflow controls of the assembly equipment. **Figure 5.14(a)** shows the SEM characterization of the Si nanoparticle array after the third assembly cycle. However, even with these modifications, the filling efficiency did not improve significantly. Nanopores remained unfilled, and Si nanoparticles continued to deposit outside the pores, as seen in **Figure 5.14(b)**. Furthermore, in the red-marked regions of **Figure 5.14(a)**, we observed physical damage to the nanopore array.

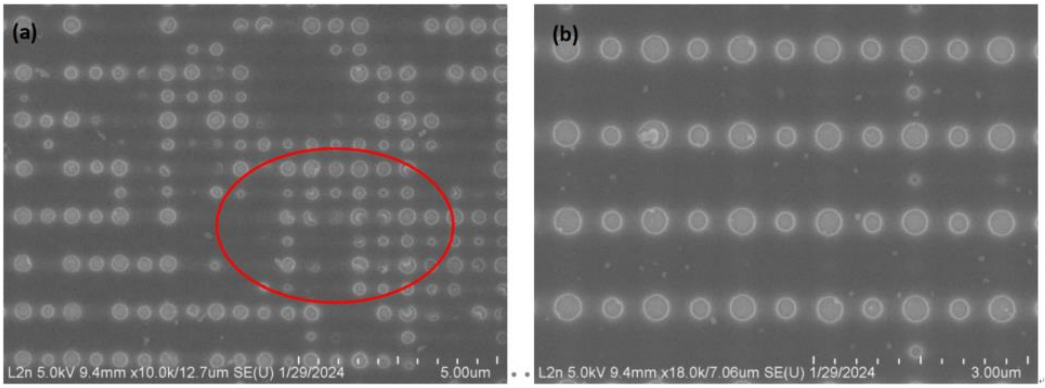


Figure 5.14: SEM images of Si nanoparticle assembly after the third cycle: (a) Red-marked area shows damage to the nanopore array, likely due to fast ethanol evaporation. (b) Zoomed-in view reveals many unfilled pores and misplaced nanoparticles. Repeating the assembly and using ethanol did not improve filling efficiency and caused substrate damage.

Our analysis suggests that the SmartForce assembly system is highly sensitive to solvent properties. Ethanol, with its high volatility, evaporates rapidly, making it challenging to control the assembly parameters effectively. Even with the temperature and airflow controls disabled, the results remained unsatisfactory, and the rapid evaporation caused damage to the nanopore arrays on the substrate. These experiments demonstrate that increasing the assembly cycles and using ethanol as the solvent did not improve the filling efficiency of Si nanoparticles into the nanopores. Consequently, we decided to try a high-concentration Si nanoparticle solution with an ethanol-DI water mixture as the solvent. The assembly parameters were set to T = 35.1° C and Q = 51 mL/min. The SEM characterization results, shown in Figure 5.15, revealed that the filling efficiency remained suboptimal. The assembly process not

only caused damage to the substrate but also led to significant aggregation of the Si nanoparticles.

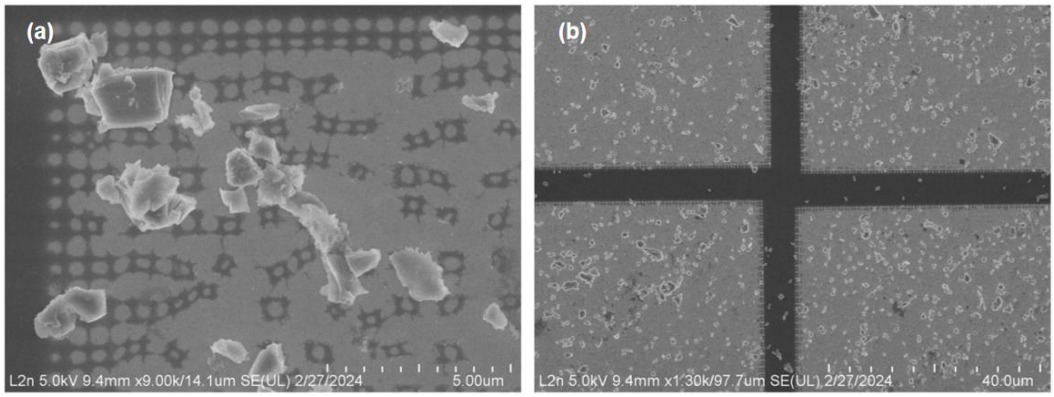


Figure 5.15: SEM images of Si nanoparticle assembly using a high-concentration ethanol – DI water mix: (a) Close-up shows strong particle aggregation and damaged nanopores. (b) Wider view reveals uneven particle distribution and surface damage.

Centrifugation and ultrasonic dispersion separated Si nanoparticles into different sizes, with smaller spherical particles in the upper fraction and larger cubic particles in the lower one. Using ZrO_2 grinding balls instead of stainless steel prevented contamination, ensuring higher purity and similar size distribution. The spherical and cubic shapes resulted from grinding stress and particle interactions. The method is reproducible, but further optimization of grinding time, speed, and centrifugation could improve size control. In conclusion, ZrO_2 grinding balls produce high-purity Si nanoparticles, and the process is reliable for advanced applications. Further adjustments could enhance precision and scalability.

The experiments highlight the challenges in achieving precise filling of Si nanoparticles into nanopore arrays. Both low- and high-concentration solutions failed to provide satisfactory results, and the use of ethanol as a solvent contributed to aggregation and substrate damage. Future work should focus on optimizing solvent composition, nanoparticle concentration, and assembly parameters to improve filling efficiency and substrate protection.

5.5 Conclusion

This chapter demonstrates the successful preparation of Si nanoparticles using the ball milling method with optimized conditions. We tested different grinding balls (stainless steel/ZrO_2) and solvents (deionized water/anhydrous ethanol) to evaluate their impact on nanoparticle quality. Stainless steel balls with deionized water caused oxidation, compromising quality. Ethanol produced uniform nanoparticles but resulted in ferrosilicon contamination. ZrO_2 balls eliminated this contamination, producing high-quality Si nanoparticles. The optimized conditions—grinding Si powder with ethanol and ZrO_2 balls—produced ~90 nm spherical and ~190 nm cubic nanoparticles. However, ethanol's high volatility made assembly difficult, causing rapid evaporation and physical damage. Using deionized water led to nanoparticle aggregation. These findings suggest that while the ball milling method produces uniform Si nanoparticles, the colloidal solutions face limitations in assembly due to instability. Future research should focus on alternative solvents, stabilizers, or assembly improvements to enhance precision.

Chapter 6

Si NPs Assembly on Complex Nano-Patterned Substrates

In this chapter, we compare the preparation methods for silicon nanoparticles (Si NPs) colloidal solutions using a kitchen blender and a ball mill, focusing on their assembly performance on nanopatterned silicon substrates. Si NPs from the kitchen blender show good size distribution, uniformity, and stable dispersion in deionized water. Combined with SmartForce microfluidic assembly, this method allows precise positioning of Si NPs onto electron beam lithography (EBL)-fabricated nanopatterned silicon substrates, achieving excellent results. In contrast, while ball milling also yields well-distributed Si NPs, the dispersion is limited to anhydrous ethanol, and the volatility and instability of ethanol hinder the assembly process.

After comparison, we chose the kitchen blender method for further studies to validate its applicability and assembly capability on complex-patterned substrates. Using SmartForce microfluidic technology, we successfully positioned Si NPs on these substrates. This approach not only provides uniformly sized nanoparticles but also enhances their applicability to various substrates. This study supports the design of silicon-based optical devices and demonstrates the potential of simple, cost-effective mechanical grinding methods for nanoparticle preparation and assembly.

Chapter 6: Si NPs Assembly on Complex Nano-Patterned Substrates

6.1 Introduction

Silicon nanoparticles (Si NPs), as a versatile functional nanomaterial, hold great potential in nanophotonics, nanoelectronics, and metasurface device fabrication. Their exceptional optical properties, high refractive index, and low loss make them ideal candidates for developing advanced all-dielectric optical devices. In our previous studies, we explored two mechanical grinding methods—kitchen blender and ball milling—for preparing size-uniform Si NPs colloidal solutions. By combining these methods with SmartForce microfluidic technology, we successfully achieved precise positioning of Si NPs on regularly patterned silicon substrates, laying a solid experimental foundation for applying Si NPs in complex nanophotonic devices.

The kitchen blender method is simple, low-cost, and produces uniformly sized Si NPs that disperse well in deionized water, making them suitable for microfluidic assembly with the SmartForce device. While it may cause some shape irregularities and equipment wear, it remains more practical than the ball milling method, which uses volatile ethanol and is less compatible with microfluidics. This chapter focuses on testing the kitchen blender method for assembling Si NPs onto complex nanopatterned silicon substrates. By adjusting temperature, flow rate, and evaporation in the microfluidic setup, the goal is to achieve precise assembly on irregular nanohole patterns. This approach broadens the method’s use in advanced optical and electronic nanodevice fabrication.

6.2 Experimental section

In this study, we developed a low-cost and efficient method to prepare and assemble silicon nanoparticles (Si NPs) on complex-patterned substrates. Si NPs were produced

using a kitchen blender, following Chaâbani et al.'s method mentioned before. Specifically, 10 g of high-purity silicon lumps were ground with 300 mL of deionized water in a Midea kitchen blender (six steel blades), operating in 3-minute intervals with 2-minute breaks for 2 hours. After grinding, the top solution was extracted, stored at 4 °C for three days, and centrifuged to collect uniformly sized NPs. This approach provided a simple and economical alternative to traditional synthesis equipment.

The nanopatterned substrates were created via electron beam lithography (EBL) on cleaned and plasma-treated n-type silicon wafers with a 300 nm SiO_2 layer and a 150 nm PMMA coating, as detailed in the previous chapter. To ensure strong bonding between the Si NPs and the substrate, a silanization step was carried out using APTES in ethanol for 3 hours, forming chemical bonds between particles and substrate.

For assembly, microfluidic capillary force-assisted techniques were used. The Si NP solution was introduced into a sealed Smart Force microfluidic device under controlled airflow and temperature. As the droplets evaporated, capillary forces guided the nanoparticles into the Einstein nanopattern. This integrated method allowed precise and stable NP assembly, offering a cost-effective route for fabricating complex metasurface structures.

6.3 Results and Discussion

6.3.1 Reasons for Choosing Kitchen Blender-Prepared Si NPs for Assembling Complex Metasurface Structures

Figure 6.1 illustrates the assembly performance of silicon nanoparticles (Si NPs) prepared using a kitchen blender and a ball mill on nanopatterned substrates with nanohole arrays. These results clearly highlight the advantages of Si NPs prepared with the kitchen blender in metasurface assembly and further underscore the limitations of Si NPs prepared via ball milling in similar applications. This conclusion

provides valuable experimental insights for the design and assembly of more complex metasurface structures.

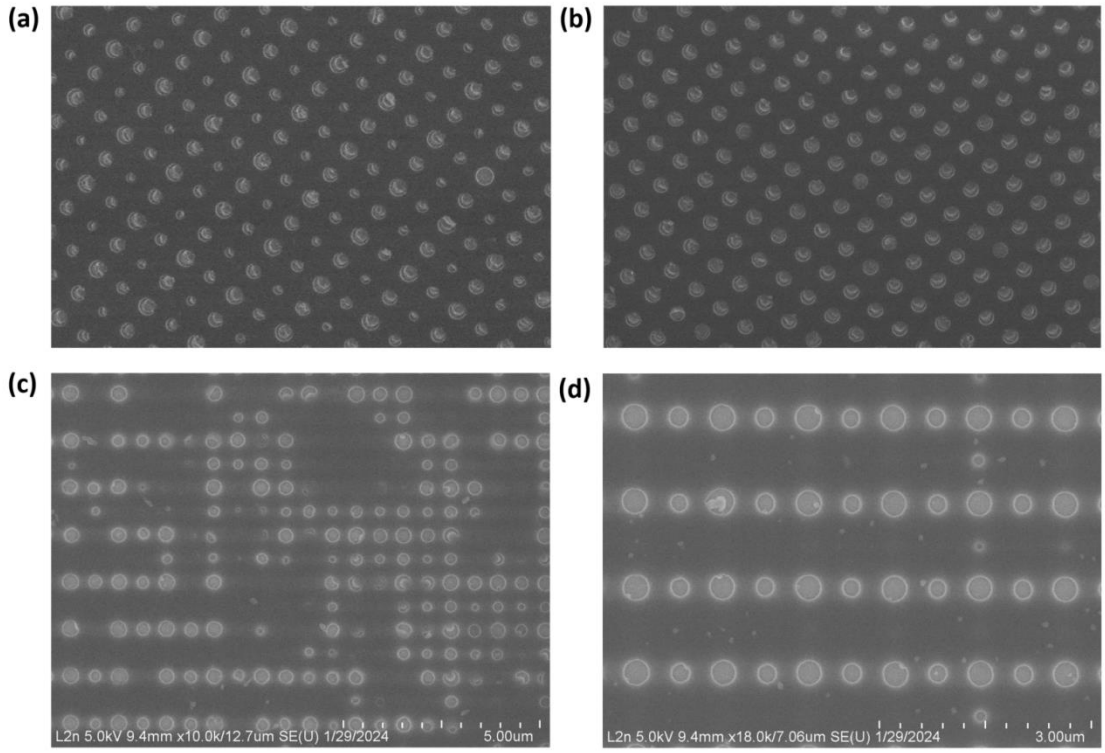


Figure 6.1: SEM images show the assembly of Si nanoparticles (Si NPs) from two preparation methods on nanohole-patterned substrates. (a, b) Si NPs made with a kitchen blender exhibit uniform size, stable dispersion in water, and high filling efficiency, maintaining substrate integrity. (c, d) Si NPs from ball milling show good size control but suffer from ethanol-induced aggregation and volatility, leading to lower filling efficiency and substrate damage.

Specifically, Si NPs prepared using the kitchen blender exhibit excellent size uniformity and dispersion stability, as shown in **Figures 6.1(a) and (b)**. This stability is attributed to their efficient dispersion in deionized water and the precise particle positioning enabled by capillary force-driven microfluidic assembly. This method achieves high filling rates in nanopatterned arrays while avoiding dynamic instabilities caused by solvent properties, thereby ensuring assembly efficiency and substrate integrity. Under conditions that are both cost-effective and efficient, this approach demonstrates great potential for precise metasurface assembly, providing robust

technical support for the development of nanophotonic devices and functional surfaces.

Compared with the kitchen blender method, Si NPs prepared by ball milling show good size control but face serious dispersion issues due to the high volatility of ethanol, as shown in **Figures 6.1(c) and (d)**. This leads to frequent aggregation, low filling efficiency, and damage to the nanopatterned substrate, making the method unsuitable for high-precision metasurface assembly. In contrast, Si NPs prepared using the kitchen blender method offer better dispersion stability in water, high filling rates, and minimal substrate damage. They are more compatible with microfluidic assembly and meet the precision and efficiency requirements of complex metasurface fabrication. This comparison highlights the importance of choosing appropriate nanoparticle preparation methods and solvents based on specific application needs. Future research could focus on optimizing blender parameters, fine-tuning microfluidic assembly conditions, and applying the method to more complex metasurface designs. These efforts would support the development of advanced nanophotonic and electronic devices across various fields.

6.3.2 Assembly of Complex Patterned Substrate: Einstein Pattern

The Einstein pattern, with its intricate details and complex geometric structure, is widely used in nanofabrication and surface engineering as a test pattern, as shown in **Figure 6.2**. This design includes fine facial contours, expressive features, and diverse curves with sharp transitions, providing rigorous experimental validation conditions for complex patterned substrate designs**[176]**. The assembly of the Einstein pattern serves as a comprehensive test to evaluate the precision, uniformity, and flexibility of silicon nanoparticle (Si NPs) assembly methods.

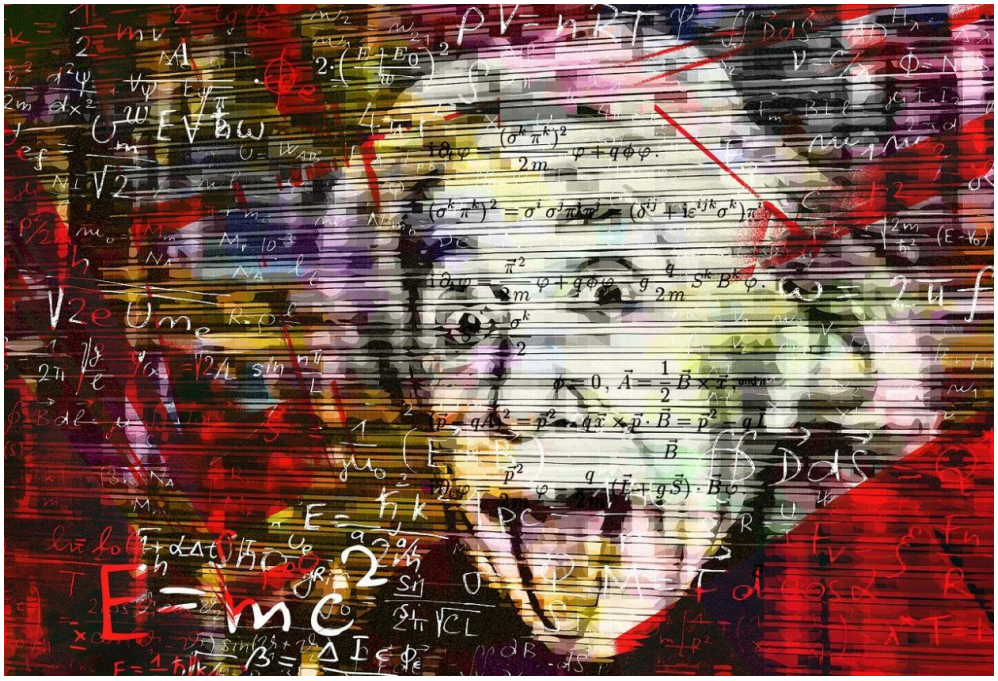


Figure 6.2: The Einstein pattern, characterized by intricate details and complex geometric structures, is widely used in nanofabrication and surface engineering as a test pattern.

The Einstein pattern, with its mix of large and fine details, is an effective test for the precision and uniformity of Si NP assembly using microfluidic methods. Successfully assembling this complex design shows the technique's ability to handle intricate surfaces. Beyond its technical value, the Einstein image adds symbolic meaning, representing science and innovation. Its complexity also tests critical factors like particle size uniformity, dispersion stability, flow control, and solvent evaporation effects. Compared to simple patterns, the recognizable Einstein image makes it easier to visually assess assembly success, strengthening the clarity and impact of the results.

6.3.2.1 Preparation of the Patterned Einstein Substrate

To assemble Si nanoparticles on the Einstein-patterned substrate, we optimized the key steps: substrate preparation, particle dispersion, microfluidic assembly, and characterization. We used n-type silicon wafers with a 300 nm SiO_2 layer, cleaned them with Neutracon and deionized water, then dried with nitrogen. Plasma treatment

improved surface adhesion. PMMA was spin-coated and baked to form a 150 nm resist layer, preparing the wafer for electron beam lithography. This ensured a clean, stable substrate for accurate patterning.

The pattern is based on Einstein's iconic image, encompassing details such as hair, eyebrows, eyes, nose, and mouth. This image was chosen primarily because of its multilayered geometric characteristics, including large-scale contour lines and intricate feature curves, which provide a comprehensive test for the fabrication of patterned substrates and the assembly performance of silicon nanoparticles (Si NPs). Using vectorization software such as Adobe Illustrator or AutoCAD, Einstein's image was processed into a binary black-and-white format**[177]**. The black regions correspond to holes formed by electron beam exposure on the patterned substrate, while the white areas represent unexposed regions. The hole diameters range from 150 nm to 300 nm, simulating surface nanostructures of varying feature sizes. The spacing between holes is 300 nm to 500 nm to prevent overlap during lithography or resolution degradation. The finalized vector graphic was saved in GDSII format, the standard input file for the electron beam lithography system**[178]**. The hole patterns were transferred to the substrate using electron beam lithography (EBL). A 150 nm thick PMMA resist layer was applied for sufficient hole depth and mechanical strength. The Raith EBL system was used for exposure, with an acceleration voltage of 20 kV and an exposure current of 200 pA for high-resolution results. The Einstein pattern was exposed point by point, with the system ensuring precise beam control and stability during exposure. After exposure, the substrate was developed using a 3:1 mixture of isopropanol (IPA) and methyl isobutyl ketone (MIBK), followed by rinsing in pure IPA and drying with high-purity nitrogen. This process ensured accurate hole patterns without any residual developer affecting the substrate.

6.3.2.2 Silanization Treatment on the Einstein Patterned Substrate

Silanization is essential for bonding silicon nanoparticles (Si NPs) to the Einstein-patterned substrate, improving adhesion and ensuring stability during assembly. It also

facilitates the removal of the PMMA template without disturbing the nanoparticle arrangement. We used 3-aminopropyltriethoxysilane (APTES) for the silanization, with the amino groups reacting with hydroxyl groups on the substrate surface. Plasma cleaning was performed on the substrate to increase surface hydroxyl groups before immersion in a solution of 40 μL APTES and 80 mL anhydrous ethanol for 3 hours at room temperature in a sealed container to maintain solution stability and prevent moisture interference. After the reaction, the substrate was rinsed in isopropanol, dried with nitrogen gas, and heated at 120℃ for 10 minutes to stabilize the silane bonds and remove residual solvent. This process ensured a uniform silane layer, enhancing nanoparticle adhesion and providing a stable surface for subsequent assembly.

6.3.2.3 Assembly of Si Nanoparticles on the Complex Einstein Nano-Patterned Substrate

In this study, we used a Midea kitchen blender (1500 W, six steel blades) to prepare Si nanoparticles (Si NPs) by grinding 10 g of high-purity silicon blocks (99.9999%) in 300 mL of deionized water (18.2 MΩ·cm). The grinding was done in 3-minute cycles with 2-minute breaks for a total of 2 hours to prevent overheating. After grinding, the solution was filtered and stored at 4°C for three days to allow larger particles to settle. The suspension was then centrifuged at 5000 rpm for 10 minutes, and the supernatant was collected and purified by repeated centrifugation.

The resulting Si NPs were assembled onto a complex Einstein-patterned substrate using capillary force-assisted microfluidic assembly. The substrate was placed in a SmartForce device, properly aligned and sealed to avoid contamination and leaks. The platform was heated to 35°C, and airflow was set at 50 mL/min to control solvent evaporation. A concentrated Si NP solution was injected, and as the solvent evaporated, capillary forces guided the particles into the nanoholes. The process was monitored in real time with an optical microscope. After complete evaporation, the Si NPs remained stably positioned for further processing.

6.3.2.4 Characterization of Si Nanoparticles Assembly Results on the Complex Einstein-Patterned Substrate

SEM imaging was used to analyze the Einstein-patterned substrate before and after assembling Si nanoparticles (Si NPs). **Figure 6.3(a)** shows the substrate after electron beam lithography (EBL) and before assembly. Regions A and B display clear, well-ordered nanopores with high structural integrity. Region A, focused on Einstein's hairline, shows densely packed nanopores (~200 nm) with uniform shape, confirming the precision of EBL. Region B, located along the facial contour, also shows accurate and detailed nanopore patterns, demonstrating the high quality of substrate fabrication. **Figure 6.3(b)** shows the substrate after Si nanoparticle (Si NP) assembly using the SmartForce device. Regions C and D confirm uniform particle filling. Region C, representing Einstein's left eye, shows nearly 100% filling, with NPs precisely positioned in each nanopore. Region D, at the end of the hairline pattern, also shows accurate and even NP distribution, even in complex areas. These results highlight the precision and reliability of microfluidic capillary assembly, proving the SmartForce system's effectiveness for complex nanofabrication tasks.

Using a dark-field microscope, we further analyzed the substrate pattern after electron beam lithography (EBL) and the substrate after silicon nanoparticle (Si NP) assembly using the SmartForce device, as shown in **Figure 6.4**. The dark-field microscopy image taken after lithography completion clearly illustrates the integrity and precision of the Einstein pattern , as shown in **Figure 6.4(a)**. The positions of the nanopores in the lithographed pattern are accurate, with uniform pore diameters and well-defined boundaries. Even in complex contour regions, such as the hairlines and facial features, the lithography process demonstrates high precision.

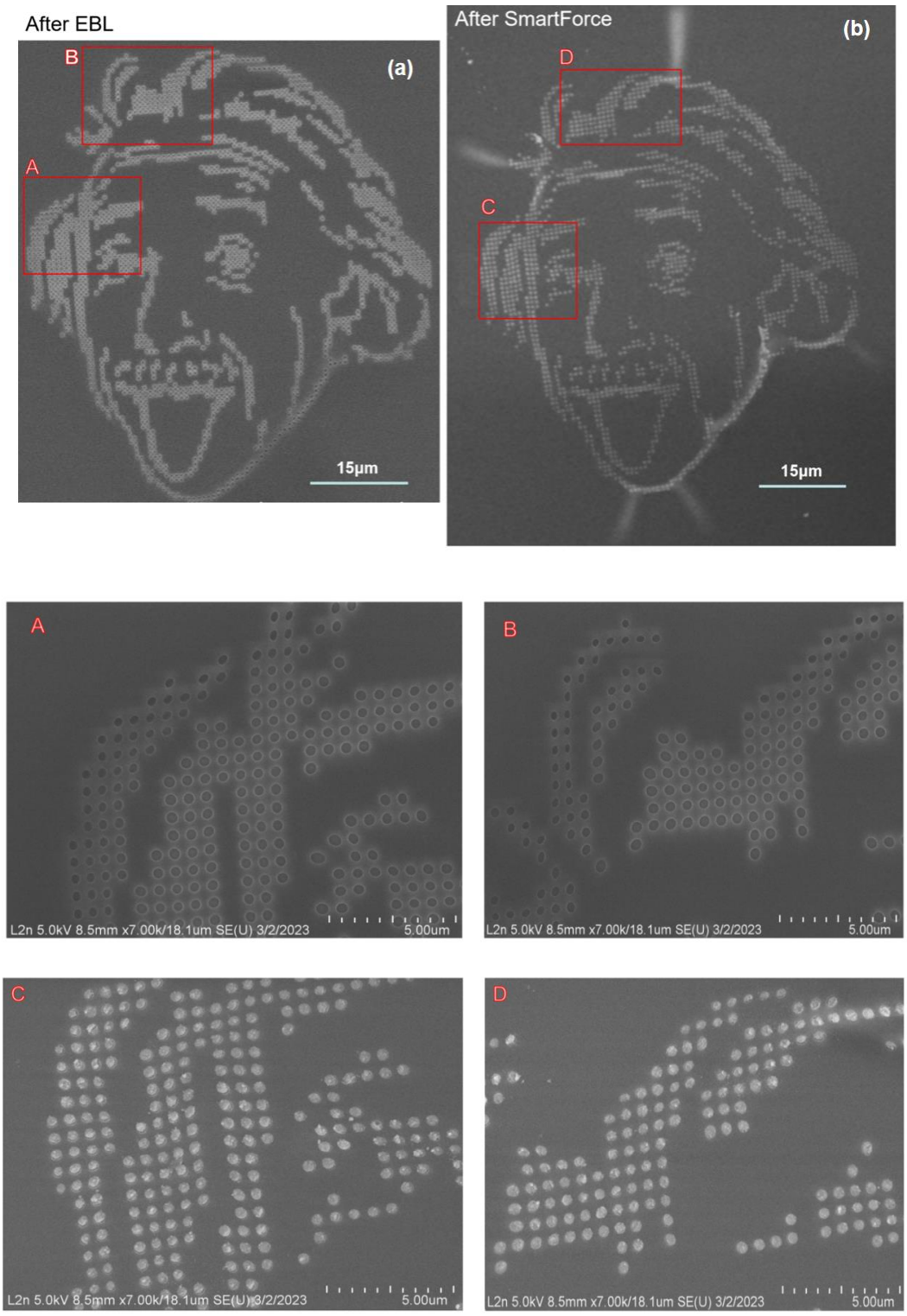


Figure 6.3: SEM images showing Si NP assembly on the Einstein-patterned substrate. (a) Before assembly: Regions A and B show uniform and well-arranged nanopores after EBL. (b) After assembly with the SmartForce device: Regions C and D show successful and uniform filling of Si NPs into the nanopores.

The geometric details of the lithography pattern faithfully replicate the designed Einstein pattern, underscoring the high reliability and consistency of the EBL process in fabricating complex nanostructures. As shown in **Figure 6.4(b),** the dark-field microscopy image taken after assembly reveals the precise placement of silicon nanoparticles on the Einstein-patterned substrate. The nanoparticles are uniformly embedded in the predesignated nanopores, maintaining the original integrity of the lithographed pattern with a very high particle filling rate. In detail-rich areas, such as the hairlines and facial contours, the uniformity and precision of particle distribution highlight the strong capabilities of the SmartForce device combined with microfluidic technology in assembling complex nanostructures.

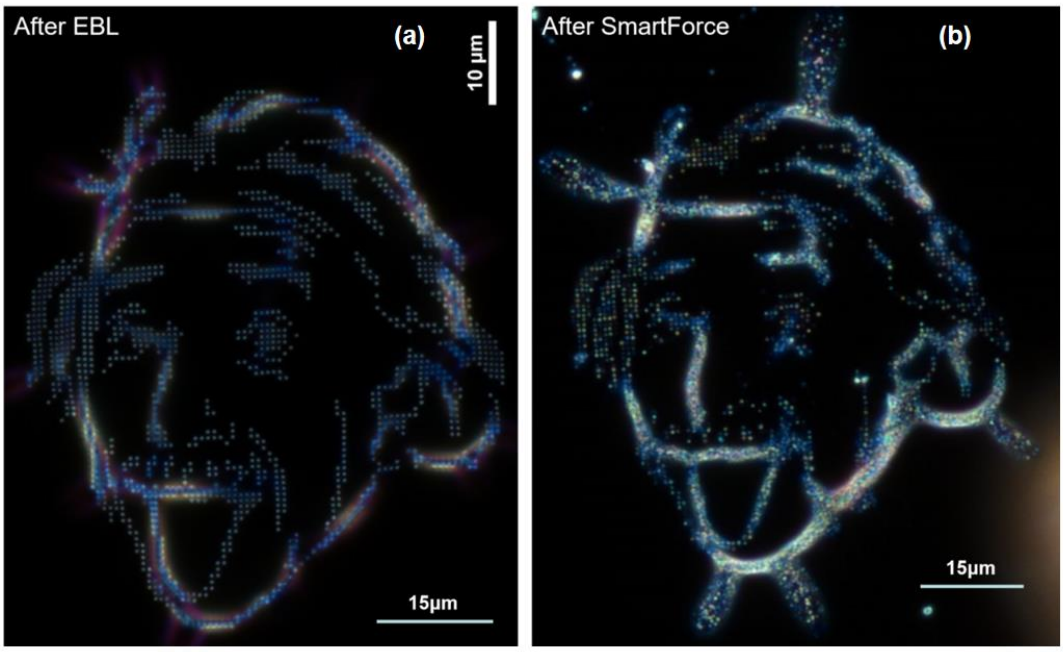


Figure 6.4: Dark-field images of the Einstein-patterned substrate before and after Si NP assembly. (a) After EBL: Clear nanopore arrangement and detailed pattern structure. (b) After SmartForce assembly: Si NPs are uniformly filled into the nanopores, preserving the original pattern integrity.

The dark-field images from both stages show that the lithography-generated pattern remains intact after nanoparticle assembly, with no significant damage or deformation. The microfluidic assembly technique ensures precise particle placement within the nanopores, even in regions with complex curves, maintaining uniform distribution.

After assembly, the Einstein pattern shows enhanced light scattering due to the high filling rate of the particles and their optical coupling with the substrate. These results confirm the effectiveness of capillary force-driven microfluidic technology for assembly on complex substrates. They also demonstrate the potential of Si nanoparticles prepared using the kitchen blender method in nanophotonic device assembly, providing strong evidence for future advancements in complex nanostructures and optical devices.

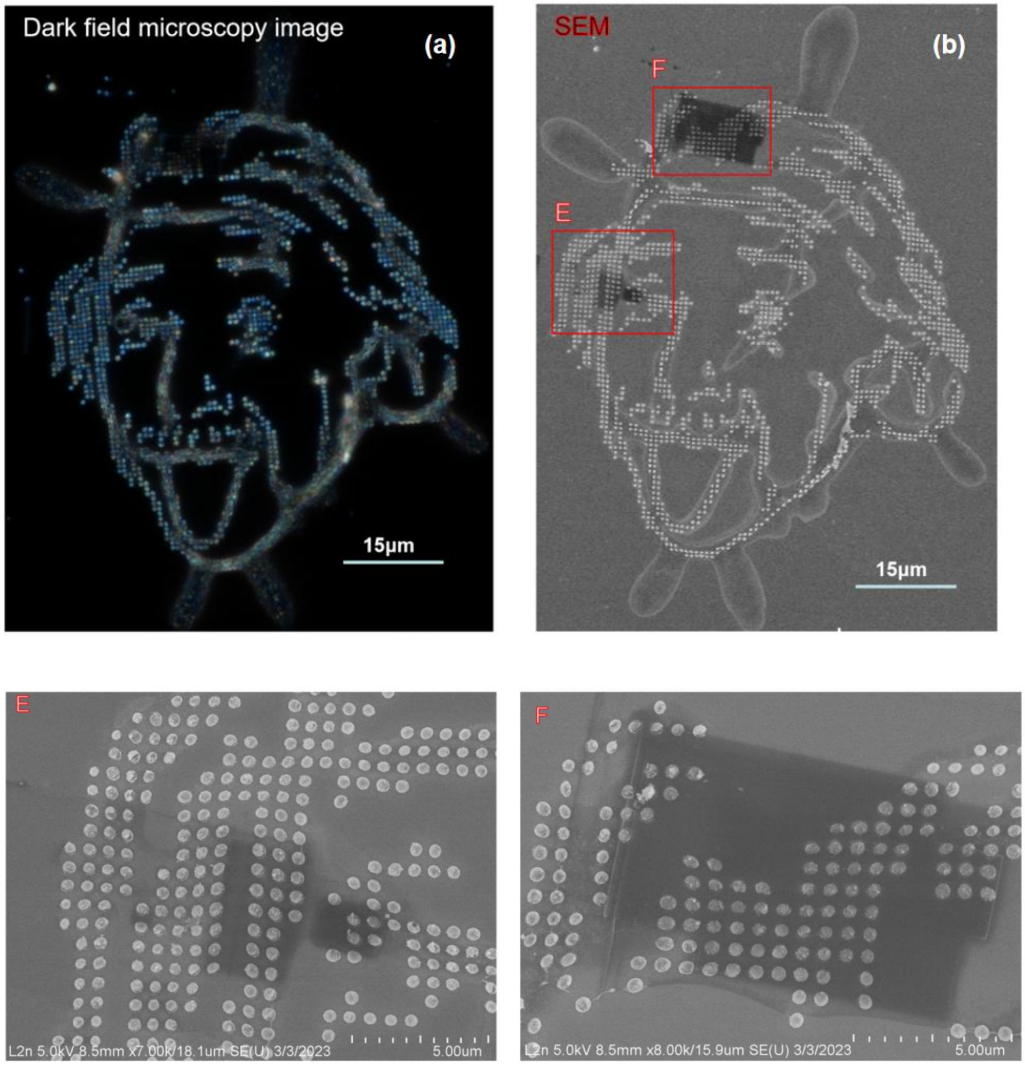


Figure 6.5: Analysis of Si NP assembly on the Einstein-patterned substrate after PMMA removal. (a) Dark-field image shows clear Einstein pattern with strong light scattering from well-positioned Si NPs. (b) SEM image confirms uniform assembly. Insets E and F show detailed views of local nanopore filling.

This analysis underscores the effectiveness of capillary force-driven microfluidic technology for precise nanoparticle assembly on complex patterned substrates and highlights the suitability of Si NPs prepared via the kitchen blender method for advanced nanophotonic applications.

Next, the assembled sample is immersed in acetone solution for soaking to remove the PMMA template, leaving only the Einstein pattern formed by silicon nanoparticles (Si NPs). The specific steps are as follows: fully submerge the sample in the acetone solution and maintain the soaking process for 3 hours to ensure that the PMMA template is thoroughly dissolved and removed. This process relies on the high solubility of PMMA in acetone and does not require additional mechanical cleaning, thereby maximizing the structural integrity of the nanoparticle assembly. Ultimately, the silicon nanoparticles remain arranged in the Einstein pattern as per the original design, further demonstrating the high precision and reliability of the assembly technique. This step not only validates the effectiveness of the assembly method but also provides a purified sample for further characterization of the assembled pattern's performance.

Figure 6.5 presents the analysis of the assembly results after removing the PMMA template, using dark-field microscopy and scanning electron microscopy (SEM). Both dark-field microscopy image on the left and SEM image on the right clearly show that silicon nanoparticles (Si NPs) have been successfully assembled onto the complex Einstein-patterned substrate, forming a complete and well-defined pattern. The dark-field microscopy image highlights the overall Einstein pattern after assembly, with light scattering characteristics emphasizing the positioning of the silicon nanoparticles, as shown in **Figure 6.5(a)**. From the image, it is evident that the particles are precisely distributed in the high-contrast regions of the substrate, demonstrating that the particles maintain excellent adhesion and positional accuracy even after the template has been removed.

The SEM image on the right further confirms this through high-resolution imaging. Images E and F specifically highlight the detailed regions of Einstein's facial features and hair, as shown in **Figure 6.5(b)**. **Image E** focuses on the facial contour lines of the Einstein pattern. It clearly shows that silicon nanoparticles (Si NPs) are uniformly filled within each nanohole, with minimal aggregation or missing particles. This demonstrates the exceptional precision of the microfluidic assembly technique in complex contour regions. **Image F** presents the detailed hair region of the Einstein pattern, characterized by intricate and densely packed lines. The particles maintain efficient and uniform filling even in these challenging areas. Additionally, after the PMMA template was removed, the particles exhibited robust chemical bonding with the substrate, with no observed detachment, further validating the effectiveness of the silanization process.

Silanization is essential for stabilizing silicon nanoparticles (Si NPs) on the substrate during and after assembly. In this study, APTES was used to form strong chemical bonds between Si NPs and the substrate, preventing particle loss during PMMA removal in acetone. This bonding improved assembly uniformity, reduced sliding, and helped preserve the original nanoparticle arrangement, even after template removal. As a result, the Einstein pattern remained intact. Dark-field and SEM imaging confirmed that silanization significantly enhanced assembly precision and long-term stability, supporting the effectiveness of the SmartForce microfluidic technique.

6.4 Conclusion

This chapter confirms that silicon nanoparticles (Si NPs) prepared using the kitchen blender method can be effectively assembled onto complex nano-patterned substrates using microfluidic technology. Compared to ball-milled particles, blender-prepared Si NPs showed better size uniformity and dispersion in water, making them more suitable for precise microfluidic assembly. The Einstein pattern was successfully fabricated on a silicon substrate using electron beam lithography (EBL), and SmartForce microfluidic assembly enabled accurate placement of Si NPs into even the most intricate parts of the pattern. Silanization with APTES ensured strong adhesion of the particles, keeping them in place after removing the PMMA template. Microscopy confirmed the clear and stable particle arrangement, demonstrating the effectiveness of this method. Overall, this simple and low-cost approach provides a reliable way to assemble Si NPs into complex structures and supports future development of advanced nano-optical and functional materials.

Chapter 7

Conclusion and Prospect

This study investigates how to prepare and assemble silicon nanoparticles (Si NPs) on nano-patterned substrates for use in optoelectronic devices. Two grinding methods—kitchen blender and ball milling—were used to produce the nanoparticles. Si NPs made with the kitchen blender showed better size uniformity and water dispersion, making them more suitable for microfluidic assembly. In contrast, ball-milled Si NPs had issues with aggregation due to ethanol's volatility. By optimizing solvent evaporation, airflow, and surface treatment, high-precision assembly was achieved on complex patterns like the Einstein image. Future work should focus on improving particle shape control, combining trapping technologies (electric, magnetic, optical), and exploring applications in photonic chips, biosensors, and advanced optical materials. This research offers a low-cost, efficient method for building nanophotonic devices and supports the development of next-generation optoelectronics.

Chapter 7: Conclusion and Prospect

7.1 Research Conclusion

This study systematically investigates the synthesis, assembly techniques, and applications of silicon nanoparticles (Si NPs) in nanophotonic devices. Through a comparative analysis of mechanical grinding methods, including the kitchen blender method and ball milling method, Si NPs were successfully synthesized with tunable size distributions and dispersibility. To achieve precise nanoparticle positioning and high-efficiency integration, the study employed SmartForce microfluidic assembly technology, enabling the controlled deposition of Si NPs onto nano-patterned substrates. The experimental results demonstrate：

7.1.1 Comparison of Si NP Preparation Methods

This study compares two mechanical grinding methods—the kitchen blender method and the ball milling method—for preparing silicon nanoparticles (Si NPs), focusing on their dispersion stability and suitability for microfluidic-assisted assembly. The kitchen blender method involves grinding high-purity silicon blocks in deionized water, offering a simple, low-cost, scalable, and environmentally friendly approach. It produces Si NPs with relatively uniform size and good dispersion, making them highly compatible with microfluidic assembly techniques. However, challenges such as irregular particle shapes and potential wear of the blender blades over time may affect performance. In contrast, the ball milling method uses high-energy impact to grind silicon powder in anhydrous ethanol, allowing for better control over particle size and morphology through adjustable milling parameters. While this method is effective for producing precisely sized particles, its reliance on volatile ethanol leads to particle aggregation during assembly and poses risks of contamination, such as FeSi, if stainless steel balls are used. Based on these comparisons, the kitchen blender method is selected as the more reliable approach due to its superior dispersion stability in water and greater compatibility with microfluidic assembly. This finding

lays a solid foundation for the low-cost, scalable fabrication of Si NP-based metasurfaces and nanophotonic devices.

7.1.2 Assembly Performance of Si NPs on Nano-Patterned Substrates

This study explores the use of SmartForce microfluidic assembly technology to precisely position silicon nanoparticles (Si NPs) on different substrates for fabricating high-performance all-dielectric metasurfaces. By controlling fluid flow and capillary forces, this method achieves uniform, scalable nanoparticle assembly essential for advanced nanophotonic devices. Si NPs prepared with the kitchen blender method showed excellent size uniformity, high packing density, and stable dispersion in water. When assembled on silicon and ITO glass substrates, they formed well-ordered arrays with consistent optical and electronic properties. Surface treatment using APTES improved adhesion and stability, preventing particle detachment during PMMA removal. Fine-tuning parameters such as evaporation rate, temperature, and flow dynamics further enhanced the precision and reproducibility of the assembly, supporting applications in photonic circuits and sensing. In contrast, Si NPs produced by ball milling faced challenges due to ethanol-based dispersion. The volatility of ethanol led to particle aggregation, uneven deposition, and structural damage during assembly. These limitations compromised the uniformity and stability of metasurface fabrication, highlighting the need for better solvents or post-treatment strategies. Overall, the kitchen blender method, combined with microfluidic assembly, proved more reliable and effective for producing high-quality, reproducible Si NP-based metasurfaces. This approach offers a scalable, low-cost pathway for next-generation applications in nanophotonics, optical sensing, and optoelectronic devices.

7.1.3 Application of Si NPs on Complex Nano-Patterned Substrates

To assess the practical potential of silicon nanoparticles (Si NPs), this study explored their assembly on complex nano-patterned substrates, such as the Einstein image array. Given the need for precise nanostructures in photonic and optoelectronic devices,

achieving accurate Si NP placement on intricate patterns is essential. By optimizing microfluidic conditions—such as solvent evaporation rate, airflow, and temperature—the study achieved uniform and precise Si NP assembly on irregular surfaces. It was found that geometric features of the nanopores (diameter, depth, spacing) directly impact assembly efficiency and quality, emphasizing the importance of pattern customization. Surface modification using APTES further improved particle adhesion and stability, ensuring reliable structures during post-processing. These results confirm that microfluidic-assisted assembly, combined with careful process design, offers a scalable and precise method for building high-performance nanostructures, supporting future development in photonic circuits and functional optical devices.

7.2 Future Prospects

Building upon the findings of this study, several promising future research directions can be explored to further enhance the fabrication, assembly, and application of Si NPs in nanophotonic and optoelectronic devices.

7.2.1 Further Optimization of Si NP Preparation Methods

To improve the size uniformity, shape control, and performance of silicon nanoparticles (Si NPs), future research should focus on optimizing the mechanical grinding process and exploring advanced synthesis methods. Key improvements include fine-tuning grinding parameters—such as speed, time, media, and blade material—to achieve more consistent particle size and shape. Real-time monitoring tools could also help adjust conditions dynamically for better reproducibility. Integrating ultrasound-assisted grinding may further enhance particle uniformity by breaking down larger particles and reducing aggregation. Surface modification techniques, like silanization or plasma treatment, can improve dispersion and chemical stability in various solvents, supporting better assembly and compatibility with hybrid materials. Additionally, alternative synthesis methods like laser ablation or chemical vapor deposition (CVD) may produce highly uniform, ultra-small Si NPs

with strong optical properties. Together, these strategies will support the scalable production of high-quality Si NPs for use in metasurfaces, photonics, and next-generation optical devices.

7.2.2 Development of High-Precision Nano-Assembly Techniques

To improve the precision and scalability of silicon nanoparticle (Si NP) assembly, future research should combine external force-driven strategies with advanced microfluidic control. Techniques such as electric fields (dielectrophoresis), magnetic fields, and optical tweezers can offer precise control over nanoparticle positioning, enabling the accurate formation of two- or three-dimensional structures. These methods enhance the spatial resolution and alignment of Si NPs, especially in complex nano-patterned environments. At the same time, optimizing microfluidic parameters—such as solvent evaporation rate, flow velocity, and concentration gradients—can significantly improve the uniformity and reliability of nanoparticle deposition. Programmable microfluidic systems could further enable on-demand and site-specific assembly, allowing for reconfigurable metasurfaces and adaptive nanostructures. By integrating external forces with dynamic microfluidic control, it becomes possible to achieve highly ordered, tunable, and scalable Si NP assemblies. These advancements will support the development of next-generation nanophotonic devices, metasurfaces, biosensors, and functional materials for applications in optics, sensing, and information processing.

7.2.3 Expanding the Application of Si NPs in Optoelectronic Devices

To expand the application of silicon nanoparticles (Si NPs) in advanced optoelectronics, future research should explore their integration into photonic chips, quantum computing, nanophotonics, and biosensing. Thanks to their excellent optical properties, high refractive index, and compatibility with semiconductor processes, Si NPs are strong candidates for next-generation photonic devices. In photonic chips, Si NPs can improve light confinement and reduce signal loss in optical waveguides and modulators, enhancing the performance of optical communication systems and

integrated photonic circuits. Combining Si NPs with 2D materials like graphene or MoS_2 could enable tunable photonic responses, ultrafast switching, and new opportunities in nanophotonics and quantum technologies. These hybrid systems may support low-power optical devices and scalable quantum architectures. In biosensing, Si NPs offer enhanced signal sensitivity, label-free detection, and real-time monitoring capabilities, making them ideal for medical diagnostics, environmental sensing, and personalized healthcare. Their integration into plasmonic or fluorescence-based sensors can enable compact, high-performance devices for early disease detection. Altogether, Si NPs hold strong potential to advance next-generation optical computing, intelligent sensing, and high-speed information processing.

7.2.4 Development of Novel Nanocomposite Materials

Future research should explore integrating Si nanoparticles (Si NPs) with advanced functional materials, especially in photovoltaics and tunable nanophotonics. Combining Si NPs with perovskites could improve photoelectric conversion efficiency by enhancing light absorption, carrier transport, and device stability, offering a path toward low-cost, high-performance solar cells. Additionally, incorporating Si NPs into organic-inorganic hybrid materials may lead to tunable photonic devices with dynamic optical properties, enabling applications in adaptive metasurfaces, reconfigurable circuits, and smart displays. These developments could drive progress in solar energy, optical sensing, and multifunctional optoelectronics, supporting efficient and sustainable nanotechnology solutions.

7.3 Research Summary

This study confirms that mechanical grinding methods—particularly the kitchen blender technique—are effective for preparing silicon nanoparticles (Si NPs) and assembling them into precise, scalable all-dielectric metasurfaces. The kitchen blender method shows strong compatibility with microfluidic-assisted assembly, producing Si NPs with good stability and uniformity. By optimizing parameters such as fluid dynamics, solvent control, and surface treatment, the study achieved high-precision

and repeatable nanoparticle placement, supporting the development of advanced nanophotonic devices.

Looking forward, as technologies in nanomanufacturing, optoelectronics, and photonic integration progress, Si NP fabrication and assembly will play an important role in future optical communication systems, biosensors, and intelligent optical devices. The ability to control particle positioning and tune optical properties—especially when combined with emerging materials like 2D materials, perovskites, and hybrid nanocomposites—opens up opportunities in quantum technologies, adaptive optics, and energy-efficient devices.

Moreover, the scalability of Si NP-based metasurfaces holds promise for real-world applications in telecommunications, diagnostics, environmental monitoring, and wearable sensors. Advancing low-cost, high-throughput nanoparticle assembly methods will be key to transitioning from lab research to commercial products. Continued improvements in synthesis, assembly precision, and material integration will help drive the development of the next generation of multifunctional nanophotonic technologies.

References

1. De Marco, M. L.; Semlali, S.; Korgel, B. A.; Barois, P.; Drisko, G. L.; Aymonier, C., Silicon-Based Dielectric Metamaterials: Focus on the Current Synthetic Challenges. *Angewandte Chemie International Edition* **2018,** *57* (17), 4478-4498.

2. Roach, L.; Idowu, E. O.; Soun, D.; O'Connor, K.; Veinot, J. G.-C.; Plain, J.; Proust, J.; Li, X.; Kociak, M.; Baron, A. In *Directional light scattering in Mie-resonant Si particles with ultra-thin plasmonic shells*, 8th International Conference on Multifunctional, Hybrid and Nanomaterials (HyMa), 2025.

3. Ali, A. M.; Ghanim, A. M.; Othman, M.; Swillam, M. A., All silicon MIR super absorber using fractal metasurfaces. *Scientific Reports* **2023,** *13* (1), 15545.

4. Hernandez, R.; Wiecha, P. R.; Poumirol, J.-M.; Agez, G.; Arbouet, A.; Ressier, L.; Paillard, V.; Cuche, A., Directional silicon nano-antennas for quantum emitter control designed by evolutionary optimization. *Journal of the Optical Society of America B* **2024,** *41* (2), A108-A115.

5. Semlali, S.; Cormary, B.; De Marco, M. L.; Majimel, J.; Saquet, A.; Coppel, Y.; Gonidec, M.; Rosa, P.; Drisko, G. L., Effect of solvent on silicon nanoparticle formation and size: a mechanistic study. *Nanoscale* **2019,** *11* (11), 4696-4700.

6. Parker, M. A.; Khaddad, S.; Fares, N.; Ghoridi, A.; Portehault, D.; Bonhommeau, S.; Amarouchene, Y.; Rosa, P.; Gonidec, M.; Drisko, G. L., Unveiling the Potential of Redox Chemistry to Form Size-Tunable, High-Index Silicon Particles. *Chemistry of Materials* **2024,** *36* (22), 10986-10993.

7. Bhat, J. A.; Rajora, N.; Raturi, G.; Sharma, S.; Dhiman, P.; Sanand, S.; Shivaraj, S.; Sonah, H.; Deshmukh, R., Silicon nanoparticles (SiNPs) in sustainable agriculture: major emphasis on the practicality, efficacy and concerns. *Nanoscale Advances* **2021,** *3* (14), 4019-4028.

8. Schlipf, J.; Berkmann, F.; Yamamoto, Y.; Reichenbach, M.; Veleski, M.; Kawaguchi, Y.; Mörz, F.; Tomm, J. W.; Weißhaupt, D.; Fischer, I. A., Robust Si/Ge

heterostructure metasurfaces as building blocks for wavelength-selective photodetectors. *Applied Physics Letters* **2023,** *122* (12).

9. Yang, W.; Xiao, S.; Song, Q.; Liu, Y.; Wu, Y.; Wang, S.; Yu, J.; Han, J.; Tsai, D.-P., All-dielectric metasurface for high-performance structural color. *Nature communications* **2020,** *11* (1), 1864.

10. Hsu, W.-L.; Chen, Y.-C.; Yeh, S. P.; Zeng, Q.-C.; Huang, Y.-W.; Wang, C.-M., Review of metasurfaces and metadevices: advantages of different materials and fabrications. *Nanomaterials* **2022,** *12* (12), 1973.

11. Zhao, Q.; Yuan, W.; Qu, J.; Cheng, Z.; Peng, G.-D.; Yu, C., Optical fiber-integrated metasurfaces: An emerging platform for multiple optical applications. *Nanomaterials* **2022,** *12* (5), 793.

12. Camacho-Morales, R.; Rocco, D.; Xu, L.; Gili, V. F.; Dimitrov, N.; Stoyanov, L.; Ma, Z.; Komar, A.; Lysevych, M.; Karouta, F., Infrared upconversion imaging in nonlinear metasurfaces. *Advanced Photonics* **2021,** *3* (3), 036002-036002.

13. Ollanik, A. J.; Oguntoye, I. O.; Hartfield, G. Z.; Escarra, M. D., Highly sensitive, affordable, and adaptable refractive index sensing with silicon-based dielectric metasurfaces. *Advanced Materials Technologies* **2019,** *4* (2), 1800567.

14. Tseng, M. L.; Jahani, Y.; Leitis, A.; Altug, H., Dielectric metasurfaces enabling advanced optical biosensors. *ACS photonics* **2020,** *8* (1), 47-60.

15. Abdelraouf, O. A.; Wang, Z.; Liu, H.; Dong, Z.; Wang, Q.; Ye, M.; Wang, X. R.; Wang, Q. J.; Liu, H., Recent advances in tunable metasurfaces: materials, design, and applications. *ACS nano* **2022,** *16* (9), 13339-13369.

16. Yang, W.; Zhou, J.; Tsai, D. P.; Xiao, S., Advanced manufacturing of dielectric meta-devices. *Photonics Insights* **2024,** *3* (2), R04-R04.

17. Kim, T.; Lee, J., Silicon nanoparticles: fabrication, characterization, application and perspectives. *Micro and Nano Systems Letters* **2023,** *11* (1), 18.

18. Chaabani, W.; Proust, J.; Movsesyan, A.; Béal, J.; Baudrion, A.-L.; Adam, P.-M.; Chehaidar, A.; Plain, J., Large-scale and low-cost fabrication of silicon mie resonators. *ACS nano* **2019,** *13* (4), 4199-4208.

19. Lam, C.; Zhang, Y.; Tang, Y.; Lee, C.; Bello, I.; Lee, S., Large-scale synthesis of ultrafine Si nanoparticles by ball milling. *Journal of Crystal Growth* **2000,** *220* (4), 466-470.

20. Zywietz, U.; Evlyukhin, A. B.; Reinhardt, C.; Chichkov, B. N., Laser printing of silicon nanoparticles with resonant optical electric and magnetic responses. *Nature communications* **2014,** *5* (1), 3402.

21. Maeng, S.-H.; Lee, H.; Kim, S., Synthesis of silicon nanoparticles using a novel reactor with an elongated reaction zone created by coaxially aligned SiH4 gas and a CO2 laser beam. *Journal of Nanoparticle Research* **2021,** *23* (6), 134.

22. Lin, N.; Han, Y.; Wang, L.; Zhou, J.; Zhou, J.; Zhu, Y.; Qian, Y., Preparation of Nanocrystalline Silicon from SiCl4 at 200° C in Molten Salt for High-Performance Anodes for Lithium Ion Batteries. *Angewandte Chemie International Edition* **2015,** *54* (12), 3822-3825.

23. Maeng, S.-H.; Lee, H.; Park, M. S.; Park, S.; Jeong, J.; Kim, S., Ultrafast carbothermal reduction of silica to silicon using a CO2 laser beam. *Scientific reports* **2020,** *10* (1), 21730.

24. Kim, K. H.; Lee, D. J.; Cho, K. M.; Kim, S. J.; Park, J.-K.; Jung, H.-T., Complete magnesiothermic reduction reaction of vertically aligned mesoporous silica channels to form pure silicon nanoparticles. *Scientific reports* **2015,** *5* (1), 9014.

25. Lin, D.; Fan, P.; Hasman, E.; Brongersma, M. L., Dielectric gradient metasurface optical elements. *science* **2014,** *345* (6194), 298-302.

26. Ubeid, M. F.; Shabat, M. M., Numerical study of antireflection coatings in waveguide structures with silicon nanoparticles interlayer. *Journal of Modern Optics* **2017,** *64* (4), 374-378.

27. Ahmad, Z.; Younis, R.; Ahmad, T.; Iqbal, M. A.; Artyszak, A.; Alzahrani, Y. M.; Alharby, H. F.; Alsamadany, H., Modulating Physiological and Antioxidant Responses in Wheat Cultivars via Foliar Application of Silicon Nanoparticles (SiNPs) Under Arsenic Stress Conditions. *Silicon* **2024,** *16* (12), 5199-5211.

28. Ji, X.; Wang, H.; Song, B.; Chu, B.; He, Y., Silicon nanomaterials for biosensing and bioimaging analysis. *Frontiers in chemistry* **2018,** *6*, 38.

29. Singh, G.; Ddungu, J. L.; Licciardello, N.; Bergmann, R.; De Cola, L.; Stephan, H., Ultrasmall silicon nanoparticles as a promising platform for multimodal imaging. *Faraday Discussions* **2020,** *222*, 362-383.

30. Valuckas, V.; Paniagua-Domínguez, R.; Maimaiti, A.; Patra, P. P.; Wong, S. K.; Verre, R.; Kall, M.; Kuznetsov, A. I., Fabrication of monodisperse colloids of resonant spherical silicon nanoparticles: applications in optical trapping and printing. *Acs Photonics* **2019,** *6* (8), 2141-2148.

31. Pan, C.; Qin, X.; Lu, M.; Ma, Q., Water soluble silicon nanoparticles as a fluorescent probe for highly sensitive detection of rutin. *ACS omega* **2022,** *7* (32), 28588-28596.

32. Jageler-Hoheisel, T.; Cordeiro, J.; Lecarme, O.; Cuche, A.; Girard, C.; Dujardin, E.; Peyrade, D.; Arbouet, A., Plasmonic shaping in gold nanoparticle three-dimensional assemblies. *The Journal of Physical Chemistry C* **2013,** *117* (44), 23126-23132.

33. Gordon, M. J.; Peyrade, D., Separation of colloidal nanoparticles using capillary immersion forces. *Applied Physics Letters* **2006,** *89* (5).

34. Renaut, C.; Dellinger, J.; Cluzel, B.; Honegger, T.; Peyrade, D.; Picard, E.; De Fornel, F.; Hadji, E., Assembly of microparticles by optical trapping with a photonic crystal nanocavity. *Applied Physics Letters* **2012,** *100* (10).

35. Balthasar Mueller, J.; Rubin, N. A.; Devlin, R. C.; Groever, B.; Capasso, F., Metasurface polarization optics: independent phase control of arbitrary orthogonal states of polarization. *Physical review letters* **2017,** *118* (11), 113901.

36. Kildishev, A. V.; Boltasseva, A.; Shalaev, V. M., Planar photonics with metasurfaces. *Science* **2013,** *339* (6125), 1232009.

37. Kamali, S. M.; Arbabi, E.; Arbabi, A.; Faraon, A., A review of dielectric optical metasurfaces for wavefront control. *Nanophotonics* **2018,** *7* (6), 1041-1068.

38. Chen, W. T.; Zhu, A. Y.; Sanjeev, V.; Khorasaninejad, M.; Shi, Z.; Lee, E.; Capasso, F., A broadband achromatic metalens for focusing and imaging in the visible. *Nature nanotechnology* **2018,** *13* (3), 220-226.

39. He, G.; Zheng, Y.; Zhou, C.; Li, S.; Shi, Z.; Deng, Y.; Zhou, Z.-K., Multiplexed manipulation of orbital angular momentum and wavelength in metasurfaces based on arbitrary complex-amplitude control. *Light: Science & Applications* **2024,** *13* (1), 98.

40. Arbabi, E.; Arbabi, A.; Kamali, S. M.; Horie, Y.; Faraon, A., Multiwavelength metasurfaces through spatial multiplexing. *Scientific reports* **2016,** *6* (1), 1-8.

41. Jung, C.; Kim, G.; Jeong, M.; Jang, J.; Dong, Z.; Badloe, T.; Yang, J. K.; Rho, J., Metasurface-driven optically variable devices. *Chemical Reviews* **2021,** *121* (21), 13013-13050.

42. Colburn, S.; Zhan, A.; Majumdar, A., Metasurface optics for full-color computational imaging. *Science advances* **2018,** *4* (2), eaar2114.

43. Jahani, S.; Jacob, Z., All-dielectric metamaterials. *Nature nanotechnology* **2016,** *11* (1), 23-36.

44. Zhong, Y.; Du, L.; Liu, Q.; Zhu, L.; Meng, K.; Zou, Y.; Zhang, B., Ultrasensitive specific sensor based on all-dielectric metasurfaces in the terahertz range. *RSC advances* **2020,** *10* (55), 33018-33025.

45. Wang, X.; Hao, H.; He, X.; Xie, P.; Liu, J.; Tan, J.; Li, H.; Wang, H.; Genevet, P.; Luo, Y., Advances in information processing and biological imaging using flat optics. *Nature Reviews Electrical Engineering* **2024**, 1-21.

46. Hu, X.; Xu, W.; Fan, Q.; Yue, T.; Yan, F.; Lu, Y.; Xu, T., Metasurface-based computational imaging: a review. *Advanced Photonics* **2024,** *6* (1), 014002-014002.

47. Wang, Y.; Zhao, C.; Wang, J.; Luo, X.; Xie, L.; Zhan, S.; Kim, J.; Wang, X.; Liu, X.; Ying, Y., Wearable plasmonic-metasurface sensor for noninvasive and universal molecular fingerprint detection on biointerfaces. *Science Advances* **2021,** *7* (4), eabe4553.

48. Wang, Z.; Chen, J.; Khan, S. A.; Li, F.; Shen, J.; Duan, Q.; Liu, X.; Zhu, J., Plasmonic metasurfaces for medical diagnosis applications: A review. *Sensors* **2021,** *22* (1), 133.

49. Binion, J. D.; Lier, E.; Hand, T. H.; Jiang, Z. H.; Werner, D. H., A metamaterial-enabled design enhancing decades-old short backfire antenna technology for space applications. *Nature communications* **2019,** *10* (1), 108.

50. Agreda, A.; Wu, T.; Hereu, A.; Treguer-Delapierre, M.; Drisko, G. L.; Vynck, K.; Lalanne, P., Tailoring iridescent visual appearance with disordered resonant metasurfaces. *ACS nano* **2023,** *17* (7), 6362-6372.

51. Khorasaninejad, M.; Chen, W.-T.; Oh, J.; Capasso, F., Super-dispersive off-axis meta-lenses for compact high resolution spectroscopy. *Nano letters* **2016,** *16* (6), 3732-3737.

52. Gigli, C.; Li, Q.; Chavel, P.; Leo, G.; Brongersma, M. L.; Lalanne, P., Fundamental limitations of Huygens' metasurfaces for optical beam shaping. *Laser & Photonics Reviews* **2021,** *15* (8), 2000448.

53. Ni, X.; Kildishev, A. V.; Shalaev, V. M., Metasurface holograms for visible light. *Nature communications* **2013,** *4* (1), 2807.

54. Zheng, G.; Mühlenbernd, H.; Kenney, M.; Li, G.; Zentgraf, T.; Zhang, S., Metasurface holograms reaching 80% efficiency. *Nature nanotechnology* **2015,** *10* (4), 308-312.

55. Hossain, M. I.; Yumnam, N.; Qarony, W.; Salleo, A.; Wagner, V.; Knipp, D.; Tsang, Y. H., Non-resonant metal-oxide metasurfaces for efficient perovskite solar cells. *Solar Energy* **2020,** *198*, 570-577.

56. Kuznetsov, A. I.; Miroshnichenko, A. E.; Brongersma, M. L.; Kivshar, Y. S.; Luk'yanchuk, B., Optically resonant dielectric nanostructures. *Science* **2016,** *354* (6314), aag2472.

57. Khorasaninejad, M.; Chen, W. T.; Devlin, R. C.; Oh, J.; Zhu, A. Y.; Capasso, F., Metalenses at visible wavelengths: Diffraction-limited focusing and subwavelength resolution imaging. *Science* **2016,** *352* (6290), 1190-1194.

58. Staude, I.; Schilling, J., Metamaterial-inspired silicon nanophotonics. *Nature Photonics* **2017,** *11* (5), 274-284.

59. Genevet, P.; Capasso, F.; Aieta, F.; Khorasaninejad, M.; Devlin, R., Recent advances in planar optics: from plasmonic to dielectric metasurfaces. *Optica* **2017,** *4* (1), 139-152.

60. Zhan, A.; Colburn, S.; Trivedi, R.; Fryett, T. K.; Dodson, C. M.; Majumdar, A., Low-contrast dielectric metasurface optics. *ACS photonics* **2016,** *3* (2), 209-214.

61. Liu, S.; Sinclair, M. B.; Saravi, S.; Keeler, G. A.; Yang, Y.; Reno, J.; Peake, G. M.; Setzpfandt, F.; Staude, I.; Pertsch, T., Resonantly enhanced second-harmonic generation using III–V semiconductor all-dielectric metasurfaces. *Nano letters* **2016,** *16* (9), 5426-5432.

62. Lee, G.; Yu, E.-S.; Ryu, Y.-S.; Seo, M., The perspectives of broadband metasurfaces and photo-electric tweezer applications. *Nanophotonics* **2022,** *11* (9), 1783-1808.

63. Engelberg, J.; Levy, U., The advantages of metalenses over diffractive lenses. *Nature communications* **2020,** *11* (1), 1991.

64. He, Y.; Song, B.; Tang, J., Optical metalenses: fundamentals, dispersion manipulation, and applications. *Frontiers of Optoelectronics* **2022,** *15* (1), 24.

65. Zhou, G.; Qu, S.-W.; Chen, B.; Zeng, Y.; Chan, C. H., Metasurface-based Fourier lens fed by compact plasmonic optical antennas for wide-angle beam steering. *Optics Express* **2022,** *30* (12), 21918-21930.

66. Tamim, A. M.; Hasan, M. M.; Faruque, M. R. I., Highly efficient metasurface polarization converter at far-infrared range. *Frontiers in Physics* **2022,** *10*, 890356.

67. Chen, M. K.; Wu, Y.; Feng, L.; Fan, Q.; Lu, M.; Xu, T.; Tsai, D. P., Principles, functions, and applications of optical meta-lens. *Advanced Optical Materials* **2021,** *9* (4), 2001414.

68. Yu, P.; Li, J.; Liu, N., Electrically tunable optical metasurfaces for dynamic polarization conversion. *Nano Letters* **2021,** *21* (15), 6690-6695.

69. Thibault, S. In *Consumer electronic optics: how small a lens can be using metasurfaces*, Current Developments in Lens Design and Optical Engineering XX, SPIE: 2019; pp 30-35.

70. Zhang, S.; Wong, C. L.; Zeng, S.; Bi, R.; Tai, K.; Dholakia, K.; Olivo, M., Metasurfaces for biomedical applications: imaging and sensing from a nanophotonics perspective. *Nanophotonics* **2020,** *10* (1), 259-293.

71. Qin, J.; Jiang, S.; Wang, Z.; Cheng, X.; Li, B.; Shi, Y.; Tsai, D. P.; Liu, A. Q.; Huang, W.; Zhu, W., Metasurface micro/nano-optical sensors: principles and applications. *ACS nano* **2022,** *16* (8), 11598-11618.

72. Choi, S.; Zuo, J.; Das, N.; Yao, Y.; Wang, C., Scalable Nanoimprint Manufacturing of Functional Multilayer Metasurface Devices. *Advanced Functional Materials* **2024**, 2404852.

73. Yoon, G.; Tanaka, T.; Zentgraf, T.; Rho, J., Recent progress on metasurfaces: applications and fabrication. *Journal of Physics D: Applied Physics* **2021,** *54* (38), 383002.

74. Wang, S.; Wu, P. C.; Su, V.-C.; Lai, Y.-C.; Chen, M.-K.; Kuo, H. Y.; Chen, B. H.; Chen, Y. H.; Huang, T.-T.; Wang, J.-H., A broadband achromatic metalens in the visible. *Nature nanotechnology* **2018,** *13* (3), 227-232.

75. Wang, Y.; Chen, Q.; Yang, W.; Ji, Z.; Jin, L.; Ma, X.; Song, Q.; Boltasseva, A.; Han, J.; Shalaev, V. M., High-efficiency broadband achromatic metalens for near-IR biological imaging window. *Nature communications* **2021,** *12* (1), 5560.

76. Su, V.-C.; Chu, C. H.; Sun, G.; Tsai, D. P., Advances in optical metasurfaces: fabrication and applications. *Optics express* **2018,** *26* (10), 13148-13182.

77. Tseng, M. L.; Lin, Z. H.; Kuo, H. Y.; Huang, T. T.; Huang, Y. T.; Chung, T. L.; Chu, C. H.; Huang, J. S.; Tsai, D. P., Stress-induced 3D chiral fractal metasurface for enhanced and stabilized broadband near-field optical chirality. *Advanced Optical Materials* **2019,** *7* (15), 1900617.

78. Carletti, L.; Zilli, A.; Moia, F.; Toma, A.; Finazzi, M.; De Angelis, C.; Neshev, D. N.; Celebrano, M., Steering and encoding the polarization of the second harmonic in the visible with a monolithic LiNbO3 metasurface. *ACS photonics* **2021,** *8* (3), 731-737.

79. Gorkunov, M. V.; Rogov, O. Y.; Kondratov, A. V.; Artemov, V. V.; Gainutdinov, R. V.; Ezhov, A. A., Chiral visible light metasurface patterned in monocrystalline silicon by focused ion beam. *Scientific reports* **2018,** *8* (1), 11623.

80. Martin, C.; Ressier, L.; Peyrade, J. P., Study of PMMA recoveries on micrometric patterns replicated by nano-imprint lithography. *Physica E: Low-dimensional Systems and Nanostructures* **2003,** *17*, 523-525.

81. Ressier, L.; Palleau, E.; Behar, S., Electrical nano-imprint lithography. *Nanotechnology* **2012,** *23* (25), 255302.

82. Yoon, G.; Kim, K.; Kim, S.-U.; Han, S.; Lee, H.; Rho, J., Printable nanocomposite metalens for high-contrast near-infrared imaging. *ACS nano* **2021,** *15* (1), 698-706.

83. Chen, M. K.; Zhang, J. C.; Leung, C. W.; Sun, L.; Fan, Y.; Liang, Y.; Yao, J.; Liu, X.; Yuan, J.; Xu, Y., Chiral-magic angle of nanoimprint meta-device. *Nanophotonics* **2023,** *12* (13), 2479-2490.

84. Inogamov, N. A.; Petrov, Y. V.; Khokhlov, V. A.; Zhakhovskii, V. V., Laser ablation: physical concepts and applications. *High Temperature* **2020,** *58*, 632-646.

85. Zhang, D.; Ranjan, B.; Tanaka, T.; Sugioka, K., Carbonized hybrid micro/nanostructured metasurfaces produced by femtosecond laser ablation in organic solvents for biomimetic antireflective surfaces. *ACS Applied Nano Materials* **2020,** *3* (2), 1855-1871.

86. Keil, M.; Wetzel, A. E.; Wu, K.; Khomtchenko, E.; Urbankova, J.; Boisen, A.; Rindzevicius, T.; Bunea, A.-I.; Taboryski, R. J., Large plasmonic color metasurfaces fabricated by super resolution deep UV lithography. *Nanoscale advances* **2021,** *3* (8), 2236-2244.

87. Agha, A.; Waheed, W.; Stiharu, I.; Nerguizian, V.; Destgeer, G.; Abu-Nada, E.; Alazzam, A., A review on microfluidic-assisted nanoparticle synthesis, and their applications using multiscale simulation methods. *Discover Nano* **2023,** *18* (1), 18.

88. VIALLET, B.; MARTIN, C.; RESSIER, L.; GRISOLIA, J.; PEYRADE, J. P., Localization of octadecyltrimethoxysilane self-assembled monolayers by a combination of bottom-up and top-down approaches. *Silanes and Other Coupling Agents, Volume 4* **2007,** *4*, 153.

89. Behar, S.; Viallet, B.; Grisolia, J.; Sangeetha, N.; Ressier, L. In *A bottom-up approach to developing innovative resistive sensors*, 2013 Eurpoean Microelectronics Packaging Conference (EMPC), IEEE: 2013; pp 1-5.

90. Liu, J.; Guillemeney, L.; Choux, A.; Maître, A.; Abécassis, B.; Coolen, L., Fourier-imaging of single self-assembled CdSe nanoplatelet chains and clusters reveals out-of-plane dipole contribution. *ACS photonics* **2020,** *7* (10), 2825-2833.

91. Hu, J.; Bandyopadhyay, S.; Liu, Y.-h.; Shao, L.-y., A review on metasurface: from principle to smart metadevices. *Frontiers in Physics* **2021,** *8*, 586087.

92. Farcau, C.; Moreira, H.; Viallet, B.; Grisolia, J.; Ressier, L., Tunable conductive nanoparticle wire arrays fabricated by convective self-assembly on nonpatterned substrates. *ACS nano* **2010,** *4* (12), 7275-7282.

93. Teulon, L.; Hallez, Y.; Raffy, S.; Guerin, F. o.; Palleau, E.; Ressier, L., Electrostatic directed assembly of colloidal microparticles assisted by convective flow. *The Journal of Physical Chemistry C* **2018,** *123* (1), 783-790.

94. Alias, A. B.; Huang, H.-Y.; Yao, D.-J., A review on microfluidics: An aid to assisted reproductive technology. *Molecules* **2021,** *26* (14), 4354.

95. Ni, S.; Leemann, J.; Buttinoni, I.; Isa, L.; Wolf, H., Programmable colloidal molecules from sequential capillarity-assisted particle assembly. *Science advances* **2016,** *2* (4), e1501779.

96. Virganavičius, D.; Juodėnas, M.; Tamulevičius, T.; Schift, H.; Tamulevičius, S., Investigation of transient dynamics of capillary assisted particle assembly yield. *Applied Surface Science* **2017,** *406*, 136-143.

97. Pioli, R.; Fernandez-Rodriguez, M. A.; Grillo, F.; Alvarez, L.; Stocker, R.; Isa, L.; Secchi, E., Sequential capillarity-assisted particle assembly in a microfluidic channel. *Lab on a Chip* **2021,** *21* (5), 888-895.

98. Yun, H. S.; Meijs, Z. C.; Park, G.; Fu, Y.; Isa, L.; Yoon, D. K., Controlling liquid crystal boojum defects on fixed microparticle arrays via capillarity-assisted particles assembly. *Journal of Colloid and Interface Science* **2023,** *645*, 115-121.

99. Liu, Y.; Yang, G.; Hui, Y.; Ranaweera, S.; Zhao, C. X., Microfluidic nanoparticles for drug delivery. *Small* **2022,** *18* (36), 2106580.

100. Shillingford, C.; Kim, B. M.; Weck, M., Top-down heterogeneous colloidal engineering using capillary assembly of liquid particles. *ACS nano* **2021,** *15* (1), 1640-1651.

101. Das Gupta, T.; Martin-Monier, L.; Yan, W.; Le Bris, A.; Nguyen-Dang, T.; Page, A. G.; Ho, K.-T.; Yesilköy, F.; Altug, H.; Qu, Y., Self-assembly of nanostructured

glass metasurfaces via templated fluid instabilities. *Nature nanotechnology* **2019,** *14* (4), 320-327.

102. Flauraud, V.; Mastrangeli, M.; Bernasconi, G. D.; Butet, J.; Alexander, D. T.; Shahrabi, E.; Martin, O. J.; Brugger, J., Nanoscale topographical control of capillary assembly of nanoparticles. *Nature nanotechnology* **2017,** *12* (1), 73-80.

103. Mayer, M.; Schnepf, M. J.; König, T. A.; Fery, A., Colloidal Self-Assembly Concepts for Plasmonic Metasurfaces. *Advanced Optical Materials* **2019,** *7* (1), 1800564.

104. Gupta, V.; Probst, P. T.; Goßler, F. R.; Steiner, A. M.; Schubert, J.; Brasse, Y.; König, T. A.; Fery, A., Mechanotunable surface lattice resonances in the visible optical range by soft lithography templates and directed self-assembly. *ACS applied materials & interfaces* **2019,** *11* (31), 28189-28196.

105. Timpu, F.; Hendricks, N. R.; Petrov, M.; Ni, S.; Renaut, C.; Wolf, H.; Isa, L.; Kivshar, Y.; Grange, R., Enhanced second-harmonic generation from sequential capillarity-assisted particle assembly of hybrid nanodimers. *Nano letters* **2017,** *17* (9), 5381-5388.

106. Meijs, Z. C.; Yun, H. S.; Fandre, P.; Park, G.; Yoon, D. K.; Isa, L., Pixelated Physical Unclonable Functions through Capillarity-Assisted Particle Assembly. *ACS Applied Materials & Interfaces* **2023,** *15* (45), 53053-53061.

107. Stolle, A.; Szuppa, T.; Leonhardt, S. E.; Ondruschka, B., Ball milling in organic synthesis: solutions and challenges. *Chemical Society Reviews* **2011,** *40* (5), 2317-2329.

108. Koch, C. C. In *The synthesis of non-equilibrium structures by ball-milling*, Materials Science Forum, Trans Tech Publ: 1992; pp 243-262.

109. Okabayashi, H.; Shimizu, I.; Nishio, E.; Connor, C. O., Diffuse reflectance infrared Fourier transform spectral study of the interaction of 3-aminopropyltriethoxysilane on silica gel. Behavior of amino groups on the surface. *Colloid and Polymer Science* **1997,** *275*, 744-753.

110. Mohammed, A.; Abdullah, A. In *Scanning electron microscopy (SEM): A review*, Proceedings of the 2018 international conference on hydraulics and pneumatics—HERVEX, Băile Govora, Romania, 2018; pp 7-9.

111. Joshi, J.; Homburg, S. V.; Ehrmann, A., Atomic force microscopy (AFM) on biopolymers and hydrogels for biotechnological applications—Possibilities and limits. *Polymers* **2022,** *14* (6), 1267.

112. Gao, P. F.; Lei, G.; Huang, C. Z., Dark-field microscopy: recent advances in accurate analysis and emerging applications. *Analytical Chemistry* **2021,** *93* (11), 4707-4726.

113. Babick, F., Dynamic light scattering (DLS). In *Characterization of nanoparticles*, Elsevier: 2020; pp 137-172.

114. Manley, S.; Davidovitch, B.; Davies, N. R.; Cipelletti, L.; Bailey, A.; Christianson, R. J.; Gasser, U.; Prasad, V.; Segre, P.; Doherty, M., Time-dependent strength of colloidal gels. *Physical review letters* **2005,** *95* (4), 048302.

115. Scaffardi, L. B.; Pellegri, N.; De Sanctis, O.; Tocho, J. O., Sizing gold nanoparticles by optical extinction spectroscopy. *Nanotechnology* **2004,** *16* (1), 158.

116. Kim, I.; Ansari, M. A.; Mehmood, M. Q.; Kim, W. S.; Jang, J.; Zubair, M.; Kim, Y. K.; Rho, J., Stimuli-responsive dynamic metaholographic displays with designer liquid crystal modulators. *Advanced Materials* **2020,** *32* (50), 2004664.

117. Jia, X.; Yang, F.; Liu, X.; Li, M.; Xu, S., Fast nonuniform metasurface analysis in FDTD using surface susceptibility model. *IEEE Transactions on Antennas and Propagation* **2019,** *68* (10), 7121-7130.

118. Lesina, A. C.; Vaccari, A.; Berini, P.; Ramunno, L., On the convergence and accuracy of the FDTD method for nanoplasmonics. *Optics Express* **2015,** *23* (8), 10481-10497.

119. Chen, W. T.; Zhu, A. Y.; Capasso, F., Flat optics with dispersion-engineered metasurfaces. *Nature Reviews Materials* **2020,** *5* (8), 604-620.

120. Li, Z.; Dai, Q.; Mehmood, M. Q.; Hu, G.; yanchuk, B. L.; Tao, J.; Hao, C.; Kim, I.; Jeong, H.; Zheng, G., Full-space cloud of random points with a scrambling metasurface. *Light: Science & Applications* **2018,** *7* (1), 63.

121. Chen, W. T.; Zhu, A. Y.; Sisler, J.; Bharwani, Z.; Capasso, F., A broadband achromatic polarization-insensitive metalens consisting of anisotropic nanostructures. *Nature communications* **2019,** *10* (1), 355.

122. Park, J.; Jeong, B. G.; Kim, S. I.; Lee, D.; Kim, J.; Shin, C.; Lee, C. B.; Otsuka, T.; Kyoung, J.; Kim, S., All-solid-state spatial light modulator with independent phase and amplitude control for three-dimensional LiDAR applications. *Nature nanotechnology* **2021,** *16* (1), 69-76.

123. Joo, W.-J.; Kyoung, J.; Esfandyarpour, M.; Lee, S.-H.; Koo, H.; Song, S.; Kwon, Y.-N.; Song, S. H.; Bae, J. C.; Jo, A., Metasurface-driven OLED displays beyond 10,000 pixels per inch. *Science* **2020,** *370* (6515), 459-463.

124. Chu, H.; Li, Q.; Liu, B.; Luo, J.; Sun, S.; Hang, Z. H.; Zhou, L.; Lai, Y., A hybrid invisibility cloak based on integration of transparent metasurfaces and zero-index materials. *Light: Science & Applications* **2018,** *7* (1), 50.

125. Kristensen, A.; Yang, J. K.; Bozhevolnyi, S. I.; Link, S.; Nordlander, P.; Halas, N. J.; Mortensen, N. A., Plasmonic colour generation. *Nature Reviews Materials* **2016,** *2* (1), 1-14.

126. Kumar, K.; Duan, H.; Hegde, R. S.; Koh, S. C.; Wei, J. N.; Yang, J. K., Printing colour at the optical diffraction limit. *Nature nanotechnology* **2012,** *7* (9), 557-561.

127. Khorasaninejad, M.; Capasso, F., Metalenses: Versatile multifunctional photonic components. *Science* **2017,** *358* (6367), eaam8100.

128. Deng, L.; Deng, J.; Guan, Z.; Tao, J.; Chen, Y.; Yang, Y.; Zhang, D.; Tang, J.; Li, Z.; Li, Z., Malus-metasurface-assisted polarization multiplexing. *Light: Science & Applications* **2020,** *9* (1), 101.

129. Miroshnichenko, A. E.; Liu, W.; Neshev, D.; Kivshar, Y. S.; Kuznetsov, A. I.; Fu, Y. H.; Luk'yanchuk, B., Magnetic light: optical magnetism of dielectric nanoparticles. *Optics and Photonics News* **2012,** *23* (12), 35-35.

130. Benson, O., Assembly of hybrid photonic architectures from nanophotonic constituents. *Nature* **2011,** *480* (7376), 193-199.

131. Fan, J. A.; Wu, C.; Bao, K.; Bao, J.; Bardhan, R.; Halas, N. J.; Manoharan, V. N.; Nordlander, P.; Shvets, G.; Capasso, F., Self-assembled plasmonic nanoparticle clusters. *science* **2010,** *328* (5982), 1135-1138.

132. Wang, L.; Ng, R. J. H.; Safari Dinachali, S.; Jalali, M.; Yu, Y.; Yang, J. K., Large area plasmonic color palettes with expanded gamut using colloidal self-assembly. *Acs Photonics* **2016,** *3* (4), 627-633.

133. Verre, R.; Odebo Länk, N.; Andrén, D.; Šípová, H.; Käll, M., Large-Scale Fabrication of Shaped High Index Dielectric Nanoparticles on a Substrate and in Solution. *Advanced Optical Materials* **2018,** *6* (7), 1701253.

134. Castilla, M.; Schuermans, S.; Gérard, D.; Martin, J.; Maurer, T.; Hananel, U.; Markovich, G.; Plain, J.; Proust, J., Colloidal Synthesis of Crystalline Aluminum Nanoparticles for UV Plasmonics. *ACS photonics* **2022,** *9* (3), 880-887.

135. Goris, B.; Guzzinati, G.; Fernández-López, C.; Pérez-Juste, J.; Liz-Marzán, L. M.; Trügler, A.; Hohenester, U.; Verbeeck, J.; Bals, S.; Van Tendeloo, G., Plasmon mapping in Au@ Ag nanocube assemblies. *The Journal of Physical Chemistry C* **2014,** *118* (28), 15356-15362.

136. Glotzer, S. C.; Solomon, M. J., Anisotropy of building blocks and their assembly into complex structures. *Nature materials* **2007,** *6* (8), 557-562.

137. Vigderman, L.; Khanal, B. P.; Zubarev, E. R., Functional gold nanorods: synthesis, self-assembly, and sensing applications. *Advanced materials* **2012,** *24* (36), 4811-4841.

138. Nepal, D.; Onses, M. S.; Park, K.; Jespersen, M.; Thode, C. J.; Nealey, P. F.; Vaia, R. A., Control over position, orientation, and spacing of arrays of gold nanorods using chemically nanopatterned surfaces and tailored particle–particle–surface interactions. *Acs Nano* **2012,** *6* (6), 5693-5701.

139. Shevchenko, E. V.; Talapin, D. V.; Kotov, N. A.; O'Brien, S.; Murray, C. B., Structural diversity in binary nanoparticle superlattices. *Nature* **2006,** *439* (7072), 55-59.

140. Zhong, M.-C.; Liu, A.-Y.; Zhu, R., Optical assembling of micro-particles at a glass–water interface with diffraction patterns caused by the limited aperture of objective. *Applied Sciences* **2018,** *8* (9), 1522.

141. Smith, B. D.; Mayer, T. S.; Keating, C. D., Deterministic assembly of functional nanostructures using nonuniform electric fields. *Annual review of physical chemistry* **2012,** *63*, 241-263.

142. Nie, Z.; Fava, D.; Kumacheva, E.; Zou, S.; Walker, G. C.; Rubinstein, M., Self-assembly of metal–polymer analogues of amphiphilic triblock copolymers. *Nature materials* **2007,** *6* (8), 609-614.

143. Roach, L.; Hereu, A.; Lalanne, P.; Duguet, E.; Tréguer-Delapierre, M.; Vynck, K.; Drisko, G. L., Controlling disorder in self-assembled colloidal monolayers via evaporative processes. *Nanoscale* **2022,** *14* (9), 3324-3345.

144. Honegger, T.; Berton, K.; Picard, E.; Peyrade, D., Determination of Clausius–Mossotti factors and surface capacitances for colloidal particles. *Applied Physics Letters* **2011,** *98* (18).

145. Pileni, M.-P., Nanocrystal self-assemblies: fabrication and collective properties. ACS Publications: 2001; Vol. 105, pp 3358-3371.

146. Jang, J.; Jeong, H.; Hu, G.; Qiu, C. W.; Nam, K. T.; Rho, J., Kerker-conditioned dynamic cryptographic nanoprints. *Advanced Optical Materials* **2019,** *7* (4), 1801070.

147. Holtz, J. H.; Asher, S. A., Polymerized colloidal crystal hydrogel films as intelligent chemical sensing materials. *Nature* **1997,** *389* (6653), 829-832.

148. Haick, H., Chemical sensors based on molecularly modified metallic nanoparticles. *Journal of Physics D: Applied Physics* **2007,** *40* (23), 7173.

149. Del Nero, J.; De Araujo, R.; Gomes, A.; De Melo, C., Theoretical and experimental investigation of the second hyperpolarizabilities of methyl orange. *The Journal of chemical physics* **2005,** *122* (10), 104506.

150. Gourevich, I.; Pham, H.; Jonkman, J. E.; Kumacheva, E., Multidye nanostructured material for optical data storage and security labeling. *Chemistry of materials* **2004,** *16* (8), 1472-1479.

151. Amlani, I.; Rawlett, A. M.; Nagahara, L. A.; Tsui, R. K., An approach to transport measurements of electronic molecules. *Applied Physics Letters* **2002,** *80* (15), 2761-2763.

152. Maier, S. A.; Brongersma, M. L.; Kik, P. G.; Meltzer, S.; Requicha, A. A.; Atwater, H. A., Plasmonics—a route to nanoscale optical devices. *Advanced materials* **2001,** *13* (19), 1501-1505.

153. Steemers, F. J.; Ferguson, J. A.; Walt, D. R., Screening unlabeled DNA targets with randomly ordered fiber-optic gene arrays. *Nature biotechnology* **2000,** *18* (1), 91-94.

154. Malaquin, L.; Kraus, T.; Schmid, H.; Delamarche, E.; Wolf, H., Controlled particle placement through convective and capillary assembly. *Langmuir* **2007,** *23* (23), 11513-11521.

155. Pallandre, A.; Glinel, K.; Jonas, A. M.; Nysten, B., Binary nanopatterned surfaces prepared from silane monolayers. *Nano Letters* **2004,** *4* (2), 365-371.

156. Ansari, M. A.; Waseem, M. H.; Kim, I.; Mahmood, N.; Jeong, H.; Tahir, F. A.; Tauqeer, T.; Mehmood, M. Q.; Rho, J. In *Highly efficient visible hologram through dielectric metasurface*, Journal of Physics: Conference Series, IOP Publishing: 2018; p 012003.

157. Yager, T.; Chikvaidze, G.; Wang, Q.; Fu, Y., Graphene hybrid metasurfaces for mid-infrared molecular sensors. *Nanomaterials* **2023,** *13* (14), 2113.

158. Yu, P.; Li, Z.; Han, M.; Yu, J., Growth of Vertical Graphene Sheets on Silicon Nanoparticles Well-Dispersed on Graphite Particles for High-Performance Lithium-Ion Battery Anode. *Small* **2024,** *20* (17), 2307494.

159. Cao, C.; Steinrück, H. G.; Shyam, B.; Toney, M. F., The atomic scale electrochemical lithiation and delithiation process of silicon. *Advanced Materials Interfaces* **2017,** *4* (22), 1700771.

160. Zhao, Q.; Zhou, J.; Zhang, F.; Lippens, D., Mie resonance-based dielectric metamaterials. *Materials today* **2009,** *12* (12), 60-69.

161. Dohnalová, K.; Gregorkiewicz, T.; Kůsová, K., Silicon quantum dots: surface matters. *Journal of Physics: Condensed Matter* **2014,** *26* (17), 173201.

162. Adeoye, A. E.; Adeaga, O.; Ukoba, K., Chemical Vapour Deposition (CVD) and Physical Vapour Deposition (PVD) techniques: Advances in thin film solar cells. *Nigerian Journal of Technology* **2024,** *43* (3), 479-489.

163. McEnaney, J. M.; Schaak, R. E., Solution synthesis of metal silicide nanoparticles. *Inorganic Chemistry* **2015,** *54* (3), 707-709.

164. Bowser, C. J.; Jones, B. F., Mineralogic controls on the composition of natural waters dominated by silicate hydrolysis. *American Journal of Science* **2002,** *302* (7), 582-662.

165. Kudryashov, S. I.; Nastulyavichus, A. A.; Ivanova, A. K.; Smirnov, N. A.; Khmelnitskiy, R. A.; Rudenko, A. A.; Saraeva, I. N.; Tolordava, E. R.; Kharin, A. Y.; Zavestovskaya, I. N., High-throughput laser generation of Si-nanoparticle based surface coatings for antibacterial applications. *Applied Surface Science* **2019,** *470*, 825-831.

166. Zhu, Y.; Wang, H.; Ong, P., Preparation and thermal stability of silicon nanoparticles. *Applied surface science* **2001,** *171* (1-2), 44-48.

167. Islam, M. M.; Abdellaoui, I.; Moslah, C.; Sakurai, T.; Ksibi, M.; Hamzaoui, S.; Akimoto, K., Electrodeposition and characterization of silicon films obtained through electrochemical reduction of SiO2 nanoparticles. *Thin Solid Films* **2018,** *654*, 1-10.

168. Fouda, A.; Salem, A.; El-Tantawy, F.; Salem, H.; Duraia, E. S. M., Hydrothermal synthesis of high quality graphene nanosheets anchored by uniform and well distributed silicon nanoparticles. *Superlattices and Microstructures* **2018,** *124*, 240-247.

169. Hench, L. L.; West, J. K., The sol-gel process. *Chemical reviews* **1990,** *90* (1), 33-72.

170. Ward, D. A.; Ko, E. I., Preparing catalytic materials by the sol-gel method. *Industrial & engineering chemistry research* **1995,** *34* (2), 421-433.

171. Atkins, T. M.; Louie, A. Y.; Kauzlarich, S. M., An efficient microwave-assisted synthesis method for the production of water soluble amine-terminated Si nanoparticles. *Nanotechnology* **2012,** *23* (29), 294006.

172. Serrano-Bayona, R.; Chu, C.; Liu, P.; Roberts, W. L., Flame synthesis of carbon and metal-oxide nanoparticles: flame types, effects of combustion parameters on properties and measurement methods. *Materials* **2023,** *16* (3), 1192.

173. Qingyu, M.; Bing, G.; Qingliang, Z.; Li, H. N.; Jackson, M. J.; Linke, B. S.; Xichun, L., Modelling of grinding mechanics: A review. *Chinese Journal of Aeronautics* **2023,** *36* (7), 25-39.

174. Zhang, L.; Suto, T.; Noguchi, H.; Waida, T., An overview of applied mechanics in grinding. *Manufacturing Review(USA)* **1992,** *5* (4), 261-273.

175. Basset, D.; Matteazzi, P.; Miani, F., Designing a high energy ball-mill for synthesis of nanophase materials in large quantities. *Materials Science and Engineering: A* **1993,** *168* (2), 149-152.

176. Oliveira, J. G.; Barabási, A.-L., Darwin and Einstein correspondence patterns. *Nature* **2005,** *437* (7063), 1251-1251.

177. Illustrator, A., Adobe Illustrator. *adobe. com,[Online]. Available* **2021**.

178. Pereira, M.; Baruah, B. In *A novel GDSII compression technique*, 25th Annual BACUS Symposium on Photomask Technology, SPIE: 2005; pp 1066-1073.

Chapter 8

French Summary

Les nanoparticules de silicium (Si NPs) présentent des propriétés optiques remarquables, telles qu'un indice de réfraction élevé et de faibles pertes, qui en font des matériaux idéaux pour la fabrication de métasurfaces tout-diélectriques. Grâce à des méthodes de préparation simples et efficaces, comme le broyage mécanique avec un blender de cuisine, il est possible d'obtenir des particules uniformes et bien dispersées, compatibles avec des techniques d'assemblage innovantes. Parmi celles-ci, l'assemblage assisté par microfluidique se distingue par sa précision, sa flexibilité et son faible coût, permettant l'organisation contrôlée des nanoparticules sur des substrats nanostructurés. Cette approche, fondée sur les forces capillaires et l'évaporation dirigée, favorise la fabrication de structures complexes aux performances optiques avancées, tout en répondant aux exigences de durabilité, de miniaturisation et d'intégration dans les technologies photoniques modernes.

Chapter 8: French Summary

8.1 Introduction aux nanoparticules de silicium (Si NPs) et aux métasurfaces : principes, fabrication et assemblage

Les nanoparticules de silicium (Si NPs) sont bien adaptées aux métasurfaces diélectriques grâce à leur fort indice de réfraction, leurs faibles pertes optiques et leur compatibilité avec les procédés CMOS. Elles sont aussi appréciées pour leur stabilité thermique, leur solidité et leur faible coût, ce qui les rend utiles dans l'optoélectronique, l'aérospatiale et d'autres domaines. Contrairement aux méthodes top-down complexes et coûteuses, l'assemblage microfluidique bottom-up est plus simple, économique et adapté à la production à grande échelle. En utilisant l'évaporation du solvant et les forces capillaires, cette méthode permet de positionner précisément les Si NPs sur des substrats nanopatternés. Elle facilite ainsi la fabrication de métasurfaces complexes et ouvre des perspectives prometteuses en photonique, détection, télécommunications et imagerie.

8.2 Fundamentals of Metasurfaces and Assembly Techniques

Les métasurfaces sont des équivalents bidimensionnels des métamatériaux, composées d'un réseau d'éléments nanostructurés appelés « méta-atomes », espacés à l'échelle sublongueur d'onde. Chaque méta-atome, par sa forme, sa taille et sa composition, est conçu pour manipuler localement la phase, l'amplitude et la polarisation de la lumière incidente, offrant ainsi un contrôle optique inédit. En ajustant finement ces paramètres, les métasurfaces permettent la réalisation de fonctions avancées telles que lentilles plates (métalenses), filtres optiques, modulateurs de faisceau et convertisseurs de polarisation. Comme illustré dans la **Figure 8.1**, elles peuvent aussi contrôler des propriétés comme l'absorption, la transmission, la réflexion ou encore la résonance. Grâce à leur compacité et leur grande efficacité, les métasurfaces trouvent des applications variées en imagerie,

télécommunications, détection et optique quantique, ouvrant la voie à une nouvelle génération de dispositifs photoniques ultra-performants.

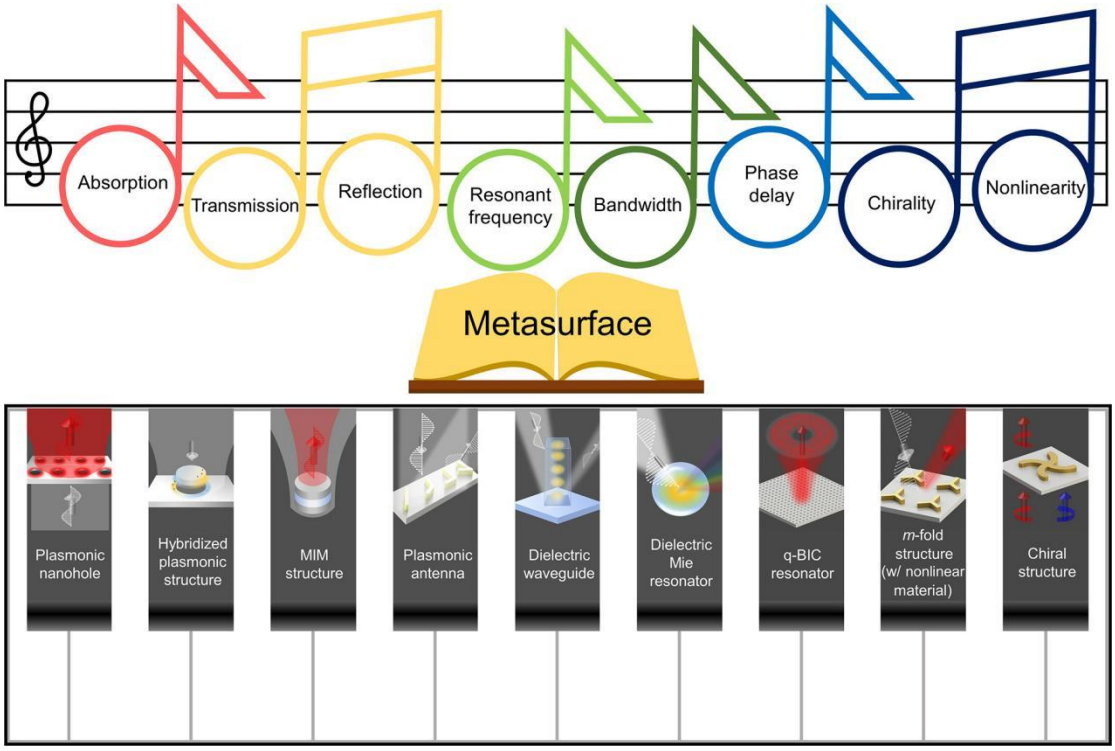


Figure 8.1: Schéma des principes fondamentaux des dispositifs à métasurfaces et de leurs propriétés optiques.

8.3 Préparation des nanoparticules de silicium (Si NPs) et conception expérimentale

Ce chapitre présente une approche complète pour la préparation et l'assemblage de nanoparticules de silicium (Si NPs) sur des substrats nanopatternés. Deux méthodes de broyage, le mixeur de cuisine et le broyeur à billes, ont été utilisées pour produire des Si NPs de tailles contrôlées. La lithographie électronique permet la fabrication précise des motifs, tandis que la silanisation améliore l'adhésion des particules. L'assemblage microfluidique assisté par capillarité assure un dépôt ordonné dans les motifs, suivi du retrait du PMMA. Des outils comme le SEM, l'AFM, la microscopie en champ sombre, la spectroscopie d'extinction et les simulations FDTD ont permis d'analyser les propriétés structurales et optiques des structures obtenues.

8.3.1 Méthodes de préparation des matériaux

Pour préparer les nanoparticules de silicium (Si NPs), deux méthodes mécaniques ont été utilisées : le mixeur de cuisine et le broyeur à billes. La méthode du mixeur, illustrée en **Figure 8.2**, est simple, rapide et économique. Elle permet d'obtenir des Si NPs bien dispersées dans l'eau, idéales pour l'assemblage microfluidique. Des blocs de silicium pur sont broyés dans de l'eau ultrapure, puis les particules sont récupérées après décantation et centrifugation.

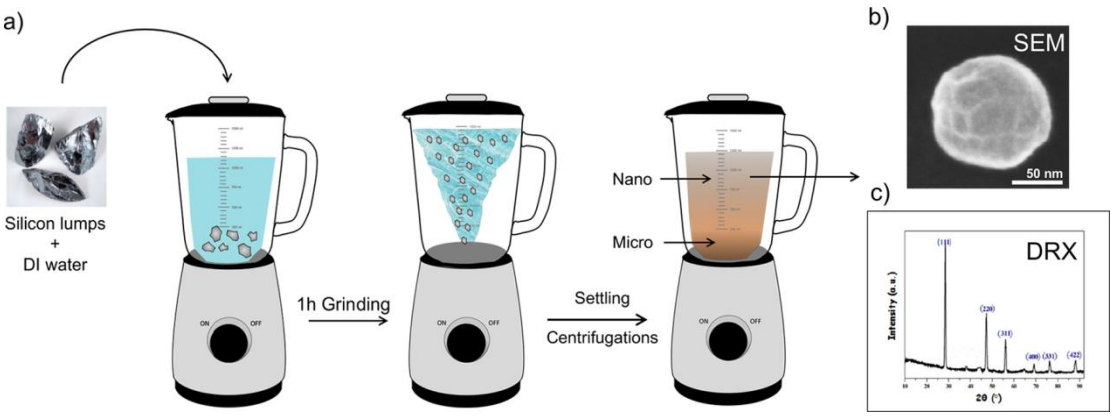


Figure 8.2: (a) Schéma du procédé de préparation des nanoparticules de silicium colloïdales (broyage et clarification). (b) Image MEB à fort grossissement d'une nanoparticule de silicium cristalline déposée sur un substrat. (c) Diagramme de diffraction des rayons X (XRD) montrant la phase du silicium.

Le broyage à billes offre un meilleur contrôle sur la taille et la forme des particules, avec la possibilité d'obtenir des NPs sphériques ou cubiques. Toutefois, l'utilisation d'éthanol comme solvant peut compliquer l'assemblage. En combinant ces deux méthodes, on obtient une solution flexible et efficace, adaptée aux différentes exigences de la fabrication de métasurfaces.

8.3.2 Experimental design of capillary force assisted Si nanoparticle assembly

Cette section présente l'assemblage des nanoparticules de silicium (Si NPs) sur des substrats nanopatternés, réalisé par capillarité à l'aide d'un système microfluidique. Les substrats ont été fabriqués par lithographie électronique (EBL) sur du silicium recouvert de SiO_2 (300 nm). Après nettoyage, une couche de PMMA (150 nm) a été déposée par spin coating (**Figure 8.3**), puis les motifs ont été définis par EBL (**Figure 8.4a**). Pour fixer les Si NPs, une étape de silanisation a été réalisée avec une solution d'APTES et d'éthanol. Cette réaction crée des liaisons chimiques entre les particules et le substrat (**Figure 8.4b**). L'assemblage s'effectue ensuite par évaporation lente de la solution de Si NPs, les forces capillaires guidant les particules dans les cavités du motif.

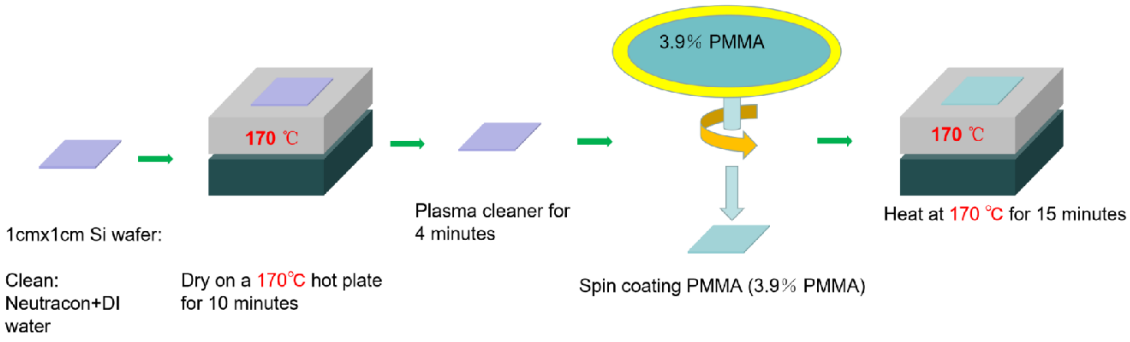


Figure 8.3: Schéma du procédé de spin coating du PMMA.

Après assemblage, le PMMA est retiré à l'acétone, laissant les particules fixées grâce à la silanisation. Des images SEM et en champ sombre confirment la qualité de l'alignement. Ce procédé simple et efficace permet d'obtenir des structures stables et bien organisées, utiles pour des applications en optique et en électronique.

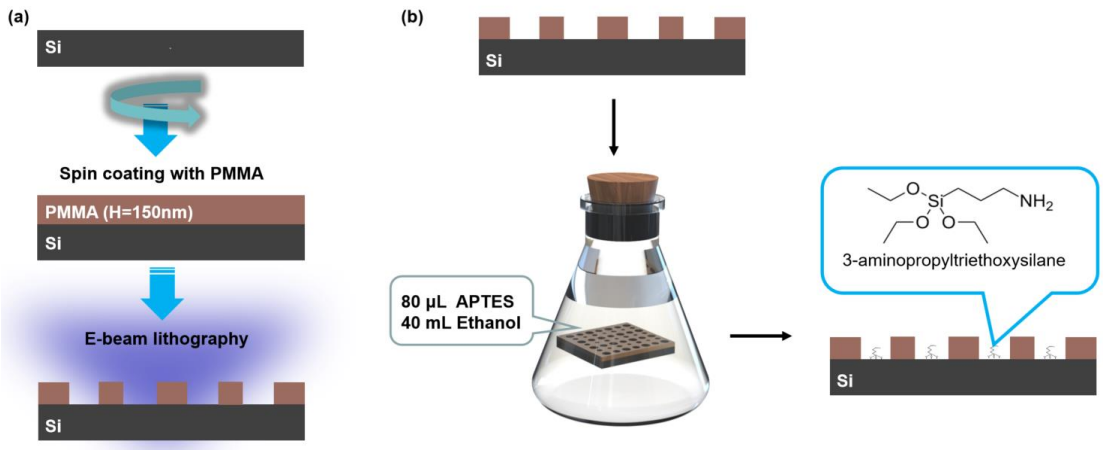


Figure 8.4: (a) Organigramme du processus de fabrication d'un substrat nanopatterné par lithographie électronique. (b) Schéma du processus de réaction de silanisation.

Dans cette étude, l'assemblage des nanoparticules de silicium (Si NPs) a été réalisé à l'aide d'un dispositif microfluidique Smart Force, qui permet de contrôler précisément l'évaporation et les forces capillaires dans une chambre fermée. Une solution concentrée de Si NPs est injectée dans un canal microfluidique, où l'évaporation lente, régulée par l'air et la température, entraîne le dépôt progressif des particules dans les rainures du substrat nanopatterné (**Figure 8.5**). Le processus dure environ une journée. La qualité de l'assemblage dépend de plusieurs paramètres clés : profondeur et diamètre des rainures, température du substrat, vitesse d'évaporation et déplacement du liquide.

Après l'assemblage, le gabarit en PMMA est retiré par un bain d'acétone de trois heures. Grâce à la silanisation préalable, les Si NPs restent solidement fixées sur le substrat. Cette étape est essentielle : elle libère la surface des particules pour des applications optiques ou fonctionnelles, améliore les propriétés de surface, et prépare l'échantillon pour d'éventuels traitements supplémentaires.

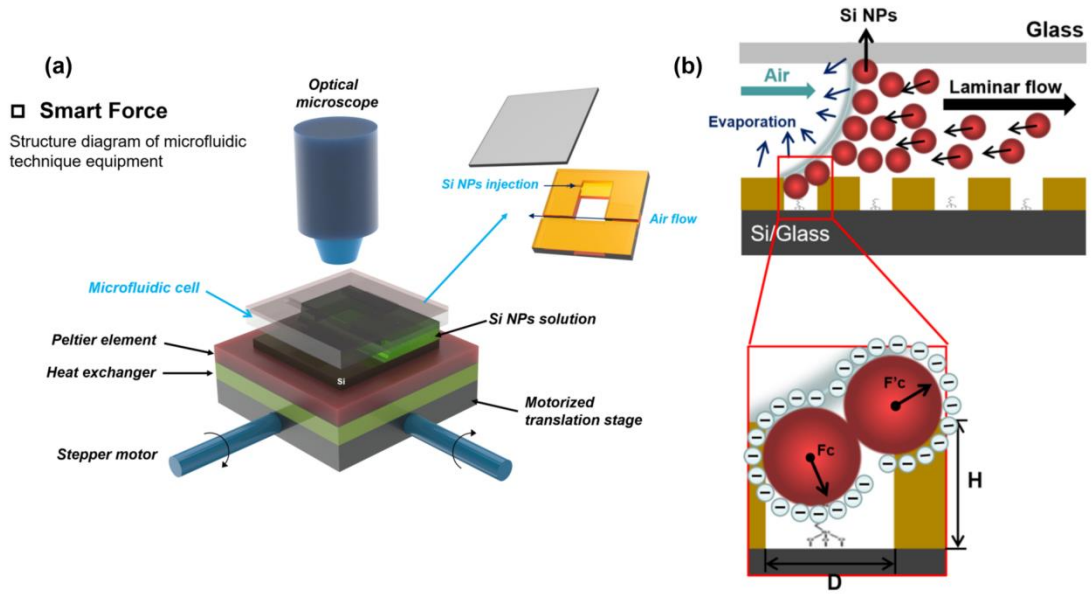


Figure 8.5: (a) Montage expérimental conçu pour l'assemblage convectif et capillaire contrôlé des nanoparticules de silicium sur un substrat nanopatterné, avec régulation de la température par un élément Peltier. (b) Schéma de l'assemblage assisté par force capillaire des nanoparticules de silicium.

8.3.3 Characterization tools and data analysis methods

Cette section présente les outils de caractérisation et les méthodes d'analyse utilisés pour étudier les propriétés des nanoparticules de silicium (Si NPs) et de leurs structures assemblées. La caractérisation précise des aspects morphologiques, structurels et optiques est essentielle pour valider les méthodes de préparation et d'assemblage. Pour cela, nous avons utilisé la microscopie électronique à balayage (SEM), la microscopie à force atomique (AFM) et la microscopie en champ sombre (DFM) afin d'observer les structures physiques des NPs. La diffusion dynamique de la lumière (DLS) et la spectroscopie d'extinction ont permis d'analyser les propriétés optiques et la taille des particules. Enfin, des simulations FDTD ont apporté un appui théorique pour comprendre les interactions lumière–matière dans les nanostructures. L'ensemble de ces techniques offre une évaluation complète, utile pour optimiser le processus d'assemblage et explorer ses applications futures.

8.3.4 Conclusions

Ce chapitre présente une approche complète pour la préparation et l'assemblage de nanoparticules de silicium (Si NPs) sur des substrats nanopatternés. Deux méthodes mécaniques ont été utilisées : le mixeur de cuisine, simple et économique, adapté à l'assemblage microfluidique, et le broyeur à billes, offrant un bon contrôle sur la taille des particules. La lithographie électronique (EBL) a permis de créer des motifs précis, tandis que la silanisation à l'APTES a assuré une bonne fixation des particules. L'assemblage, réalisé par capillarité dans un système microfluidique, a donné des structures uniformes et bien alignées. Les analyses par SEM, AFM, microscopie en champ sombre et spectroscopie d'extinction ont confirmé la qualité des structures, soutenues par des simulations FDTD. Cette méthode intégrée offre une base solide pour des applications en nanophotonique, capteurs optiques et dispositifs multifonctionnels.

8.4 Assemblage microfluidique des nanoparticules de silicium

Les métasurfaces sont constituées de réseaux nanostructurés nécessitant un agencement précis. Dans cette étude, nous avons utilisé un mixeur domestique pour broyer des blocs de silicium et obtenir des nanoparticules (Si NPs), ensuite assemblées sur un substrat structuré par techniques microfluidiques. L'assemblage, guidé par les forces capillaires issues de l'évaporation de gouttelettes, permet aux Si NPs de se positionner dans des pièges nanofabriqués. Cette méthode contourne les limites des approches top-down classiques, notamment leur coût et leur complexité. Nos résultats soulignent l'importance de la qualité des NPs, de la silanisation et du bon contrôle des paramètres pour garantir un assemblage réussi. Cette approche représente une solution simple et efficace pour fabriquer des métasurfaces dans divers domaines.

8.4.1 Introduction

Les métasurfaces sont formées de réseaux périodiques de nanostructures appelées méta-atomes, dont la forme et la composition permettent de contrôler la lumière (phase, transmission, réflexion). Elles sont utilisées dans l'imagerie, les lentilles ultra-minces ou les dispositifs anti-contrefaçon. Pour réduire les pertes optiques des matériaux plasmoniques, les nanoparticules diélectriques comme le silicium offrent une alternative efficace. Parmi les méthodes d'assemblage, celle assistée par capillarité permet un positionnement précis des NPs grâce à l'évaporation contrôlée d'une solution. Dans cette étude, nous avons produit des Si NPs à l'aide d'un mixeur domestique, puis utilisé la silanisation pour les fixer au substrat. Enfin, un système microfluidique a permis un assemblage uniforme dans des motifs nanostructurés. Cette approche simple, précise et reproductible ouvre des perspectives pour des applications en photonique, capteurs et nanotechnologie.

8.4.2 Partie expérimentale

Dans cette expérience, nous avons combiné la nanostructuration, la silanisation et l'assemblage assisté par capillarité pour aligner avec précision des nanoparticules de silicium (Si NPs) sur un substrat. Comme montré à la **Figure 8.6a**, une couche de PMMA de 150 nm est déposée sur un substrat verre-silicium, puis gravée par lithographie électronique pour créer un réseau régulier de nanoholes servant de gabarit d'assemblage. Ensuite, le substrat est silanisé dans une solution d'APTES et d'éthanol (**Figure 8.6b**), ce qui renforce l'adhérence chimique des NPs. Lors de l'assemblage (**Figure 8.6c**), l'évaporation contrôlée de la solution induit un flux qui dirige les Si NPs vers les nanoholes grâce aux forces capillaires. La profondeur et le diamètre des trous, ainsi que les conditions d'évaporation, jouent un rôle clé dans la qualité de l'alignement.

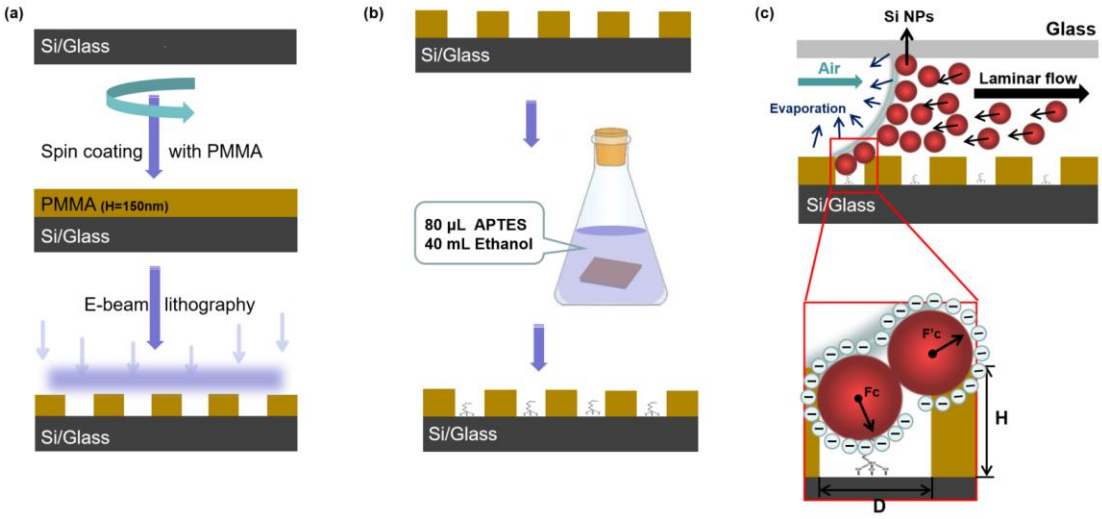


Figure 8.6: (a) Préparation du substrat : dépôt de PMMA puis lithographie E-beam. (b) Silanisation : immersion dans une solution d'APTES (80 µL) et d'éthanol (40 mL). (c) Assemblage : l'évaporation crée un flux qui concentre les Si NPs à l'interface, où les forces capillaires les déposent dans les nanoholes. La profondeur (*H*) et le diamètre (*D*) des trous influencent l'assemblage.

8.4.3 Résultats et discussion

La qualité morphologique et colloïdale des nanoparticules de silicium (Si NPs) est essentielle pour garantir un assemblage efficace. Dans cette étude, les Si NPs ont été préparées selon la méthode de Wajdi et al., en broyant des blocs de silicium dans de l'eau déionisée à l'aide d'un mixeur domestique (**Figure 8.7a**). Après décantation et centrifugation, une solution colloïdale stable est obtenue. Le potentiel zêta mesuré à – 33,5 mV confirme une bonne stabilité électrostatique, limitant l'agrégation. Les images SEM révèlent des particules sphériques de taille homogène, favorables aux applications optiques. La **Figure 8.7b** montre également des images optiques illustrant des effets de diffusion colorés, liés à la taille des particules, ouvrant des perspectives pour les capteurs optiques et dispositifs plasmoniques.

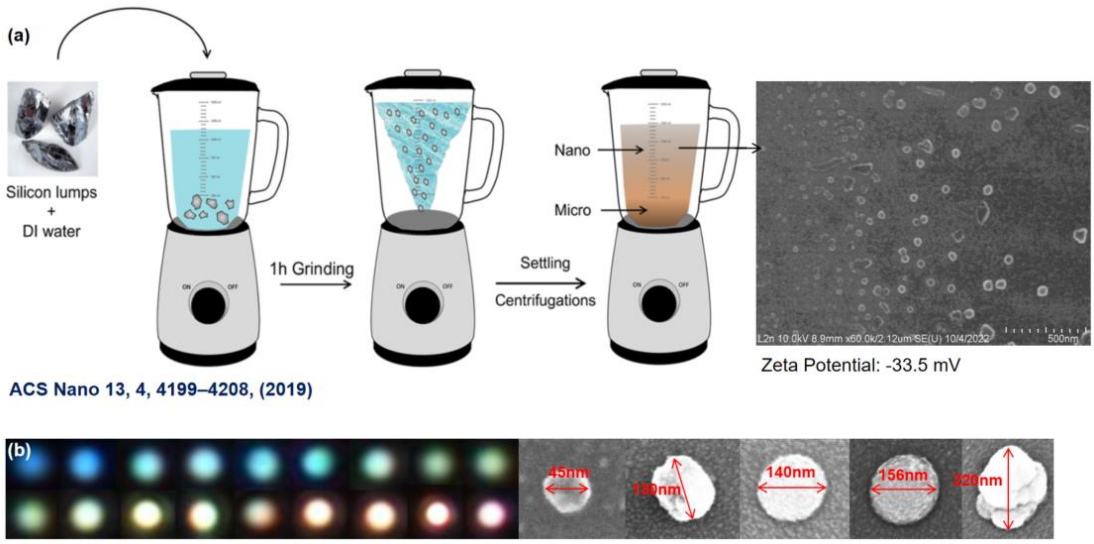


Figure 8.7: (a) Schéma du broyage au mixeur pour obtenir des Si NPs. Après décantation et centrifugation, une suspension stable est obtenue (zêta : -33,5 mV). Image SEM montrant leur forme. (b) Images optiques et SEM des Si NPs (45–220 nm), avec des couleurs variées dues à la diffusion selon la taille.

Comme illustré dans la **Figure 8.8**, nous avons comparé plusieurs ratios : (a) 5 g Si / 300 mL DI; (b) 10 g Si / 300 mL DI; (c) 20 g Si / 300 mL DI. Le mélange 10 g / 300 mL a produit les NPs les plus homogènes et dispersées. Un ratio trop élevé (20 g) a conduit à des agrégats, tandis qu'un ratio trop bas (5 g) a produit trop peu de NPs.

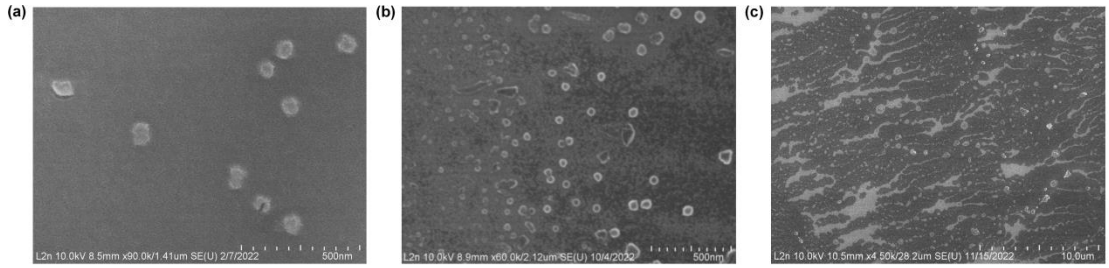


Figure 8.8: Images SEM des Si NPs obtenues avec trois rapports de préparation :(a) 5 g Si + 300 mL DI; (b) 10 g Si + 300 mL DI; (c) 20 g Si + 300 mL DI.

Le rapport optimal est 10 g / 300 mL. Cette étape de préparation, à la fois simple, peu coûteuse et reproductible, fournit une base fiable pour les applications en nanophotonique, détection optique, et catalyse. Les tailles uniformes et la stabilité colloïdale obtenues sont des critères essentiels pour les futures optimisations. Pour

concentrer davantage la solution, nous avons simplement chauffé le liquide sur une plaque chauffante. Cette étape, sans ajout de solvants organiques, est écologique et permet d'ajuster la concentration pour une assemblage plus efficace.

Pour valider l'assemblage assisté par capillarité, nous avons conçu un substrat en silicium comportant deux zones de nanoholes (**Figure 8.9**). La Zone 1 contient des motifs carrés avec des trous de diamètres variés (150 à 300 nm), tandis que la Zone 2 présente un réseau uniforme de trous de 300 nm, tous espacés de 600 nm. Cette configuration permet de comparer l'efficacité d'assemblage selon la géométrie. Pour assurer la stabilité des Si NPs après l'assemblage, une silanisation préalable a été réalisée afin de fixer les particules au substrat et éviter leur décollement lors du retrait du PMMA.

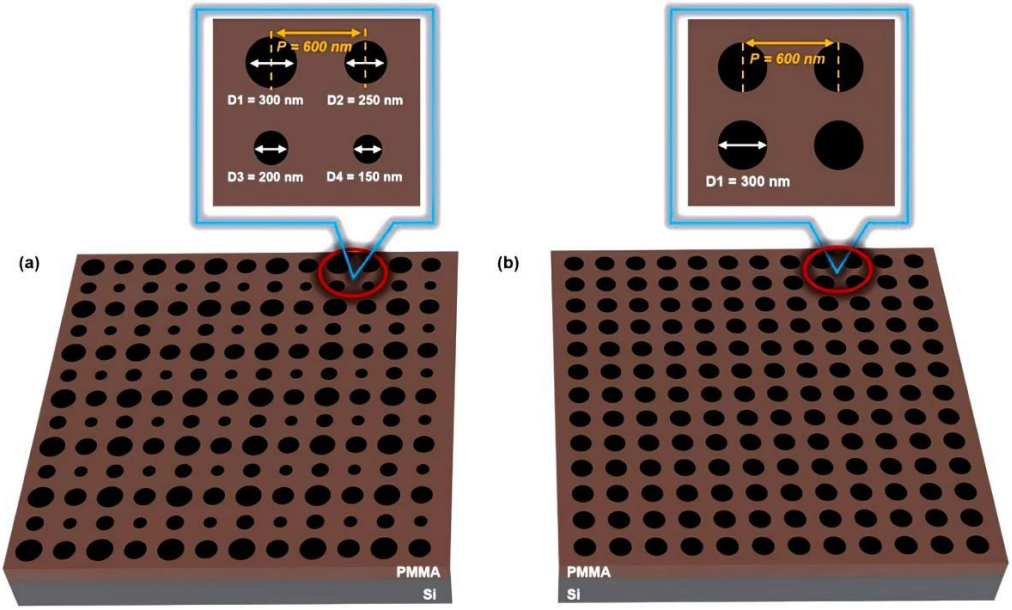
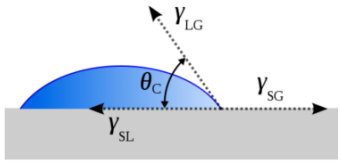
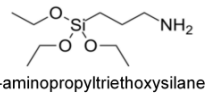


Figure 8.9: (a) Zone 1 : réseau de nanoholes avec quatre tailles différentes (150, 200, 250, 300 nm) — périodicité : 600 nm. (b) Zone 2 : réseau uniforme avec des trous de 300 nm — périodicité : 600 nm.

Cette architecture à double zone constitue une plateforme idéale pour étudier l'impact des dimensions des pièges nanométriques sur l'efficacité de capture et l'organisation des NPs. Ce design modulaire peut être exploité pour des études comparatives, tout en servant de base pour des dispositifs optiques avancés.

La réaction de silanisation a été réalisée dans un récipient hermétique, contenant un mélange d'APTES (80 µL) et d'éthanol (40 mL). Pour garantir le succès de l'assemblage ultérieur, il était indispensable de vérifier l'efficacité de cette modification chimique. Illustré par la **Figure 8.10**, trois échantillons de substrats en silicium ont été préparés pour mesurer l'angle de contact avant et après traitement : Échantillon 1 : substrat soumis uniquement à une irradiation UV (témoin); Échantillons 2 & 3 : même traitement UV suivi d'une silanisation. Les résultats de mesure de l'angle de contact ont été les suivants : Échantillon 1 : 4,31° (surface très hydrophile); Échantillons 2 & 3 : 62,60° et 62,63°. Ces valeurs sont en accord avec la littérature scientifique, où la densité de greffage de l'APTES augmente significativement après silanisation, entraînant une élévation de l'angle de contact de 22° à près de 70°.





3-aminopropyltriethoxysilane

	Si+UV Light	Si+UV Light+silanization reaction[soak the sample in amixture of ethanol(40mL) and APTES(80µL) for 3 hours]	
Sample	1	2	3
Contact angle (θc)	4.31	62.60 [10]	62.63
Surface free energy		46.14 mN/m Part dispersive: 31.41 Part polarize: 14.72 [11]	46.89 mN/m Part dispersive: 32.76 Part polarize: 14.13

Figure 8.10: Mesure de l'angle de contact des substrats de Si avant et après la silanisation.

Passage de 4,3° à plus de 62°, confirmant le succès de la modification chimique. Cette analyse confirme la réussite de la réaction de silanisation, qui joue un rôle fondamental dans la fixation des Si NPs au substrat. Elle garantit la stabilité mécanique et chimique nécessaire au retrait du PMMA et à l'intégrité des assemblages finaux. Cette méthode est également transposable à d'autres substrats ou types de fonctionnalisation, élargissant ses perspectives d'application en

nanofabrication.

Nous avons utilisé un dispositif microfluidique appelé Smart Force pour assembler les Si NPs sur des substrats de silicium nanopatternés. Comme illustré en **Figure 8.11(a)**, le contrôle de la température (35,6 °C) et du flux d'air (50,2 mL/min) induit une évaporation dirigée du liquide. Cette évaporation crée une zone d'accumulation à l'interface air-liquide où les Si NPs se concentrent avant d'être guidées, par force capillaire, dans les nanoholes du substrat. La surface du substrat a été préalablement silanisée, offrant un angle de contact récessif ~62°, optimal pour le dépôt capillaire.

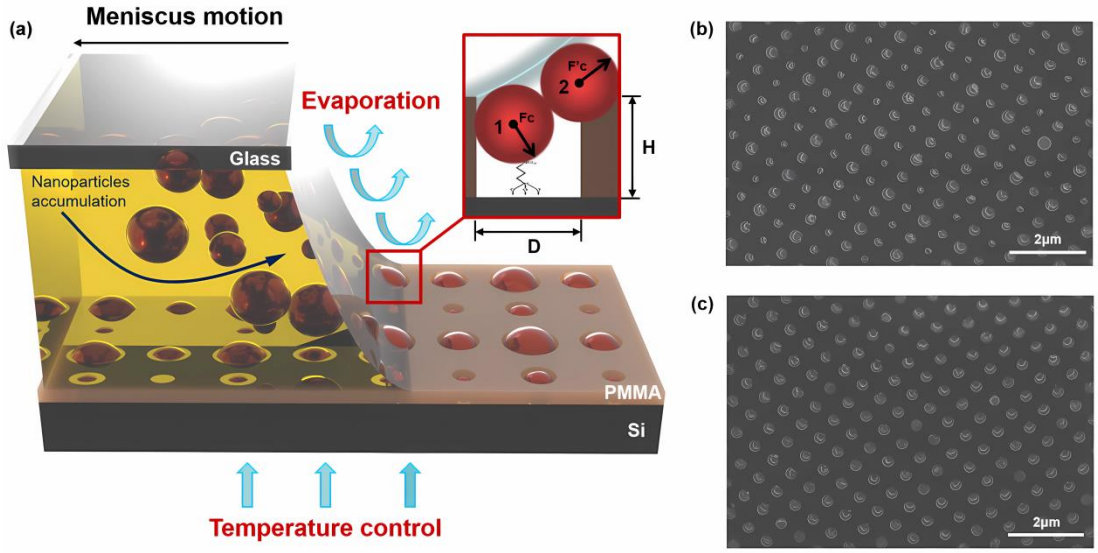


Figure 8.11: (a) Schéma du processus d'assemblage capillaire dans Smart Force : les forces capillaires (Fc) poussent les NPs dans les pièges nanométriques. (b) Image SEM d'un assemblage aléatoire – Zone 1. (c) Image SEM – Zone 2 montrant le dépôt unitaire de NPs.

Comme détaillé en **Figure 8.11(a)**, le ménisque exerce une force capillaire Fc sur une nanoparticule (NP_1), la poussant dans un nanohole. Cette force est partiellement transmise à une seconde nanoparticule (NP_2), qui est expulsée du piège — garantissant un dépôt unitaire. L'imagerie SEM confirme que dans les zones 1 et 2, les NPs sont déposées avec une précision proche de 99 % dans les matrices PMMA, illustré par la **Figure 8.11 (b), (c)**. Pour obtenir les propriétés optiques, la matrice de PMMA est dissoute dans l'acétone (3 h). Comme le montre la **Figure 8.12**, les NPs

restent fixées au substrat après retrait, confirmant le rôle clé de la silanisation. Les images AFM en encart confirment la précision d'assemblage. Les spectres d'extinction montrent des résonances optiques dans l'infrarouge proche (NIR), indiquant un fort potentiel pour des dispositifs optiques actifs.

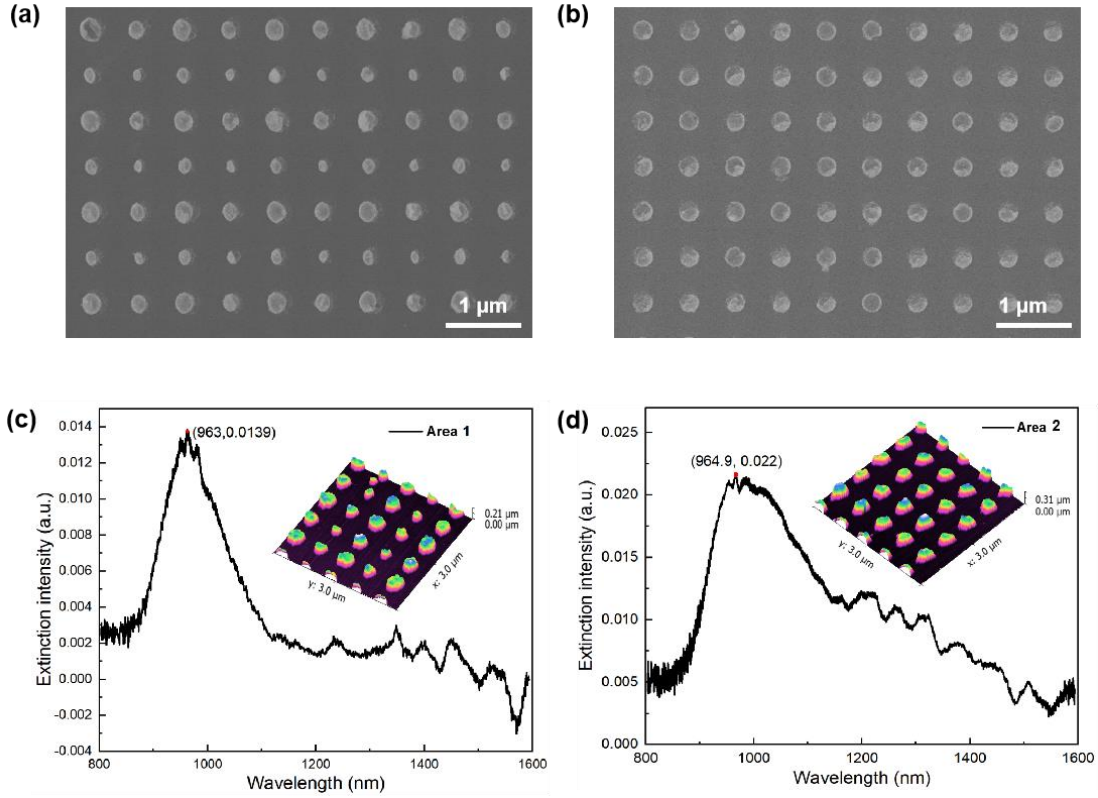


Figure 8.12: (a–b) Images SEM des zones 1 et 2 après retrait du PMMA – NPs bien fixées. (c–d) Spectres d'extinction et images AFM associées – résonances observées en NIR.

La **Figure 8.13** montre des images en champ sombre avant et après retrait du PMMA. On observe clairement la persistance des NPs sur le substrat, validant la solidité de l'assemblage.

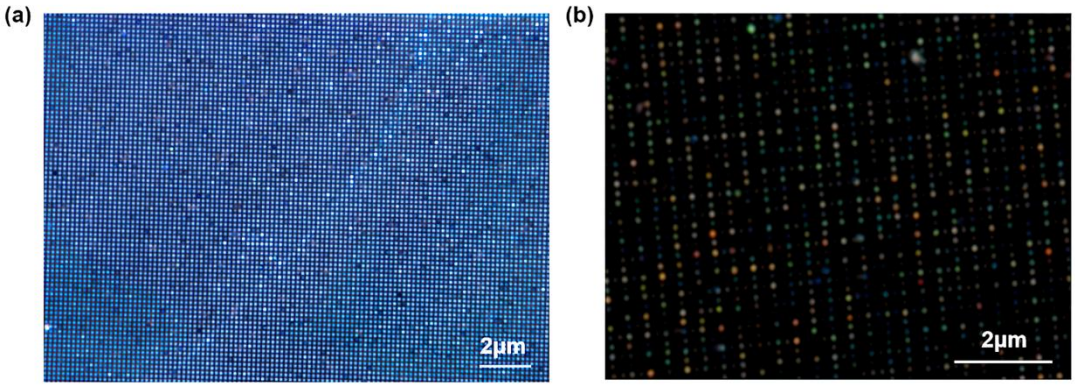


Figure 8.13: (a) Image champ sombre avec matrice PMMA (b) Image après retrait du PMMA – NPs toujours présentes.

Nous avons mesuré la taille moyenne des NPs déposées dans les 4 types de trous (Zone 1) : 151 ± 20 nm; 197 ± 15 nm; 236 ± 10 nm; 288 ± 14 nm. La **Figure 8.14** illustre l'analyse statistique des tailles (histogrammes) ainsi que les couleurs RGB observées par microscopie. Une corrélation claire entre taille des NPs et couleur diffusée (du rose au bleu) est observée.

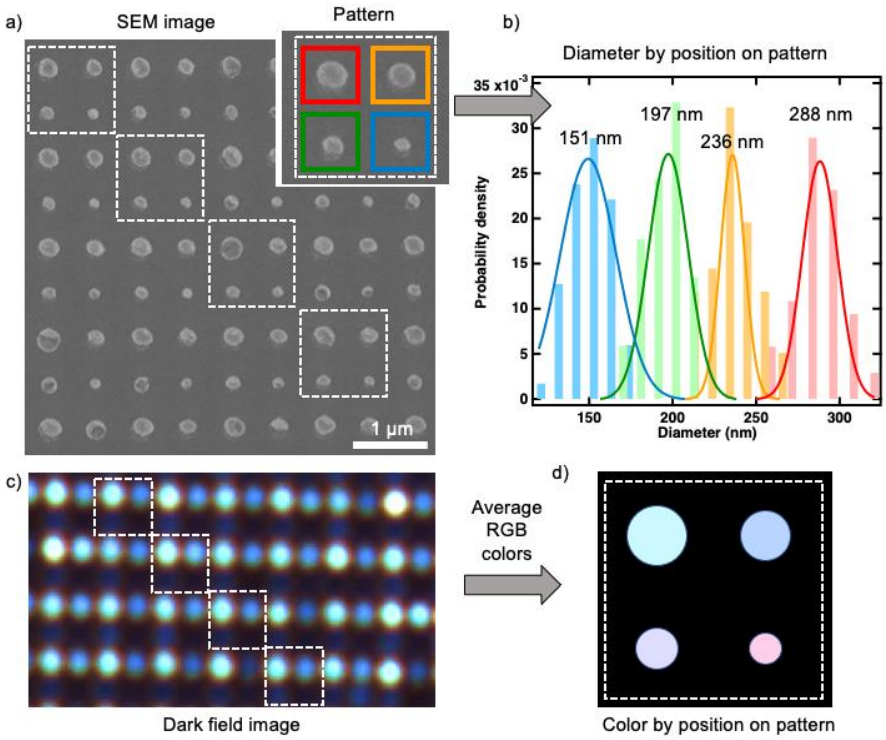


Figure 8.14: (a) Zoom SEM sur les 4 types de trous. (b) Histogrammes des tailles de NPs piégées. (c) Image champ sombre correspondante. (d) Représentation schématique des couleurs RGB.

Grâce à l'imagerie SEM, AFM et en champ sombre, nous avons démontré un assemblage précis, reproductible et optiquement actif. La variation contrôlée des tailles de trous permet de moduler la capture et les propriétés optiques des Si NPs. Cette approche pose une base solide pour des applications en photonique, détection optique, et métasurfaces intelligentes. Ce protocole multi-étapes démontre l'efficacité d'un assemblage de NPs de Si précis, en combinant nanopatterning et dynamique des fluides. Cette méthode pose une base solide pour l'étude des propriétés optiques et électroniques des NPs, ainsi que pour leurs applications fonctionnelles futures.

8.4.4 Analyse auxiliaire des expériences de référence

En complément des expériences réussies, nous avons analysé plusieurs échantillons d'assemblage non réussi, afin d'identifier les facteurs clés conditionnant le succès. La **Figure 8.15(a) et (d)** montre des zones où aucune NP n'est présente dans les nanoholes. Après un bain dans l'acétone pendant 3 heures, les images SEM (**15b et 15e**) et AFM (**15c et 15f**) confirment l'absence de particules : seules des traces résiduelles de PMMA subsistent.

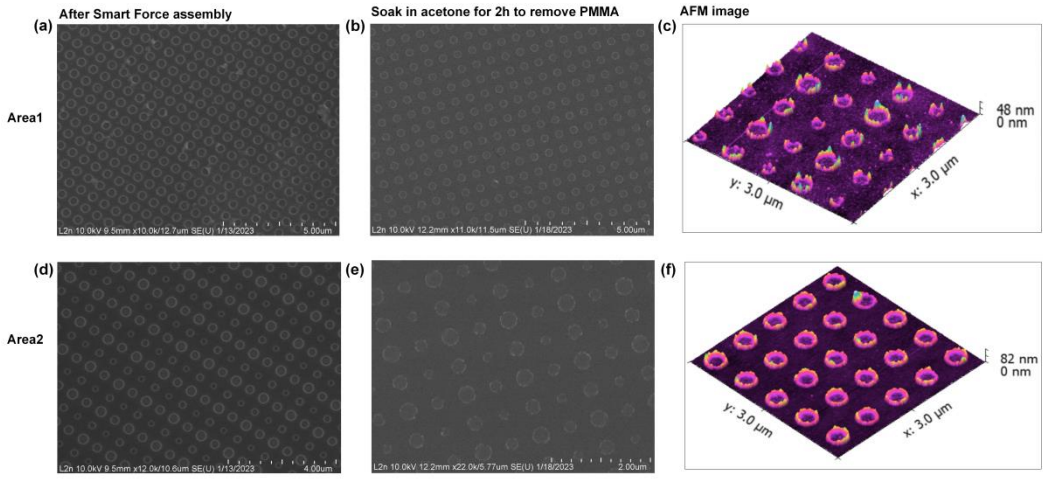


Figure 8.15: (a–c) Zone 1 : avant/après retrait du PMMA + AFM – aucune NP observée. (d–f) Zone 2 : même résultat, absence totale de NPs.

La **Figure 8.16** montre que l'absence de NPs est également visible via imagerie optique. Contrairement aux résultats réussis, ici aucun signal lumineux caractéristique des NPs n'est détecté après retrait du PMMA.

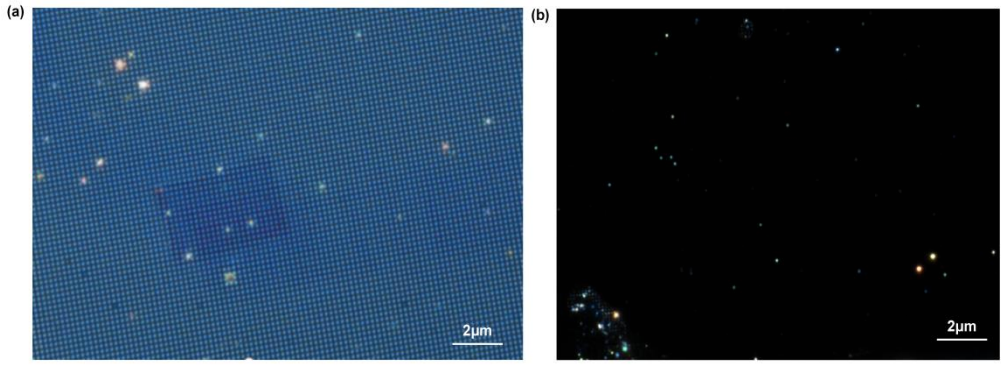


Figure 8.16: (a) Image champ sombre avec PMMA. (b) Après retrait du PMMA – aucune NP observée.

Dans ces essais, la concentration des Si NPs était trop faible (non évaporée), empêchant la formation d'une zone d'accumulation à proximité du ménisque. Inversement, une concentration trop élevée a entraîné une surchauffe de surface par accumulation excessive, rendant l'analyse difficile. Pour y remédier, les échantillons ont été trempés dans l'acétone et soumis à un nettoyage par ultrasons. Pourtant, comme le montre la **Figure 8.17**, des NPs sont toujours présentes, attestant l'efficacité de la silanisation chimique.

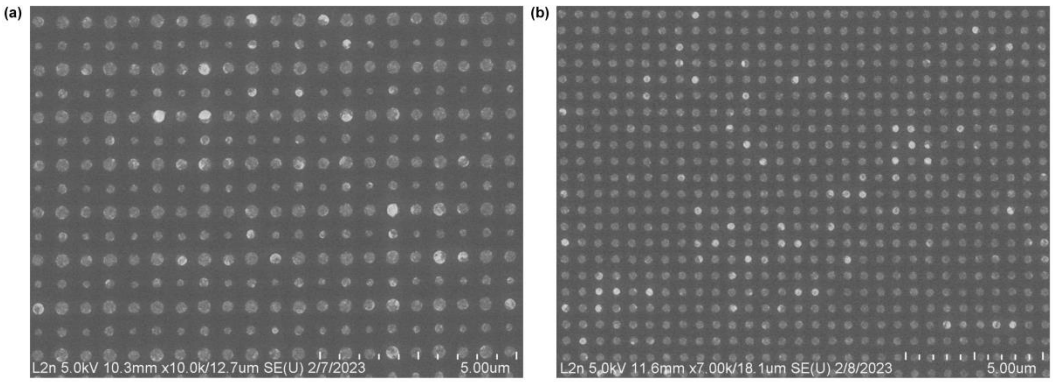


Figure 8.17: (a–b) Images SEM des zones 1 et 2 après trempage prolongé + ultrasons – des NPs persistent sur le substrat.

Cette analyse comparative confirme que le succès de l'assemblage dépend fortement de la concentration en Si NPs. Une concentration trop faible empêche le dépôt ; une concentration excessive entraîne des dépôts incontrôlés. La réaction de silanisation, quant à elle, garantit une fixation chimique robuste des NPs, même après nettoyage

intensif. Ces résultats mettent en lumière la nécessité d'un contrôle précis des paramètres expérimentaux (concentration, mouillage, température), renforçant la fiabilité et reproductibilité de la méthode d'assemblage proposée.

8.4.5 Résultats de simulation FDTD avec Lumerical

La méthode de simulation FDTD (Finite-Difference Time-Domain) via le logiciel Lumerical est utilisée ici pour analyser la réponse optique des structures assemblées. Cette technique permet de modéliser les interactions lumière–matière à l'échelle nanométrique. La **Figure 8.18** présente le schéma des deux zones simulées : Zone 1 : un "pixel" comprend quatre nanoholes de diamètres différents (D_1 = 300 nm, D_2 = 250 nm, D_3 = 200 nm, D_4 = 150 nm); Zone 2 : réseau uniforme avec des nanoholes de 300 nm. L'onde lumineuse incidente est polarisée selon x, et se propage dans la direction z. Le pas du réseau est P = 600 nm dans les deux directions.

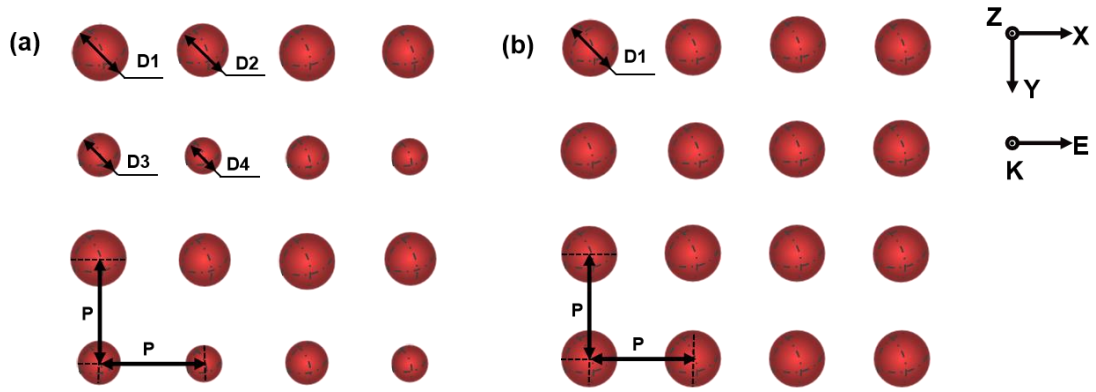


Figure 8.18: Schéma des métasurfaces simulées avec des nanoparticules sphériques de silicium. L'irradiation est effectuée par onde plane monochromatique à incidence normale. Les paramètres géométriques P, D_1-D_4 sont définis.

La **Figure 8.19(a), (c)** montre le spectre d'extinction expérimental et simulé pour la zone 1 et zone 2. Un légèr décalage vers le bleu (blue-shift) est observé dans la simulation, attribué : À un retrait incomplet du PMMA (voir **Figure 8.15**). À une différence morphologique : les simulations supposent des NPs parfaitement sphériques, ce qui diffère de la réalité. Malgré cela, la concordance globale reste forte, validant la fiabilité des modèles. Les cartes de champ électrique normalisé (**Figure**

8.19b, d) montrent une résonance dipolaire nette autour de 963 nm (zone 1) et 964.9 nm (zone 2). Les cartes de champ magnétique (**Figure 8.20**) renforcent cette observation.

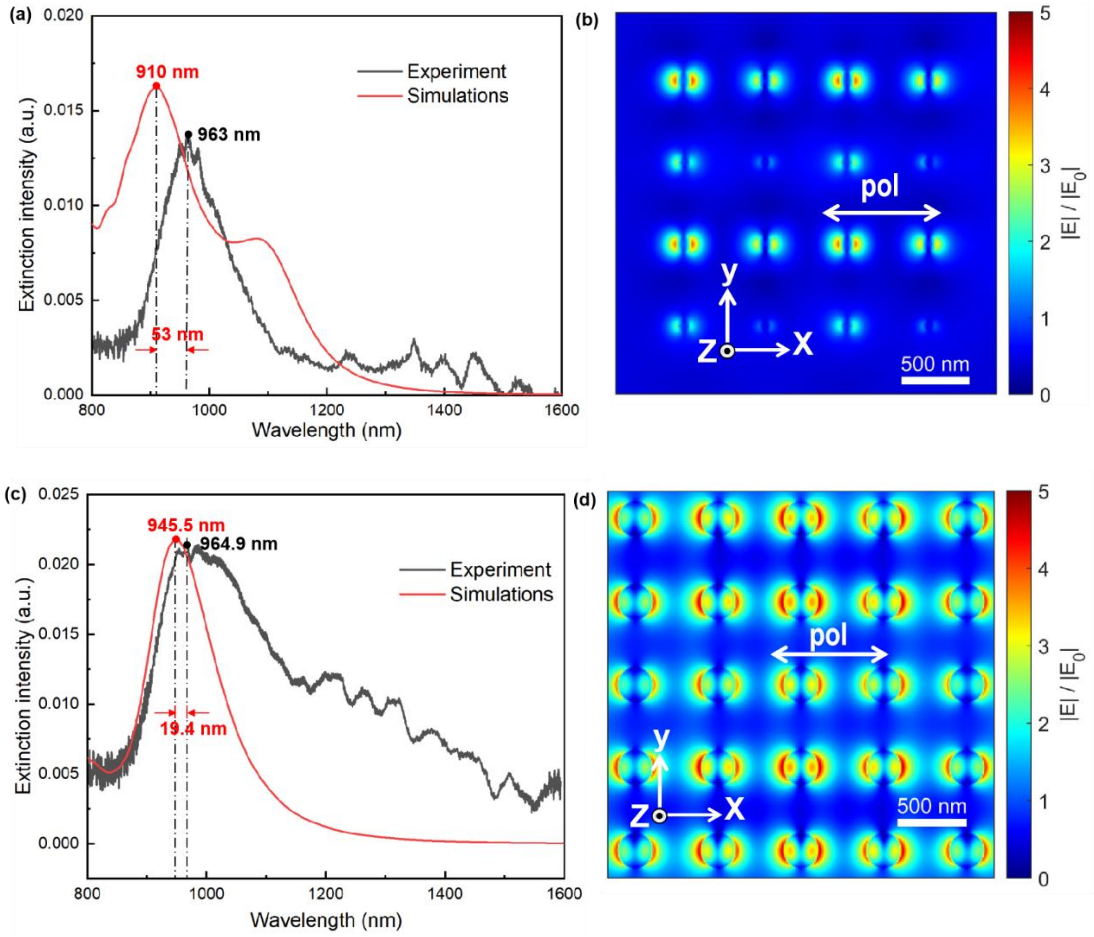


Figure 8.19: (a) Spectre d'extinction zone 1 : courbe noire (exp.) vs rouge (simulation). (b) Carte du champ électrique normalisé – zone 1. (c) Spectre d'extinction zone 2. (d) Carte du champ électrique – zone 2.

Les résonances optiques simulées et mesurées dans le domaine NIR (800–1600 nm) confirment le potentiel des métasurfaces à base de Si NPs pour des applications avancées : capteurs optiques, spectroscopie, dispositifs photoniques, détection de sécurité. Les écarts restants soulignent l'importance d'affiner les modèles numériques pour mieux représenter les conditions expérimentales réelles.

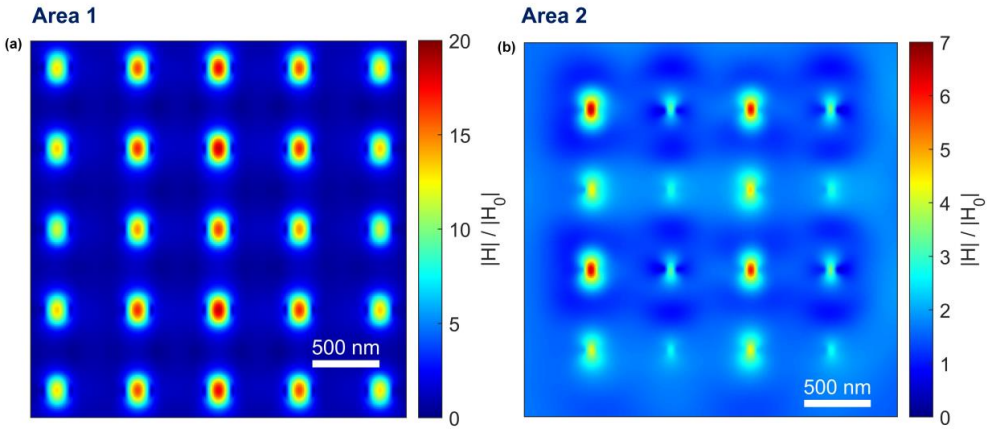


Figure 8.20: Cartes du champ magnétique normalisé : (a) Zone 1; (b) Zone 2.

8.4.6 Conclusions

Dans cette étude, nous présentons une méthode efficace et peu coûteuse d'assemblage de nanoparticules de silicium (Si NPs) sur des substrats nanopatternés en silicium, basée sur l'utilisation d'un mixeur de cuisine pour la préparation des particules. Celles-ci, de forme sphérique et de taille homogène, sont fixées sur le substrat grâce à une silanisation chimique qui améliore également l'angle de mouillage. L'assemblage est réalisé dans un canal microfluidique via des forces capillaires, avec un contrôle précis de la température et du flux d'air (dispositif Smart Force). Les résultats montrent un taux de remplissage proche de 99 % dans les nanoholes, une bonne stabilité des structures sur plus de deux mois, et des résonances optiques dans le proche infrarouge, validées par SEM, AFM, spectroscopie et simulations FDTD. Cette méthode précise, reproductible et adaptée au passage à l'échelle ouvre des perspectives prometteuses en nanophotonique, détection optique, imagerie, et dispositifs anti-contrefaçon.

8.5 Méthode de broyage à billes et assemblage sur substrats en verre ITO

8.5.1 Introduction

Le silicium (Si) est un matériau clé en nanotechnologie en raison de ses excellentes propriétés optiques et de sa grande capacité énergétique. De nombreuses méthodes de fabrication de nanoparticules de Si ont été développées, telles que le dépôt chimique en phase vapeur, l'ablation laser, la synthèse hydrothermale et le broyage mécanique. Dans ce chapitre, nous avons choisi la méthode de broyage à billes en raison de sa simplicité, de son faible coût et de sa capacité à produire des nanoparticules à grande échelle avec une bonne homogénéité de taille.

8.5.2 Méthodologie expérimentale

Dans cette étude, des nanoparticules de silicium (Si NPs) ont été préparées à l'aide d'un broyeur à haute énergie (Emax), comme illustré à la **Figure 8.21**. Deux types de billes de broyage ont été utilisés : des billes en acier inoxydable de 3 mm et des billes en zircone (ZrO_2) de 1 mm, combinées à deux solvants : eau déionisée (DI) et éthanol (ETOH). Le broyage a été réalisé à 500 rpm pendant 4 heures. Après broyage, 85 % de la solution supérieure a été récupérée, stockée au froid, décantée, puis centrifugée pour isoler les Si NPs. La concentration a ensuite été augmentée par évaporation du solvant, et les particules caractérisées par SEM ou DLS.

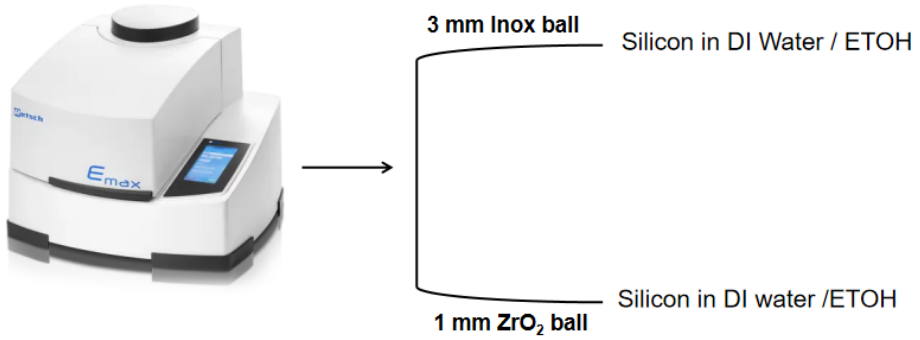


Figure 8.21: Schéma du broyage à billes pour produire des Si NPs avec un broyeur Emax, utilisant des billes Inox (3 mm) ou ZrO_2 (1 mm) dans l'eau ou l'éthanol. Le type et la taille des billes influencent les propriétés des particules.

La lithographie par faisceau d'électrons (EBL) a été utilisée pour fabriquer des substrats en verre ITO nanostructurés. Les substrats (1 cm × 1 cm) ont d'abord été nettoyés par ultrasons, séchés, puis activés par plasma. Une couche uniforme de PMMA (150 nm) a été déposée par spin coating (**Figure 8.22**) avant gravure par EBL pour créer un réseau de nano-trous (**Figure 8.23a**). La silanisation, étape essentielle pour fixer les Si NPs sur le substrat après retrait du PMMA, a été réalisée avec l'APTES. Le substrat activé a été exposé à un mélange d'APTES et d'éthanol pendant 3 heures pour former des liaisons silane-substrat stables (**Figure 8.23b**).

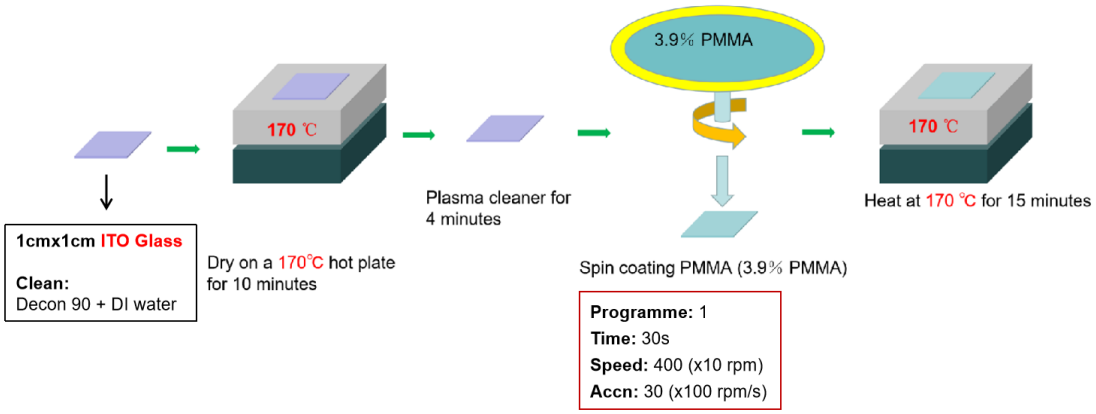


Figure 8.22: Schéma du procédé de dépôt par centrifugation (spin coating) du PMMA.

Enfin, des techniques microfluidiques ont été utilisées pour assembler les Si NPs sur les substrats nanostructurés via des forces capillaires. Le dispositif Smart Force a

permis un dépôt précis en contrôlant l'évaporation des gouttelettes dans des canaux microfluidiques. La température et le flux d'air ont été ajustés pour assurer une distribution homogène des particules dans les structures nanométriques.

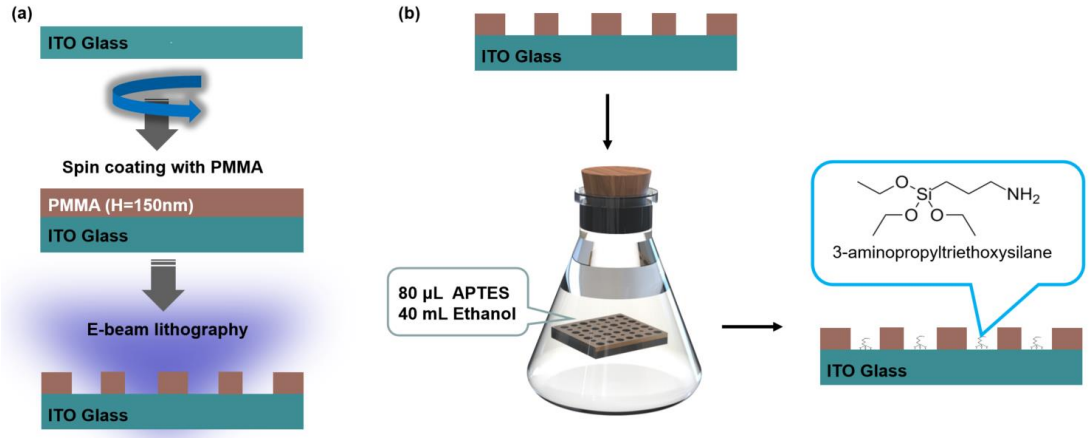


Figure 8.23: (a) Schéma du protocole expérimental de fabrication du substrat en verre ITO nanostructuré par lithographie électronique. (b) Illustration du processus de réaction de silanisation.

8.5.3 Résultats et discussion

Le broyage à billes est une méthode efficace pour obtenir des nanoparticules de silicium (Si NPs) homogènes. Dans cette section, nous étudions l'effet de différents paramètres : type de billes (acier ou ZrO_2), solvant (eau ou éthanol), vitesse et durée de broyage. L'objectif est d'optimiser le procédé pour produire des particules stables, bien dispersées et peu contaminées. Par ailleurs, bien que le mixeur de cuisine permette une préparation rapide de Si NPs, cette méthode présente des limites. L'usure des lames due à la dureté du silicium engendre des particules de taille irrégulière (**Figure 8.24**), et la solution colloïdale obtenue a tendance à s'agglomérer avec le temps, réduisant la qualité de l'assemblage.

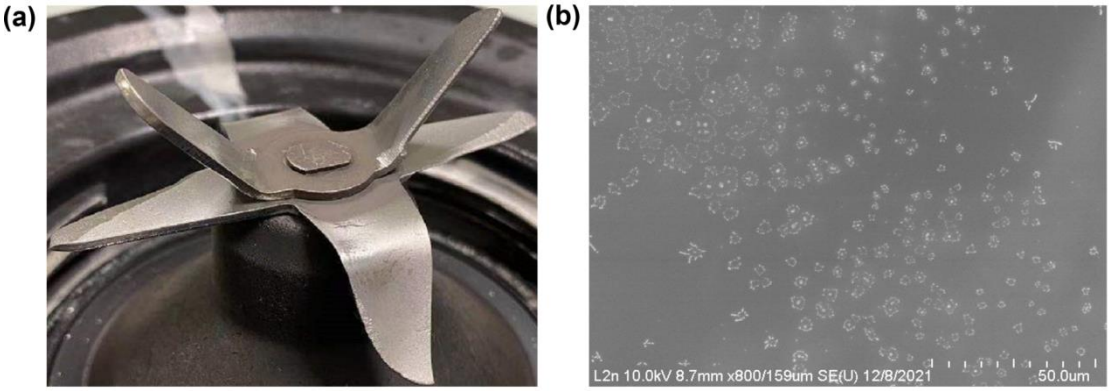


Figure 8.24: (a) Lames du mixeur endommagées après broyage du silicium. (b) Image SEM montrant des Si NPs irrégulières, causées par ces défauts.

L'agrégation des Si NPs affecte directement la qualité de l'assemblage dans les réseaux nanoporeux. Comme observé dans les **Figures 8.25(a) et 25(b)**, les petites nanoparticules remplissent les plus petits pores (150–200 nm), mais les plus grands pores sont souvent occupés par des agrégats de plusieurs particules, au lieu d'un remplissage individuel précis. Cela résulte à la fois de l'irrégularité des particules et de leur vieillissement.

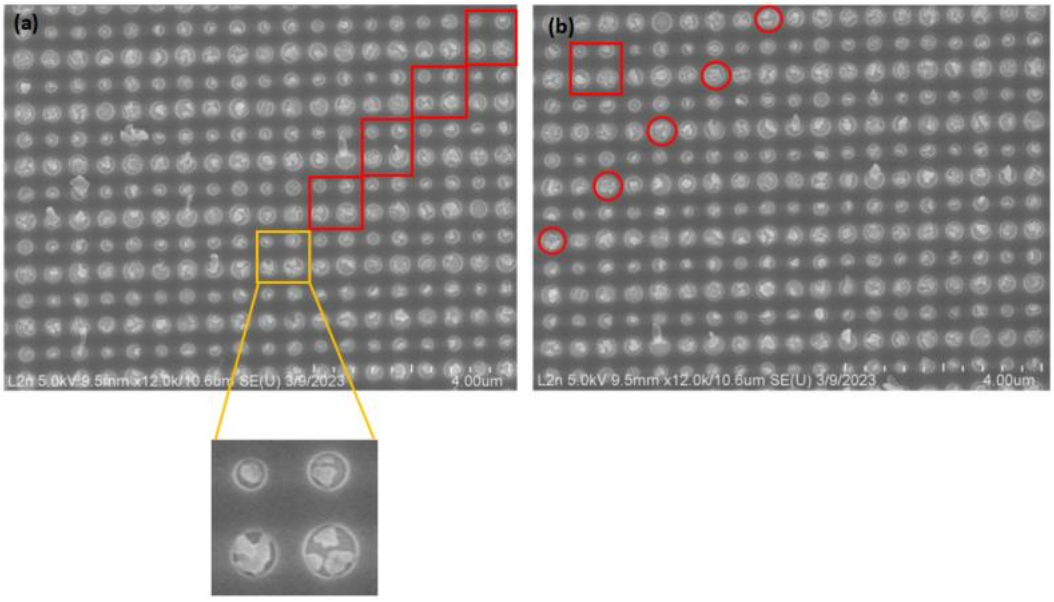


Figure 8.25: (a) Image SEM montrant l'assemblage de Si NPs dans un réseau de nanopores sur verre ITO. Les pores (150 à 300 nm) sont remplis selon leur taille. (b) Image SEM montrant l'agglomération de petites NPs dans les grands pores, compromettant l'assemblage un-à-un.

Les nanoparticules de silicium (Si NPs) obtenues par mixeur présentent souvent des formes irrégulières, ce qui nuit à leur assemblage précis par capillarité. Cela est dû à un écart de taille avec les motifs cibles et à une stabilité colloïdale limitée. Bien que cette méthode soit simple et économique, elle ne convient pas aux applications nécessitant une grande précision. Des techniques complémentaires comme la centrifugation, le tamisage ou des méthodes plus avancées (broyage à billes, ablation laser) peuvent améliorer la qualité des NPs. À l'inverse, le broyage à billes permet d'obtenir des Si NPs plus homogènes. Lors de nos essais (**Figure 8.26**), un mélange de 1 g de silicium et 30 mL d'eau déionisée a été broyé à 2000 rpm pendant 20 à 60 minutes avec 60 billes en acier inoxydable. Après centrifugation, une fine couche d'oxyde a été observée en surface, indiquant une oxydation liée à l'eau. Cela suggère que l'eau n'est pas un solvant idéal pour ce procédé.

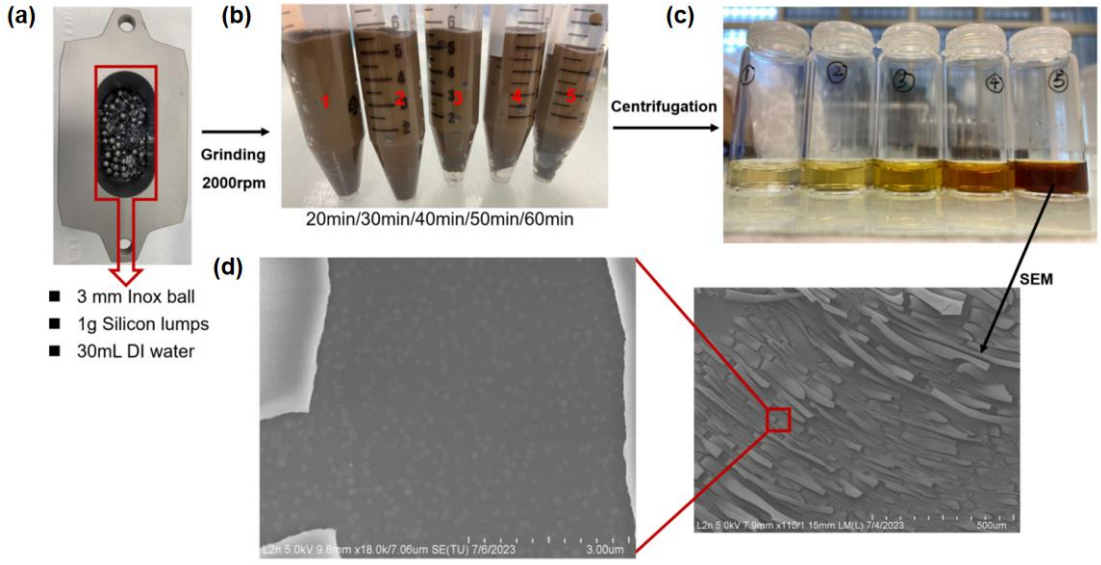


Figure 8.26: (a) Broyeur Emax avec 60 billes Inox (3 mm), 1 g de Si et 30 mL d'eau DI. (b) Évolution de la solution colloïdale après 20 à 60 min de broyage à 2000 rpm. (c) Centrifugation montrant différentes sédimentations. (d) Images SEM : Si NPs bien réparties avec une fine couche oxydée en surface.

Avec l'éthanol comme solvant (**Figure 8.27**), des nanoparticules sphériques d'environ 150 nm ont été obtenues. Toutefois, une contamination par du ferrosilicium (FeSi), liée à l'usure des billes en acier, a été détectée après 50 minutes de broyage. Après 60

minutes, un changement de forme vers des particules cubiques a également été observé. Cette contamination limite l'usage de billes en acier pour les applications exigeant une grande pureté. Pour y remédier, on peut utiliser des billes plus résistantes (zircone, carbure de tungstène), ajuster les paramètres de broyage, ou appliquer une séparation magnétique. En résumé, le broyage à billes est efficace, mais son optimisation est nécessaire pour garantir la qualité des nanoparticules.

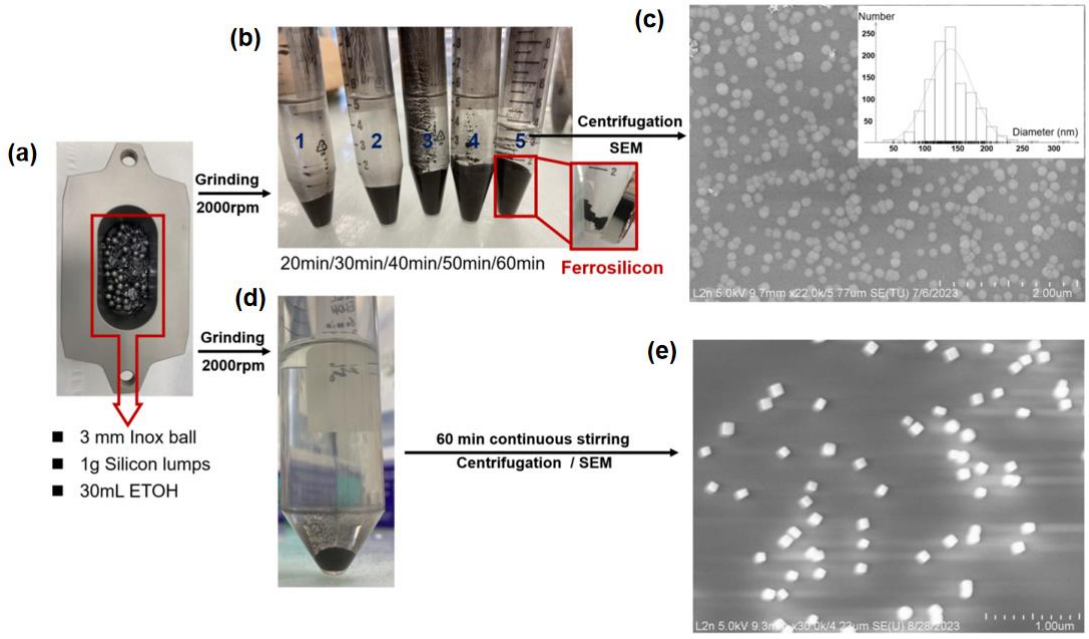


Figure 8.27: (a) Broyeur Emax avec 60 billes en acier (3 mm), 1 g de Si et 30 mL d'éthanol, à 2000 rpm. (b) Solutions après 20–60 min : sédiments croissants (ferrosilicium détecté). (c) Image SEM : NPs sphériques (~150 nm) après 60 min. (d) Solution après 60 min : forte sédimentation. (e) Image SEM : transition vers une forme cubique.

Nous avons observé que les nanoparticules de silicium (Si) préparées avec de l'éthanol (ETOH) présentent des formes plus régulières que celles obtenues avec de l'eau déionisée (DI), comme illustré dans les **Figures 8.27 et 26**. Toutefois, l'utilisation de billes en acier inoxydable provoque une contamination par le ferrosilicium, ce qui altère la forme des particules et complique la purification. Pour éviter ce problème, nous avons remplacé les billes en acier par des billes en ZrO_2 (oxyde de zirconium).

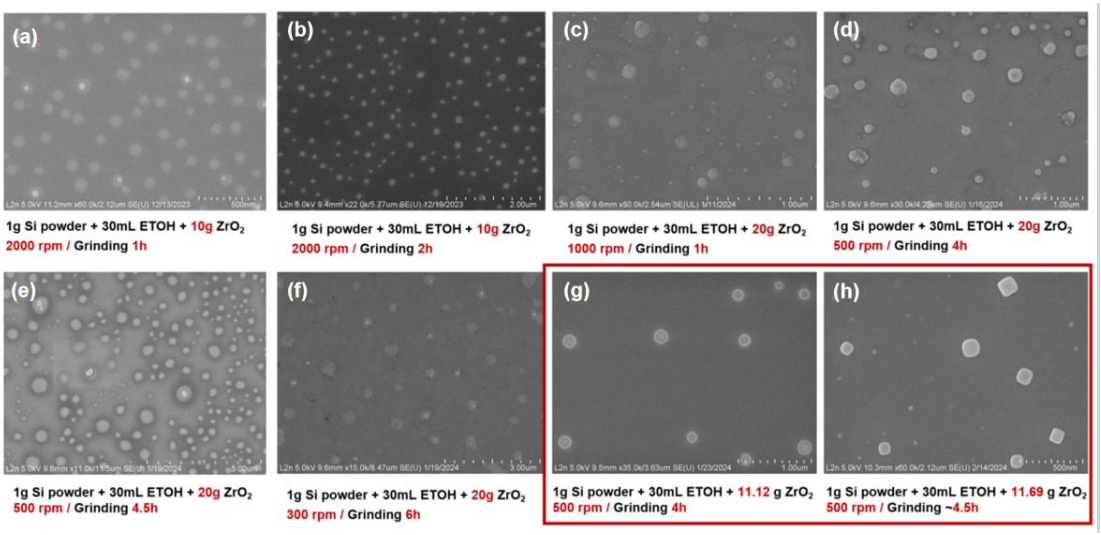


Figure 8.28: Images SEM de Si NPs préparées avec des billes ZrO_2. (a–b) À 2000 rpm, une durée plus longue améliore la forme. (c–f) Baisse de vitesse ou temps excessif : dispersion faible ou agglomération. (g–h) Conditions optimales (1 g Si, 10 g billes ZrO_2, 30 mL éthanol, 500 rpm, 4–4,5 h) : NPs cubiques homogènes. Résultat : broyage efficace, sans contamination.

Une série d'essais (**Figure 8.28**) a permis d'optimiser les paramètres expérimentaux. Les meilleures conditions ont été obtenues avec 1 g de poudre de Si, 30 mL d'éthanol anhydre et ~10 g de billes ZrO_2, broyés à 500 rpm pendant 4 heures. Les résultats (Figures 8g et 8h) montrent des nanoparticules homogènes avec une bonne dispersion.

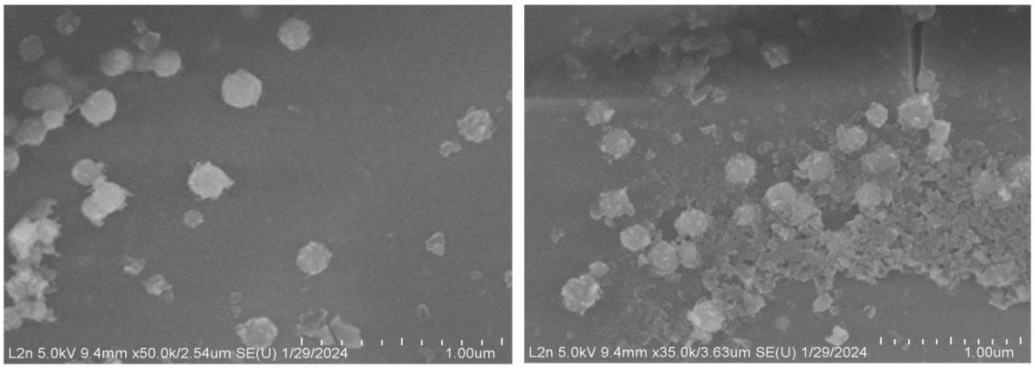


Figure 8.29: Images SEM de Si NPs préparées avec des billes ZrO_2 et de l'eau déionisée. Forte agglomération observée, indiquant que l'eau favorise l'oxydation et n'assure pas une bonne dispersion.

Pour évaluer l'effet du solvant, une autre expérience a été réalisée avec de l'eau DI dans les mêmes conditions. Comme le montre la **Figure 8.29**, une forte agglomération a été observée. Cela confirme que l'eau DI n'est pas adaptée au broyage, même avec des billes en ZrO_2, car elle favorise l'oxydation et la formation d'amas, réduisant la qualité de la solution colloïdale.

En utilisant les paramètres optimisés, nous avons préparé avec succès des nanoparticules de silicium (Si) par broyage à billes. Comme illustré à la **Figure 8.30(a)**, 1 g de poudre de Si, 30 mL d'éthanol anhydre et 11,43 g de billes en ZrO_2 ont été broyés à 500 rpm pendant 4 heures. La solution obtenue a ensuite été soumise à deux étapes de centrifugation, suivies d'une dispersion ultrasonique pour assurer une distribution homogène des particules. L'analyse SEM des fractions supérieures et inférieures a révélé deux populations distinctes : des nanoparticules sphériques d'environ 90 nm dans la couche supérieure (**Figure 8.30b**) et des nanoparticules cubiques d'environ 190 nm dans la couche inférieure (**Figure 8.30c**). Ces résultats confirment la capacité du protocole à séparer efficacement les tailles de particules, et sont cohérents avec ceux obtenus précédemment avec des billes en acier inoxydable, mais sans contamination au ferrosilicium.

La reproductibilité des formes sphériques et cubiques indique un bon contrôle du procédé. L'utilisation de billes en ZrO_2 améliore la pureté sans altérer la taille ou la forme des particules. Des réglages supplémentaires (durée, vitesse, centrifugation) peuvent affiner la distribution selon les besoins. L'observation en champ sombre (Figure 31) confirme la régularité des nanoparticules, un critère essentiel pour des applications en microfluidique ou en électronique.

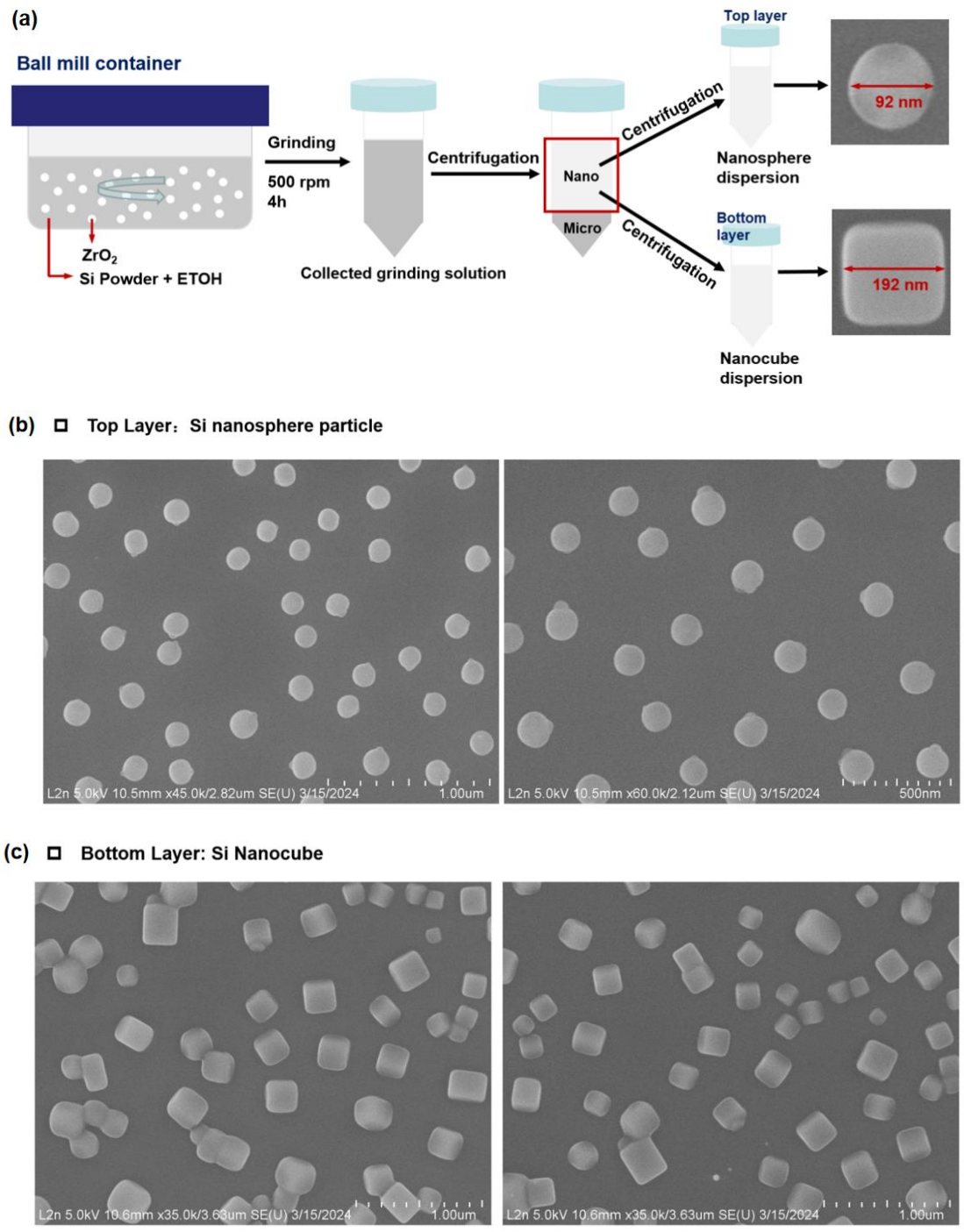


Figure 8.30: (a) Schéma du broyage à billes avec billes ZrO_2 et éthanol anhydre. (b) Image SEM de la couche supérieure : particules sphériques (~92 nm). (c) Couche inférieure : particules cubiques (~192 nm). La morphologie des Si NPs est contrôlable par réglage des paramètres.

En conclusion, le broyage à billes avec des billes en ZrO_2 constitue une méthode fiable et reproductible pour produire des nanoparticules de Si pures, bien définies et adaptées aux applications technologiques avancées. L'ensemble du protocole offre une base solide pour un développement futur et une mise à l'échelle contrôlée.

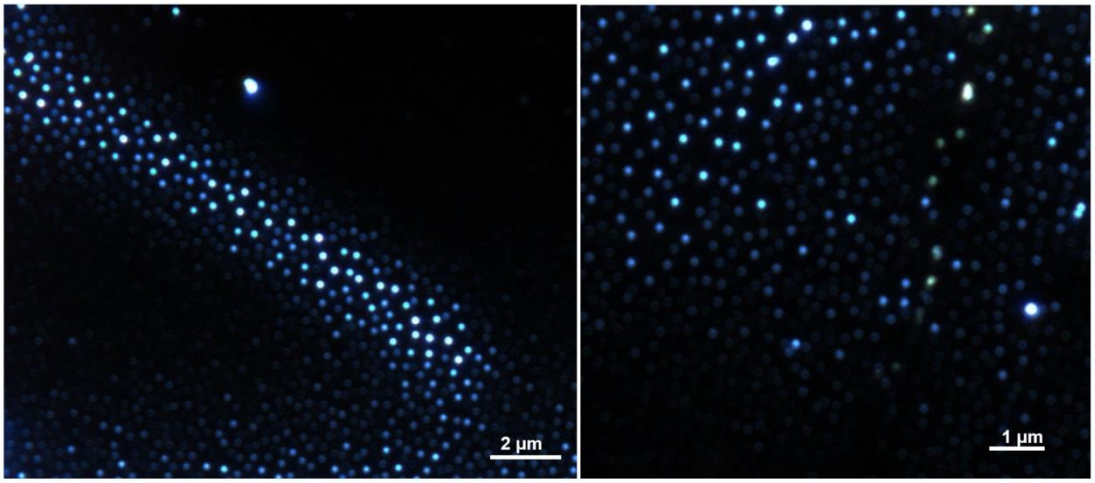


Figure 8.31: Images en champ sombre de Si NPs broyées à billes : contours nets indiquant des particules de forme régulière et homogène.

8.5.4 Dispersion et assemblage des nanoparticules

Pour faciliter l'assemblage des nanoparticules de silicium (Si) préparées par broyage à billes, nous avons étudié l'effet du solvant sur leur dispersion. Une solution colloïdale a été obtenue en broyant 1 g de poudre de Si avec 10 g de billes en ZrO_2 dans 30 mL d'éthanol (ETOH) à 500 rpm pendant 4,5 heures, puis centrifugée. L'analyse SEM (**Figure 8.32a**) a montré des particules sphériques bien définies. Lorsque l'ETOH a été complètement évaporé puis remplacé par de l'eau déionisée (DI), les particules ont subi une forte agglomération et une perte de forme (**Figure 8.32b**). Pour limiter ce phénomène, nous avons modifié le protocole en n'évaporant l'ETOH que partiellement avant d'ajouter l'eau DI. Cette approche a permis de mieux préserver la morphologie des particules (**Figure 8.32c**), bien qu'une certaine agglomération persiste (**Figure 8.32d**). Ces résultats montrent que le rapport ETOH/DI doit être soigneusement ajusté pour garantir une dispersion stable.

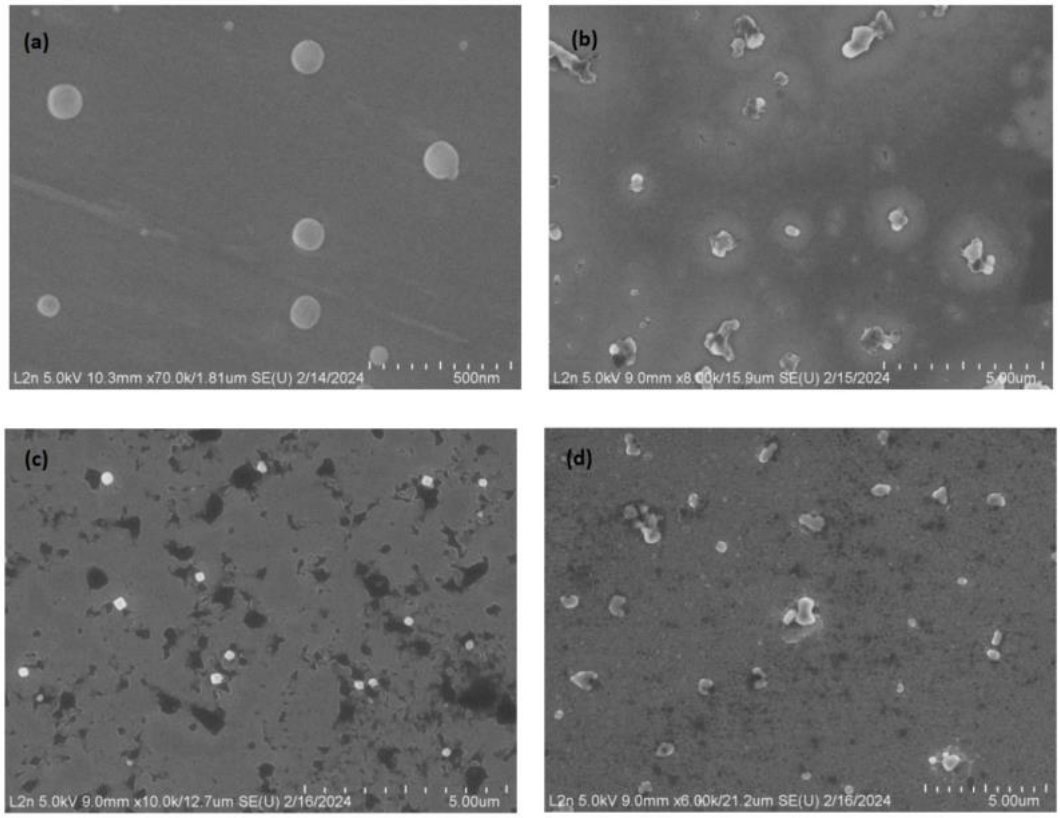


Figure 8.32: Caractérisation SEM des Si NPs selon les conditions d'évaporation : (a) Dans l'éthanol, les particules sont sphériques et régulières ; (b) après remplacement complet par l'eau, forte agglomération ; (c) après évaporation partielle et ajout d'eau, dispersion améliorée ; (d) mélange éthanol/eau : quelques agglomérats présents.

Nous avons ensuite tenté d'assembler ces particules dans des réseaux de nanopores à l'aide de la microfluidique assistée par forces capillaires. Malgré deux cycles d'assemblage, les particules n'ont pas été correctement positionnées dans les pores (**Figure 8.33a**). L'analyse SEM a révélé des pores vides (cercles 1 et 2) et des particules mal déposées sur le substrat (cercles 3 et 4, **Figure 8.33b**). Cela pourrait être dû à une faible concentration en particules ou à des paramètres d'assemblage inadaptés.

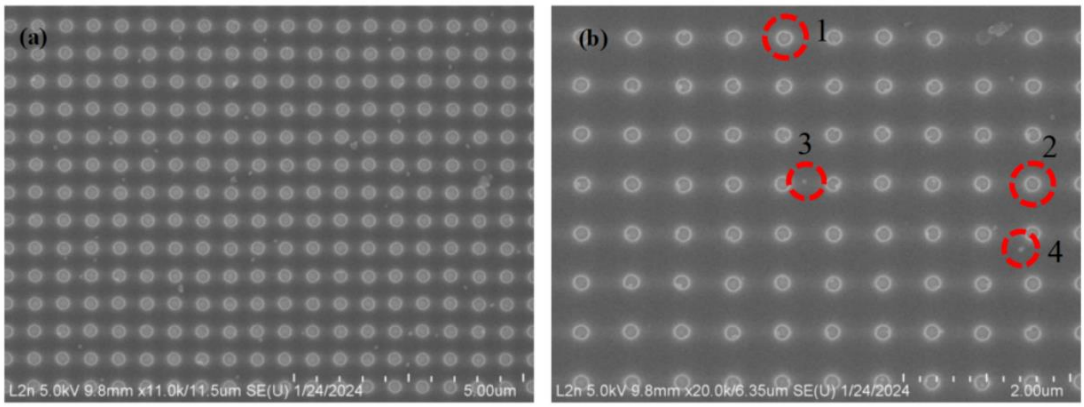


Figure 8.33: Caractérisation SEM de l'assemblage des Si NPs sur réseaux nanoporeux : (a) Vue globale après deux cycles montrant un assemblage imprécis ; (b) zoom sur des pores vides (1,2) et des particules mal positionnées (3,4). Cela met en évidence l'impact d'une faible concentration et de paramètres d'assemblage inadéquats.

Pour améliorer l'efficacité de remplissage, nous avons augmenté le nombre de cycles et réduit le taux d'évaporation de l'éthanol en désactivant le chauffage et la ventilation. Toutefois, même après un troisième cycle (**Figure 8.34**), des pores restaient vides, et des dommages physiques au substrat ont été observés. L'évaporation rapide de l'éthanol rend le contrôle du processus difficile et fragilise les réseaux de nanopores.

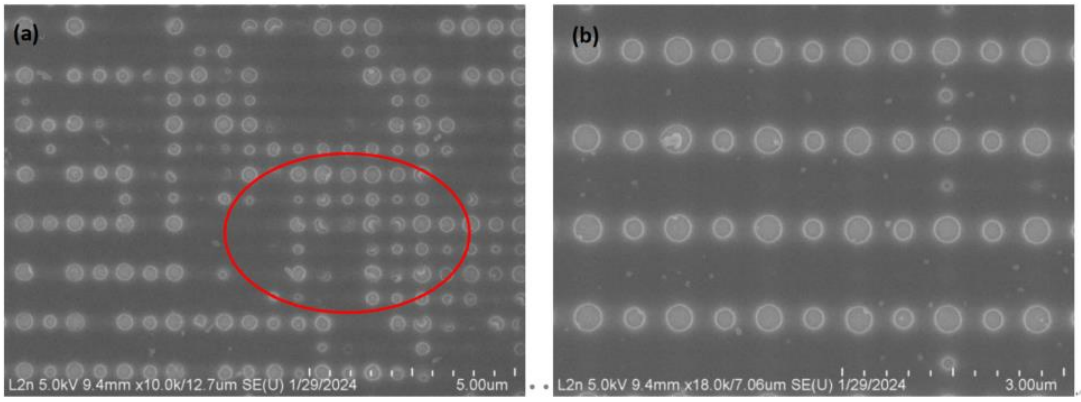


Figure 8.34: Images SEM après un troisième cycle : (a) Dommages au réseau dus à l'évaporation rapide de l'éthanol ; (b) Pores vides et particules mal placées. L'éthanol reste inefficace pour un assemblage précis.

Nous avons également testé une solution à haute concentration de nanoparticules de Si, utilisant un mélange éthanol/eau déionisée (ETOH/DI) comme solvant (T = 35,1 °C ; Q = 51 mL/min). Comme le montre la **Figure 8.35**, cette approche a entraîné une forte agglomération des particules ainsi que des dommages au substrat, sans amélioration significative de l'efficacité de l'assemblage. Ces résultats mettent en évidence plusieurs défis : une faible concentration en particules réduit les chances de remplissage des nanopores, tandis que l'évaporation rapide de l'éthanol perturbe la distribution homogène des particules et fragilise les structures du substrat. De plus, augmenter la concentration des nanoparticules sans ajuster d'autres paramètres expérimentaux tend à accentuer le phénomène d'agglomération, rendant l'assemblage encore moins efficace.

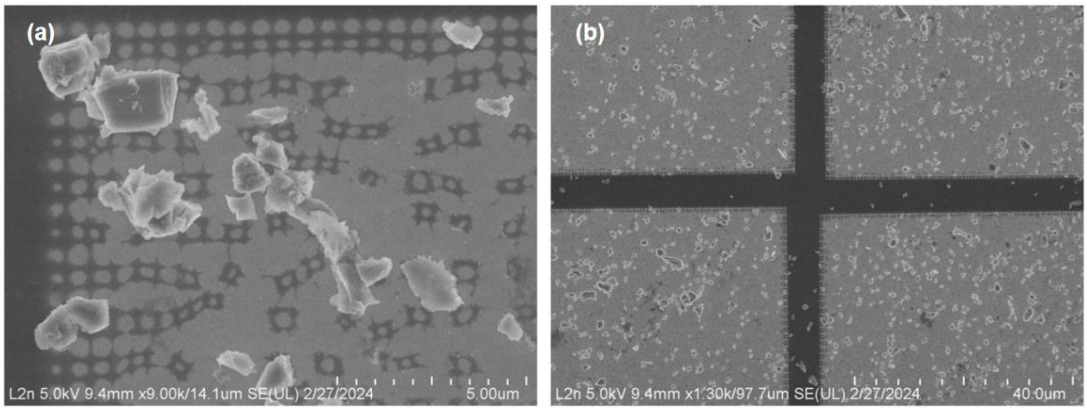


Figure 8.35: Images SEM de l'assemblage avec un mélange éthanol/eau DI : (a) Amas de particules et dommages aux nanopores ; (b) Répartition inégale et agglomérations sur le substrat.

En conclusion, la composition du solvant, la concentration des nanoparticules et les paramètres d'assemblage doivent être soigneusement optimisés. L'utilisation d'un solvant moins volatil et le développement d'un protocole d'assemblage plus doux pourraient permettre d'améliorer à la fois l'efficacité de remplissage et la protection des substrats nanostructurés.

8.5.5 Conclusion

Ce chapitre a montré qu'il est possible de produire des nanoparticules de silicium (Si) par broyage à billes en ajustant les conditions. L'usage de billes en acier avec de l'eau entraîne une oxydation, tandis que l'éthanol donne des particules bien définies mais contaminées par du ferrosilicium. L'utilisation de billes en ZrO_2 a permis d'éviter cette contamination. En broyant 1 g de Si dans 30 mL d'éthanol à 500 rpm pendant 4 h, nous avons obtenu des particules sphériques (~90 nm) et cubiques (~190 nm). Cependant, l'éthanol s'évapore trop vite pendant l'assemblage, ce qui rend le processus instable et abîme le PMMA. Remplacer l'éthanol par de l'eau provoque une forte agglomération. Ainsi, bien que la qualité des particules soit bonne, la stabilité de la solution colloïdale reste un problème. Des efforts futurs devront se concentrer sur l'amélioration des solvants ou l'adaptation des protocoles pour un assemblage plus efficace.

8.6 Assemblage de nanoparticules de Si sur des substrats nano-structurés complexes

Ce chapitre compare deux méthodes de préparation de nanoparticules de silicium (Si NPs) : le mixeur de cuisine et le broyeur à billes. Les Si NPs produites par mixeur sont bien dispersées dans l'eau déionisée, ce qui facilite leur assemblage sur des substrats nanostructurés via la technologie microfluidique SmartForce. À l'inverse, les particules obtenues par broyage à billes, bien que homogènes, ne se dispersent que dans l'éthanol, un solvant trop volatil pour un assemblage stable. Ainsi, nous avons privilégié la méthode du mixeur, qui permet un positionnement précis des Si NPs sur des motifs complexes, ouvrant la voie à la fabrication de dispositifs optiques en silicium à bas coût.

8.6.1 Introduction

Les nanoparticules de silicium (Si NPs) sont des matériaux polyvalents, idéaux pour la nanophotonique, la nanoélectronique et la fabrication de métasurfaces, grâce à leur

fort indice de réfraction et leurs faibles pertes optiques. Dans nos travaux, nous avons préparé des Si NPs par deux méthodes mécaniques : le blender domestique et le broyeur à billes. Le blender, simple et peu coûteux, produit des Si NPs bien dispersées dans l'eau, compatibles avec l'assemblage microfluidique. Le broyage à billes donne aussi des particules uniformes, mais leur dispersion dans l'éthanol rend l'assemblage plus difficile. Ainsi, le blender s'avère plus adapté, notamment pour l'assemblage sur des substrats à motifs complexes. Dans ce chapitre, nous exploitons cette méthode pour positionner précisément des Si NPs sur des motifs irréguliers en silicium, en optimisant les paramètres microfluidiques comme la température et l'évaporation. L'objectif est d'étendre cette approche à la fabrication de dispositifs nanophotoniques et électroniques sur mesure.

8.6.2 Méthodologie expérimentale

Dans cette étude, nous avons développé une méthode simple et économique pour assembler des nanoparticules de silicium (Si NPs) sur des motifs nanométriques de type Einstein. Les Si NPs ont été préparées à l'aide d'un blender domestique, en broyant 10 g de silicium pur avec 300 mL d'eau déionisée par cycles pour éviter la surchauffe. Après décantation et centrifugation, une solution colloïdale stable a été obtenue. Les substrats, fabriqués par lithographie électronique (EBL) sur du silicium recouvert de SiO_2, ont été nettoyés, recouverts de PMMA puis fonctionnalisés par silanisation avec une solution d'APTES pour fixer chimiquement les NPs. L'assemblage a été réalisé à l'aide d'un dispositif microfluidique Smart Force, exploitant l'évaporation et les forces capillaires pour guider les Si NPs dans les motifs. Ce procédé a permis un dépôt précis et reproductible des particules, montrant l'efficacité de cette approche pour fabriquer des métasurfaces complexes à faible coût.

8.6.3 Results and Discussion

Comme expliqué précédemment, cette comparaison illustre la performance d'assemblage des nanoparticules de silicium (Si NPs) préparées par blender domestique et par broyage à billes sur des substrats nanopatronnés. Les résultats

montrent que les Si NPs obtenues avec le blender sont nettement supérieures pour l'assemblage de métasurfaces, tandis que celles obtenues par broyage à billes présentent des limites importantes dans des applications similaires. Les Si NPs du blender, montrées en **Figures 8.36(a) et (b)**, se distinguent par une excellente uniformité de taille et une dispersion stable. Leur dispersion efficace dans l'eau déionisée, combinée à l'assemblage microfluidique basé sur des forces capillaires, permet un taux de remplissage élevé tout en préservant l'intégrité du substrat. Cette méthode, à la fois économique et efficace, offre un potentiel prometteur pour l'assemblage précis de métasurfaces et soutient le développement de dispositifs nanophotoniques fonctionnels.

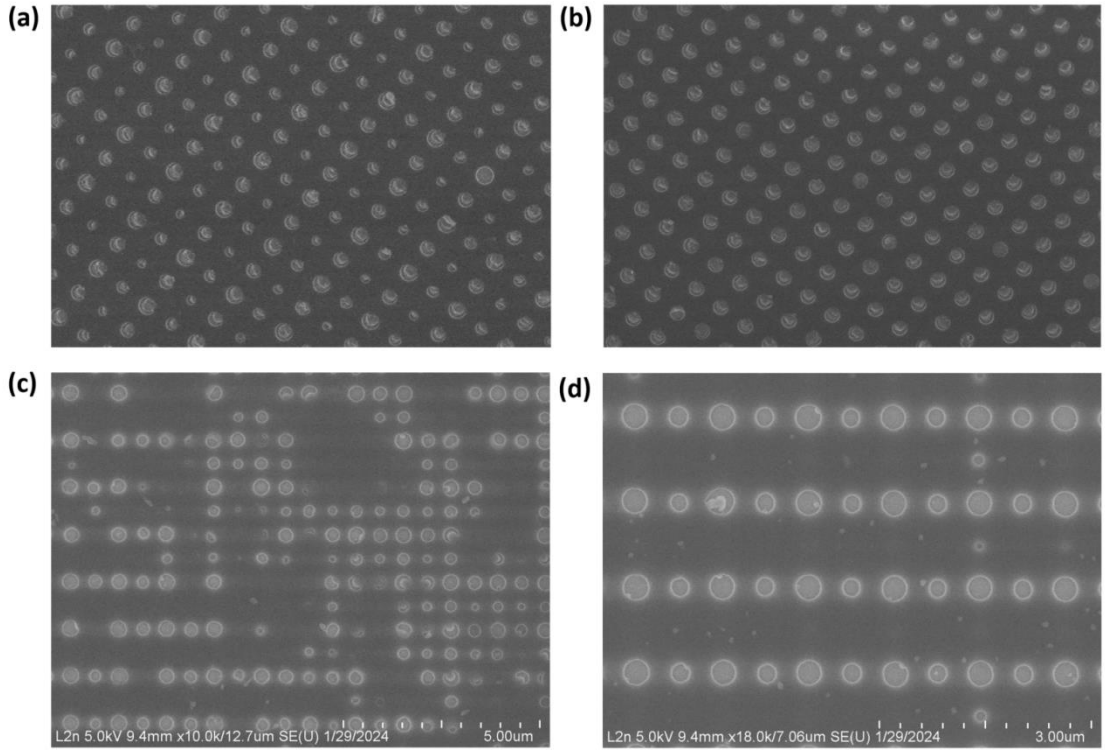


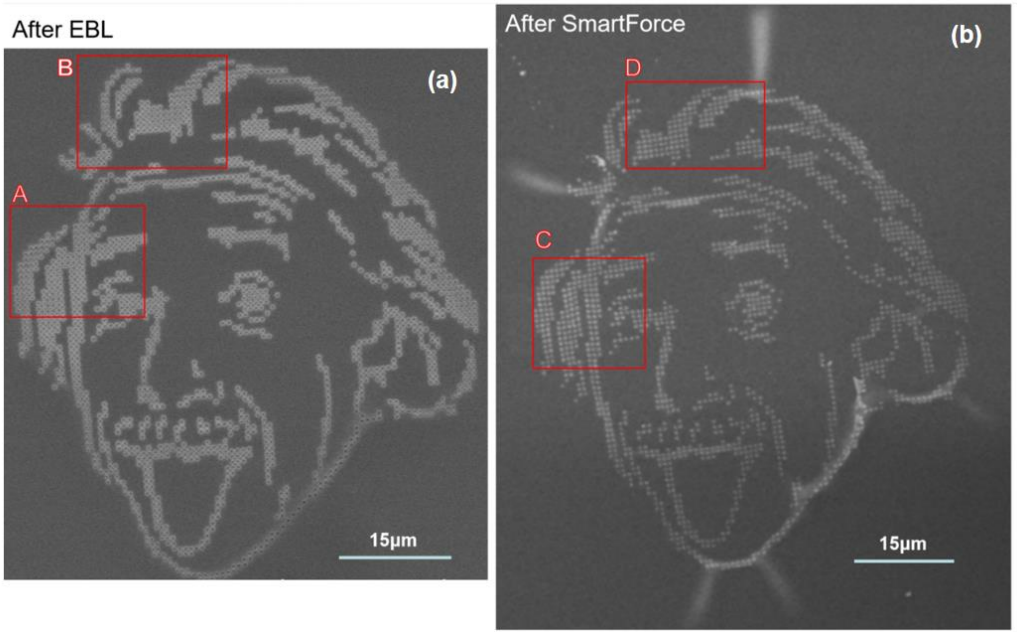
Figure 8.36: Images MEB de l'assemblage des Si NPs : (a, b) Celles du blender sont homogènes, stables et bien assemblées ; (c, d) Celles du broyeur sont instables et endommagent le substrat.

Les Si NPs obtenues par broyage à billes, illustrées en **Figures 8.36(c) et (d)**, présentent une instabilité liée à la volatilité de l'éthanol, causant une agrégation fréquente et des dommages aux substrats nanopatternés. Cela réduit l'efficacité de

l'assemblage, en particulier pour les applications demandant précision et stabilité. En comparaison, les Si NPs préparées avec un blender offrent un meilleur taux de remplissage sans détériorer les structures, ce qui les rend plus adaptées aux métasurfaces complexes. Des améliorations futures pourraient porter sur les paramètres de préparation et sur la conception de structures multifonctionnelles.

Le motif d'Einstein, riche en détails et courbes fines, sert ici de modèle de test pour valider la précision et la régularité de l'assemblage des Si NPs. Ces nanoparticules, produites par broyage au blender, ont été déposées sur des substrats en silicium fortement dopé, recouverts de PMMA puis gravés par lithographie électronique (EBL). Une silanisation à l'APTES a permis de fixer les Si NPs chimiquement. L'assemblage microfluidique basé sur l'évaporation guidée a ensuite permis le dépôt précis des particules dans les nanoholes du motif Einstein. Les conditions expérimentales (température, flux, évaporation) ont été optimisées pour garantir un alignement uniforme.

Enfin, une analyse MEB a été réalisée pour évaluer la qualité du motif. La **Figure 8.37(a)** montre le substrat après EBL mais avant l'assemblage : la zone A (cheveux d'Einstein) présente une forte densité de nanoholes bien définis (~200 nm de diamètre), tandis que la zone B (contour du visage) confirme la finesse du motif.



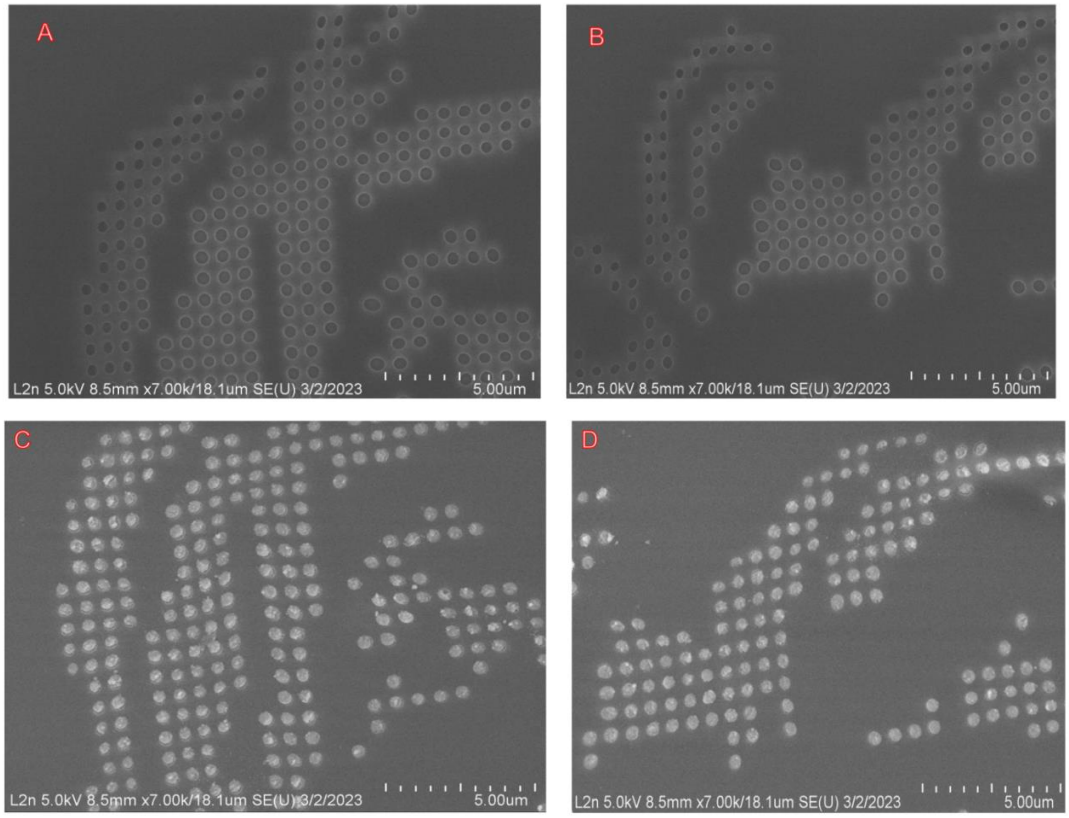


Figure 8.37: Images MEB montrant l'assemblage des Si NPs sur le substrat à motifs Einstein avant et après le processus. (a) Substrat après EBL, avant l'assemblage. Les régions A et B montrent l'uniformité et l'agencement des nanopores. (b) Substrat après assemblage avec le dispositif SmartForce. Les régions C et D montrent le remplissage réussi des nanopores par les Si NPs.

Figure 8.37(b) illustre la surface du substrat après assemblage des Si NPs via la technologie SmartForce. Les zones C (œil gauche) et D (extrémité des cheveux) montrent un taux de remplissage des nanopores proche de 100 %, avec une distribution uniforme des particules, même dans les zones complexes. Cela démontre la haute précision de l'assemblage capillaire assisté par microfluidique. L'analyse par microscopie en champ sombre (**Figure 8.38**) complète ces observations. L'image **Figure 8.38(a)** montre le motif d'Einstein obtenu après lithographie avec une excellente fidélité géométrique. L'image **Figure 8.38(b)** après assemblage révèle que les Si NPs sont bien intégrées dans les nanopores, sans altération du motif initial. Une diffusion lumineuse renforcée est observée, liée à l'interaction optique entre les particules et le substrat.

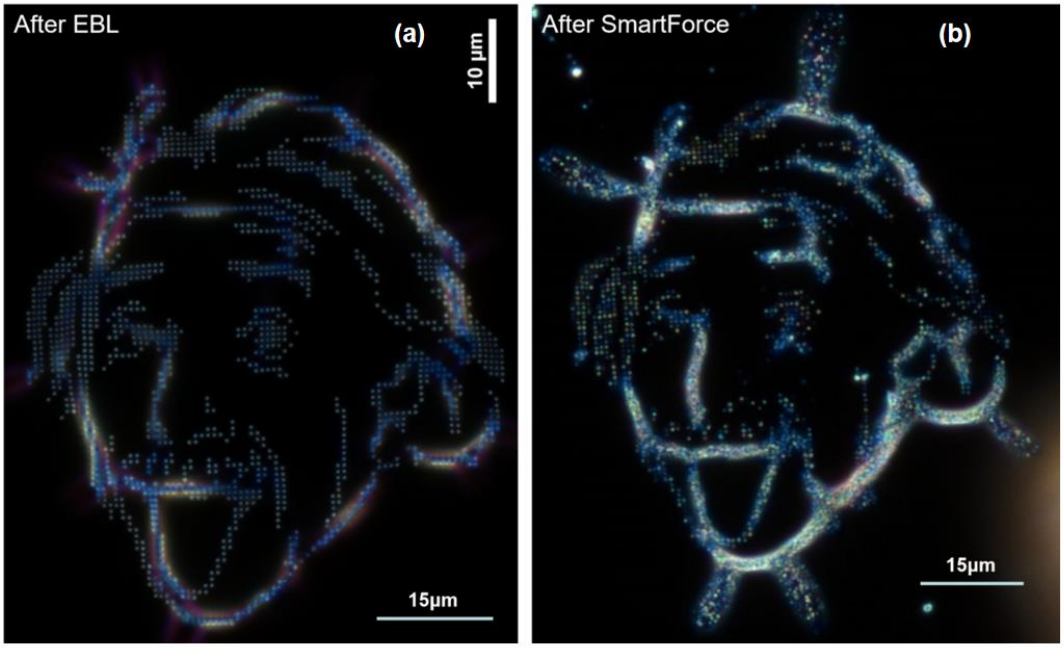


Figure 8.38: Images en microscopie à fond noir du substrat à motifs Einstein avant et après l'assemblage des nanoparticules de silicium (Si NPs). (a) Après lithographie électronique : l'image montre l'arrangement précis des nanopores et les caractéristiques géométriques définies. (b) Après assemblage SmartForce : l'image révèle le remplissage réussi des nanopores par les Si NPs, tout en préservant la structure originale du motif.

Pour finaliser l'assemblage, l'échantillon est immergé dans l'acétone pendant 3 heures afin de dissoudre la couche de PMMA, ne laissant que les Si NPs en place. Cette étape confirme la robustesse de l'assemblage, sans besoin de nettoyage mécanique, préservant ainsi la structure du motif. **Figure 8.39** présente l'analyse post-dissolution par microscopie en champ sombre (**Figure 8.39a**) et MEB (**Figure 8.39b**). Les images confirment que les Si NPs restent bien positionnées, formant un motif clair et défini. Les zones E (contours du visage) et F (cheveux) révèlent une bonne homogénéité du remplissage, sans agrégation ni perte de particules, même dans les zones à forte densité.

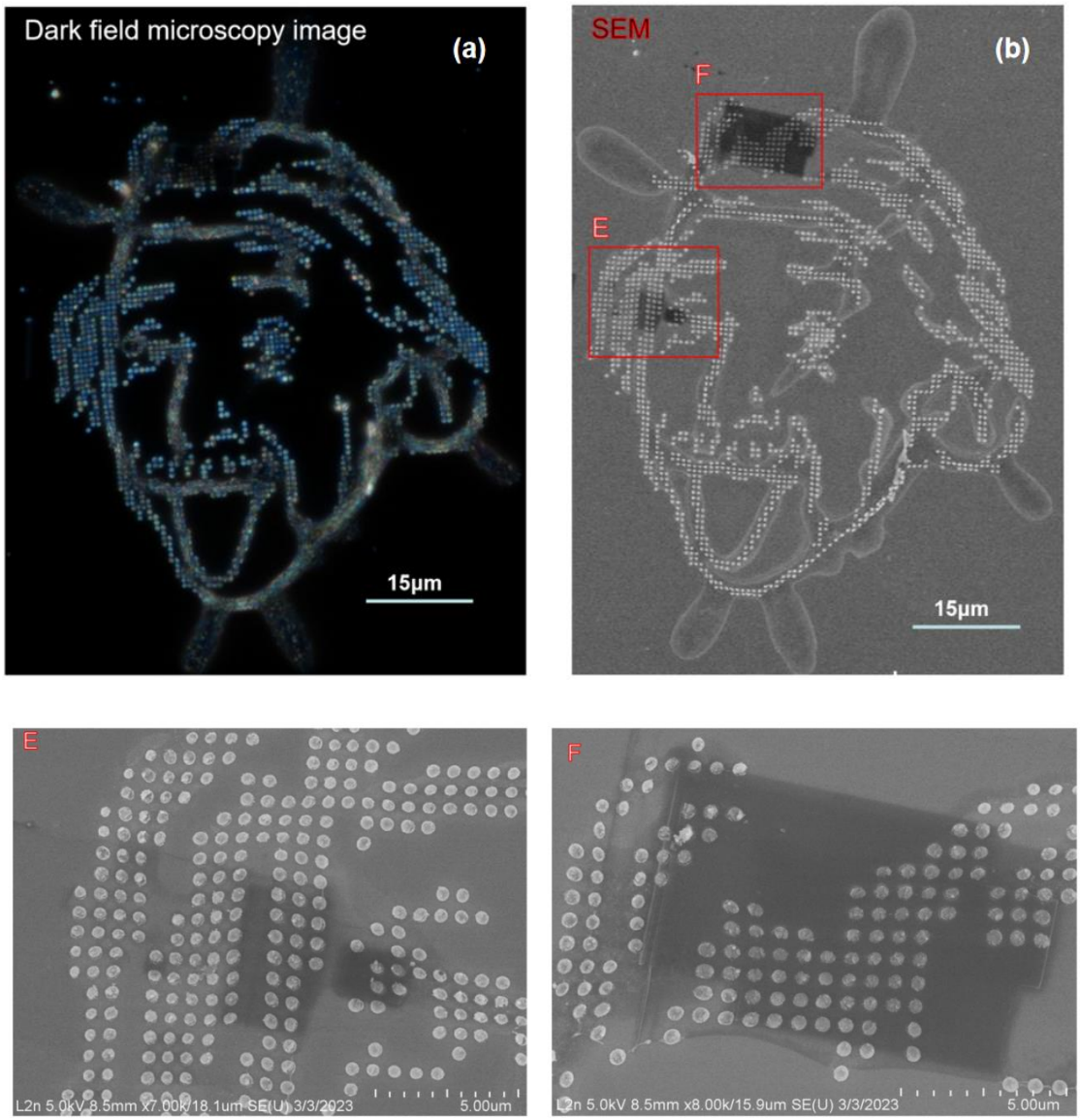


Figure 8.39: Analyse des résultats d'assemblage des Si NPs sur le substrat à motifs Einstein après retrait du PMMA, en microscopie à fond noir et MEB. (a) L'image à fond noir montre l'ensemble du motif Einstein avec un positionnement précis des Si NPs, souligné par une diffusion lumineuse accrue. (b) L'image MEB illustre le substrat après assemblage. Les encarts E et F offrent des vues haute résolution de certaines zones.

La réaction de silanisation, réalisée avec l'APTES, joue un rôle clé. Elle crée une liaison chimique forte entre les Si NPs et le substrat via des liaisons siloxane, augmentant l'adhérence et la stabilité du motif. Elle améliore également la précision de l'assemblage et prévient le déplacement des particules pendant les étapes de

traitement, notamment durant l'immersion dans l'acétone. En combinant microscopie optique et électronique, cette étude valide l'efficacité de la technologie SmartForce et du procédé de silanisation pour l'assemblage précis de structures nanométriques complexes. Elle démontre également la faisabilité d'utiliser des Si NPs obtenues par mixeur domestique pour des applications en nanophotonique avancée.

8.6.4 Conclusion

Ce chapitre montre qu'il est possible d'assembler efficacement des nanoparticules de silicium (Si NPs) sur des motifs complexes en combinant une méthode simple de broyage au mixeur avec la technologie microfluidique. Par rapport au broyage à billes, les Si NPs obtenues au mixeur sont plus homogènes et stables dans l'eau, facilitant leur dépôt précis. Un motif d'Einstein a été fabriqué par lithographie électronique, et les Si NPs y ont été insérées avec précision grâce à l'évaporation contrôlée dans le système SmartForce. La silanisation à l'APTES a renforcé l'adhésion des particules, assurant leur maintien après le retrait du PMMA. Les observations confirment un assemblage stable et uniforme, y compris dans les zones fines du motif. Cette méthode simple et peu coûteuse est prometteuse pour la fabrication de métasurfaces complexes en nanophotonique et en électronique.

Juan XIN

Doctorat : Matériaux, Mécanique, Optique et Nanotechnologie

Année 2025

De la synthèse à l'assemblage : étude de la fabrication d'une métasurface à base de silicium

Cette étude compare deux méthodes de fabrication de nanoparticules de silicium (Si NPs) : le mixeur de cuisine et le broyage à billes, et évalue leur assemblage sur des substrats nano-structurés pour développer des métasurfaces diélectriques en silicium à faible coût et haute précision. Le mixeur de cuisine, basé sur le broyage de silicium (10 g / 300 mL d'eau déionisée) suivi d'une centrifugation, produit des Si NPs sphériques (45–220 nm) avec une dispersion stable (potentiel Zeta -33,5 mV), adaptées à une production à grande échelle. Le broyage à billes avec des billes de ZrO_2 dans l'éthanol anhydre génère des Si NPs (90–190 nm), mais la volatilité de l'éthanol entraîne l'agrégation des particules et des dommages au substrat. Grâce à la lithographie par faisceau d'électrons (EBL) et à la silanisation (APTES/éthanol), l'assemblage assisté par force capillaire atteint un taux de remplissage >99 % sur un motif complexe comme le « motif d'Einstein ». Les Si NPs issues du mixeur de cuisine montrent une précision d'assemblage exceptionnelle, confirmée par microscopie. L'optimisation du traitement de silanisation améliore l'adhésion des particules et préserve l'intégrité du motif après retrait du gabarit PMMA. En conclusion, la méthode du mixeur de cuisine, plus économique et stable en phase aqueuse, surpasse le broyage à billes et offre une solution fiable pour la fabrication de métasurfaces optiques complexes, ouvrant de nouvelles perspectives en nanophotonique et électronique.

Mots clés : nanosilicium – lithographie par faisceau d'électrons – métasurfaces – chimie des surfaces – autoassemblage – microfluidique.

From Synthesis to Assembly: Study of a Silicon based Metasurface Fabrication

This study compares two methods for fabricating silicon nanoparticles (Si NPs): the kitchen blender method and ball milling, and evaluates their assembly on nano-structured substrates to develop low-cost, high- precision dielectric silicon-based metasufaces. The kitchen blender method, based on grinding silicon (10 g / 300 mL deionized water) followed by centrifugation, produces spherical Si NPs (45–220 nm) with stable dispersion (Zeta potential -33.5 mV), making it suitable for large-scale production. In contrast, ball milling with ZrO_2 balls in anhydrous ethanol generates Si NPs (90–190 nm), but ethanol's high volatility causes particle aggregation and substrate damage, limiting its application. Through electron beam lithography (EBL) and silanization (APTES/ethanol), capillary force-assisted assembly achieves a filling rate of over 99% on complex patterns such as the "Einstein pattern." Si NPs produced by the kitchen blender method exhibit exceptional assembly precision, confirmed by microscopy. Optimized silanization treatment enhances particle adhesion and maintains pattern integrity after PMMA template removal. In conclusion, the kitchen blender method, being more cost-effective and stable in an aqueous phase, outperforms ball milling and offers a reliable solution for the large-scale fabrication of complex optical metasurfaces, opening new perspectives in nanophotonics and electronics.

Keywords: nanosilicon – lithography, electron beam – metasurfaces – surface chemistry – self-assembly (chemistry) – microfluidics.

Thèse réalisée en partenariat entre :

CHINA SCHOLARSHIP COUNCIL

utt UNIVERSITÉ DE TECHNOLOGIE TROYES

Ecole Doctorale "Sciences pour l'Ingénieur"